Synthesis of Nanometer-size Inorganic Materials for the Examination of Particle Size Effects on Heterogeneous Catalysis

by

Sean Christian Emerson

A Dissertation

Submitted to the Faculty

of the

WORCESTER POLYTECHNIC INSTITUTE

in partial fulfillment of the requirements for the

Degree of Doctor of Philosophy

in

Chemical Engineering

by

_____

May 2000

APPROVED:

_____

Dr. William R. Moser, Major Advisor

_____

Dr. Ravindra Datta, Department Head

_____

Dr. Yi Hua Ma

_____

Dr. Satya Shivkumar

Abstract

The effect of acoustic and hydrodynamic cavitation on the precipitation of inorganic catalytic materials, specifically titania supported gold, was investigated. The overall objective was to understand the fundamental factors involved in synthesizing nanometer-size catalytic materials in the 1–10 nm range in a cavitating field. Materials with grain sizes in this range have been associated with enhanced catalytic activity compared to larger grain size materials.

A new chemical approach was used to produce titania supported gold by co-precipitation with higher gold yields compared to other synthesis methods. Using this approach, it was determined that acoustic cavitation was unable to influence the gold mean crystallite size compared to non-sonicated catalysts. However, gold concentration on the catalysts was found to be very important for CO oxidation activity. By decreasing the gold concentration from a weight loading of 0.50% down to approximately 0.05%, the rate of reaction per mole of gold was found to increase by a factor of 19.

Hydrodynamic cavitation at low pressures (6.9–48 bar) was determined to have no effect on gold crystallite size at a fixed gold content for the same precipitation

technique used in the acoustic cavitation studies. By changing the chemistry of the precipitation system, however, it was found that a synergy existed between the dilution of the gold precursor solution, the orifice diameter, and the reducing agent addition rate. Individually, these factors were found to have little effect and only their interaction allowed gold grain size control in the range of 8–80 nm.

Further modification of the system chemistry and the use of hydrodynamic cavitation at pressures in excess of 690 bar allowed the systematic control of gold crystallite size in the range of 2–9 nm for catalysts containing $2.27 \pm 0.17\%$ gold. In addition, it was shown that the enhanced mixing due to cavitation led to larger gold yields compared to classical syntheses. The control of gold grain size was gained at the loss of CO activity, which was attributed to the formation of non-removable sodium titanate species. The increased mixing associated with cavitation contributed to the activity loss by partially burying the gold and incorporating more of the sodium titanate species into the catalysts.

This work produced the first evidence of hydrodynamic cavitation influencing the gold crystallite size on titania supported gold catalysts and is the only study reporting the control of grain size by simple mechanical adjustment of the experimental parameters. Despite the low activity observed due to sodium titanate, the methodology of adjusting the chemistry of a precipitating system could be used to eliminate such species. The approach of modifying the chemical precipitation kinetics relative to the dynamics of cavitation offers a general scheme for future research on cavitational processing effects.

Acknowledgments

I would like to thank Professor Moser for the opportunity to be his Ph.D. student and to work on this dissertation. I have learned a great many things about research from him. I also want to thank the members of my committee for taking the time out of their busy schedules to participate in my proposal and defense. In addition, there are several other people who deserve special thanks and contributed to this dissertation in different ways.

Aaron Coolidge has been a great friend who has given me encouragement when times were difficult. No better or more knowledgeable friend could anyone ask for. I want to thank him for the times when he forced me to leave the lab for dinner every month or two so that I could remain sane.

I also want to thank my fellow lab partner, Ivo Krausz, for sharing this experience with me. In both the good times and the bad, it has always been a pleasure to work along side him, and I consider him a great friend. He deserves special thanks for helping me correct the document you are reading; any errors you find are of course my fault.

For several years now, there has been a small “Dutch colony” in our department,

of which Ivo is a member. From these folks, I have gained a greater appreciation of the world at large, and found their observations and view points both helpful and entertaining. Among the colony members, both past and present, who I would like to acknowledge are: Hans van Dongeren, Simon Logtenberg, and Michiel Nijemeisland.

All of the graduate students in the Chemical Engineering department, and some from the Materials Science department, have been great friends during the time I have been here. However, there are a few who I am particularly glad to have known: Erik Engwall and Chris Heath, for their many interesting conversations and useful advice; Ípek Güray, for being one of the nicest people I have ever met; and Bridget Smyser, for her sense of humor and perspective on doing a Ph.D.

I would like to particularly thank Josef Find for his insight into my research and his very useful suggestions. I wish that he had been a post doc in our lab earlier, so that I might have had more time to learn from him. It was good having someone like him in the lab to help us.

My friends from my undergraduate days, John Dunkelberg, Shawn Zimmerman, Joachim Heck, Doug Higgins, and Brian King, have always been patient with me, even if I never had much time to spend with them outside of the lab these last five years. Once I rejoin the real world, I look forward to spending much more time having great intellectual conversations and getting back to regular gaming.

Several other students I have met during my time here deserve recognition for their contribution to my thesis. Robert Borelli and Corey Maynard were particularly helpful in making the time for me to use the nuclear reactor, not to mention

being great guys to hang out with. During the course of my research, I have had the honor to interact with several MQP students who are among some of the best people I have ever known: Harold Booth, Christopher Coote, Kim Farrell, Matthew Freimuth, Hsing-yi Maria Ko, Chris Milici, Tom Morikis, Laura Paré, and Joanna Rosner.

Douglas White and Giacomo Ferraro deserve special thanks for all their help with making and maintaining the equipment used in this thesis. Nothing would ever get done in the Department without them.

I especially want to thank my parents for their support and encouragement all of these years. Their love and understanding has allowed me to be the person I am today, and for that I will be eternally grateful.

Lastly, I want to dedicate this dissertation to my fiancé, Susan McKay. Her patience and love allowed me to continue through both the easy and difficult times of these last five years. I thank every day that she is in my life, and look forward to spending the rest of it with her.

All that is gold does not glitter,
    Not all those who wander are lost;
The old that is strong does not wither,
    Deep roots are not reached by the frost.
From the ashes a fire shall be woken,
    A light from the shadows shall spring;
Renewed shall be blade that was broken:
    The crownless again shall be king.

— J. R. R. Tolkien

Contents

List of Figures

List of Tables

Nomenclature

a	Lattice parameter for fcc unit cell; also fitting coefficient
b	Fitting coefficient
b_n	Coefficients from DOE model
C_L	Speed of sound in a liquid
C_p	Pressure coefficient
C_{pmin}	Theoretical pressure coefficient at which cavitation will occur
c	Fitting coefficient
D	Diameter
D_o	Orifice diameter
D_{rel}	Relative metal cluster diameter
d	Distance from acoustic source
F	Molar flow rate

f	Frequency of acoustic field
G	Free energy
G_V	Free energy per unit volume
I	Intensity of an ultrasonic probe
I_0	Ultrasonic intensity at tip or edge of acoustic source
k	Polytropic coefficient
m	Mass
N_E	Total number of edge atoms in a metal cluster
N_S	Total number of surface atoms in a metal cluster
N_T	Total number of atoms in a metal cluster
n_{fcc}	Number of atoms in an fcc unit cell
P	Hydrostatic pressure surrounding bubble
P_{collapse}	Pressure generated on the collapse of a cavitation bubble
p	Pressure
p_0	Initial pressure upstream of an orifice
p_2	Final recovery pressure downstream of an orifice
p_∞	Uniform pressure far away from orifice or bubble

p_A	Pressure amplitude of ultrasonic field
p_{amb}	Ambient pressure
p_B	Pressure inside bubble
p_{G_0}	Initial gas pressure in a bubble
p_{LC}	Lowest pressure reached in a sonicated liquid, $p_{amb} - p_A$
p_o	Pressure inside an orifice
p_V	Vapor pressure
q	Heat of phase transformation
R	Time varying radius of a cavitation bubble; also recycle ratio in recycle reactor
R_0	Initial bubble radius
R_c	Critical bubble nucleation radius
$R_{\max}$	Maximum bubble radius
r	Radius of a microcrystal, cavitation bubble, or atom
r_A	CO oxidation rate
r_c	Critical radius for a phase transformation
Re	Reynolds number

S	Surface area per mass of metal
T	Temperature
T_∞	Uniform temperature far from bubble
T_B	Bubble temperature
T_b	Bulk phase transformation temperature
t	Time
u	Velocity
u_∞	Uniform velocity far away from orifice or bubble
u_o	Velocity through an orifice
V	Volume
V_{fcc}	Volume of a face-center cubic unit cell
W	Work generated on bubble collapse; also catalyst weight
$\dot{W}$	Power output from bubble collapse
α	Attenuation coefficient for acoustic propagation in a liquid; also fraction recycled in recycle reactor
β	Orifice to pipe diameter ratio

γ	Ratio of heat capacity at constant pressure to heat capacity at constant volume, typically 1.40 for ideal gases
δ	Thickness of liquid layer around a bubble
ϵ	Strain; also energy dissipation per unit mass of liquid
μ	Dynamic viscosity
μ_L	Dynamic liquid viscosity
ν	Cluster order number
ν_L	Kinematic liquid viscosity
Π_n	Dimensionless Buckingham pi term
ρ	Density
ρ_L	Liquid density
ρ_V	Vapor density
σ	Surface free energy or surface tension
σ_i	Incipient cavitation number
σ_T	Throat cavitation number
τ	Time of pressure recovery
ω	$2\pi f$

Chapter 1

Executive Summary

The overall objective of this research was to understand the fundamental factors involved in synthesizing nanometer-size catalytic materials in the 1–10 nm range in a cavitating field. Specifically, this research was directed towards understanding the ability of acoustic and hydrodynamic cavitation to affect the metal dispersion and crystallite size of a supported metal catalyst. One objective was to determine whether either form of cavitation could be used to systematically alter the grain size of both a support and the metal on a support in the catalytically important 1–10 nm grain size range by a simple adjustment of the experimental apparatus. Supported metal catalysts with metal particle sizes less than 10 nm exhibit enhanced catalytic activity compared to larger grain size metals. Another objective of this research was to determine whether the high shear generated in cavitational processing could be used to provide near molecular mixing leading to materials with high phase purity. The material system investigated in this research was titania supported gold for

carbon monoxide (CO) oxidation. Thus, a specific objective was to determine whether the gold grain size could be controlled by cavitational processing as an alternative to poorly controlled synthesis techniques available in the literature.

The first part of this dissertation was the development of an ultrasonic precipitation setup to study the general effects of acoustic cavitation on the precipitation of a range of inorganic materials. For most of the materials studied, only modest effects on the crystallite size, as measured by x-ray line broadening analysis, were observed. However, the degree of control varied from system to system, with the most dramatic adjustment of crystallite size occurring for the precipitation of cerium oxide.

Based on the knowledge gained from these initial experiments, the research focused on understanding the effects of cavitational processing on the synthesis of titania supported gold. A new chemical approach to the formation of titania supported gold was developed using the coprecipitation of the metal precursors with ammonium hydroxide/cetyltrimethylammonium chloride. This synthesis approach allowed a very simple and efficient means of producing titania supported gold with gold yields of $84 \pm 9\%$ compared to other synthesis approaches in the literature which have gold yields varying from 18 to 60%. Using this synthesis system, the effects of acoustic cavitation and gold metal concentration on the final catalysts were investigated. It was determined that acoustic cavitation was unable to influence the gold mean crystallite size for this system compared to non-sonicated catalysts.

However, gold concentration on the catalysts was found to be very important

in the control of CO oxidation activity. By decreasing the gold concentration from a weight loading of 0.50% down to approximately 0.05%, the rate of reaction per mole of gold was found to increase by a factor of 19. This increase in reactivity below 0.5% gold was also observed in later catalytic work in this research, suggesting that this concentration represents a region for the gold/titania system, below which the dispersion of gold on the titania increases dramatically, leading to smaller, more active gold particles.

Given the results of the acoustic cavitation studies, the next phase of this research turned to the study of hydrodynamic cavitation on the control of gold crystallite size at a constant gold concentration. It was determined that hydrodynamic cavitation at low pressures (6.9–48 bar) had no effect on the gold crystallite size at a fixed gold content. However, it was discovered that by changing the chemistry of the precipitation system, effects of cavitation were observed. For the system of gold precipitation using hydrazine as a reducing agent, it was found that a synergy existed between the dilution of the gold precursor solution, the orifice diameter in the cavitational processing equipment, and the reduction of the hydrazine addition rate. The individual effects of these three factors were found to be negligible and only their interaction allowed gold crystallite size control in the range of 8–80 nm. However, equipment size and pumping limitations prevented further laboratory investigation into the control of the gold crystallite size in the 1–10 nm range.

Thus, in the final portion of this research, the system chemistry was again modified, and processing equipment capable of higher system pressures was used to investigate the effect of cavitation on gold crystallite size at a fixed gold concentra-

tion on the catalysts. Using a combination of sodium hydroxide and hydrazine, it was shown that gold could be synthesized less than 10 nm at gold weight loadings less than 3%. Furthermore, the use of hydrodynamic cavitation at pressures in excess of 689.5 bar (10,000 psig) allowed the systematic control of gold crystallite size in the range of 2–9 nm for catalysts containing 2.27 $\pm$ 0.17% gold. In addition, it was shown that the enhanced mixing due to hydrodynamic cavitation led to greater incorporation of gold into the catalysts compared to classical synthesis without cavitation. This grain size control was related primarily to dynamic system pressure, and not to other variables such as Reynolds number, throat cavitation number, or the orifice diameter. The cavitation effects at high pressures were explained in terms of fluid mechanics principles and information available from hydrodynamic simulations in the literature. Trends observed in modeling calculations performed in this research supported this explanation.

The fluid dynamics calculations performed for this thesis predicted trends in the relationship of mechanical processing conditions to relative bubble sizes, lifetimes, and energetics. This computational work guided the experimental program in the selection of parameters to use in the cavitation experiments, as well as aiding in the explanation of the high pressure synthesis results. Furthermore, a dimensional analysis of the variables, using the Buckingham Pi method, involved in hydrodynamic cavitation was applied to the synthesis of nanostructured titania and piezoelectrics to understand strain induced during cavitational synthesis. This enabled the prediction of the cavitation conditions necessary to achieve the greatest strain and to better understand the relative importance of throat cavitation number

and Reynolds number on inducing strain.

The control of gold crystallite size in the high pressure experiments was gained at the loss of CO activity compared to other catalysts synthesized in this research. This activity loss was attributed primarily to the formation of non-removable sodium titanium oxide species which acted as a catalytic poison. In addition, the increased mixing associated with the high pressure cavitation processing contributed to this decreased activity by partially burying some of the gold beneath the surface of the catalyst supports, as well as incorporating more of the sodium containing poisons into the catalysts.

This work resulted in the first experimental evidence of hydrodynamic cavitation being able to influence the gold crystallite size on titania supported gold catalysts. Despite the low activity observed due to sodium poisoning, the methodology of adjusting the chemistry of a precipitating system could be used to eventually eliminate catalytic inhibitor species. Thus, the approach of modifying the chemical system so that the chemical kinetics are slower than the dynamics of cavitation bubble collapses, as was done several times throughout this work, offers a general scheme for future research projects on cavitational processing effects to be pursued.

Chapter 2

Introduction

2.1 General overview

This research on the synthesis of nanometer-size materials was directed towards the understanding of the fundamental science involved in the processing of inorganic materials in the presence of acoustic and hydrodynamic cavitation. The effects of acoustic cavitation on liquid phase synthesis, sometimes referred to as sonochemistry, have been studied extensively [1–4]. However, little or no work has been done to determine the external effects such as micromixing, particle damage, and local temperature fluctuations, due to cavitation bubble collapses on heterogeneous precipitation systems. Furthermore, no studies of this kind have been performed using hydrodynamically generated cavitation.

The motivation for this investigation was to determine whether cavitational processing of precipitating inorganic systems could be used to reduce and control

the grain sizes of the synthesized materials in the 1–50 nm range. The resulting small grain size materials should exhibit improved phase purities and physical properties which differ from micron-size particles of the same compounds. Such nanometer-size materials should also exhibit enhanced catalytic activity either due to frontier electron theory [5], or due to a higher edge to stable basal plane ratio, leading to more reactive sites of low coordination [6], particularly in the 1–5 nm range.

There are numerous methods for the production of nanometer-size materials. Some of these are traditional, such as high-energy mechanical attrition via ball-milling, sol-gel synthesis, and incipient wetness. Others are more recent developments, such as the use of surfactants to form inverse micelles by Wilcoxon's group [7–9], and the use of polymers to stabilize metal clusters by Busser [10]. Some involve the use of high temperature, such as the rapid thermal decomposition of precursors in solution (RTDS) method developed by Matson [11, 12], and Moser's high temperature aerosol decomposition (HTAD) process [13]. The vaporization of metals or other compounds is another common approach, and is often used for the study of gas phase metal clusters [14, 15], as well as being the basis for Siegel's gas-condensation process [16, 17]. A source for backgrounds on many of these techniques can be found in reference [18].

The use of acoustic or hydrodynamic induced cavitation appears to be a promising means for the synthesis of nanostructured materials [4, 19–22]. Cavitation is the formation of vapor or gas bubbles in a liquid caused by a reduction in pressure at constant temperature [1, 23–25]. After cavitation bubbles are formed by a

dynamic pressure reduction, they are then subjected to a pressure increase, which causes the bubbles to collapse.

During bubble collapse, extremely high temperatures and pressures are encountered inside the cavity which can induce chemical reactions. The occurrence of these special reactions in a cavity is typically described as *sonochemistry*, since acoustic cavitation has been used to extensively study this phenomenon. In addition to the high pressures and temperatures experienced inside the bubbles, fluid *microjets* and *shockwaves* emanate from the bubble collapses which have the ability to cause great damage to materials through impact and erosion. This rapid bubble growth and collapse can be induced either by an ultrasonic sound source (acoustic cavitation) or high energy mixing devices such as Microfluidics' Microfluidizer™ or a Five Star Technologies "Controlled Flow Cavitation™" device (hydrodynamic cavitation).

The equipment necessary for the cavitational synthesis of nanometer-size materials is commercially available. Accordingly, this type of synthesis technique could easily be scaled up from laboratory techniques due to the availability of larger equipment. Furthermore, cavitational synthesis can be performed on a continuous flow basis, unlike some of the other techniques mentioned above, which further lends to its adaptation to a large-scale commercial environment.

Given the potential advantages of hydrodynamic and acoustic cavitation, this research investigated the various factors which can be used to control the synthesis of inorganic materials in the nanometer-size range for catalytic applications. Because cavitation is a complex phenomenon, the overall approach employed was

to develop an empirical relationship between observed crystallite sizes and the various synthesis and cavitational processing parameters. The experimental program was assisted by theoretical information available in the literature, as well as theoretical calculations performed during the research. The greater objective was to relate the trends observed from the experimental data to the theoretical aspects of cavitation.

2.2 Direction and organization of the thesis

The remainder of this chapter is devoted to an overview of the motivation for this research: grain size effects on catalytic activity. The second chapter covers in more detail the phenomenon of cavitation. The differences between acoustic and hydrodynamic cavitation are discussed with respect to a fundamental mathematical treatment of bubble dynamics. Based on this framework, some anticipated effects of cavitation on inorganic precipitation are presented.

A considerable amount of work was performed on the development of an ultrasonic precipitation setup. The general effects of acoustic cavitation on a wide range of inorganic materials were studied, and are the subject of Chapter 5, which is based on a paper which resulted from this work [26]. With the knowledge gained from these experiments, the research focused on understanding the effects of cavitational processing on the synthesis of titania supported gold for the oxidation of carbon monoxide (CO).

Although supported and unsupported gold in large grain sizes shows little or

no catalytic activity, supported gold catalysts show high activity for a variety of reactions when the grain size is reduced below 20 nm [27–29]. The synthesis of supported nanometer-size gold has been the subject of much research, making this system suitable for investigating cavitational processing effects. Chapter 6 details the investigation of cavitational processing, primarily with ultrasound, on titania supported gold, as well as the effect of gold concentration on catalytic activity.

CO oxidation was chosen as an appropriate catalytic test reaction for this research. Due to the absence of secondary reactions, this test reaction has no selectivity issues which could confuse the results. In addition, CO oxidation is not equilibrium limited under the operating conditions used in this work. CO oxidation is not only a good test reaction for particle size effects, but is also an important environmental and industrial reaction. The oxidation of CO is primarily of importance for the treatment of hydrocarbon combustion emissions. In addition, other useful applications of this reaction are the removal of CO from air in submarines and space craft, the oxidation of CO in CO_2 lasers, respirator masks, CO gas sensors, and the removal of CO from the reformate feed for fuel cells [28, 30–32].

Chapters 7 & 8 describe the subsequent research on the synthesis of titania supported gold using hydrodynamic cavitation. By altering the chemistry of the precipitation, the use of hydrodynamic cavitation at pressures in excess of 689.5 bar (10,000 psig) allowed the systematic control of gold crystallite size in the range of 2–9 nm for catalysts containing $2.27 \pm 0.17\%$ gold. In addition, it was shown that the enhanced mixing due to hydrodynamic cavitation led to greater incorporation of gold into the catalysts compared to classical synthesis without cavitation. These

observations are especially important to catalysis since nanometer-size metallic particles in the desired range of 1–10 nm could be synthesized in varying grain sizes by simple mechanical adjustment.

This grain size control was related primarily to dynamic system pressure, and not to other variables such as Reynolds number, throat cavitation number, or the orifice diameter. The cavitation effects at high pressures were explained in terms of fluid mechanics principles and information available from hydrodynamic simulations in the literature. Trends observed in modeling calculations performed in this research in Chapter 3 also supported this explanation. This thesis resulted in the first experimental evidence of hydrodynamic cavitation being able to influence the gold crystallite size on titania supported gold catalysts. Furthermore, the approach of modifying the precipitation chemistry to alter the chemical kinetics with respect to the dynamics of cavitation bubble collapses, as was done several times throughout this work, offers a general scheme for future research projects on cavitational processing effects to be pursued.

2.3 Grain size effects on catalytic activity

Nanometer-sized materials hold the promise of producing better performance catalysts. The higher intrinsic surface area per unit volume of a compound which is less than 50 nm in diameter can lead to higher activity. With a higher concentration of low coordination sites, the specific selectivity for some reactions may also be improved. In addition, the thermodynamics of such small particles may allow the

low temperature stabilization of metastable phases and the synthesis of pure phase homogeneous compounds.

The physical properties of nanostructured compounds are significantly different from those of the bulk phase (greater than 100 nm grain sizes), as well as those of the constituent atoms. These properties can be organized into two categories: chemical and structural. Following a brief review of some of the chemical properties of materials whose size are in the range of 1–50 nm, an analysis of their structure will be considered. The implications of these chemical and structural changes for catalysis will then be discussed.

2.3.1 Physical properties of nanostructured materials

Fundamental property changes

Materials which are less than 100 nm in size begin to exhibit changes in their fundamental properties. For example, the melting point [17, 33] and heat capacity [34] of nanostructured materials can be much less than those of the bulk phase. Their magnetic properties may also vary from those of the bulk metal, as in the case of iron [7]. The electronic properties of nanostructured semiconductors can be changed with grain size. Laurich synthesized nanometer-sized GaP and GaAs clusters to study the quantum confinement of charge carriers that occur in nanoclusters which lead “to distinct electronic levels, having energies higher than the bandgap of the bulk material (blue shift). [35]”

Optical properties

The optical properties of nanometer-sized particles also exhibit changes from those in the bulk. Wilcoxon *et al.* have developed techniques for the synthesis of metal colloids with fine grain dimensions [7–9]. Figure 2.1 shows experimental data for gold clusters in a cationic micelle system [8, 9]. When different metals were synthesized in a colloid form, it was noticed that the wavelength of light absorbed by different grain sizes shifted more than was predicted by various theories. From Figure 2.1, it is obvious that as the grain size of nanostructured materials decreases, the absorbed wavelength blueshifts toward shorter wavelengths (*i.e.* the materials appear more red).

Hardness, strain rate, and grain boundary diffusion

Several physical properties change simply due to the increased number of surface atoms in the grain boundaries of small particles. Siegel demonstrated that the microhardness of nanometer-sized metal oxides is much greater than that of micrometer-sized oxides of the same material (see Figure 2.2) [16, 17]. Smaller grained ceramics also have greater sinterability. In addition, the strain rate sensitivity of metal oxides increases as the grain size decreases, which suggests that nanometer-sized materials have greater ductility and formability due to their increased number of grain boundaries (see Figure 2.3) [16]. The increased number of atoms in the grain boundaries, coupled with the small size, leads to enhanced diffusivities compared to bulk materials.

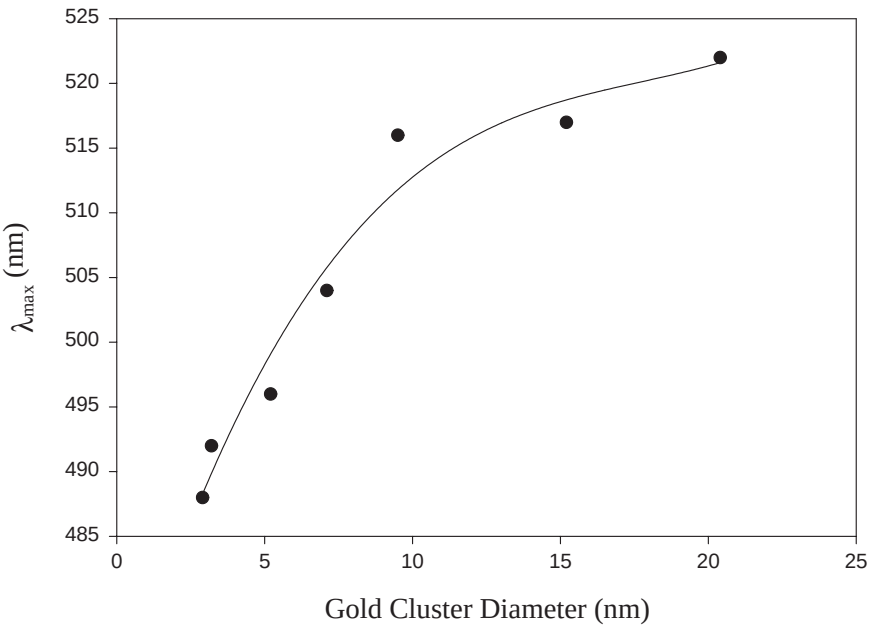

Figure 2.1: Optical wavelength absorbance blueshift for gold clusters in a cationic micelle system [8].

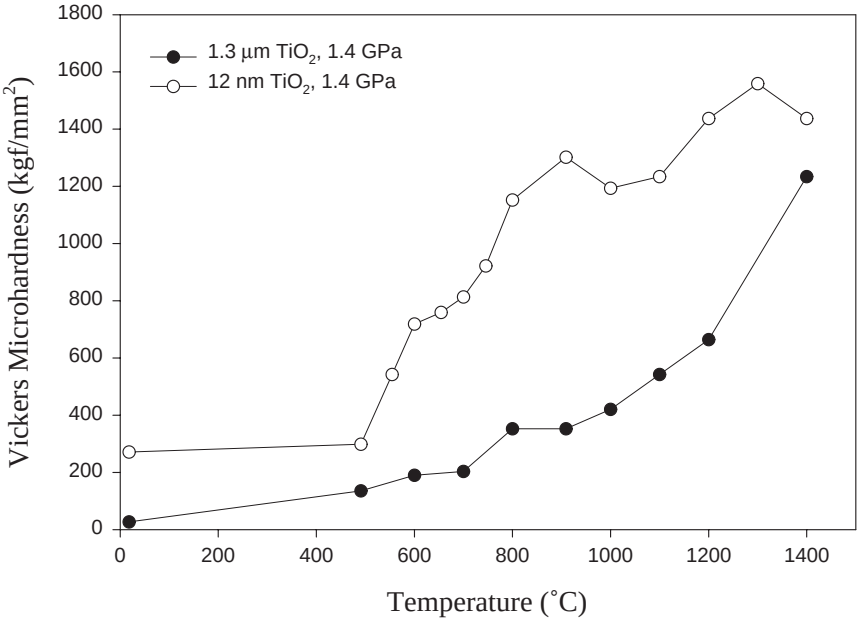

Figure 2.2: Vickers microhardness of two different grain sizes of TiO_2 (rutile) measured at room temperature as a function of one-half hour sintering at successively increased temperatures [16].

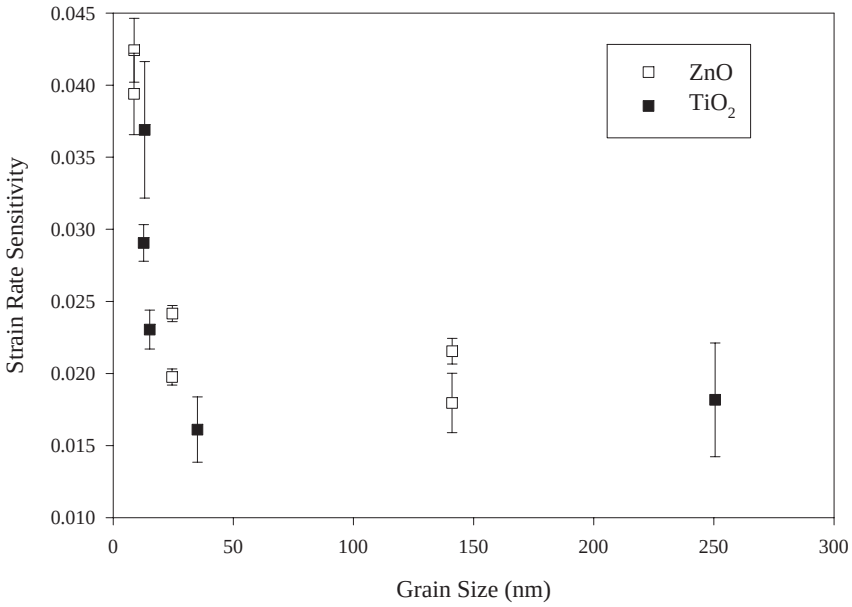

Figure 2.3: Strain rate sensitivity of nanophase TiO_2 and ZnO as a function of grain size [16].

Phase stability

As Siegel points out, it may be possible to stabilize metastable phases in the nanometer-size range [17]. Most phase equilibria data are for bulk phase (micrometer-size) systems and may not apply to nanometer-size materials due to the unique thermodynamic nature of small particles. For example, Smyser *et al.* have shown that the use of 20–30% of nanostructured alumina can inhibit the phase transformation of small grain zirconia from the tetragonal to monoclinic phase [36].

This size effect on phase stability can be best explained following the argument of Garvie [37]. For a spherical particle, the free energy, G, can be expressed as the summation of a bulk volumetric contribution and a surface contribution as shown in Equation 2.1.

$$G = \frac{4}{3}\pi r^3 G_V + 4\pi r^2 \sigma \tag{2.1}$$

In this equation, r represents the radius of the microcrystal, G_V is the free energy per unit volume of the crystal, and σ denotes the surface free energy of the particle. Following this definition, the free energy difference for the transformation between two phases can then be expressed in the form of Equation 2.2.

$$\Delta G = \frac{4}{3}\pi r^3 \Delta G_V + 4\pi r^2 \Delta\sigma \tag{2.2}$$

At some critical size, the volumetric and surface terms will balance each other, and the ΔG will be zero. At this critical point, Equation 2.2 can then be solved to

determine the critical radius for phase transformation, r_c, shown in Equation 2.3.

$$r_c = -\frac{3\Delta\sigma}{\Delta G_V} \tag{2.3}$$

By expanding the volumetric free energy term in a Taylor's series around the transformation temperature of a very large crystal, Equation 2.3 can then be expressed in a more useful form

$$r_c = \frac{-3\Delta\sigma}{q(1 - T/T_b)} \tag{2.4}$$

where T_b is the bulk phase transformation temperature, and q is the heat of phase transformation [37].

Equation 2.4 allows the quantitative determination of the critical radius of phase transformation at different temperatures, neglecting the effects of strain and stress. Below this critical radius, the surface energy term in Equation 2.2 dominates, and determines the overall free energy for phase transformation. Thus, it is possible from a thermodynamic argument to stabilize metastable phases in nanometer-sized materials and prevent the formation of compounds predicted by bulk phase equilibria data.

Ionization potential

One of the more well-known and well-studied properties of nanostructured materials, particularly elemental clusters, is ionization potential. As the grain size of elemental clusters decreases, the ionization potential increases. In bulk materials, the ionization potential is equivalent to the electron affinity, but in very small

metal clusters, the ionization potential quite frequently is greater than the electron affinity [15]. Figures 2.4 & 2.5 show the typical variation in ionization potential with elemental cluster size. The fluctuation in some of the values are partly due to electron shell changes with the change in cluster size, which can complicate the ionization potential analysis of some metals such as copper [38].

Baetzold [40–43] performed a series of molecular orbital calculations on small metal clusters (less than 20 atoms). He predicted the increase in ionization potential with decreasing grain size, as well as a decrease in the electron affinity. He also observed an increase in the average bond energy per atom with increasing number of atoms in a cluster which approached the bulk metal value [43]. His results showed differences in bonding between small clusters and the corresponding bulk metals [43]. Baetzold concluded from his calculations that larger clusters would be better catalytic centers than small clusters because of the trends in bonding energy per atom and electron affinity with size. He also concluded that larger clusters could "bind atoms more strongly than small clusters [43]." However, it should be noted that larger clusters, according to Baetzold, are on the order of 15–20 atoms, which is equivalent to a grain size range of 0.75–1 nm.

Adsorption

The adsorption characteristics of small metal clusters are also quite different from micrometer-size bulk metal. Henry *et al.* measured the activation energy for desorption of carbon monoxide from MgO supported Pd [44]. They discovered that the activation energy increased with decreasing grain size from a value of

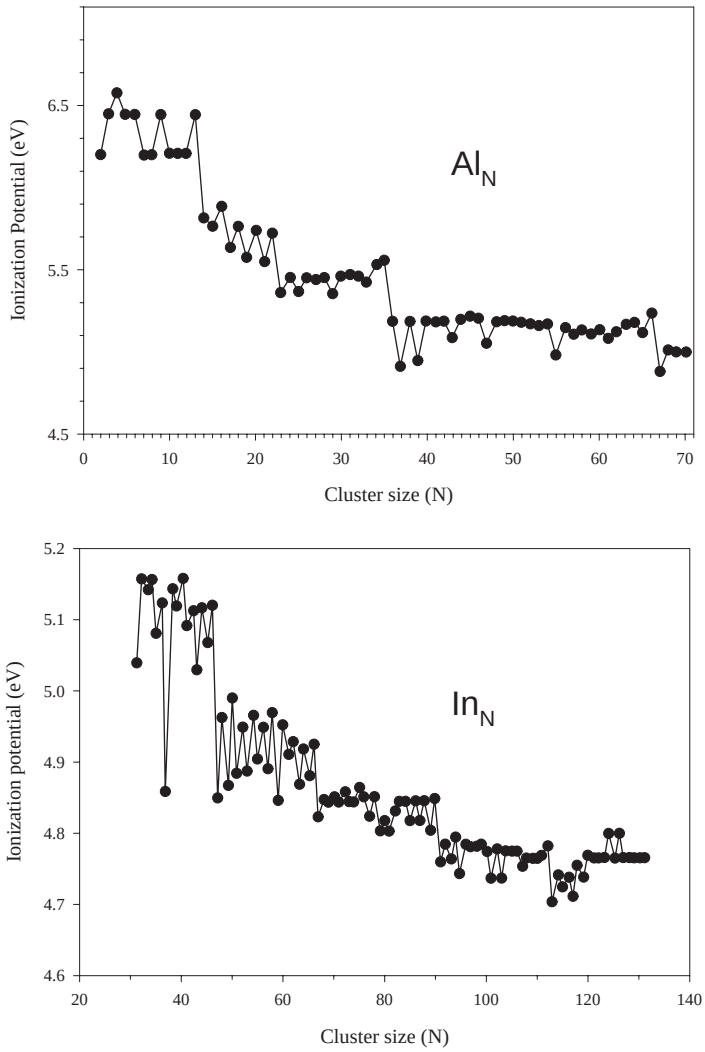

Figure 2.4: Ionization potentials of trivalent clusters (aluminum and indium) [14, 39].

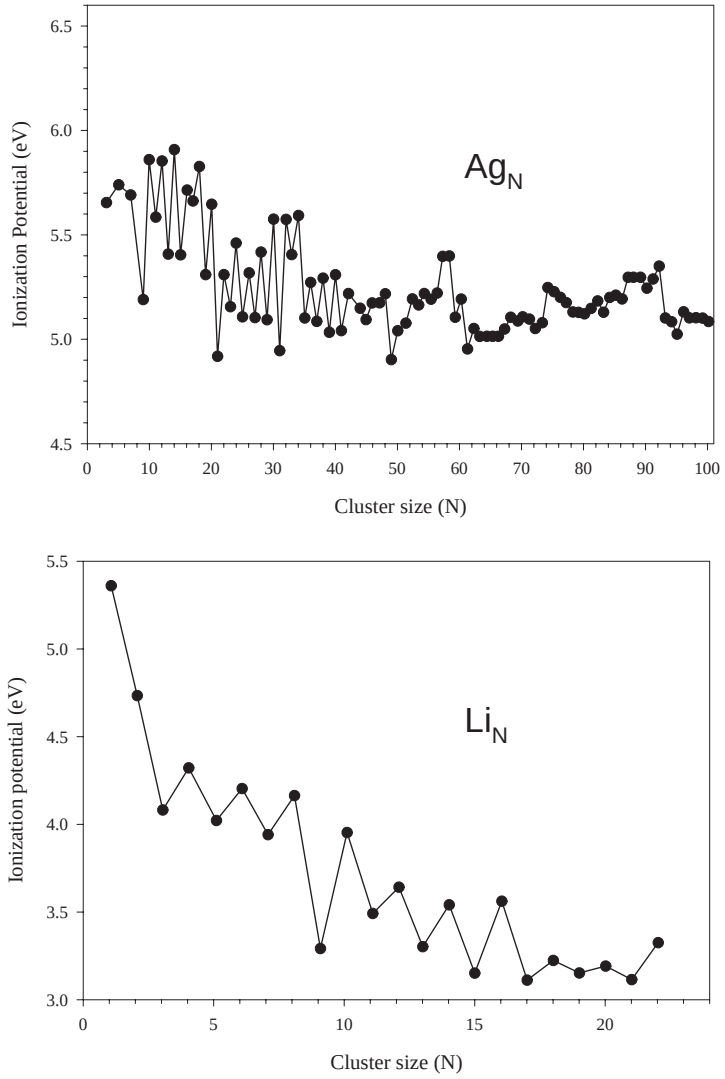

Figure 2.5: Ionization potentials of silver and lithium [39].

30 kcal/mol at 5 nm to 40 kcal/mol at 2 nm. In contrast, Stará *et al.* studied the desorption of carbon monoxide on alumina supported Pd and found that 27 nm Pd particles exhibited desorption activation energies comparable to bulk Pd(111), but that the desorption energy for 2.5 nm Pd was approximately 30% lower [45]. In addition, they also observed a second desorption peak in their temperature programmed desorption (TPD) spectra for the 2.5 nm Pd which was not present in larger grain particles.

Both research groups compared their data to the literature and observed similar contradictions. However, they looked more closely at the structures of the different metals and supports and found that the morphology of the metal with respect to the support could explain the differences. For example, when Pd is supported on alumina, the Pd particles have (111) planes parallel with the support. Stará also observed that the shapes of Pd on MgO(100) clusters under an electron microscope appeared to be half octahedra which had (100) planes parallel with the support surface and (111) faces and (100) truncations on the top [45]. Both groups concluded that the adsorption of CO appears to correspond with the type and number of edges or steps. Therefore, as the grain size of a well defined cluster decreases, the proportion of (111) and (100) planes correspondingly changes, resulting in the desorption trends observed.

The sticking probability for oxygen reacting with nickel was examined by Andersson *et al.* and they found that the probability increased from about 10 Ni atoms up until about 20 Ni atoms, where it remained constant up to 30 Ni atoms [46]. They explain this phenomenon based on electronic structure, rather than physical

structure, since smaller clusters have higher ionization potentials. Since oxidation involves electron transfer, smaller clusters would then be expected to be less reactive. However, this change in oxygen reactivity occurs only in clusters containing less than 20 Ni atoms, which are less than 1 nm in size, so ionization potential alone cannot explain the adsorption behavior of nanostructured materials.

Another interesting adsorption behavior of nanometer-size materials is that a large number of hydrogens can be bound to small transition metal clusters [15,47]. Cluster sizes consisting of less than 40 atoms (less than approximately 1 nm) exhibit a hydrogen to metal ratio (H/M) greater than unity, particularly in the case of rhodium, as shown in Figure 2.6. The high chemisorptive capacity of supported rhodium catalysts has been observed experimentally for rhodium clusters with grain sizes less than 3 nm, although the phenomenon has been attributed to hydrogen spillover [48]. This increased hydrogen sorptive capacity suggests that the use of small molecule (hydrogen and carbon monoxide) chemisorption to determine the number of exposed surface atoms (active sites) in catalysis may be inaccurate for very small grain size metals.

Salama *et al.* also observed an increase of hydrogen uptake due to smaller Pt particles [49]. The Pt was dispersed on two different supports, a pure silica with a Pt grain size of 17.8 Å and a titania/silica with a Pt grain size of 7.9 Å. The increase of metal dispersion due to the dispersed titania on silica may also be the cause of increased strong metal-support interaction (SMSI) between the Pt and the titania [49]. SMSI in the platinum/titania system is most likely due to the diffusion of titania across the Pt/titania surface to form a Pt-Ti bond [50].

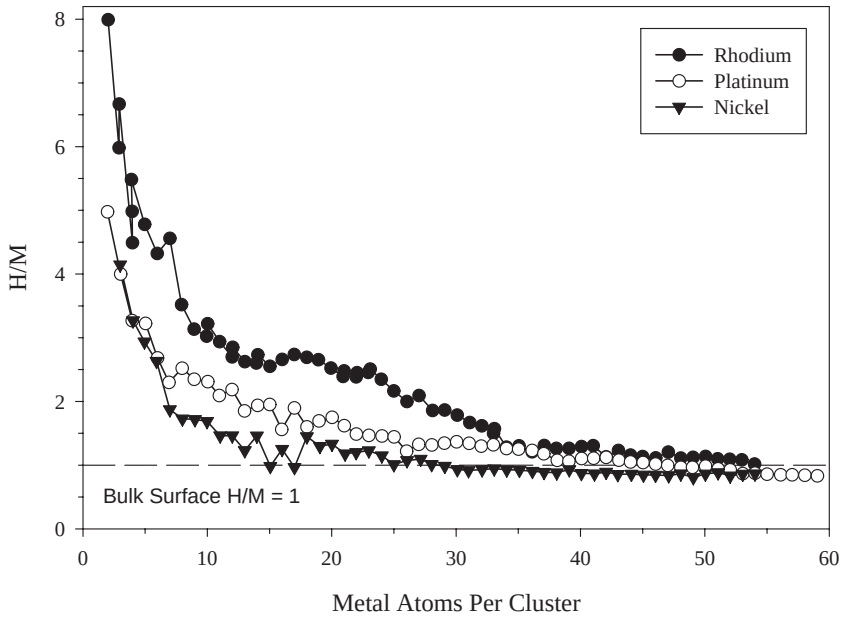

Figure 2.6: Hydrogen uptake for rhodium, platinum, and nickel cations as a function of cluster size. H/M is the measured hydrogen to metal stoichiometry of the cluster [15].

Since grain boundary diffusion may be faster for nanostructured materials, smaller particles might form this SMSI more readily.

2.3.2 Structural characteristics of nanometer-size materials

Equilibrium structure

As the grain size of nanostructured materials decreases, there will come a point when there are insufficient atoms to maintain the bulk crystal lattice structure. For example, Hoare and Pal made free energy stability calculations on the structures of nanometer-sized clusters and concluded that "no fcc lattice-type cluster with less than 50 atoms is likely to exist in significant concentrations in a condensing monatomic vapour, so long as two-body central adhesive forces are operative. [34]" Since many metals used for catalysis are face-centered cubic (FCC), the obvious question then becomes what structure do nanometer-size metals conform to when their grain size diminishes? And following that, what effect does the structure have on catalytic performance?

Several structures have been proposed over the years for nanostructured clusters. The two most likely to commonly exist are the icosahedron (Figure 2.7) and the truncated octahedron (Figure 2.8). Both structures consist of primarily (111) planes which are present on the triangular faces of the icosahedron and the hexagonal faces of the truncated octahedron(cubo-octahedron) [33,44]. The square planar surfaces of the truncated octahedron are (100) planes, which are absent in the icosahedral structure [33].

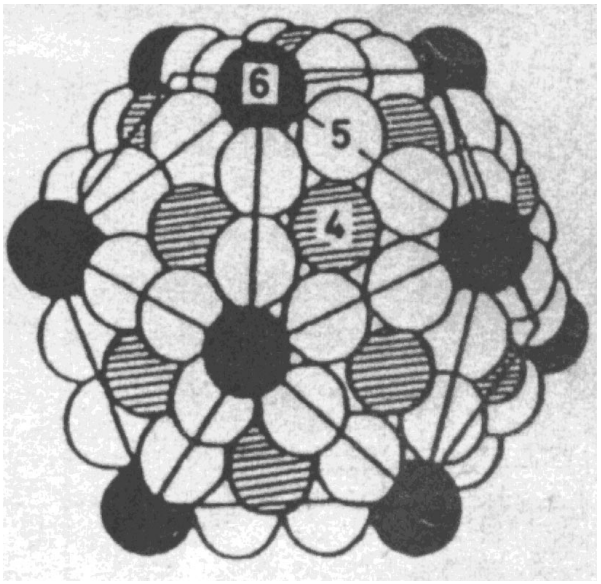

Figure 2.7: Icosahedron structure [51].

Allpress and Sanders calculated the energy of different structures of small clusters and found that when a cluster is less than about 200 atoms the order of stability is: icosahedron > octahedron > tetrahedron > pentagonal bipyramid [52]. However, they admit that these calculations ignore the influence of a support, which might change the order of stability or even result in more truncated structures. Montejano-Carrizales showed that the icosahedral structure may be more stable for very small numbers of atoms, but that the cubo-octahedron is more prominent for large numbers of atoms in a structure [51].

There is some experimental data to confirm the existence of these structures. For example, Henry *et al.* observed a truncated octahedron structure for Pd on MgO at 673 K, but note that the equilibrium shape of the Pd depends on the surface

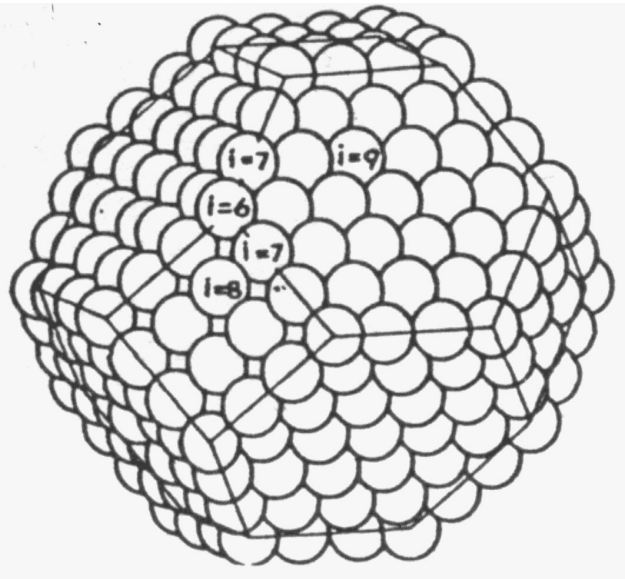

Figure 2.8: Truncated octahedron (cubo-octahedron) structure [6, 44]. Numbers on the faces indicate coordination.

temperature, becoming "flat rough clusters" at low temperature and transforming to a truncated tetrahedron at high temperatures [44]. Parks *et al.* provide more data on gas phase metal clusters of Fe, Co, Ni, and Cu [38] . It appears that one of two structures is stable below around 50–55 atoms: a double icosahedron (like Ni_{19}) and an octahedron (like Co_{19}). It also appears that several different structures are stable for Co_{18-19}, so the picture is complicated for transition metals in very small clusters. In the range of 55–150 atoms, the icosahedral structure is present, although it eventually disappears as the number of atoms increases.

Given the experimental data and theoretical calculations, a simplified model of metal cluster growth can be constructed. At very small cluster sizes less than 1 nm, the structure is more likely to be an icosahedron. As the grain size increases, the equilibrium shape will become a truncated octahedron. However, as Henry points out, there is only a small energy difference between the two structures, so both may be possible above 1 nm [44]. This negligible difference makes itself known when a thorough structural analysis is performed for nanostructured materials (see below). At some much larger grain size, there will then be sufficient atoms to form a stable FCC crystal lattice.

The existence of either the icosahedron or truncated octahedron has some interesting implications for the properties of nanostructured materials. The nearest neighbor distances are smaller than those of bulk compounds, with the difference in bond length being offset by the increased number of bonds, and this may lead to differences in electronic properties. In addition, there is a low degree of coordination for the surface atoms. Perhaps just as important may be the presence of

a high proportion of (111) planes (a total absence of (100) planes in the case of the icosahedron). Following the argument of Burton [33], if a property, such as catalytic activity, depends on the presence of either (111) or (100) planes, then that property will change drastically as the percentage of (111) planes decreases with increasing grain size until the bulk FCC structure is obtained.

Structure dimensional analysis

The volume of a face-centered cubic metal unit cell is simply the cube of the lattice parameter (see Equation 2.5).

$$V_{\text{fcc}} = a^3 \tag{2.5}$$

The relationship between the lattice parameter and the radius of the metal atom can be easily shown to be:

$$a = \frac{4r}{\sqrt{2}} \tag{2.6}$$

from a geometrical analysis which assumes the atoms are hard spheres touching one another. In order to put the dimensions of nanometer-size metal clusters into perspective, we need to define a suitable volume for a cluster. For this analysis, we shall assume that a metal cluster will have a volume equal to the volume of the FCC unit cell times the total number of atoms in the cluster (N_T) and divided by the number of atoms in the unit cell (see Equation 2.7).

$$V = \frac{N_T \times V_{fcc}}{n_{fcc}} \tag{2.7}$$

Since there are four atoms in the FCC structure, substitution of Equations 2.5 & 2.6 into Equation 2.7 results in the description of cluster volume we will be considering here.

$$V = N_T \frac{\left(4r/\sqrt{2}\right)^3}{4} \tag{2.8}$$

Many studies of small clusters tend to describe the size of the clusters in terms of the number of atoms contained within them. However, it is more practical to use a measurable dimension to characterize the size of a nanostructured particle. Transmission electron microscopy (TEM) and x-ray line broadening analysis via Scherrer's equation [53] enable us to measure an approximate diameter of nanometer-size materials. Therefore, theoretical calculations should be made in terms of an effective diameter for metal clusters. If we equate the cluster volume defined in Equation 2.8 to the volume of an equivalent sphere, this will enable us to define a diameter for cluster size calculations (Equation 2.9).

$$\begin{aligned} V &= \frac{\pi D^3}{6} \\ \frac{\pi D^3}{6} &= N_T \frac{\left(4r/\sqrt{2}\right)^3}{4} \\ D &= \left(\frac{3}{2\pi}\right)^{\frac{1}{3}} \left(\frac{4}{\sqrt{2}}\right) r \sqrt[3]{N_T} \end{aligned} \tag{2.9}$$

This can be further simplified for convenience to:

$$D = 2.211 r \sqrt[3]{N_T} \tag{2.10}$$

If a further definition of a relative diameter is made by normalizing the cluster diameter by the diameter of a single atom:

$$D_{\text{rel}} = \frac{D}{2r} \tag{2.11}$$

then we obtain a dimensionless parameter which can be used to calculate cluster properties for different FCC metals simultaneously. After substituting Equation 2.10 into this new expression (Equation 2.11), we obtain the parameter D_{rel} originally defined by van Hardeveld and Hartog [6].

$$D_{\text{rel}} = 1.105\sqrt[3]{N_T} \tag{2.12}$$

Thus, if calculations are made with respect to D_{rel}, it is easy to calculate the approximate actual diameter by multiplying by the diameter of a specific FCC metal atom. A brief survey of metals typically used for catalysis indicates that an approximate diameter of 0.136 nm could be used for this calculation in the absence of a specific value (see Table 2.1 on page 42).

Obviously, these two expressions (Equations 2.10 & 2.12) are approximate. The assumption of equating the actual cluster volume to that of a sphere necessarily breaks down as the cluster size and number of atoms decreases to only a few atoms. In the limit of one atom, Equation 2.10 predicts that the diameter should be 2.211 times the radius of a metal atom instead of the expected $2r$. However, if this limitation is recognized, then the use of Equations 2.10 & 2.12 is justified for qualitative comparison between different FCC metal systems and for an overall

understanding of the structure changes which occur in reducing cluster dimensions below 50 nm.

Two of the more possible structures for small metal clusters before the FCC structure is established are the icosahedron (Figure 2.7) and truncated octahedron (also called a cubo-octahedron, Figure 2.8). Thus, these cluster configurations can be used as an approximate model of the real clusters which form either in the gas phase or on the surface of another material. For the icosahedron, Montejano-Carrizales and Morán-López give analytical formulas for the total number of atoms (N_T) and the total number of surface atoms (N_S) as a function of cluster order, ν (see Equations 2.13 & 2.14).

$$N_T = 10\frac{\nu^3}{3} + 5\nu^2 + 11\frac{\nu}{3} + 1 \tag{2.13}$$

$$N_S = 10\nu^2 + 2 \tag{2.14}$$

The cluster order is defined as the number of shells added to a single atom to complete the next closed, stable structure. For example, for an icosahedron, the first cluster ($\nu = 1$) consists of a central atom surrounded by 12 other atoms. The second cluster ($\nu = 2$) consists of a layer of 42 atoms surrounding the first 13 which gives an icosahedron of 55 atoms, and so forth.

For the truncated octahedron, the analytical formulas of Henry *et al.* [44] can be modified to calculate the total number of atoms, the total number of surface atoms, as well as the number of edge atoms (N_E) as a function of cluster order. The original formulas were derived in terms of the number of atoms in equivalent

edges, m, which indirectly means that the number of shells (cluster order) is $m-1$.

$$N_T = 16(\nu+1)^3 - 33(\nu+1)^2 + 24(\nu+1) - 6 \tag{2.15}$$

$$N_S = 30(\nu+1)^2 - 60(\nu+1) + 32 \tag{2.16}$$

$$N_E = 36(\nu+1) - 48 \tag{2.17}$$

This last formula (Equation 2.17) is of particular importance because the edge atoms are those with the lowest number of near neighbor atoms (lowest coordination).

Given these formulas, there are three values of interest to nanometer-size metal clusters which can be calculated. The first of these is the percentage of surface atoms. The fraction of surface atoms can be expressed as the ratio of the number of surface atoms to the total number of atoms, N_S/N_T. Using Equation 2.12, the dimensionless relative diameter (D_{rel}) can be calculated for each structure, since the total number of atoms can now be calculated from Equations 2.13 & 2.15 for each cluster order.

Figure 2.9 shows the percentage of surface atoms for both the icosahedron and truncated octahedron as a function of D_{rel}. One interesting feature of this graph is that there appears to be a negligible difference in the results between the two probable structures. This is similar to the results obtained by van Hardeveld and Hartog, who looked at octahedrons and cubo-octahedrons and showed that the trends in the number of surface atoms in those two structures were essentially

the same [6]. Another feature of this plot is that below a D_{rel} of 50, 10% or more of the atoms in each structure are surface atoms. This value corresponds to approximately 6.8 nm using an average atomic radius of 0.136 nm (see above) and Equation 2.11. Thus, metal clusters below a grain size of 7 nm should begin to exhibit properties different from those of the bulk FCC metal.

Qualitatively, Figure 2.9 agrees with the calculations of Siegel [16, 17]. He assumed a simple grain boundary with varying thicknesses for his calculations of percentage surface atoms versus grain diameter. Siegel's results, reproduced in Figure 2.10, are nearly identical to those in Figure 2.9 for an assumed grain boundary thickness of approximately 0.5 nm.

The other two properties which can be calculated from Equations 2.13–2.17 are the percentage of edge sites in a cluster, N_E/N_T, and the percentage of edge sites on the surface of a cluster, N_E/N_S. Since there appears to be very little difference in the results between the icosahedron and the truncated octahedron, using the formulas for the truncated octahedron for these calculations, particularly N_E/N_S, is justified. Figure 2.11 shows both measurements of surface atoms for a truncated octahedron as a function of D_{rel}. The results for N_E/N_T show that the number of edge atoms become non-negligible below a D_{rel} of around 20 (2.7 nm). Of greater interest, however, is that the number of edge atoms on the surface compared to the total number of surface atoms, N_E/N_S become prominent (greater than 10% of the surface) at a D_{rel} of 30 (4.1 nm), which was confirmed by Henry *et al.* [44]. As this parameter increases with decreasing grain size, the mean coordination number of the atoms in a given cluster will decrease from the bulk value, as the edge atoms

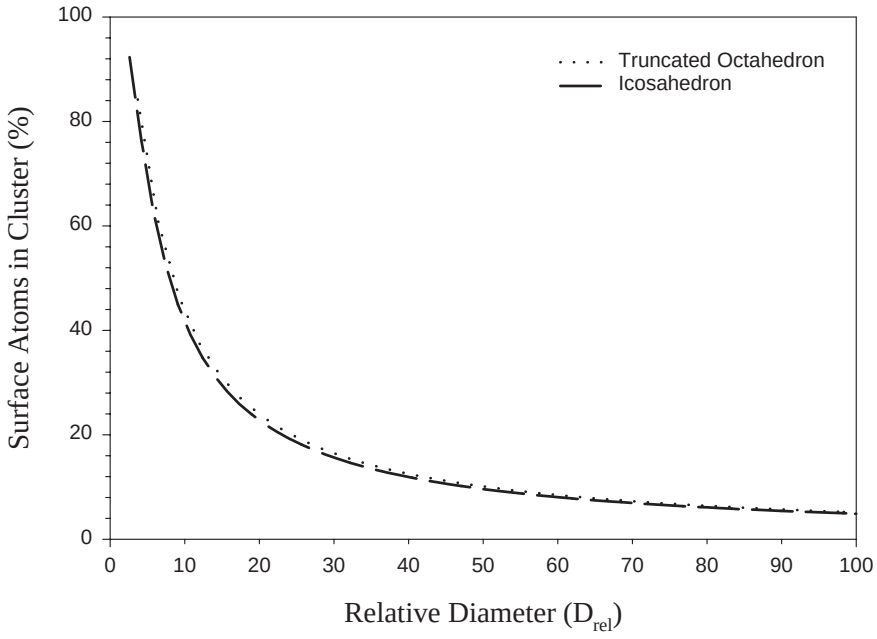

Figure 2.9: Calculated percentage of surface atoms in truncated octahedral and icosahedral FCC metal clusters.

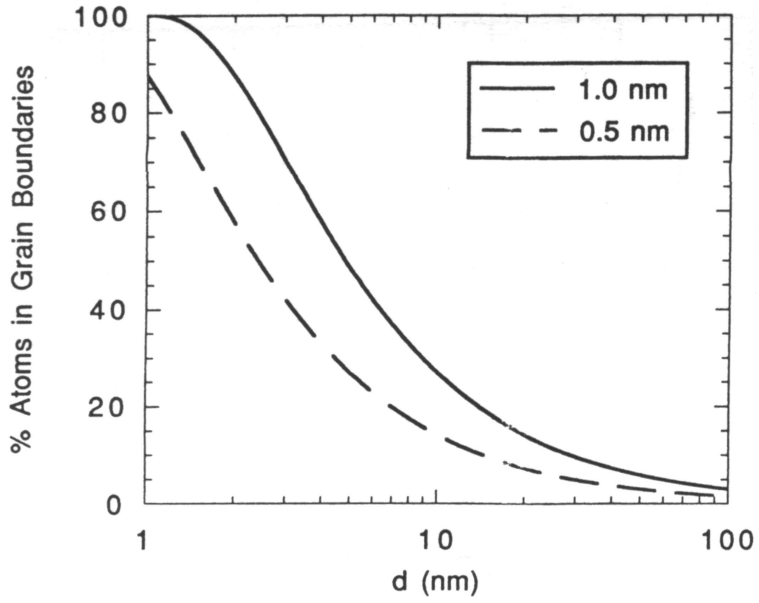

Figure 2.10: Range of percentage of atoms in grain boundaries of a nanophase material as calculated by Siegel [16].

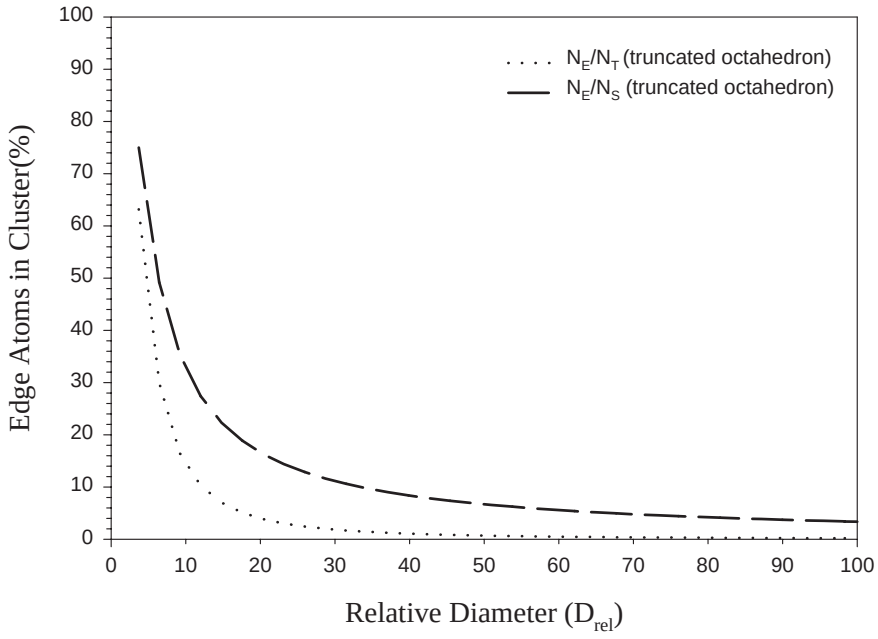

Figure 2.11: Calculated percentage of edge atoms in truncated octahedral and icosahedral FCC metal clusters.

are those with the lowest number of near neighbors. These results, combined with the change in the total number of surface atoms, suggests strongly that nanometer-size materials below a grain diameter of 5 nm should exhibit different properties from bulk phase materials on structural arguments alone.

For comparison purposes, five metals commonly used in catalysts: platinum, palladium, gold, rhodium, and nickel, were used in calculations of the number of surface atoms and edge atoms in a truncated octahedral structure. Figures 2.12 & 2.13 show the calculated values for each metal of N_S/N_T and N_E/N_S, respectively, versus the actual grain size calculated from Equation 2.10. In qualitative agreement with the general results obtained from the calculations involving D_{rel}, both ratios appear to become significant in metal clusters below a grain size of 10 nm.

In both figures, it is apparent that there is some variation in the calculations for the various metals chosen. Table 2.1 shows the atomic radii of the five metals as calculated from the FCC lattice parameter by Equation 2.6. Also shown in the table are values for N_E/N_S and N_S/N_T calculated for a 5 nm and a 20 nm particle composed of each metal. These values are plotted in Figure 2.14 for convenience. For 20 nm particles, which are not expected to have many surface atoms (less than 10%), there is very little change in the percentage of surface or edge atoms in the surface as a function of atomic radius. However, for 5 nm particles there is approximately a 14.3% change in the fraction of surface atoms and a 15.1% change in the fraction of edge atoms in the surface for a corresponding 15.7% change in the atomic radius from nickel to gold. These numbers are approximate only, since

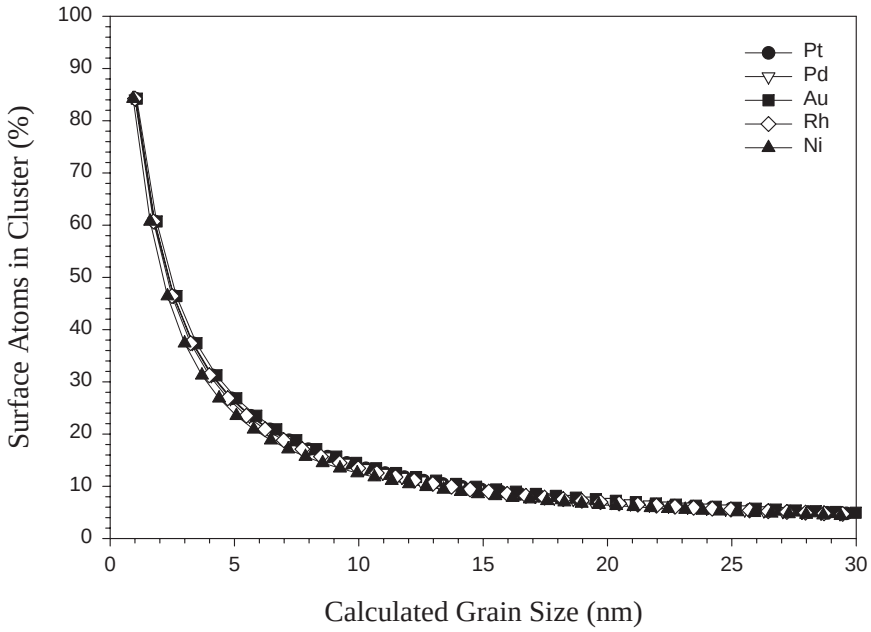

Figure 2.12: Calculated percentage of surface atoms in truncated octahedral clusters for various catalytic FCC metals.

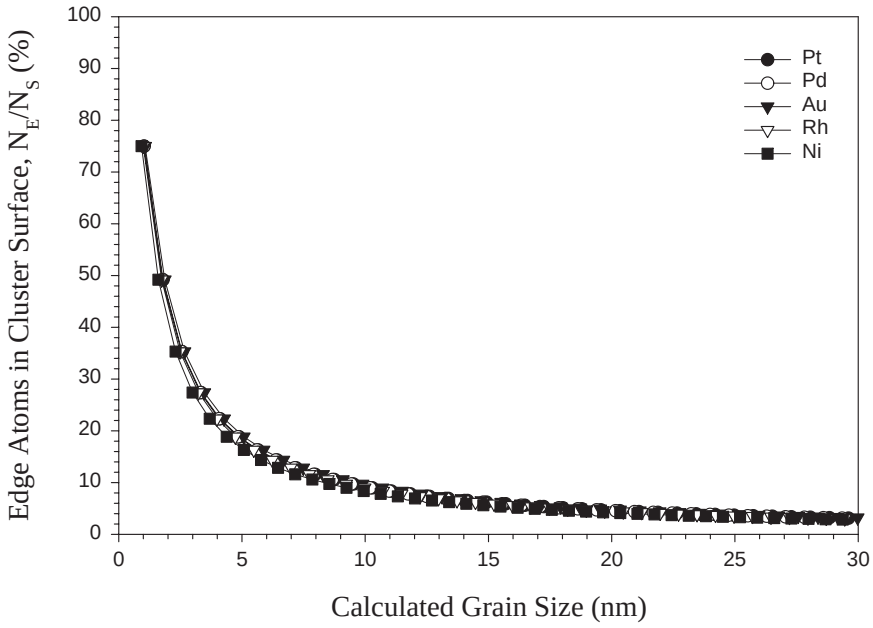

Figure 2.13: Calculated percentage of edge atoms in truncated octahedral clusters for various catalytic FCC metals.

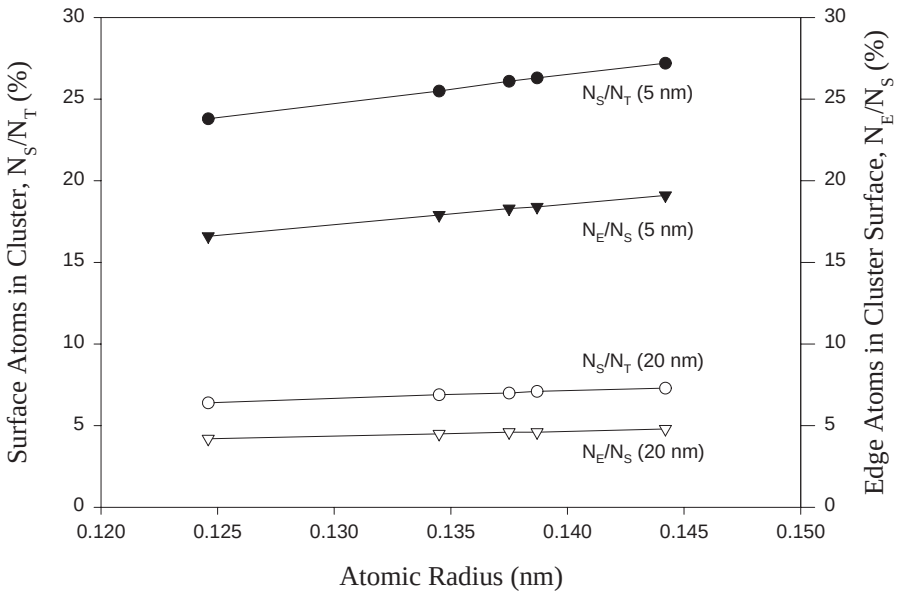

Figure 2.14: Variation of calculated number of surface and edge atoms with atom size in an FCC metal truncated octahedron cluster.

they were calculated from Equations 2.13–2.17, which were originally intended to be used only for discrete cluster levels. Nevertheless, the results indicate a one-to-one correspondence between the distribution of surface atoms in a metal cluster and the size of the cluster atoms. This suggests that larger radii metals may exhibit properties different from the bulk phase at larger grain sizes compared to smaller radii materials.

Table 2.1: Calculated variation in the number of surface and edge atoms in a truncated octahedron for 5 nm and 20 nm clusters.

FCC Metal	Lattice Param. (nm)	Atomic Radius (nm)	N_S/N_T (%) (5 nm)	N_E/N_S (%) (5 nm)	N_S/N_T (%) (20 nm)	N_E/N_S (%) (20 nm)
Au	0.40782	0.1442	27.2	19.1	7.3	4.8
Pt	0.39236	0.1387	26.3	18.4	7.1	4.6
Pd	0.38903	0.1375	26.1	18.3	7.0	4.6
Rh	0.38032	0.1345	25.5	17.9	6.9	4.5
Ni	0.35240	0.1246	23.8	16.6	6.4	4.2

Lattice parameter values are from reference [54].

2.3.3 Structure sensitivity in catalysis

One way of classifying heterogeneous catalyzed reactions is structure-sensitivity. A reaction can be determined to be structure-sensitive if the turnover rate (TOR) is sensitive to the details of the metal surface. The TOR of a reaction can be defined as the number of molecules reacted or formed per active site per unit time. If a structure-sensitive reaction were catalyzed by a transition metal, such as platinum or palladium, it would then be expected to exhibit changes in the TOR as a function of metal grain size or metal dispersion. Structure-insensitivity can

therefore be defined to mean that the TOR is not affected by changes in the catalyst structure such as the grain size.

Somorjai provides a convenient listing of commonly studied reactions classified by their structure-sensitivity [55]. This listing is reproduced in Table 2.2. From this table it would appear that many hydrocarbon reactions involving hydrogen, particularly the hydrogenation of ethylene and benzene, have been determined by many researchers to be structure-insensitive. Also, structure-sensitivity would appear to be independent of the catalyst metal, since platinum, nickel, and iron are involved in both structure-sensitive and structure-insensitive reactions.

Nanometer-scale effects

The origin of structure-sensitivity may be directly linked with the properties of nanostructured materials. For example, Siegel measured the decomposition of H_2S over titania at 500 °C and found that the higher surface area of nanostructured titania was more active than conventional-size titanias [17]. In all cases, structure-sensitivity is observed to occur in systems where the grain size is 50 nm or less. In addition, many of these reactions go through a maximum in rate followed by a sharp drop in activity as the grain size of the active metal is reduced below 10 nm.

A typical example is the work of Doesburg *et al.* for methanol synthesis on copper/zinc oxide/alumina catalysts [56]. Their work, shown in Figure 2.15, exhibits a maximum for the synthesis of methanol at 7 nm followed by a decrease in activity as a function of the active metal grain size. In some structure-sensitive reactions no maximum rate is observed, but the increase in rate with decreasing

Table 2.2: Common structure-sensitive and structure-insensitive reactions.

Structure-sensitive	Structure-insensitive
Hydrogenolysis	Ring opening
Ethane: Ni	Cyclopropane: Pt
Methylcyclopentane: Pt	
	Hydrogenation
Isomerization	Benzene: Pt
Isobutane: Pt	Ethylene: Pt, Rh
Hexane:Pt	Carbon Monoxide: Ni, Rh, Ru, Mo, Fe
Cyclization	Dehydrogenation
Hexane: Pt	Cyclohexane: Pt
Heptane: Pt	
	Hydrodesulfurization
Ammonia synthesis	Thiophene: Mo
Fe, Re	
Hydrodesulfurization	
Thiophene: Re	

Reproduced from reference [55].

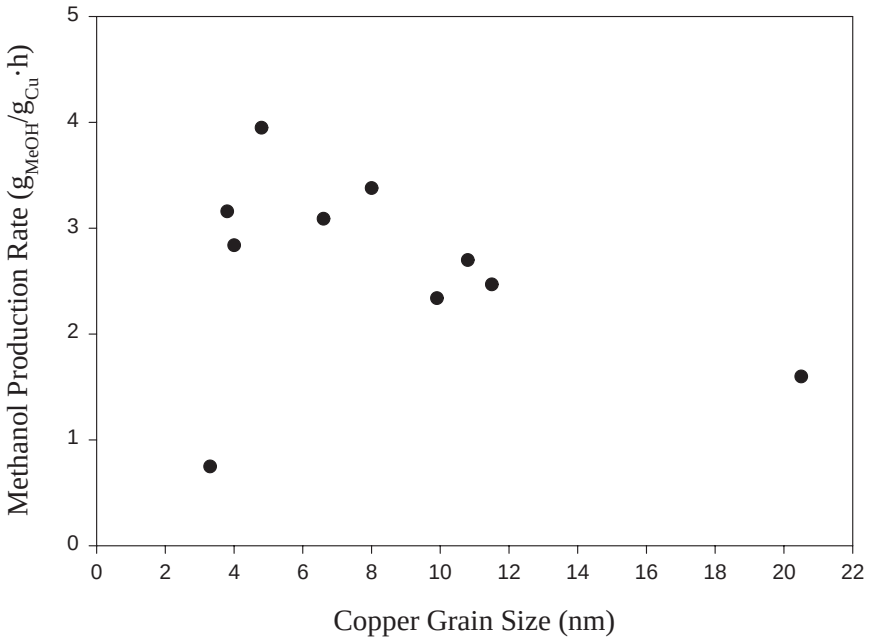

Figure 2.15: Rate of formation of methanol as a function of copper grain size for low pressure synthesis of methanol at 70 bar and 240 °C over $Cu/ZnO/Al_2O_3$ [56].

grain size is still found. In still others, the opposite trend is observed, as in the case of ammonia synthesis, where the TOR calculated by hydrogen chemisorption increases with increasing iron grain size.

Hydrogenation structure-sensitivity

The hydrogenation of hydrocarbons is considered one of the prime examples of structure-insensitivity. However, there are some examples of hydrogenation reactions where structure-sensitivity is observed. Wilcoxon studied the hydrogenation of pyrene in hexadecane versus palladium cluster size and found that the rate increased with decreasing grain size [8]. The large change in activity occurred in the range of 2–10 nm, which is also where other physical properties, such as the optical absorbance differ from their bulk values (see Figure 2.1). Masson *et al.* observed a maximum in the TOR for ethylene hydrogenation at grain sizes below 2 nm independent of the support, as shown in Figure 2.16 [57]. Both platinum on silica and platinum on alumina were used for the hydrogenation.

Cusumano showed that the rate of a 1 nm platinum catalyst had six times the activity of an 8.5 nm catalyst for cyclohexene dehydrogenation [58]. Similarly, Busser *et al.* synthesized a series of polymer-stabilized rhodium catalysts in the range of 1–5 nm [10]. Their results for cyclohexene hydrogenation are shown in Figure 2.17 and also demonstrate a six-fold increase in activity over a short particle size range.

Benzene hydrogenation, also considered a structure-insensitive reaction, has been observed to exhibit all three types of structure-sensitive reactivity behavior.

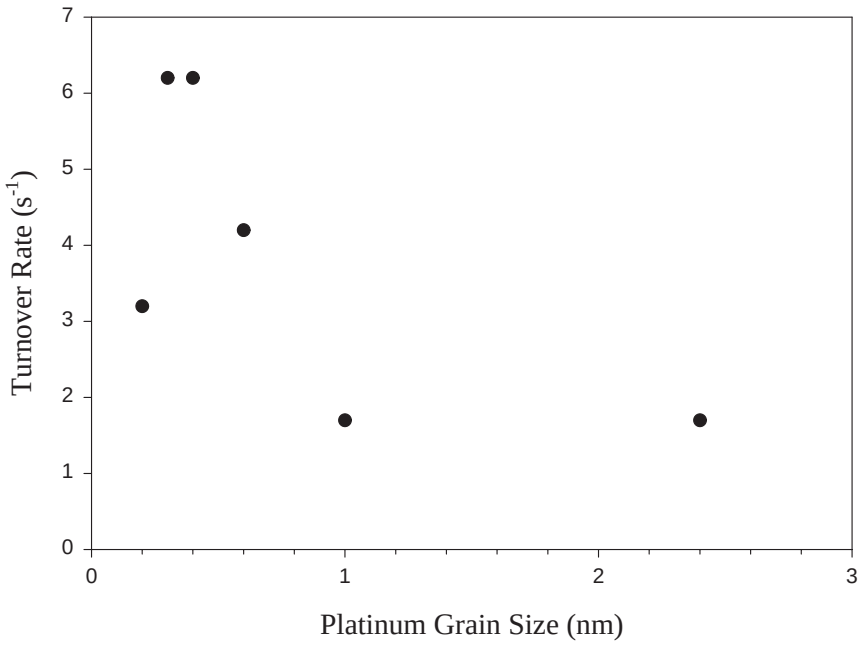

Figure 2.16: Ethylene hydrogenation rate as a function of platinum grain size at 100 °C for alumina supported platinum catalysts [57].

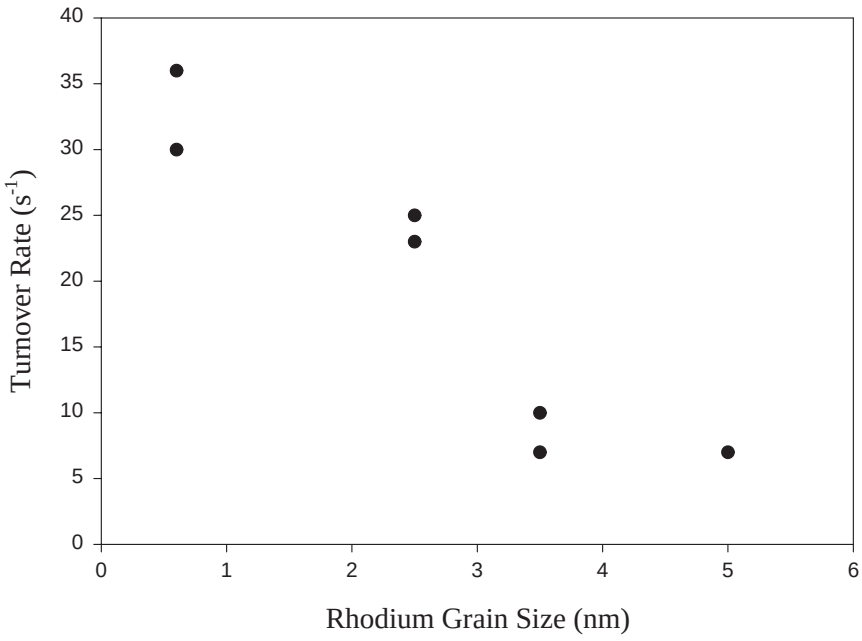

Figure 2.17: Cyclohexene hydrogenation rate as a function of rhodium grain size at 50 °C for polymer-stabilized rhodium particles [10].

For example, Fuentes and Figueras studied the hydrogenation of benzene over ceria supported rhodium catalysts [59]. When the grain size of rhodium is calculated from their dispersion data and plotted in Figure 2.18, it is clear that at grain sizes above 10 nm, the TOR would be considered structure-insensitive. However, below 10 nm, which is to say a high dispersion of rhodium, the TOR goes through a maximum around 4 nm and then decreases below the TOR of the bulk around 1 nm.

Taylor and Staffin synthesized a series of nickel catalysts supported on silica and silica-alumina and tested them for benzene hydrogenation [60]. Both types of supported materials exhibited a decreasing rate with decreasing nickel content, although the rate of the silica-alumina supported catalyst decreased more rapidly than the silica one, suggesting that the support may have some influence on the rate. Nikolajenko *et al.* synthesized Ni-MgO catalysts with varying nickel content and observed the opposite trend [61]. Their data, reproduced in Figure 2.19, shows that the benzene hydrogenation rate increases with decreasing nickel content, in contrast to the data of Taylor. Since lower concentrations on a surface should lead to reduced grain size, decreasing metal content can be associated with decreasing grain size.

Oxidation structure-sensitivity

Oxidation reactions are known to be affected by changes in the catalytic surface. For example, it is well known that molybdenum oxide is structure-sensitive for the mild oxidation of propylene [62–65]. The activity of propylene oxidation is

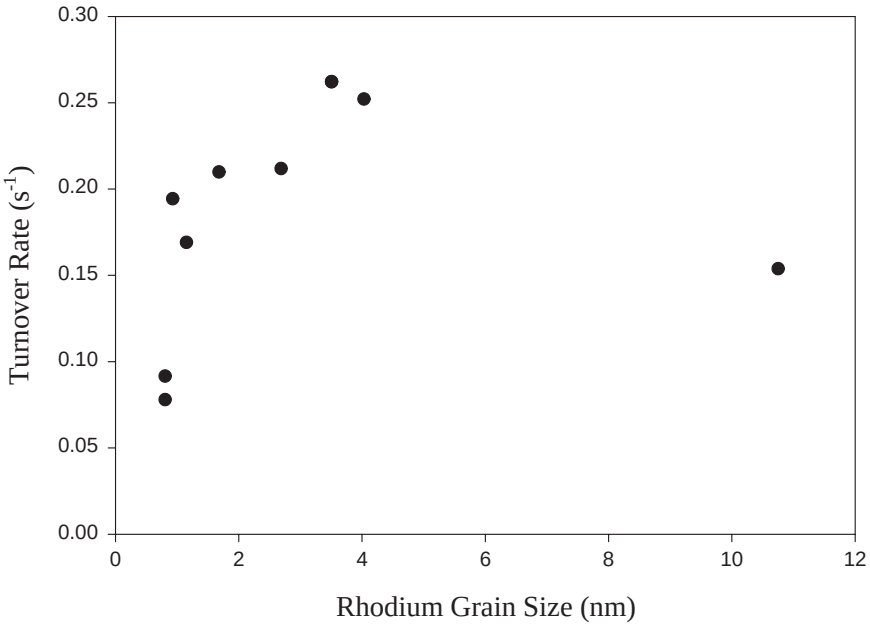

Figure 2.18: Benzene hydrogenation rate as a function of rhodium grain size at 50 °C for alumina supported rhodium catalysts [59].

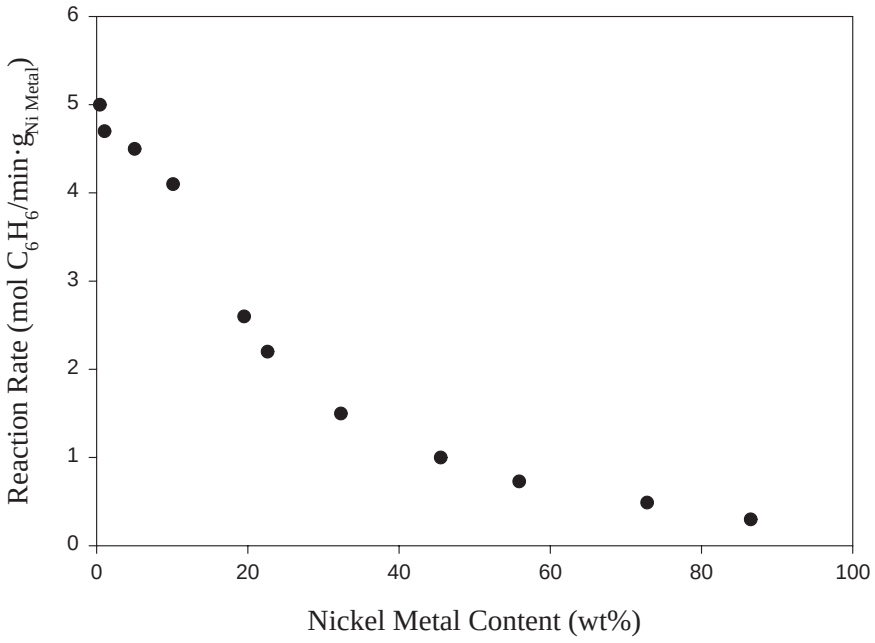

Figure 2.19: Benzene hydrogenation rate as a function of nickel concentration at 40 °C for MgO supported nickel catalysts [61].

strongly dependent on the ratio of edges to basal planes. It is generally agreed upon that the crystal edges are more active and selective because they are the sites with lower coordination. This phenomenon has also been observed for oxidation reactions on vanadia [62, 65]. Goncharova *et al.* showed that there was a 20-fold increase in the rate of ethylene epoxidation with an increase in grain size, especially in the range of 30–50 nm [66]. They attributed this effect to a change in the surface of the silver particles (*e.g.* planar versus defect regions).

Total oxidation reactions also appear to exhibit structure-sensitivity. For example, Sarkas *et al.* observed a 3–6-fold increase in activity with small grained Li-MgO versus a conventionally prepared material for methane oxidation [67]. Stará *et al.* saw the activation energy of carbon monoxide oxidation over Pd on alumina decrease with decreasing grain size of Pd which they attributed to higher reactivity of small particles [68].

The most striking total oxidation results, however, are those of Haruta *et al.* for the oxidation of carbon monoxide over gold [28]. One of the interesting features of their reactivity data is that gold produced the results, since gold has been considered in the past to be a poor catalytic material. However, their data, shown in Figure 2.20, clearly show that the oxidation rate of carbon monoxide over gold increases by a factor of 6–7 below a gold grain size of 5 nm independent of the support material.

2.3.4 Implications for catalysis

Given the interesting physical and structural properties of nanostructured materials, combined with the interesting catalytic structure-sensitive phenomena that has

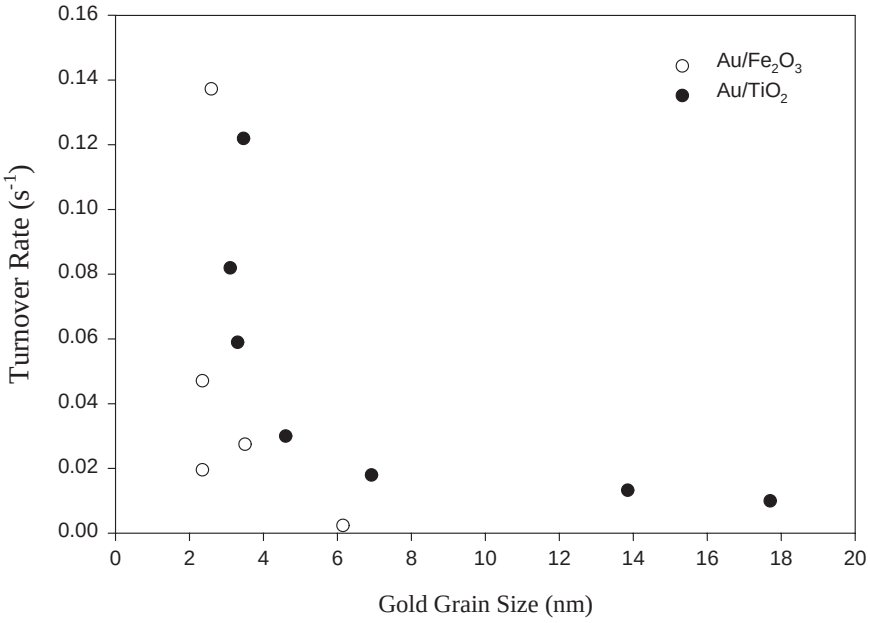

Figure 2.20: Carbon monoxide oxidation rate as a function of gold grain size at 0 °C for TiO_2 and α-Fe_2O_3 supported gold catalysts [28].

been observed, it is difficult to make a general picture of the effect nanometer-size catalytic materials have on heterogeneous catalysis. For example, the structure-sensitive behavior observed for reactions normally considered structure-insensitive may be due to electronic or chemical properties of the small metal particles, or may simply be due to their structural characteristics.

Perturbation molecular orbital hypothesis

The very well-known variation in ionization potential with decreasing grain size suggests that a molecular orbital approach can explain the different structure-sensitive results [5,40–43]. A schematic representation of a perturbation molecular orbital explanation (PMO) is shown in Figure 2.21. The ionization potential of a single metal atom is expected to be the highest, given the trends observed experimentally. As a result, the energy level of the d-orbitals available for donation in a reaction will be much higher with respect to the vacuum level than the corresponding anti-bonding orbitals in a typical reactant. As more metal atoms are added to the first atom, a cluster begins to form, whose non-bonding orbitals are now at a lower energy level. At this point, the energy level may still be too high for a favorable reaction to occur.

As more atoms are added to a metal cluster, and the corresponding grain size increases to the 1–2 nm range, the energy level of the donating electron orbital will approach the energy level of the reactant. Thus, the energy barrier for the donation of electrons diminishes, and the reactivity should increase. This trend may then continue until a grain size of 5–7 nm is reached, at which point the energy

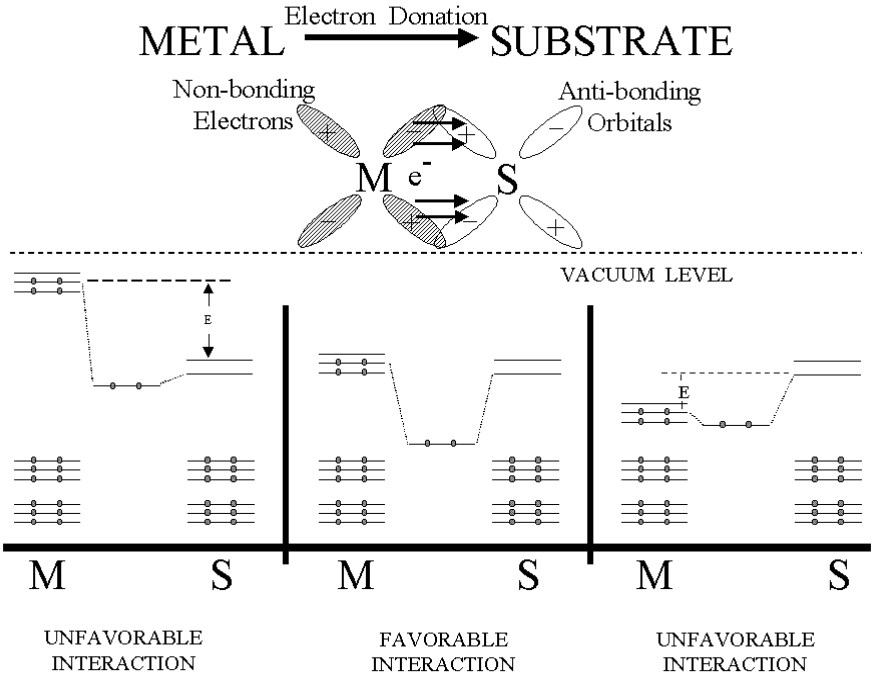

Figure 2.21: Perturbation molecular orbital theory explanation for reactivity changes. As metal atoms are added to a cluster, the energy levels of the d-orbital electrons available for donation change with respect to the anti-bonding orbitals of a reactant. As the difference between the energy levels changes, the energy barrier for electron donation changes.

level of the cluster begins to become lower than those of a typical reactant. In this cluster size region, a maximum in TOR would then be expected with perhaps a corresponding minimum in the activation energy of the reaction.

Eventually, the cluster size will grow to the point where there is again a large energy barrier for the facile donation of electrons. As a result, as the grain size increases, the reactivity should diminish relative to the maximum at 5–7 nm and eventually fall to the bulk reactivity observed at large grain sizes. This value will necessarily be somewhat higher than the reactivity of a single metal atom.

To describe the structure-sensitivity in terms of the PMO hypothesis, changes in ionization potential due to support materials must be taken into account. The large changes in ionization potential occur at very small grain sizes for gas phase metal clusters, less than 1 nm, which is much smaller than the 3–7 nm where the changes in catalytic behavior have been observed. However, the nature of the support material can alter the ionization potentials of supported metal clusters and shift them to higher values occurring at larger cluster sizes.

Structural hypothesis

Although the PMO argument for structure-sensitivity is certainly viable, an alternative structural argument can be made to explain the observed catalytic data. For a structural argument to be valid, it must not only agree with the observed structure-sensitivity data, it must also agree with the different observed phenomena for the same metal, as in the case of benzene hydrogenation over nickel. This may mean that support interactions and pretreatment of the catalysts have to be included in

the model.

McLeod and Gladden have performed an important mathematical study which can help in the development of an overall structural argument [69]. They developed a Monte Carlo simulation to describe the reaction of two molecules (*e.g.* ethylene and hydrogen) on a catalytic surface. In one set of simulations, they varied the cluster size required for adsorption on their "metal clusters" and observed the TOR as a function of grain size. The size of the active site was represented by increasing the size of the "reactant." This was designed to simulate the need for an ensemble of atoms on a metal crystallite as the active site. What they discovered was that at vary large grain sizes (greater than 10 nm), the TOR was constant. However, below approximately 10 nm there was a decrease in the TOR for all assumptions of active site size. They attributed this to an adsorption inhibition caused by a decrease in the number of active sites.

McLeod and Gladden performed another interesting simulation where they decided to make only the edges of the metal clusters on the surface active. When the size of the active site required was small, then the TOR was proportional to the number of active sites lying on particle edges. However, when the size of the active site was increased, the TOR went through a maximum as the grain size was decreased. McLeod and Gladden explained this phenomenon as a "trade off between having a high proportion of active sites, as will occur for small metal particles, and a reduction in the adsorption rate due to the influence of the particle boundary. [69]"

Based on this simulation information, and knowledge of the properties of nano-

structured materials already described, the following hypothesis can be proposed, which is sketched in Figure 2.22 as a function of the dimensionless grain size, D_{rel}, defined earlier. There are three types of observed structure-sensitivity: (1) the TOR decreases with a decreasing grain size or metal content; (2) the TOR increases with decreasing grain size or metal content; and (3) the TOR increases with decreasing grain size or metal content, but then reaches a maximum and begins to decrease. In all cases, it will be assumed that there is some bulk TOR which all catalysts of a particular metal will achieve above a grain size of 100 nm. For the purposes of Figure 2.22, this rate will be assumed to be attained above a D_{rel} of approximately 37, which would correspond to 10 nm.

In the first case, denoted I, the TOR decreases with a decreasing grain size. This essentially means that the TOR does not depend on the number of edge sites, which increases as grain size decreases, but may depend on a specific Miller index plane. For example, if the metal cluster on a supported catalyst maintains a truncated octahedral shape and is most active for a reaction due to (100) planes, then as the grain size is decreased, the number of (100) planes decreases at the expense of (111) planes, and thus the TOR will decrease accordingly.

The support may also play a role in this first case. If a reaction requires (111) planes, the previous argument would not work, as the truncated octahedron has a proportionally higher number of (111) faces as the grain size is decreased. However, the actual metal cluster on the support is more likely to be a half truncated octahedron. This half octahedron can, for example, be oriented to have a (111) plane exposed parallel to the surface or a (100) plane exposed based on the choice of

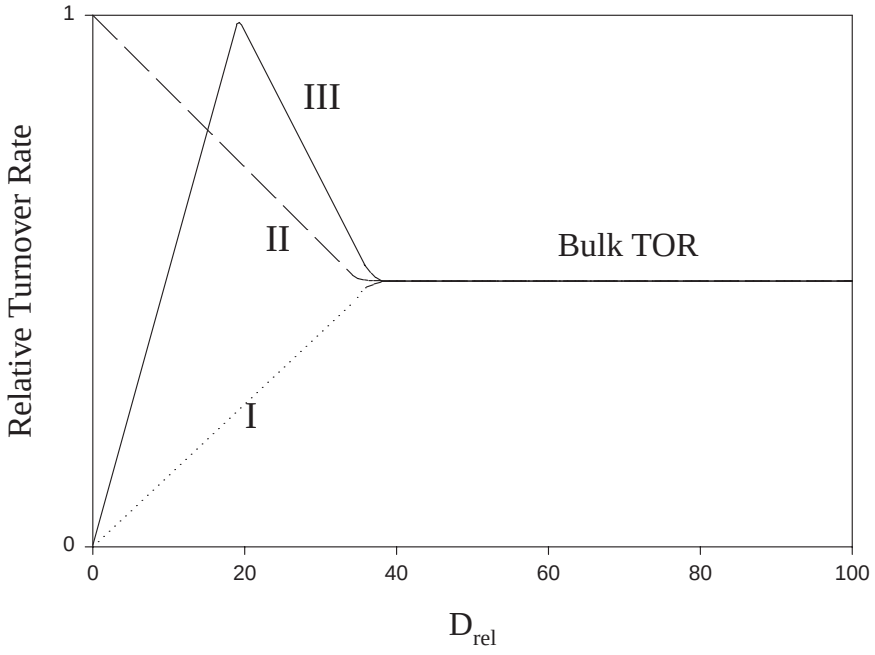

Figure 2.22: Hypothesis for nanometer-sized structure-sensitivity. (I) Region proportional to number of active sites; (II) Region proportional to number of low-coordination sites; (III) Region proportional to number of low-coordination sites followed by inhibition.

support, since the metal cluster must orient itself with the surface. Thus a reaction could depend on (111) planes, or no planes at all, and still exhibit an increasing TOR with increasing grain size.

Case II describes the situation where the TOR increases with decreasing grain size or metal content. This means that the reaction rate is most likely dependent on low-coordination active sites, such as the edge sites on a metal crystallite. As the grain size decreases, the number of uncoordinated edge sites increases, thus explaining the dependency. However, the TOR could also be dependent on a specific Miller index on a crystallite surface which increases with decreasing grain size, such as the (111) plane on a truncated octahedron. This would only be true if the TOR increases in proportion with the total surface area of the metal particles or the surface area of the specific plane.

For the situations where a given metal can exhibit both case I and case II behavior for the same reaction, an external phenomenon such as pretreatment conditions or the choice of support is responsible. As in case I, the support can affect the orientation of the crystal plane parallel to the surface, and thus change the concentration of that specific plane. In addition, the support or pretreatment conditions, including the reaction conditions could possibly activate the edge sites for a given reaction (*e.g.* by changing their oxidation states). The support could also change the geometry of the metal cluster. It is also not unreasonable to expect that the electronic state of the nanostructured metal could make the edge sites more active in exactly the way predicted by the PMO hypothesis.

Case III is a special exception to case II, where the reaction exhibits a maximum

in the TOR as the grain size is decreased. Here, as in case II, the reaction rate is most likely dependent on the concentration of low-coordination edge sites, but at some low grain size an inhibition of the reaction takes place. This inhibition could take the form suggested by McLeod and Gladden, where a certain number of atoms in an ensemble at an edge are required to adsorb the reactants, and when the grain size decreases below some value, the number of ensembles begins to decrease.

Just as likely, however, may be an inhibition in the TOR caused by a SMSI effect [49]. Since the grain boundary diffusion rates of nanometer-sized materials increase as the grain size decreases, it seems likely that the support could react with some of the metal clusters and thus decrease the overall catalytic activity. As the grain size approaches 1–2 nm, the influence of changing ionization potentials may also make itself felt by changing the reactivity of the low-coordination sites. Finally, increased desorption activation energies may make a small contribution to decreasing the TOR if the reactants are more strongly adsorbed to the metal cluster.

Given this particular hypothesis, all reactions catalyzed by transition metals should exhibit one of the above three cases at some extremely small grain size. However, the point of onset for structure sensitivity will be different. In some systems, case I and II behavior may occur in grain sizes ranging from 1 nm to upwards of 50 nm. In other catalytic systems, the behavior may not be observed until a grain size of 1 nm is achieved.

The method of synthesis and selection of support for the metals most likely controls the onset of structure-sensitivity (cases I–III), which may also explain why many experimenters observe structure-insensitivity for a particular reaction, but

others observe structure-sensitivity. Furthermore, the above hypothesis implicitly assumes that all metal clusters are of the same grain size, or have a very narrow grain size distribution. Thus, the distribution of cluster sizes can affect the onset and type of structure-sensitivity.

Chapter 3

Cavitation and Bubble Dynamics

3.1 Cavitation inception and effects

3.1.1 The cavitation phenomenon

Cavitation is the formation of vapor or gas bubbles in a liquid caused by a reduction in pressure at constant temperature [23, 24]. This is in contrast to the nucleation of bubbles due to an increase in temperature above the saturated vapor/liquid temperature, which is called boiling. The dynamic pressure reduction can be achieved in many different ways, such as the rapid movement of a propeller through a fluid, but the discussion here will focus on the use of ultrasound (acoustic cavitation) and flow through a restriction (hydrodynamic cavitation). After cavitation bubbles are formed by a dynamic pressure reduction, they are then subjected to a pressure increase, the growth of the bubbles will be stopped and the bubbles will begin to collapse. If there is only vapor within the bubbles, the collapse will be more severe

than if there is gas inside the cavity.

During the bubble collapse, extremely high temperatures and pressures are encountered inside the cavity which can induce chemical reactions. The occurrence of these special reactions in a cavity is typically described as *sonochemistry*, since acoustic cavitation has been used to extensively study this phenomenon. At the end of the collapse, the bubbles may break into several other bubbles, or disappear due to condensation of the vapor and dissipation of the gas back into solution, or the bubbles may rebound and subsequently collapse again. Regardless, two additional phenomena occur outside the cavity after the collapse: the formation of a fluid *microjet* and/or a *shockwave* emanating from the collapse region. The effects of these microjets and shockwaves are well known to engineers, as they have the potential to cause large amounts of damage to materials through impact and erosion (*e.g.* cavitational pump erosion).

3.1.2 Acoustic versus hydrodynamic cavitation

In acoustic cavitation, the dynamic pressure reduction is caused by ultrasonic waves passing through a fluid [1]. The ultrasound induces a series of compression and rarefaction cycles which then give rise to localized areas of high and low pressure. When the low pressure regions drop below the vapor pressure of the fluid, cavitation bubbles are formed. Next, when the compression cycle increases the pressures in these regions, the bubbles collapse. Thus, ultrasound causes the continuous formation and collapse of bubbles within a static fluid.

Hydrodynamic cavitation due to a flowing liquid is a much more complicated

phenomenon to describe. Typically, a special pressure coefficient, the cavitation number, is used to describe the degree of cavitation. The form of the cavitation number can easily be derived from Bernoulli's equation (for negligible friction loss and without gravitational effects) as shown in Equations 3.1 & 3.2, where the subscript, o, is used to designate the pressure and velocity within a flow restriction (*i.e.* an orifice).

$$\begin{aligned} p + \frac{1}{2}\rho u^2 &= p_o + \frac{1}{2}\rho u_o^2 \\ p - p_o &= \frac{1}{2}\rho u_o^2 - \frac{1}{2}\rho u^2 \end{aligned} \tag{3.1}$$

$$\sigma = C_p = \frac{p - p_o}{\frac{1}{2}\rho u_o^2} = 1 - \left(\frac{u}{u_o}\right)^2 \tag{3.2}$$

In Equation 3.2, the pressure outside of the orifice can be defined either as the upstream or downstream pressure. Typically, p_o is replaced with the vapor pressure of the fluid, p_V, in recognition that the pressure inside the orifice must be at the vapor pressure or below in order for cavitation to occur. For this work, a throat cavitation number (σ_T) will be used where the pressure outside of the orifice will be represented by the upstream pressure. This definition of the throat cavitation number is represented symbolically by Equation 3.3.

$$\sigma_T = \frac{p - p_V}{\frac{1}{2}\rho u^2} \tag{3.3}$$

3.1.3 Nucleation of cavitation bubbles

Heterogeneous nucleation from stabilized gas bubbles

Homogeneous nucleation of bubbles within a liquid is very rare for most systems. Typically, the walls of a container or pipe serve as sites for the heterogeneous nucleation of gas and vapor bubbles by lowering the free energy needed for a cavity to grow and thus lowering the nucleation energy barrier [1, 23, 24, 70]. In addition, contaminating particles suspended in the liquid can also stabilize gas cavities and thus form sites for heterogeneous nucleation. If pre-existing gas cavities exist which are stabilized at a size greater than the critical nucleus size, then the nucleation energy barrier is effectively reduced to zero.

The presence of stabilized gas bubbles, either on a pipe wall or on microscopic particles in the liquid, is in fact the reason that cavitation can occur at ambient conditions. Theoretically, many liquids should be able to withstand tensile stresses on the order of 3×10^4 atmospheres, and thus withstand any attempt to form cavities within them [23]. Tensile strength measurements have confirmed that much lower stresses are required to form cavities in water and other fluids. In practice, cavitation can be induced acoustically at approximately 1 atm, and this is now accepted as being due to the bubble nuclei stabilized by crevices [70].

When the pressure in a fluid drops sufficiently below a certain value, which may be near the vapor pressure of the fluid, the gas and vapor nuclei begin to grow and eventually collapse, giving rise to cavitation. For any given system, the point at which cavitation will occur is difficult to predict without relying on empirical

data. In fact, even this is very difficult to do in practice. Data from different water tunnels around the world using the same flow geometry show a large variability in the measurement of cavitation inception [23]. The effects due to microscopic particle and gas contamination thus make reproducibility difficult.

Pressure coefficient analysis of hydrodynamic cavitation inception

In flowing systems, the pressure coefficient can be redefined as a function of position, x,

$$C_p(x) = \frac{p(x) - p_\infty}{\frac{1}{2}\rho u_\infty^2} \tag{3.4}$$

where p_∞ and u_∞ are the pressure and velocity of a uniform, upstream flow [23]. At some position, x^*, within the flow, C_p and p will be at a minimum. This value, $C_p(x^*)$, will be designated C_{pmin}, and can be used to describe nucleation of cavitation bubbles in the flow. Note that with this definition, C_{pmin} is a negative number. Also, both $C_p(x)$ and C_{pmin} are functions of the Reynolds number for steady, viscous flows of a fixed geometry.

Assuming that for a given flow system, the value of C_{pmin} is known, then the cavitation number, σ, rewritten as Equation 3.5, can be compared to determine whether cavitation will occur.

$$\sigma = \frac{p_\infty - p_V}{\frac{1}{2}\rho u_\infty^2} \tag{3.5}$$

Three cases can be described for a flowing liquid: (1) when the value of the cavitation number, σ, is greater than $-C_{pmin}$; (2) when the value of σ is equal to

$-C_{pmin}$; and when σ is less than $-C_{pmin}$. In the first case, the pressure of the fluid is everywhere greater than its vapor pressure, and thus no cavitation can occur. When the cavitation number is equal to $-C_{pmin}$, then the minimum pressure in the flow is equal to the vapor pressure of the liquid for an infinitesimally small time at position x^*, and it may be possible to nucleate bubbles in the fluid. In the third case, the pressure in the flow is less than the vapor pressure for a finite time period, and cavitation is certain. The value of the cavitation number when cavitation actually occurs is usually termed the *incipient* cavitation number, designated by σ_i.

For a hypothetical flow, the value of σ_i will be equal to $-C_{pmin}$. In practice, however, this is not the case, and σ_i must be determined empirically for a given flow system. In a real system, nucleation will not occur at $\sigma = -C_{pmin}$ because the liquid has a tensile strength which must be overcome for nucleation to occur, and a finite residence time must be spent at $p < p_V$ for a nucleus to grow. Residence time effects can actually cause a reduction in the theoretical value of σ_i. In addition, as C_{pmin} is dependent on the Reynolds number, σ_i may also vary with the Reynolds number. Turbulence can add to these complications by causing an increase in the value of σ_i [23]. The presence of contaminant gas in the fluid can alter bubble nucleation, as described above, and can also cause an increase in σ_i. In addition, geometric effects, such as the ratio of an orifice diameter to a pipe diameter or the aspect ratio of an orifice plate, can alter the fluid dynamics and further complicate matters [71, 72].

3.1.4 General effects of cavitation

The effects of cavitation can be classified into two areas—those occurring inside a collapsing cavity, and those occurring outside the cavity. Of the two, the effects outside the cavity are more well known to mechanical designers, and is of more concern for this thesis. There are very few beneficial applications of cavitation, such as high speed cavitating water jets for rock-cutting and dental applications [23]. As a result, most engineers and the literature, have been more concerned with avoiding cavitation than controlling it.

External effects

The presence of cavitation leads to three main external effects: noise, alteration of fluid flow, and material damage. The high frequency noise associated with cavitation is due to the collapse of cavities and is usually considered a nuisance. However, the considerable noise generated is very detrimental for military naval crafts as it gives away the location of vessels to the enemy.

Cavitation modifies the flow of liquids. One side effect of this flow modification is the lessening of the force which can be applied to a surface. This can result in the limiting of the thrust on ship propellers and ship speed [1,24]. In centrifugal pumps there is a drop in both the head and efficiency due to the presence of cavitation. These losses typically give rise to a decrease in power and output in pumps and turbines [24].

Cavitation damages solid flow boundaries by removing material from the sur-

face. It has been found that cavitation can damage all types of solids. Regardless of the fluid employed, or the material being damaged, the cavitation damage also appears identical to that caused by water cavitation [24]. Mechanical force has been found to be the major factor that causes cavitation damage. This factor is always present, even when other means, such as chemical or electrochemical attack are also acting on a surface [24].

The formation of microjets, due to asymmetric bubble collapse near a boundary, and pressure shockwaves lead to impacts on the surface and the mechanical damage (see Figures 3.1 & 3.2) [1, 23–25]. There are different approaches to account for the shockwave produced from a cavity collapse, but an approximate relationship for the pressure peak amplitude, p_p, given by Brennan is

$$p_p \approx 100 \frac{R_M p_\infty}{r} \tag{3.6}$$

where R_M is the maximum bubble radius, and r is the distance from the bubble [23]. Thus, for an external pressure of 1 bar, with $r = R_M$, a pressure wave of approximately 100 bar would be experienced in the fluid approximately one radius distance from the bubble. This relationship is for the pressure wave produced by a single bubble, but it is well known that the coherent collapse of a cloud of bubbles does more damage and produces more noise than the collapse of a single bubble [23]. However, the majority of the modeling work in the literature is for a single bubble collapse, due to the complicated nature of the phenomenon, and a complete explanation for the increased damage, which occurs commonly in nature,

is not yet available.

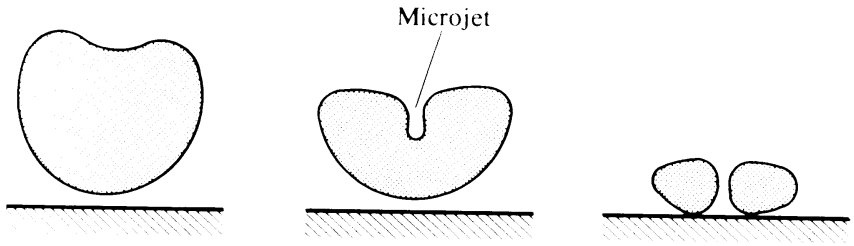

Figure 3.1: Schematic representation of successive stages of nonsymmetrical cavity collapse with microjet impingement against a metallic surface [25].

One interesting side effect due to the shockwaves and microjets produced by the bubble collapses is increased agitation. This local microscopic mixing has the effect of increasing the mass transfer of some reactions by at least a factor of two, as Hagenson and Doraiswamy have shown [73]. Thus, although the collapse of bubbles during cavitation has the potential to do great damage to surfaces, the turbulence produced may lead to advantages in mixing, especially where mass transfer and diffusion processes are involved.

Internal effects

The system inside a collapsing cavity is highly energetic. Upon collapse, the pressure and the temperature within a bubble increases dramatically [1–4, 23, 24]. The values for cavity collapses in water are typically on the order of 2000–4000 °C and 100–400 atm depending on the cavitation conditions [74, 75]. For example, Fujikawa and Akamatsu calculated the maximum temperature for a 1.0 mm bubble

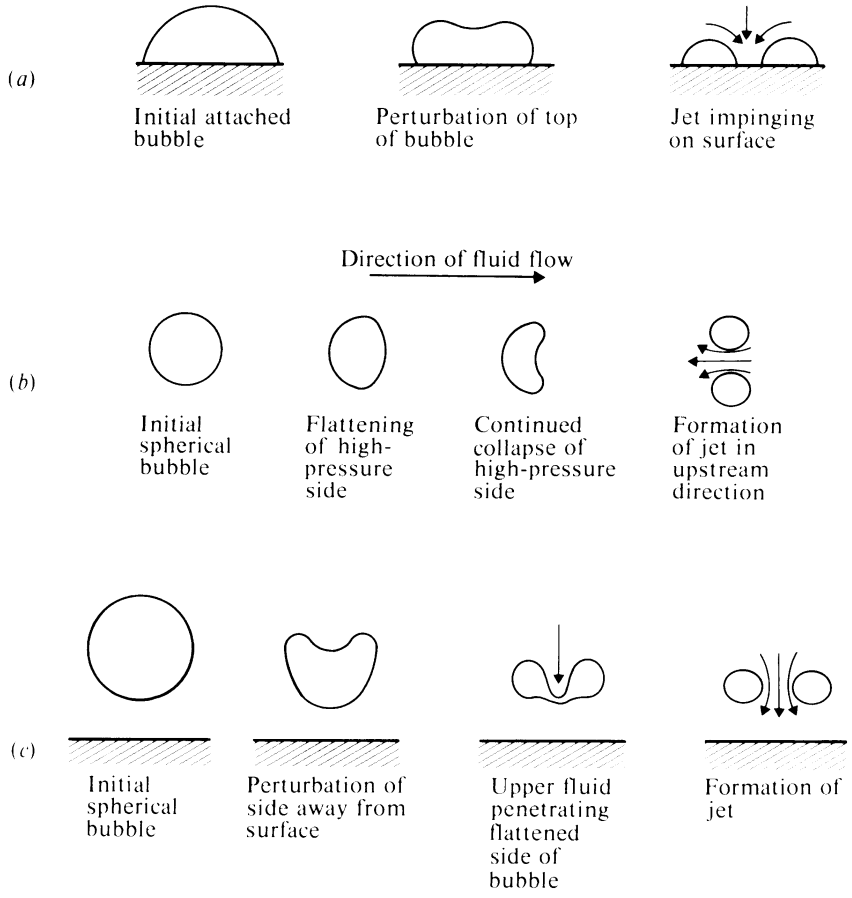

Figure 3.2: Jet collapse models. (a) Hemispherical bubble attached to wall. (b) Bubble moving into pressure gradient. (c) Bubble collapsing near wall. [24, 25].

which collapses in a constant external pressure field. When they accounted for heat transfer and condensation effects, the maximum temperature at the bubble center was 6700 K and at the bubble interface, the maximum temperature was 3413 K [76]. If the bubble was uniform and the collapse was adiabatic, the temperature would be 8786 K.

At the extreme temperatures and pressures experienced inside a cavitation bubble, several vapor phase chemical reactions can occur. In the case of water, which is the standard medium for cavitation experiments, the conditions inside the bubble cause the water vapor to decompose and form free radicals, especially hydroxyl radicals. The presence of small quantities of these radicals allows for interesting chemistry to take place, such as the oxidation of KI.

If a suitable precursor species can be introduced in vapor form inside a cavitation bubble, then it is possible to decompose that species to form a nanostructured solid. For example, Suslick and co-workers examined a wide range of alloy and nanostructured metal particle syntheses by irradiating solutions of the corresponding metal carbonyls with ultrasound [21]. The metal carbonyls, once exposed to the high temperature and pressure within the collapsing bubbles, were decomposed and formed these very small metal particles.

The radicals produced in the high temperature and high pressure environment also have the potential to affect the bulk solution once they are released at the end of the bubble collapse. The OH·, H·, and H_2O_2 which are formed from water can cause secondary oxidation and reduction reactions. One of the well-known systems involving cavitation is the Weissler reaction, where potassium iodide is

oxidized to form small concentrations of iodine [74, 75, 77–79]. The reactions involved are

$$\begin{aligned} 2KI + 2O\dot{H} &\rightarrow 2KOH + I_2 \\ O\dot{H} + O\dot{H} &\rightarrow H_2O_2 \\ 2H\dot{O}_2 + 2KI &\rightarrow 2KOH + I_2 + 2O_2 \\ H\dot{O}_2 + H\dot{O}_2 &\rightarrow H_2O_2 + 2O_2 \\ 2O + 2I^- + 2H_2O &\rightarrow I_2 + O_2 + 2KOH + H_2 \end{aligned}$$

and when a catalyst, such as ammonium molybdate, is combined with sonication, the hydrogen peroxide is oxidized so that the only product formed is iodine [75].

$$H_2O_2 + 2KI \rightarrow 2KOH + I_2$$

In the presence of carbon tetrachloride, the reaction rate is increased due to the formation of chlorine, chlorine radicals, and HOCl inside the cavitation bubbles [74].

To summarize, the external effects of cavitation are shockwaves and microjets which can cause damage to materials but can also lead to increased micromixing. In addition, a great deal of noise is produced as well as the alteration of fluid flow characteristics which are undesirable in process situations (*e.g.* cavitation in pumps). The internal effect of cavitation is to cause local high temperature and pressure environments. In these regions, chemical reactions can occur that would not normally proceed in the bulk fluid and thus lead to enhanced rates of reactions

and the formation of nanometer-size materials.

3.2 Bubble dynamics

A mathematical model can be helpful in providing a guide for an experimental program such as this thesis. Thus, in this section a model for the dynamics of a cavitation bubble collapse will be developed in order to better understand the variables involved. The application of this model to acoustic and hydrodynamic cavitation will then be discussed, followed by numerical simulation results for the hydrodynamic cavitation case to suggest what factors will influence experiments.

3.2.1 Derivation of the Rayleigh-Plesset equation

There are several different approaches to deriving the Rayleigh-Plesset equation which describes the expansion or collapse of a spherical cavity. Most start from either a mechanical energy balance or a fluid dynamics approach, with the latter being more common. The derivation given here is similar to that given in most textbooks on the subject, although there are subtle differences when attempting to describe the behavior of both gas and vapor within a bubble. One of the most detailed derivations to describe the dynamics of a cavity, which is often quoted in most books and journal articles, is that of Fujikawa and Akamatsu [76]. Their model, although it includes much detail, such as mass and heat transfer effects across a bubble boundary and fluid compressibility, is rather unwieldy for practical use.

Since the concepts and basic features of cavitation can be captured in a simpler model, the derivation described here will be as simple as possible, and closely follows that of Brennan [23]. The approach given below, although pertaining to the expansion and collapse of a single bubble, is that most commonly used in the mathematical modeling of cavitation, where it is assumed that the behavior of all other bubbles in the system is identical. In addition, many researchers in the literature (*e.g.* [74, 75, 80]) choose to neglect the effects of viscosity and bubble surface tension to further simplify the numerical solution of the problem, as Lord Rayleigh did in his original derivation [81]. The following is thus a middle ground between the overly simplified result of Lord Rayleigh and the highly complex result of Fujikawa and Akamatsu. A few investigators have used a version identical or similar to this one in their cavitational modeling (*e.g.* [82–85]).

Simple vapor filled bubble collapse

From the conservation of mass (continuity), the velocity (u) at any radial position (r) and time (t) is represented by (see schematic, Figure 3.3):

$$u(r,t) = \frac{F(t)}{r^2} \tag{3.7}$$

where the time dependent function, $F(t)$ can be described by:

$$F(t) = \left[1 - \frac{\rho_V(T_B)}{\rho_L}\right] R^2 \frac{dR}{dt} \tag{3.8}$$

In most cases, $\rho_V(T_B) << \rho_L$, so we can neglect evaporation and condensation effects. Thus, assuming zero mass transport across the bubble interface, $F(t)$ can be given as Equation 3.9.

$$F(t) = R^2 \frac{dR}{dt} \tag{3.9}$$

If we assume that the fluids to be represented by this model are Newtonian, then we can use the Navier-Stokes form of the Equations of Motion in the radial direction to describe the bubble expansion or collapse, as shown in Equation 3.10.

$$-\frac{1}{\rho_L}\frac{\partial p}{\partial r} = \frac{\partial u}{\partial t} + u\frac{\partial u}{\partial r} - \nu_L\left[\frac{1}{r^2}\frac{\partial}{\partial r}\left(r^2\frac{\partial u}{\partial r}\right) - \frac{2u}{r^2}\right] \tag{3.10}$$

If we then substitute Equation 3.7 into Equation 3.10, the term involving ν_L is eliminated, and we are left with Equation 3.11.

$$-\frac{1}{\rho_L}\frac{\partial p}{\partial r} = \frac{1}{r^2}\frac{dF(t)}{dt} - \frac{2F(t)^2}{r^5} \tag{3.11}$$

Integrating from $r = r \rightarrow \infty$ and $p = p \rightarrow p_\infty$ yields Equation 3.12.

$$\frac{p - p_\infty}{\rho_L} = \frac{1}{r}\frac{dF(t)}{dt} - \frac{1}{2}\frac{F(t)^2}{r^4} \tag{3.12}$$

In order to complete this derivation, a boundary condition for the bubble wall and $F(t)$ must be provided. $F(t)$ will be assumed to be Equation 3.9 above, and a force balance on the bubble wall yields the boundary condition shown in

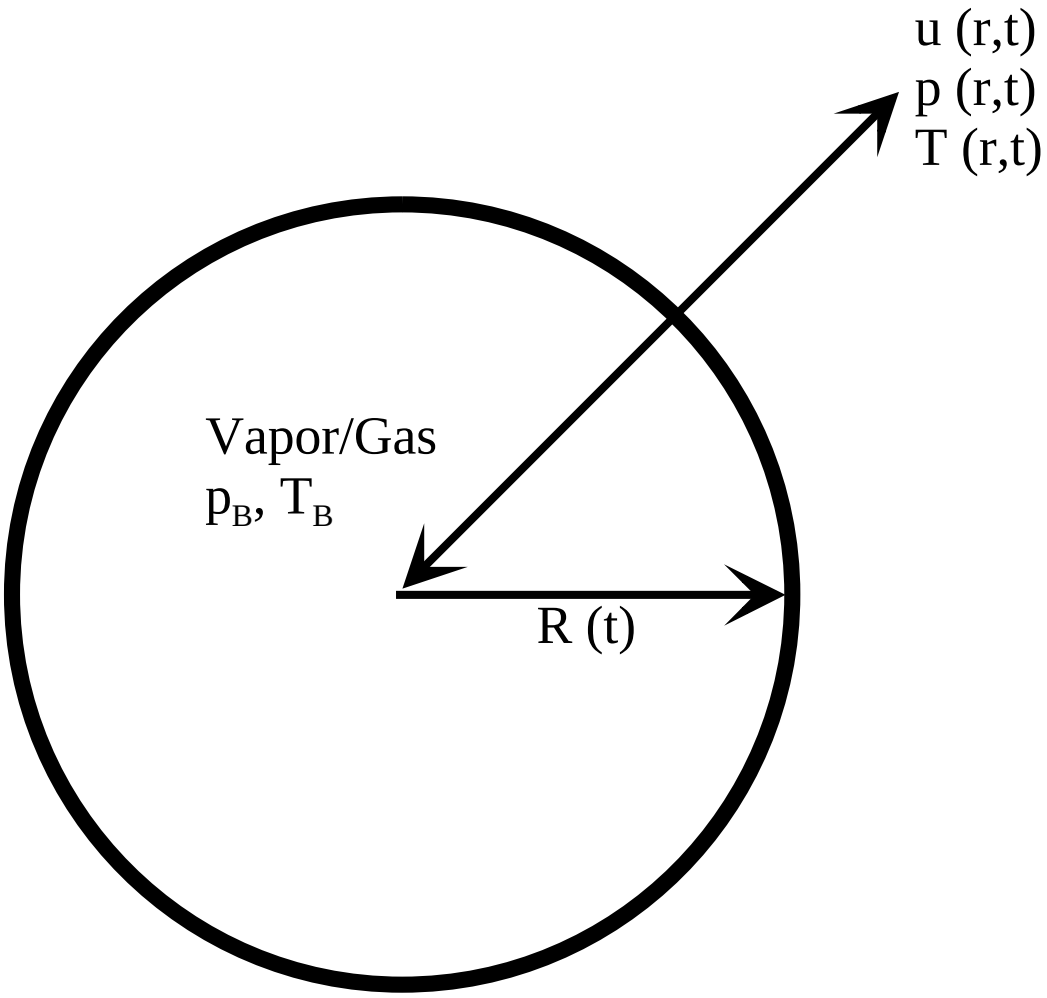

Figure 3.3: Schematic of bubble dynamics model. A bubble of internal temperature (T_B) and pressure (p_B) expands or collapses in the radial direction (r) with a radius of $R(t)$ and a velocity, $u(t)$.

Equation 3.13.

$$p_B + \frac{2\sigma}{R} = p_{r=R} + \frac{4\mu}{3}\left(\frac{\partial u}{\partial r} - \frac{u}{r}\right) \tag{3.13}$$

Given the use of Equation 3.9, it follows that the equations for the bubble wall velocity can be represented by Equation 3.14.

$$\begin{aligned} u &= \frac{R^2}{r^2}\frac{dR}{dt} \\ \frac{du}{dr} &= \frac{-2R^2}{r^3}\frac{dR}{dt} \end{aligned} \tag{3.14}$$

Combining Equation 3.12, where $p = p_{r=R}$, with Equations 3.13 & 3.14 yields the Rayleigh-Plesset equation for bubble dynamics, shown in Equation 3.15.

$$\frac{p_B(t) - p_\infty(t)}{\rho_L} = R\frac{d^2R}{dt^2} + \frac{3}{2}\left(\frac{dR}{dt}\right)^2 + \frac{4\mu_L}{\rho_L R}\frac{dR}{dt} + \frac{2\sigma}{\rho_L R} \tag{3.15}$$

As mentioned above, this result is somewhat of a simplified description of bubble dynamics during cavitation. It neglects such things as heat and mass transfer across the bubble boundary, as well as condensation and compressibility effects. Although these factors have some contribution to the magnitude of the results obtained through the use of Equation 3.15, the general trends are still predicted accurately, which is why some researchers choose to use it. Also as mentioned previously, some investigators simplify this equation by neglecting the viscous and surface tension terms, as Lord Rayleigh did, in order to simplify computation when performing simulations. This is especially done when Equation 3.15 must be solved simultaneously with other differential equations.

Adiabatic collapse with polytropic gas & vapor filled bubble

In almost all situations, a certain amount of gas, typically air, will inevitably be trapped within a bubble cavity. There are several ways to account for this, depending on the complexity of the model (*e.g.* whether there is transport across the boundary). For the derivation just given, a simplified approach to modifying it for gas content is to represent the pressure inside the bubble as the summation of the vapor pressure plus the gas pressure (assumed to behave polytropically) at any given bubble size,

$$p_B(t) = p_V(T_B) + p_{G_0}\left(\frac{T_B}{T_\infty}\right)\left(\frac{R_0}{R}\right)^{3k} \tag{3.16}$$

where p_{G_0} is the initial gas pressure in the bubble. The change in gas pressure with bubble radius can either be assumed to be isothermal, in which case $k = 1$, or adiabatic, where $k = \gamma$. In the latter case, γ typically takes the value of 1.40 for an ideal gas such as air.

Plugging this expression into Equation 3.15 and rearranging, yields a modified form of the Rayleigh-Plesset equation to account for gas content.

$$\frac{p_V(T_\infty) - p_\infty(t)}{\rho_L} + \frac{p_V(T_B) - p_V(T_\infty)}{\rho_L} + \frac{p_{G_0}}{\rho_L}\left(\frac{T_B}{T_\infty}\right)\left(\frac{R_0}{R}\right)^{3k} = R\frac{d^2R}{dt^2} + \frac{3}{2}\left(\frac{dR}{dt}\right)^2 + \frac{4\mu_L}{\rho_L R}\frac{dR}{dt} + \frac{2\sigma}{\rho_L R} \tag{3.17}$$

This expression can further be simplified by neglecting the second term on the left hand side, as the temperature within the liquid has been assumed to be uni-

form for these derivations due to the small time scale involved. For similar reasons, the temperature ratio in the gas pressure term can also be neglected. Thus, the Rayleigh-Plesset equation accounting for a polytropic gas within a collapsing adiabatic cavity, assuming uniform temperatures within the bubble, is given by Equation 3.18.

$$\frac{p_V(T_\infty) - p_\infty(t)}{\rho_L} + \frac{p_{G_0}}{\rho_L}\left(\frac{R_0}{R}\right)^{3\gamma} = R\frac{d^2R}{dt^2} + \frac{3}{2}\left(\frac{dR}{dt}\right)^2 + \frac{4\mu_L}{\rho_L R}\frac{dR}{dt} + \frac{2\sigma}{\rho_L R} \tag{3.18}$$

3.2.2 Application to acoustic cavitation

To make use of any of the variations on the Rayleigh-Plesset equation, a description of the external pressure, $p_\infty(t)$, must be given. In the case of acoustic cavitation in a batch reactor, this profile is a simple time-varying sinusoidal function, such as Equation 3.19,

$$p_\infty(t) = p_{amb} - p_A \sin \omega t \tag{3.19}$$

where p_{amb} is the ambient pressure (usually atmospheric) and p_A is the pressure amplitude of the ultrasonic field [74, 75, 82, 84, 85]. The ω in Equation 3.19 is actually equal to $2\pi f$, where f is the frequency of the acoustic field. The intensity (I), typically in units of W/m^2, of an ultrasonic probe is related to the pressure amplitude, the density of the liquid medium, and the speed of sound in the liquid

(C_L, typically 1500 m/s) by Equation 3.20 [74,84–86].

$$I = \frac{p_A^2}{2\rho_L C_L} \tag{3.20}$$

Experimentally, the pressure amplitude can be determined from calorimetric measurements [74]. Essentially, an ultrasonic source is placed into the solution to be used experimentally, and the temperature rise due to sonication is carefully measured and used to calculate the heat generated by the probe. With careful calorimeter design, the heat generated in the system is assumed to be equal to the energy input from the ultrasonic source. The power measured in these experiments is then divided by the area of the ultrasonic source emission (typically the area of the tip, in the case of an ultrasonic probe) to yield the intensity, I. Equation 3.20, then allows the calculation of the pressure amplitude found in Equation 3.19.

Using Equation 3.20, the external pressure profile can be written in terms of the probe intensity and frequency as Equation 3.21.

$$p_\infty(t) = p_{amb} - \sqrt{2I\rho_L C_L}\sin(2\pi f t) \tag{3.21}$$

This expression for the pressure profile in a sonicated system implies that there are two major factors from the ultrasonic source which affect cavitation: intensity and frequency. For most systems studied, the frequency is either maintained constant or, by the nature of the acoustic source, cannot be changed. This is the case with many ultrasonic probes, which are typically manufactured to produce ultrasound

at a frequencies of 20 or 40 kHz. Thus, the intensity (or indirectly the amplitude) is the major adjustable factor when conducting acoustic cavitation experiments.

The intensity of an acoustic field generated by an ultrasonic source is not uniform, however, but is affected by the distance, d, from the source, as shown in Equation 3.22,

$$I = I_0 \exp(-\alpha d) \tag{3.22}$$

where I_0 is the intensity at the tip or edge of the ultrasound source, and α is the attenuation coefficient for the liquid system being irradiated [87]. This attenuation coefficient is in turn a function of the properties of the fluid system, as well as the frequency of the ultrasonic probe (see Equation 3.23).

$$\alpha = \frac{8\mu_L \pi^2 f^2}{3\rho_L C_L^3} \tag{3.23}$$

Although this degradation of the intensity with distance from the acoustic source is known, for a given set of operating conditions it is a constant, and is therefore ignored in most modeling and fitting of experimental data obtained on sonochemical systems. Typically, the system is assumed to be small enough in volume, and that the ultrasonic source is in a fixed position, so that the acoustic field is uniform and thus Equation 3.21 is considered to approximate the external field pressure.

In addition to the irradiation intensity and the frequency of the acoustic source, the initial cavity radius can affect the acoustic cavitation. Moholkar *et al.* studied the effects of these three factors in a numerical simulation utilizing a form of the Rayleigh-Plesset equation identical to Equation 3.15 [85]. Gogate and Pandit also

explored these three factors in their mathematical modeling, but also investigated the effect of the liquid medium compressibility [84]. In both studies, similar trends were observed in the simulations with regard to the intensity, frequency, and initial cavity radius.

The general trends for changes in intensity were that as the intensity was increased, the magnitude of the pressure pulse (which is directly related to the shockwaves described earlier) increased; as the intensity was increased, the ratio of the maximum bubble radius to the initial radius increased; and that the lifetime of a bubble increases with the intensity of the ultrasound. However, Gogate and Pandit also observed that after a certain initial increase in intensity, the effect on maximum bubble size decreases, and that after a certain point, the pressure of the bubble collapse begins to decrease. This suggests that there may be an optimum intensity for some systems where cavitational effects will be most intense, and that power output and the area of an acoustic source can affect cavitation, since the intensity will vary according to the area of an ultrasonic probe tip (intensity is the ratio of the power of the probe divided by the area of the probe tip).

The effect of increasing irradiation frequency was also to increase the lifetime of a bubble, as in the case of intensity. However, the effect of frequency on the maximum radius size achieved prior to collapse was negligible compared to intensity when compressibility effects are not taken into consideration. If the compressibility of the fluid is accounted for, Gogate and Pandit observed that with an increase in frequency, the lifetime of a bubble decreases; and that bubble collapses are more rapid and violent at higher frequencies. Although there seems to

be some contradiction in the results obtained based on different model assumptions, it would appear that the issue is relatively minor. As has been previously mentioned, most ultrasound generators operate at a fixed frequency.

Li and Inui observed that the use of ultrasound during the synthesis of copper/zinc/aluminum oxide catalysts during precipitation and aging promoted the formation of a hydrotalcite phase in the catalysts [88]. The presence of increased amounts of hydrotalcite in turn led to increased methanol synthesis activity. The percentage of the hydrotalcite present increased as the frequency of the ultrasound probe was increased, which corresponds with the trends observed by Gogate and Pandit, although the crystallite size of the hydrotalcite did not vary in a systematic fashion with increasing ultrasonic frequency.

Initial bubble size also appears to have an effect on acoustic cavitation. Smaller initial radii bubbles appear to grow larger than smaller ones, but their lifetimes were shorter, with higher pressure pulses being generated. Thus, smaller initial bubble sizes lead to more violent cavitational collapses [84, 85]. However, for reasons mentioned earlier in this chapter, such as dissolved gases present in the system and the vapor pressure of the system, the initial bubble size is not amenable to great control. As noted by Gogate and Pandit, the exact nuclei size is difficult to determine, but they observe from the literature that as the vapor pressure of the fluid increases, the size of the bubble will increase; and that the type of dissolved gas has an effect as well [84].

Based on their simulations on cavitation occurring in water, accounting for the compressibility of the fluid, Gogate and Pandit have proposed a correlation for the

pressure of a cavity collapse during acoustic cavitation (see Equation 3.24) [84].

$$P_{\text{collapse}} = 114(R_0)^{-1.88}(I)^{-0.17}(f)^{0.11} \tag{3.24}$$

In Equation 3.24, the collapse pressure in atmospheres is given in terms of the initial bubble radius, R_0, in mm; the ultrasonic intensity, I, is given in W/cm^2; and the frequency, f, is given in kHz. The ranges for each of these factors used for the correlation were an initial bubble size from 0.05–0.5 mm, frequency from 10–120 kHz, and intensity from 10–300 W/cm^2.

Although this correlation is an important step forward for experimentation with and design of sonochemical reactors, it suffers from the limitation that one of the factors, initial bubble size, is not easily determined for any given system. This, coupled with the fact that most ultrasonic equipment is designed to operate at a fixed frequency, suggests that the main contribution of this correlation, and other workers' simulation results, is that the intensity, and hence the amplitude, of the ultrasound source is the main controllable factor in an acoustic cavitation experiment. However, the magnitude and trend of the intensity effect appears to vary depending on the assumptions for a numerical simulation, the main difference being whether to include the effects of water compressibility. Although Gogate and Pandit offer experimental references to support their intensity trends, the differences in results further reinforce the need to perform experimental measurements on specific systems to determine the actual trends.

There have only been a few papers where the bubble dynamics represented by a

form of the Rayleigh-Plesset equation have been combined with a kinetic model of a sonochemical reaction to analyze experimental results. All of them have studied essentially the same reaction, which has become a standard in sonochemistry, the oxidation of aqueous KI to liberate iodine (sometimes referred to as the Weissler reaction) [74, 75, 82]. At present, there appears to have been no work done on the kinetic modeling of any heterogeneous systems due to their added complexity.

The Weissler reaction was modeled as a batch reactor with [75,82] and without the presence of carbon tetrachloride [74]. The reaction proceeds by the generation of radical species such as OH·, H·, and $HO_2\cdot$ which are formed from water during cavitation. When carbon tetrachloride is added to the system, the rate of iodine production is enhanced through the formation of chlorine containing radicals.

The basic procedure was to assume that the various radicals are formed inside a cavitation bubble and are then released into the bulk liquid upon collapse of the bubble. As a result, the bubble dynamics could be calculated separately to estimate the temperature and pressure inside the cavitation bubbles. This information was then used to do thermodynamic equilibrium calculations to determine the composition of the radicals and other species that would be released into the bulk solution. The species concentrations were then used in a standard kinetic model of a homogeneous liquid phase reaction network.

Unfortunately, some of the parameters of these kinetic models still had to be estimated or determined from experimental data. The initial bubble size, as discussed earlier, is not measurable experimentally, and has to be assumed for the solution of the Rayleigh-Plesset equation. The authors attempted to estimate

the critical nucleation size from equilibrium considerations by assuming that the smallest bubble which can grow is related to the lowest pressure in the system induced by the ultrasound waves. The relation they used to estimate the critical nucleation radius was

$$R_c = \frac{4\sigma}{3\,(p_v - p_{LC})} \tag{3.25}$$

where p_{LC} is the lowest pressure reached in the liquid, equal to $p_{amb} - p_A$ [74, 75]. This critical size, which should occur at p_{LC} was then related to the size which should occur at the ambient pressure, and thus the initial radius size (see Equation 3.26).

$$R_c = \sqrt{\frac{3\,(p_{amb} - p_V)\,R_0^3 + 6\sigma R_0^2}{2\sigma}} \tag{3.26}$$

Other factors which are not possible to calculate prior to modeling are the number of cavitation bubbles present in the system, and the rate constants for the kinetic equations. In practice, the number of bubbles is dependent on such things as probe intensity, ultrasound frequency, and the geometry of the reactor setup. However, for this particular reaction, the number of bubbles could be related through the kinetic equations directly to the production rate of iodine in the system, and was thus obtainable from experiments. The rate constants for the kinetic model also had to be determined from experimental data and the use of a quasi-steady state approximation. However, this is standard practice for kinetics, and thus does not detract from this modeling approach.

The results from the models were in quite good agreement with the experimental data, and even allowed for differences in the gas present in the system (*i.e.* air

versus nitrogen or argon). The advantage to this approach is that since the reaction proceeds via the internal effects of cavitation, the kinetic model and the bubble dynamics model can be decoupled. This would not be the case for a system in which the external effects of acoustic cavitation would need to be accounted for, as there would be a need for the incorporation of mass transfer; nucleation and growth rate; and mixing effects into the model. However, many of these factors are at present not easily quantifiable or are unknown for most systems.

3.2.3 Application to hydrodynamic cavitation

The application of bubble dynamics equations, such as the Rayleigh-Plesset equation, to the modeling of a hydrodynamic system is similar and yet more complicated than for an acoustic cavitation system. As in the case of ultrasound induced cavitation, an expression for the external pressure profile is necessary in order to solve the Rayleigh-Plesset equation. Two approaches have been followed to model cavitating flow through tubes and orifices: a simple linear pressure profile approximation and the use of finite element methods. Both approaches suffer from the same difficulties encountered in modeling acoustic cavitation, such as the uncertainties with regard to the initial bubble size and the number of bubbles generated in the system. However, geometric issues and the complexities of geometry on flow increase the difficulties associated with hydrodynamic cavitation modeling. As a result, the main benefit from these modeling efforts is a better understanding of the factors and their trends which may affect experiments.

A typical example of the finite element approach is that of Uchiyama for cav-

itating flow around a cylinder [80]. The finite element method (FEM) offers the most promise for a thorough simulation of hydrodynamic cavitation. The basic approach is to simultaneously solve the conservation equations for mass (continuity) and momentum (the equations of motion) numerically at the same time solving the Rayleigh-Plesset equation. In the case of the example presented here, the equation used to represent the bubble dynamics was similar to Equation 3.15, but simplified for computation by neglecting the surface tension and viscous terms. The number of bubbles present in the system needed to be estimated from experimental observations, and an arbitrary guess was made as to the initial bubble radius in the absence of data. Despite these difficulties, which are present for all cavitation modeling, the FEM approach offers advantages for computing the bubble dynamics for complicated geometric systems.

The second approach to modeling hydrodynamic cavitation is to assume a linear external pressure profile [83,85]. When a liquid flows through an orifice, as shown in Figure 3.4, the pressure, initially at an upstream value of p_0, will drop to some lower pressure. If cavitation is to occur, then this lower pressure will be at least the vapor pressure of the liquid, p_V, and often lower, as described earlier in this chapter. Once the fluid has moved through the orifice into a larger pipe, the pressure will recover somewhat to a downstream value, denoted p_2.

Based on experimental observations, Moholkar *et al.* determined that the pressure recovery after the orifice could be approximated by a linear function [83,85]. Thus, assuming that the pressure at the exit of a typical orifice was equal to the

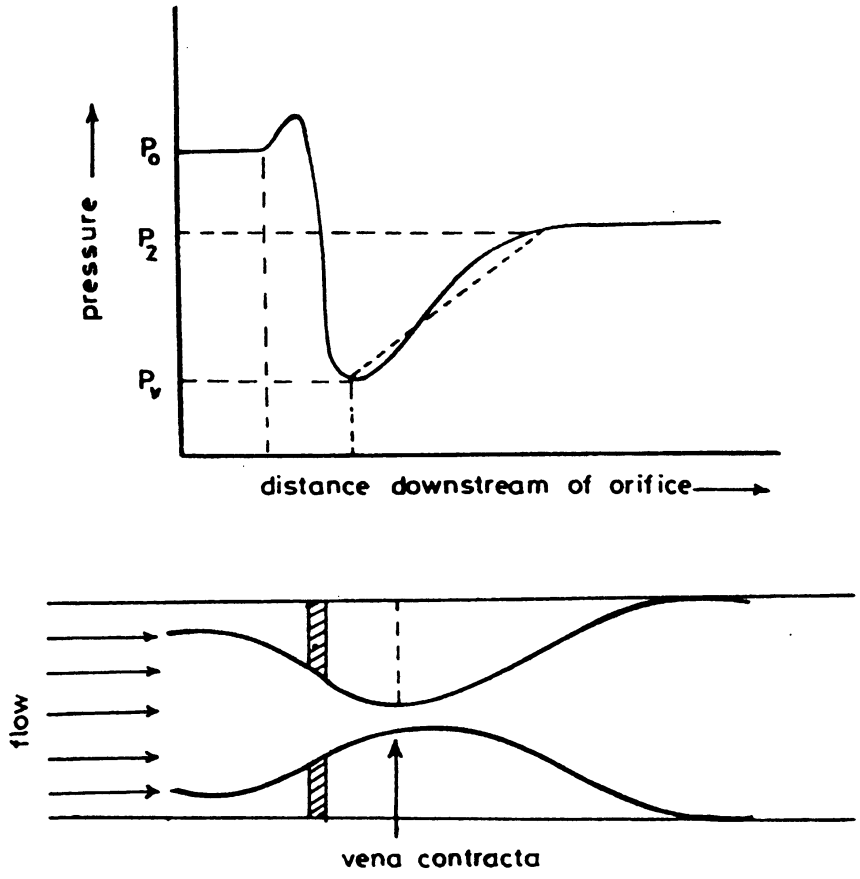

Figure 3.4: Mechanism of pressure recovery across an orifice [85].

vapor pressure of the liquid, they represented the external pressure profile by

$$p_\infty = p_V + \frac{(p_2 - p_V)}{\tau} t \tag{3.27}$$

where τ is the time of pressure recovery. This pressure recovery time, although it simplifies the analysis of the external pressure for modeling, is in itself complicated. It is a function of the diameter of the orifice, the downstream pipe diameter, the ratio of those diameters, the pressure upstream of the orifice, and the cavitation number [85].

Assuming Equation 3.27 to be valid, Moholkar *et al.* used the Rayleigh-Plesset equation, in the form of Equation 3.15, to investigate the effects due to various parameters on hydrodynamic cavitation in a fashion similar to those cited above for acoustic cavitation. The factors studied were: the final recovery pressure downstream of the orifice (p_2), the time of pressure recovery (τ), the initial bubble radius, the orifice to pipe diameter ratio (β), and the pipe size downstream of the orifice. They also attempted to introduce a turbulence model into the simulations to see the effects of the turbulence in the system [83].

From their simulations, it appears that increasing the recovery pressure results in maximizing the cavity size before the bubble collapse, as well as extending the lifetime of the bubble. The amplitude of the bubble oscillations and the magnitude of the pressure pulses resulting from them also increases with increasing recovery pressure. Thus, increasing this factor should result in more intense cavitational effects. The authors attempted to make the analogy between the recovery pressure

in hydrodynamic cavitation and intensity in acoustic cavitation.

The effect of decreasing the recovery time was to increase the lifetime of a bubble and also increase the magnitude of the pressure pulses. Thus, faster pressure recoveries have a similar result as increasing the final recovery pressure, which is consistent. Moholkar *et al*. make the analogy between the time of pressure recovery in hydrodynamic cavitation with frequency in acoustic cavitation [85].

Between the two papers, conflicting results are obtained for the effect of initial bubble radius. When the turbulence model is introduced, the trend of decreasing the initial bubble size results in higher magnitude pressure pulses [83]. However, when turbulence is not part of the model, the opposite trend is observed [85]. Thus, the simulation results leave us with an incomplete view of this factor, which in practice is out of a experimenter's control.

The authors only studied the effect of changing the orifice to pipe diameter when accounting for turbulence in their model. It was observed that increasing β resulted in increasing the lifetime of bubbles, but also a decrease in the turbulence intensity by altering the permanent head loss after the orifice [83]. However, there does not appear to be much of an effect on the maximum bubble size obtained. Similarly, the effect of pipe size downstream of the orifice was only studied for its effects when turbulence was present. It was found that increasing the pipe size downstream of the orifice results in higher pressure pulses due to an increase in the maximum cavity radius. Unfortunately, the authors did not attempt to study in detail the effects of these two factors on the recovery time, which both should affect, and which is a major controlling variable in hydrodynamic cavitation.

At present, it appears that there have been no kinetic studies equivalent to those for the sonochemical batch reactor described previously. In addition to the cavitation which occurs when liquids flow through restrictions, there are additional factors, such as fluid mixing and turbulence, which must be accounted for in such a study. Currently, most research is confined either to modeling of only the bubble dynamics or empirical work to identify the key variables involved. It is expected that eventually a kinetic modeling approach for homogeneous systems such as the Weissler reaction should be possible, however, more experimental work is required if the approach is to be applied to a heterogeneous system.

3.2.4 Hydrodynamic bubble dynamics modeling results

To better understand the complexities of hydrodynamic cavitation and guide the experimental approach taken in this dissertation, the dynamic behavior of a cavitation bubble which is formed inside an orifice in a flowing liquid stream was modeled. Calculations were made using Equation 3.18, which is a modified form of the Rayleigh-Plesset equation in which the bubble is assumed to expand and collapse adiabatically containing the fluid vapor and a polytropic gas. Heat and mass transfer effects at the bubble wall have been ignored due to the small time scale, including the possibility of vapor condensation and evaporation.

The external pressure field was assumed to be linear, varying from an initial bubble formation pressure in the orifice, $p_{\infty}(0)$, equal to or less than the vapor

pressure of water, up to a final recovery pressure (see Equation 3.28).

$$p_\infty(t) = p_\infty(0) + \frac{(p_2 - p_\infty(0))}{\tau} t \tag{3.28}$$

This was done to explore the effect of a larger pressure drop across an orifice, which is possible in a real system. The slope of this linear profile is defined by a recovery time, τ, identical to the definition used by Moholkar *et al.* (*i.e.* the time to increase in pressure from the initial pressure to the final pressure).

Simulations were made by varying the recovery time, τ, the initial bubble radius, R_0, the initial pressure, p_0, and the fully recovered pressure, p_2. Due to the nonlinearity and stiffness of Equation 3.18, standard Runge-Kutta algorithms were found to be inaccurate. Thus, stiff algorithms implemented in two different programs (the Badler-Deuflhard stiff algorithm in POLYMATH [89] and the EPISODE package in Scientist [90]) were used for the simulations for cross-checking purposes.

The results, shown in Figures 3.5–3.8, are presented in terms of the relative bubble radius, which is the radius at any given time divided by the initial radius, and the relative bubble pressure, which is the pressure within the bubble at any time divided by the external pressure at the same time. The relative bubble pressure at the point of each minimum relative radius is the maximum pressure which would develop inside the bubble on collapse. Thus, the relative bubble pressure is an indirect measure of the pressure pulse of the shockwave generated from the bubble rebound. After the first such collapse, the fate of a bubble is largely unknown. The

cavity may rebound, as indicated in the simulations, it may break into a cloud of bubbles which then expand and collapse, or the bubble may simply disintegrate.

In Figure 3.5, the initial pressure was varied from 2338 N/m^2 (the vapor pressure of water) down to 1500 N/m^2, while keeping the recovery time, recovery pressure, and initial bubble radius constant at 0.02 s, 3 bar, and 100 μm, respectively. By decreasing the initial pressure, it was observed that the frequency of the bubble collapses increased. The bubble collapses also become more severe, as indicated by the relative bubble pressure increase with decreased initial pressure. This coincides with bubble collapses to smaller relative radii.

Figure 3.6 shows the recovery time as it was varied from 0.01 s to 0.1 s while keeping the initial pressure, recovery pressure, and initial bubble radius constant at 2338 N/m^2, 3 bar, and 100 μm, respectively. By decreasing the recovery time, large increases in the bubble collapse frequency as well as the bubble collapse intensity can be obtained. As mentioned previously, the recovery time is a function of orifice diameter, downstream pipe diameter, the ratio of the orifice to pipe diameters, the cavitation number, and the pressure of the upstream orifice. For a typical experiment, the orifice diameter and pipe diameter would be fixed, indicating that the upstream pressure is a key factor in controlling the recovery time. The throat cavitation number would also be expected to be a variable in a cavitation experiment, although it is also a function of the upstream pressure. Thus, alteration of the pressure upstream of an orifice would be expected to alter the intensity and frequency of bubble collapses.

In Figure 3.7, the recovery pressure was varied from 1 bar to 5 bar while keeping

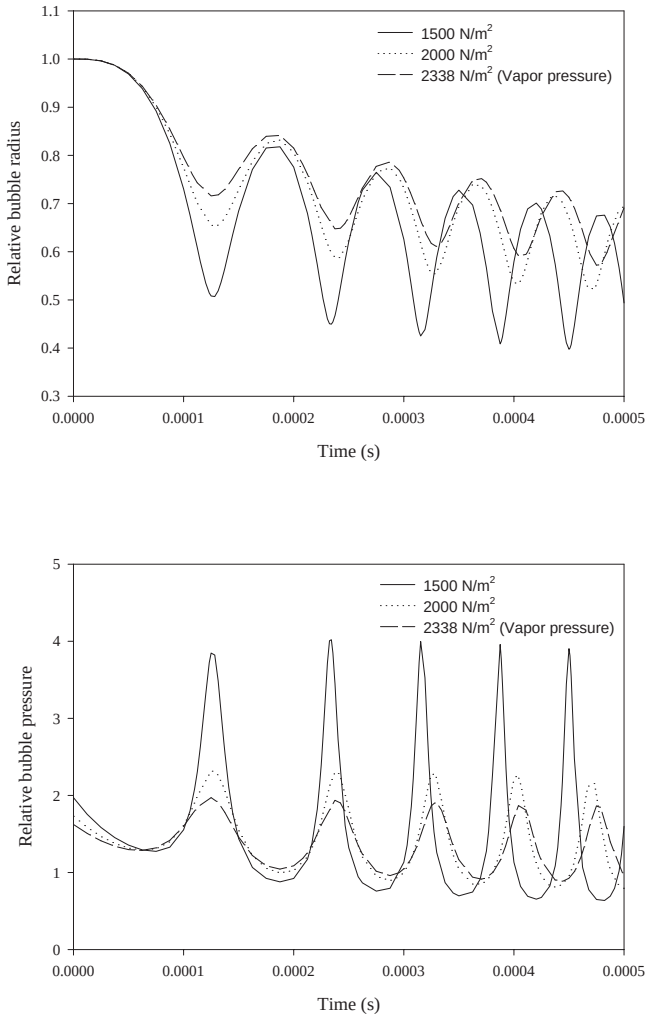

Figure 3.5: Bubble dynamics simulation on the effect of initial bubble pressure (τ=0.02 s, p_2=300000 N/m^2, R_0=100 μm).

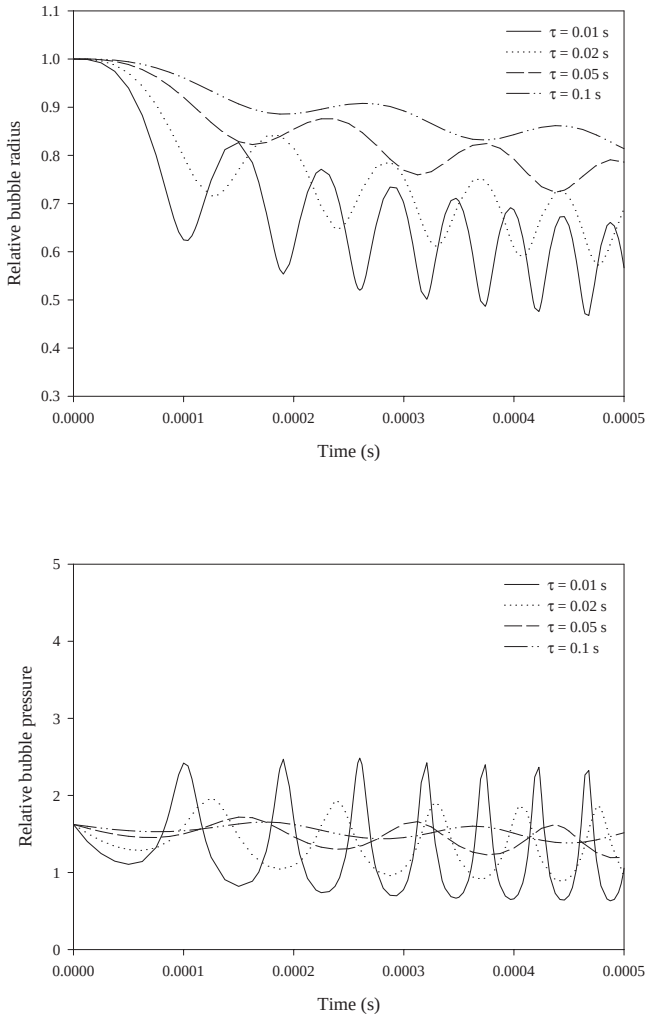

Figure 3.6: Bubble dynamics simulation on the effect of recovery time (p_0=2338 N/m^2, p_2=300000 N/m^2, R_0=100 μm).

the recovery time, initial pressure, and initial bubble radius constant at 0.02 s, 2338 N/m^2, and 100 μm, respectively. As the recover pressure is increased, the intensity and frequency of the bubble collapses increases. The recovery pressure should be strongly dependent on the pressure drop across an orifice, and thus be affected by changes in both the upstream pressure and the orifice diameter.

Finally, in Figure 3.8, the initial bubble radius was varied from 1 μm to 100 μm, while keeping the recovery time, recovery pressure, and initial pressure constant at 0.02 s, 3 bar, and 2338 N/m^2, respectively. It is clear from these simulations that a larger initial bubble radii would result in more frequent bubble collapses, and possibly more intense collapses. However, for the reasons explained earlier in this chapter, control over initial bubble size is not practical for most experiments.

To summarize the results shown in these figures, the following trends were observed: the lower the initial pressure, the quicker the recovery time, the higher the recovery pressure, and the larger the initial bubble radius; the more rapid and intense are the bubble collapses. Thus, the most intense cavitation collapses would occur (everything else being equal) with the largest pressure drop across the orifice. In addition, the quickest possible recovery time with the highest recovery pressure would be desired, which suggests that varying the upstream pressure for a fixed orifice diameter should alter the cavitation intensity. And although not controllable in practice, the largest initial bubble radius would be desired to ensure the most rapid, intense bubble collapses.

In the types of hydrodynamic cavitation devices available for this thesis, namely the HC–1, HC–2, and HC–3 described in later chapters, several factors are within

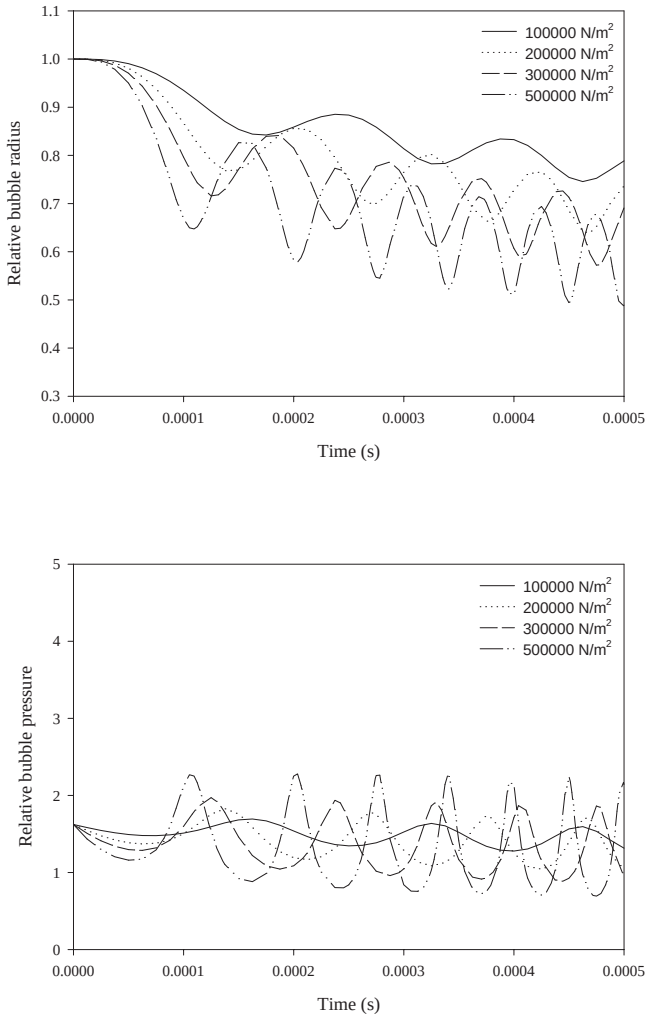

Figure 3.7: Bubble dynamics simulation on the effect of recovery pressure (τ=0.02 s, p_0=2338 N/m^2, R_0=100 μm).

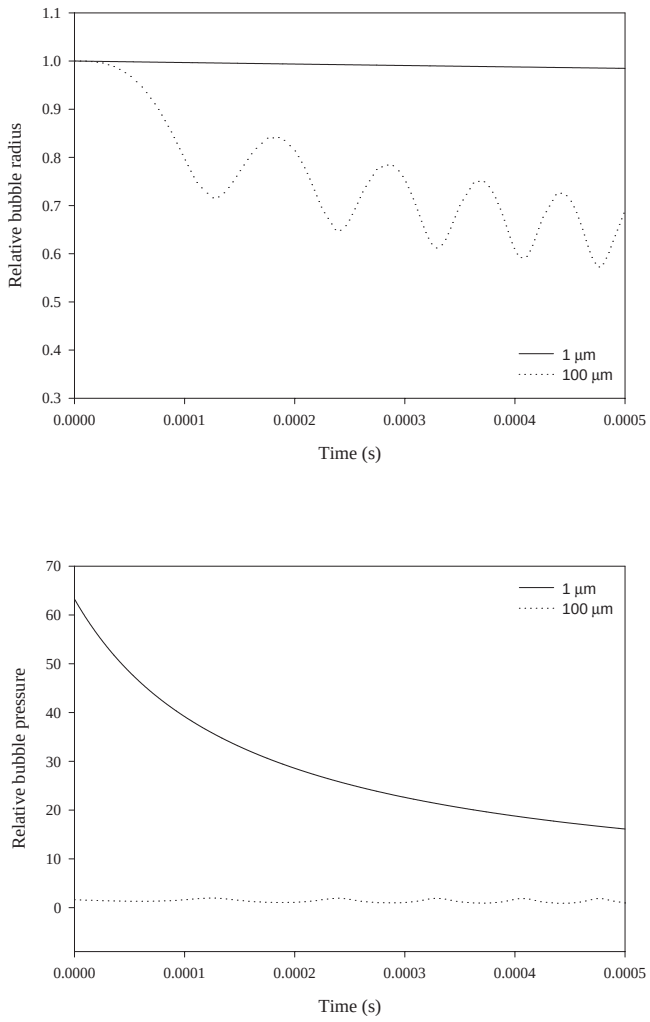

Figure 3.8: Bubble dynamics simulation on the effect of initial bubble radius (τ=0.02 s, p_0=2338 N/m^2, p_2=300000 N/m^2).

the control of an operator. The main ones are essentially orifice size and pressure. In the case of the HC–1 and HC–3, two orifices are typically used which can be varied in size, although the HC–3 can be modified to operate with a single orifice. In both of these devices, the feed pressure can also be modified somewhat independently of the choice of orifice. With the HC–2, the only machine variable is the size of a single orifice, as the device is equipped with a fixed speed pump.

From the observed trends, it would appear that using the smallest first orifice would be desired to increase the likelihood of more intense cavitation. By varying the upstream pressure on this small first orifice, the cavitation intensity and frequency could then be maximized. Where possible, a closely positioned, small-diameter second orifice, would be desired to increase the back pressure after the first orifice and attempt to increase the recovery time. Of course, some of these variables are interrelated. For example, the initial bubble size might be larger with a larger orifice size, although the pressure drop would then be less, and thus the initial pressure would not be as low. The recovery time is related to the initial pressure and the recovery pressure, as well as the distance between the orifice and the part of the device generating the recovery pressure (*e.g.* a second orifice). In the HC–1 and HC–3, this would reinforce the suggestion that varying the upstream pressure with the smallest first orifice, combined with the smallest second orifice as possible, would be desirable. Similarly, in the HC–2, this would also suggest using the smallest orifice possible.

In addition, any approach which would minimize the cavitation number, may increase the likelihood of intense cavitation, based on the information described

at the beginning of this chapter. Lowering the vapor pressure of the liquid would increase the likelihood of cavitation by decreasing the cavitation number. High velocities through an orifice would accomplish the same thing. This would also recommend the strategy of decreasing orifice diameter to try and increase cavitation intensity based on the simulation results.

3.3 Implications for effect on precipitation

The application of acoustic or hydrodynamic cavitation to a precipitation experiment may exhibit several results. The external effects of cavitation due to the expansion and rapid collapse of a cavitation bubble may result in particle size reduction or changes in nucleation rates. Precipitation in the presence of such an environment might also introduce strain into a material, even if size reduction or phase changes do not occur. The energy imparted to the solution might also cause local temperature fluctuations and micromixing, which could affect nucleation, phase changes, and enhance mass transfer.

3.3.1 External cavitation effects

Internal cavitation effects are expected to have a relatively minor influence on the precipitation of inorganic materials. The heat generated inside the bubble would not directly affect particles precipitating outside of the cavity. Precipitation would not normally be expected to occur in the vapor phase, and thus the particles formed in an experiment cannot be produced within a cavitation bubble, which by

definition contains only vapor and gas. Since the particles are formed *outside* of the bubbles, the intense pressures generated within would not have a direct influence on them. In addition, the radicals generated during the bubble collapses which are responsible for some sonochemistry, such as the Weissler reaction, are not likely to be present in sufficient quantities to influence precipitation kinetics.

Therefore, large effects, if any, produced by cavitation should come from the externally generated forces due to bubble collapse. The most obvious result should be physical damage to newly precipitated particles. As described earlier, cavitation is well known for its ability to induce severe erosion of virtually all types of materials. Thus, it is not unreasonable to suggest that in some precipitation systems the shockwaves and microjets produced by cavitation could fracture solids or affect the dispersion of separate phases on the surface of a solid.

A further effect of the shockwaves and microjets might be to affect the supersaturation, and thus the nucleation of a secondary phase. As Li and Inui point out, the mechanism for how acoustic cavitation affects some crystallization is poorly understood. However, they suggest that if there is local cooling during the expansion phase of a cavitation bubble, there might be a subsequent increase in the degree of supersaturation in the fluid [88]. This would naturally lead to the formation of nuclei which might then get dispersed after the bubble collapses. Thus, it is possible that local temperature fluctuations due to cavitation may have an effect on the precipitation of some materials.

Another possibility is that the waves and jets produced by cavitation might enhance mixing on a microscopic scale. For precipitating systems which are to

some extent mass transfer controlled, the potential increased micromixing would increase the rate of precipitation by influencing either the nucleation or subsequent crystal growth rate. Increased molecular mixing might also result in more homogeneous materials.

An additional benefit from cavitation would be the alteration of the droplet size in a microemulsion. Some researchers, such as Wakabayashi's group in Japan, have used water-in-oil (w/o) microemulsions combined with hydrazine reduction to form supported, nanostructured rhodium and palladium catalysts [91–94]. By changing the concentration of the metal salts inside of the microemulsion droplets, they were able to alter the crystallite sizes of the palladium and rhodium on the catalysts. By altering the metal grain sizes, they in turn were able to alter the catalyst activities for CO hydrogenation. Using the shockwaves generated by cavitation, it may be possible to alter the microemulsion droplet size and gain additional control over grain sizes. In the case of gold reduction, extending the analysis of metal cluster size in Chapter 2 (page 30) to the maximum gold grain size that could be formed in a microemulsion droplet, D_{droplet},

$$D = \left(2.1702 \times 10^{2}\right) \sqrt[3]{C_{\text{Au}}} \left(D_{\text{droplet}}\right) \tag{3.29}$$

shows that the gold cluster size should vary linearly with the droplet size. Initial experiments were performed to test this concept using hydrodynamic cavitation, but the devices used in this dissertation either could not function when the microemulsion was fed into them (HC–3) or generated so much mixing that the

microemulsion was destroyed (HC–2). Thus, this concept was not further investigated in this thesis.

Due to the complexity of cavitation, coupled with the additional chemistry associated with precipitation, the determination of any external cavitation effect must be investigated empirically. The trends elucidated from the mathematical modeling of bubble dynamics are clearly of assistance in determining the appropriate experiments to perform. Unfortunately, the current state of cavitation modeling does not allow *a priori* determination of the outcome of these experiments, especially in the case of hydrodynamic cavitation.

Among the factors which are not very controllable during precipitation experiments are the initial bubble radius formed during cavitation and the amount of dissolved, stabilized gas nuclei present in the system. As a result, for acoustic cavitation experiments at a fixed frequency, it would appear that the effect of cavitation can best be examined by varying the intensity/amplitude of an ultrasonic probe. Similar to the design constraints on ultrasonic probes, the variables under control in hydrodynamic cavitation devices are also rather limited. Given these design constraints, only the size of the orifice, and in some cases the system pressure, can be varied to examine the effects of hydrodynamic cavitation.

3.3.2 Power input from bubble collapse

Since external cavitation effects are expected to be the primary influence on precipitation, a general understanding of the magnitude of the power imparted to the bulk liquid by cavitation is desirable. This power may be transferred to the system

in the form of mechanical work (*i.e.* shockwave and microjet forces) as described above. The energy emitted might also result in temperature fluctuations which could affect nucleation and growth rates.

The energy emitted during the collapse of a cavitation bubble can be analyzed in terms of the adiabatic collapse of a gas-filled cavity [1]. At the moment of collapse, the bubble has an initial radius, $R_{\max}$, the hydrostatic pressure surrounding the bubble is P, the liquid layer surrounding the bubble has a thickness of δ, and the final radius after collapse will be R. Assuming that the bubble remains spherical, the work generated upon collapse will be given by Equation 3.30.

$$W = \frac{4}{3}\pi P(R_{\max}^3 - R^3) \tag{3.30}$$

In the limit of a total collapse, the final radius, R, will be zero, and thus the total work which will be transferred to the liquid surrounding the bubble will be determined by Equation 3.31.

$$W = \frac{4}{3}\pi P(R_{\max}^3) \tag{3.31}$$

To determine the power output, $\dot{W}$, from the bubble collapse, the work is merely divided by the time, t, it takes for the bubble to collapse, as shown in Equation 3.32.

$$\dot{W} = \frac{4}{3}\pi R_{\max}^3 \frac{P}{t} \tag{3.32}$$

The time for the complete collapse of the bubble was determined by Lord Rayleigh

to be:

$$t = 0.91 R_{\max} \sqrt{\frac{\rho}{P}} \tag{3.33}$$

where ρ is the density of the liquid around the bubble [1]. Substituting this time into Equation 3.32 yields Equation 3.34.

$$\dot{W} = 4.60 R_{\max}^2 \sqrt{\frac{P^3}{\rho}} \tag{3.34}$$

If it is assumed that the thickness of the liquid layer around the bubble is much smaller than $R_{\max}$, then the liquid mass which is affected by the energy generated in the collapse will be given by Equation 3.35.

$$m = 4\pi R_{\max}^2 \rho \delta \tag{3.35}$$

As a result, the energy dissipation per mass of liquid, ϵ, is equal to Equation 3.36.

$$\epsilon = \frac{\dot{W}}{m} = 0.366 \frac{1}{\delta} \left(\frac{P}{\rho} \right)^{\frac{3}{2}} \tag{3.36}$$

This final expression indicates that the amount of energy dissipated does not depend on the size of the bubble, but only on the hydrostatic pressure, liquid layer thickness, and the liquid density. Furthermore, if we assume that the liquid layer thickness around the bubble does not depend on the size of the bubble, Equation 3.36 will apply to all cavitation bubble collapses. Thus, by varying the hydrostatic pressure of the system, the energy produced by cavitation can be controlled.

3.3.3 Strain induced by flow and cavitation

In some materials, notably perovskites, it is possible to incorporate strain within their crystal structures during synthesis and subsequent processing. Thus it may be possible, for some material systems, to induce strain by synthesizing them in a hydrodynamic device, where two phenomena are occurring simultaneously: flow shear and cavitation. Through dimensional analysis, it is possible to come up with a set of dimensionless quantities which can mathematically describe the effects of flow and cavitation.

For flow through a pipe or orifice, the important variables are density, mean velocity, the cross-sectional area of the pipe or orifice, the viscosity of the fluid, and the pressure drop per unit length. In the case of cavitation, the pressure of the liquid, vapor pressure, velocity, and liquid density are the key parameters. To a lesser extent, viscosity and surface tension play a role in cavitation, but their effects can many times be ignored compared to the others as evidenced by their neglect in the Rayleigh-Plesset equation by many researchers, including Lord Rayleigh, in simulation and data fitting. Thus, to fully describe the effect of flow and cavitation on induced material strain, six variables at a minimum must be accounted for: liquid density, velocity, orifice diameter, liquid viscosity, a reference pressure (i.e. a pressure upstream or downstream of the orifice), and the vapor pressure of the liquid.

Using the well known Buckingham pi theorem, it is possible to perform a dimensional analysis by the method of repeating variables to determine the dimensionless pi terms which can be used to describe the relationship between strain and

these six variables. This method can be summarized in eight simple steps [95]:

1. List all the variables that are involved in the problem.
2. Express each of the variables in terms of basic dimensions.
3. Determine the required number of pi terms.
4. Select a number of repeating variables, where the number required is equal to the number of reference dimensions.
5. Form a pi term by multiplying one of the nonrepeating variables by the product of the repeating variables, each raised to an exponent that will make the combination dimensionless.
6. Repeat Step 5 for each of the remaining nonrepeating variables.
7. Check all the resulting pi terms to make sure they are dimensionless.
8. Express the final form as a relationship among the pi terms.

For this analysis, the basic dimensions were chosen to be force (F), length (L), and time (T). The analysis could also be determined on the basis of mass (M), instead of force, since $F = MLT^{-2}$.

There are seven variables in this problem, including strain (ϵ), which can be expressed in terms of basic dimensions as follows.

$$\epsilon = \frac{L}{L}$$

$$\begin{aligned}
\rho &= \frac{FT^2}{L^4} \\
u &= \frac{L}{T} \\
D &= L \\
\mu &= \frac{FT}{L^2} \\
p &= \frac{F}{L^2} \\
p_V &= \frac{F}{L^2}
\end{aligned}$$

As there are three reference dimensions, four $(7-3=4)$ dimensionless terms are required to describe this problem. To generate these terms, three repeating variables must be chosen which cannot themselves be combined to form a dimensionless term. For this analysis, orifice diameter (D), velocity (u), and density (ρ) were chosen as the repeating variables.

The first pi term was found to trivially be strain itself, since strain is dimensionless. The second pi term can be derived from viscosity to be the inverse of the Reynolds number as follows.

$$\begin{aligned}
\mu D^a u^b \rho^c &= \Pi_2 \\
(FTL^2)(L^a)(L^b T^{-b})(F^c T^{2c} L^{-4c}) &= F^0 L^0 T^0 \\
\Pi_2 &= \frac{\mu}{Du\rho} \qquad (3.37)
\end{aligned}$$

In a similar manner, the third and fourth pi terms become:

$$\Pi_3 = \frac{p}{u^2\rho} \tag{3.38}$$

$$\Pi_4 = \frac{p_V}{u^2\rho} \tag{3.39}$$

Thus, the relationship between strain induced in a crystal lattice, flow, and cavitation can be described mathematically as strain being a function of pi terms two through four. However, dimensional analysis does not provide the form of this function, so it has to be determined empirically.

Upon examining pi terms three and four, it is possible to simplify the function by subtracting pi term four from pi term three and then multiplying by two. This does not affect the dimensionlessness of these two pi terms, but does reduce them to the definition of the throat cavitation number (σ_T) described before.

$$\sigma_T = \frac{p - p_V}{\frac{1}{2}\rho u^2} \tag{3.40}$$

Thus, the strain will be a function of Reynolds number and throat cavitation number.

A general function that could be used to fit strain data would involve a power law expression. The simplest function which should describe the relationship between strain, Reynolds number, and the throat cavitation number would be

$$\epsilon = a\mathrm{Re}^b{\sigma_T}^c \tag{3.41}$$

where a, b, and c are determined empirically. However, this relationship would only be appropriate for materials which can incorporate strain in their crystal lattices in a similar manner and may not be appropriate for all materials.

Although not directly a part of this dissertation, collaborative work that was performed in the laboratory was able to confirm Equation 3.41 [96]. Lead zirconia titanate (PZT) with the structural formula $PbZr_{0.51}Ti_{0.49}O_3$ was synthesized in the HC–3 (described later in this dissertation) and titania was synthesized in the HC–2. The orifice diameter and feed pressure was varied over a wide range, which in turn resulted in varying values for the Reynolds number and throat cavitation number for each synthesis. After calcination, each material was analyzed via x-ray diffraction to determine the percentage of micro-strain present.

The strain data for the PZT were fitted to Equation 3.41 by a nonlinear least squares method as shown in Figure 3.9. The data correlated well, with an R^2 for the fit of 0.93. The slope of the function was 44.52, the Reynolds number exponent was -0.4250, and the cavitation number exponent was 0.1924. The data for titania were also fitted to the strain power law, as shown in Figure 3.10. The slope for titania micro-strain was 83.41, the Reynolds number exponent was -0.4829, and the cavitation number exponent was -0.0373, also with an R^2 of 0.93. The significance of these exponents is uncertain due to differences in the equipment and the materials synthesized.

Given the reasonably good fits, it would appear that for at least some systems, hydrodynamic cavitation is capable of inducing micro-strain. Furthermore, using the dimensionless analysis enables the fitting of data to a power law correlation

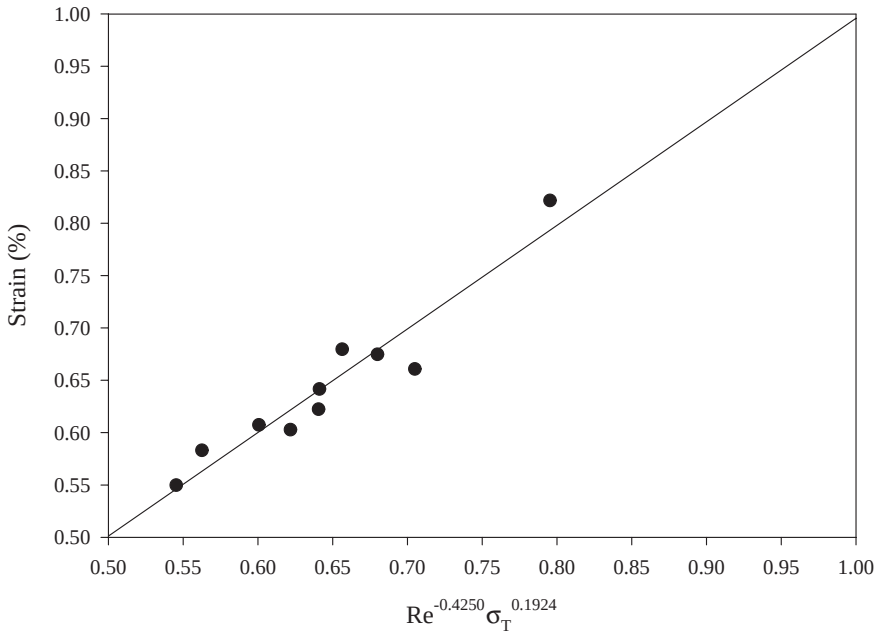

Figure 3.9: Power law correlation fitted to PZT synthesized in the HC–3 under various conditions.

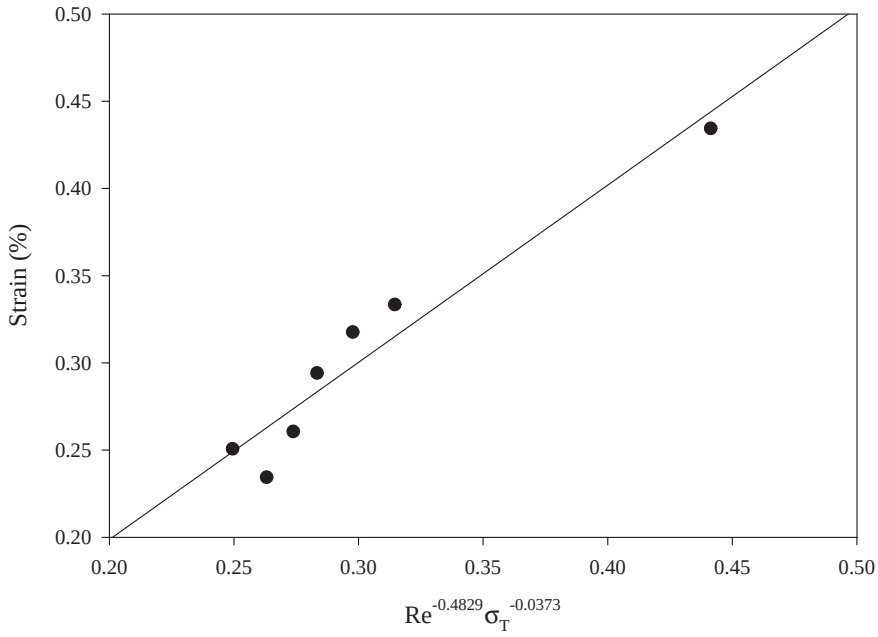

Figure 3.10: Power law correlation fitted to titania synthesized in the HC–2 under various conditions.

which could then enable the prediction of experimental conditions to maximize or minimize the amount of induced strain. This predictive ability would allow greater control over material properties which depend on the amount of micro-strain.

Chapter 4

Experimental

4.1 Introduction

The synthesis procedures for each apparatus and chapter in this dissertation are described below. Information on the methods used to characterize the materials synthesized in this research is also provided, including mathematical details on the x-ray line broadening and neutron activation techniques. Finally, an experimental description of the carbon monoxide oxidation reactor setup is provided, including details on the tests to ensure that transport limitations were absent during catalytic testing.

4.2 Synthesis procedures

4.2.1 Synthesis procedure for acoustic cavitation (Chapter 5)

Two different experimental setups were used in the synthesis of metal oxides: a flow reactor and a semi-batch reactor. The flow reactor setup is shown in Figure 4.1. For this setup, a process stream containing a metal salt or alkoxide solution was metered into the inlet of the reactor section using a peristaltic pump. This stream was mixed with a second process stream containing a precipitating agent, typically ammonium or sodium hydroxide. The result was the formation of a precipitated gel of the metal oxide components immediately before the inlet to the synthesis reactor.

The flow reactor consisted of a 20 kHz, 600-Watt Sonics & Materials Vibracell high intensity ultrasonic processor and a solid Teflon shell. The titanium alloy ultrasonic probe is screwed into the shell, which has an inlet port opening directly in front of the probe tip and an outlet port positioned above the level of the probe tip. The shell was designed such that the internal volume through which the precipitated gel must pass encounters the full intensity produced by the ultrasonic probe.

At the start of a typical experiment, the precipitating agent metering pump was turned on to fill the interaction zone of the reactor with precipitating agent. Once flow was established within the cell, the ultrasonic probe was activated. Unless otherwise noted, all experiments reported in this chapter were made with the probe amplitude set at 100%. After the probe was turned on, the salt solution feed pump was activated to begin the generation of a precipitated metal oxide

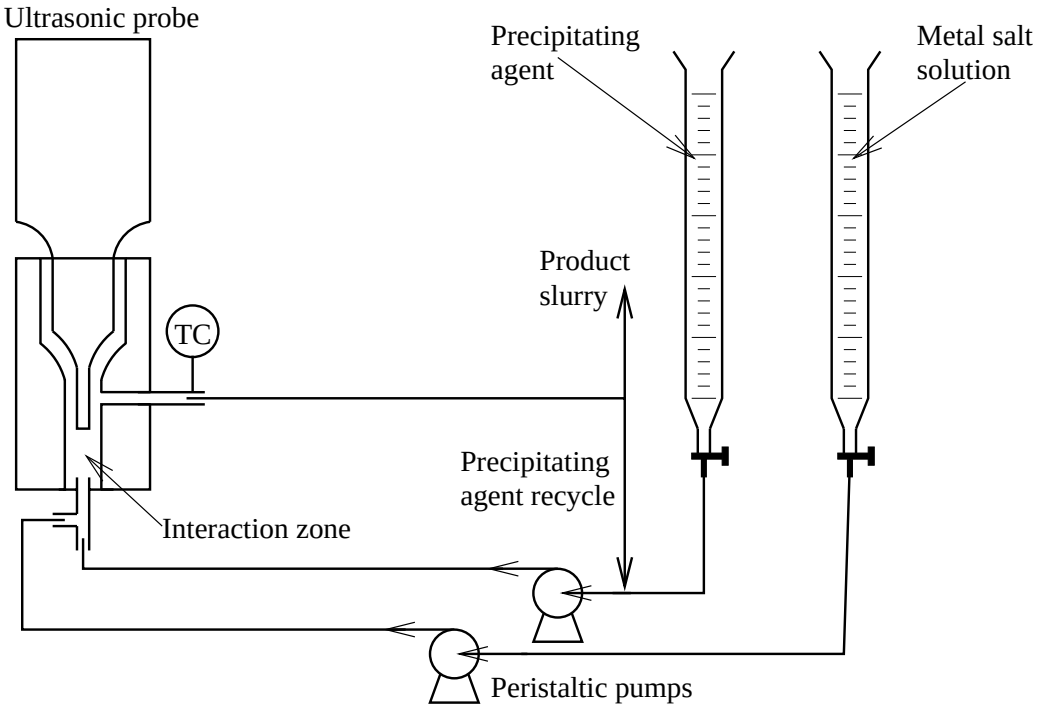

Figure 4.1: Schematic of ultrasonic continuous flow setup.

gel. Immediately upon formation, the gel encountered the ultrasonic field from the probe. The field induced acoustic, transient cavitation which could be audibly detected by the "frying bacon" sound which was produced [2]. After encountering the acoustic field, the gel solution flowed past the ultrasonic probe tip and exited the reactor where it was either collected directly, or, in the case of a recycle run, redirected back into the inlet of the reactor. During the recycle runs, the temperature of the recirculating material could be regulated by the use of an ice bath.

A schematic of the semi-batch reactor setup is shown in Figure 4.2. For this configuration, the precipitating agent was placed into a stainless steel reactor with a magnetic stir bar. The ultrasonic probe was then lowered into the precipitating agent to cause acoustic cavitation. The salt solution was then pumped into the reactor such that the flow was directed upwards toward the probe tip. The entire reactor was typically immersed in an ice bath to maintain a low temperature.

At the end of a synthesis, the product slurry was collected and then centrifuged three times, at 10 000 rpm, in a Beckman model J2-21 centrifuge equipped with a JA-10 rotor. After the first centrifugation, the supernatant solution was decanted from the concentrated slurry. For additional centrifugations, the supernatant was decanted and replaced with fresh, deionized water to wash the product. The washed solid was then dried overnight at 105 °C prior to x-ray diffraction (XRD) analysis. The dried material was then calcined to a higher temperature (*e.g.* 600 °C) to verify the identity of the product and to make a particle size estimate.

Experiments were conducted using the flow reactor where the addition of the salt solution to the precipitating agent was done over 30 minutes while the precipi-

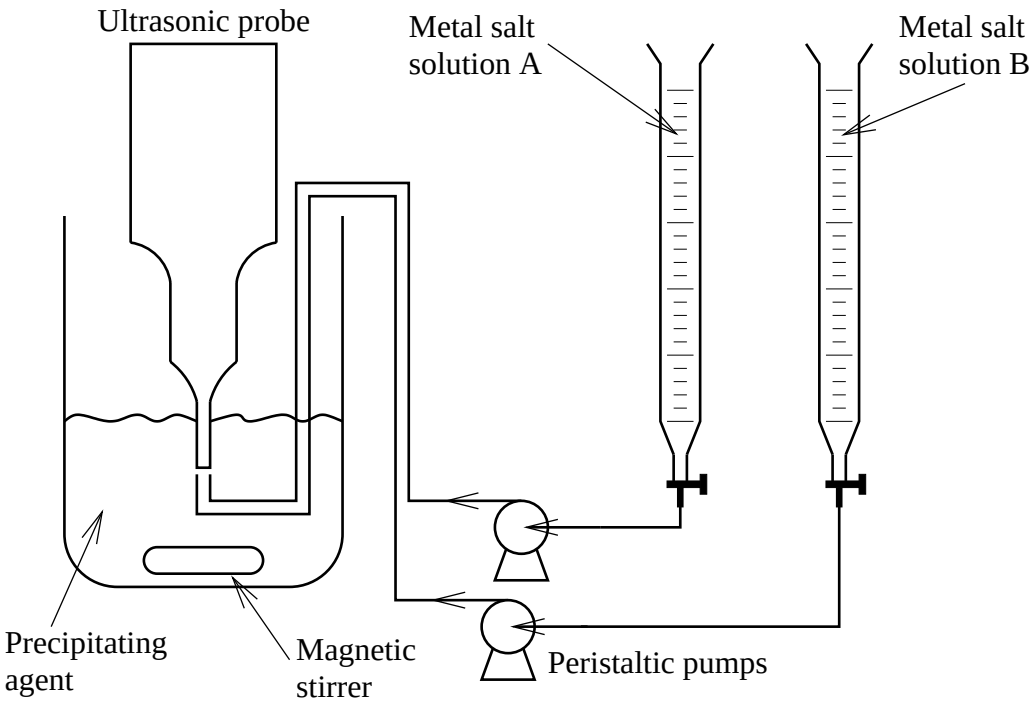

Figure 4.2: Schematic of semi-batch reactor setup.

tating agent and resultant gel were continuously recycled back into the ultrasound reactor. Other experiments precipitated the metal salt solution in one pass, *i.e.* without recycle, in the ultrasound reactor where the salt solution was added to the precipitating agent over a period of 30 minutes. Using this mode of operation, the effect of ultrasound treatment on the immediately formed gel was examined by passing the entire gel slurry back through the ultrasound reactor without recycle. This procedure was done several times, and the effect on the number of passes on grain size was studied by XRD analysis on the dried and calcined samples taken after each pass. Since some studies showed a grain size reduction as the number of passes were increased, most of the studies described here were carried out in the semi-batch reactor shown in Figure 4.2, where the total irradiation time was longer than that employed in the continuous flow reactors.

4.2.2 Gold concentration study synthesis procedures (Chapter 6)

Catalyst synthesis via acoustic cavitation

The experimental setup used for the synthesis of the catalysts was an ultrasonic flow reactor, the development of which was described in Chapter 5. The flow reactor setup is shown in Figure 4.1. For this setup, a process stream containing a 100 mL solution of chloroauric acid ($HAuCl_4 \cdot 3H_2O$), 0.88 mol/L titanium (IV) butoxide ($Ti[O(CH_2)_3CH_3]_4$), and isopropyl alcohol was metered into the inlet of the reactor section using a peristaltic pump. This stream was mixed with a second process stream (precipitating agent) containing a 1.43 mol/L aqueous ammonium

hydroxide solution and enough 25% cetyltrimethylammonium chloride (CTMA-Cl) to provide three moles of CTMA-Cl per mole of gold. The result was the formation of a precipitated gel of the metal oxide components immediately before the inlet to the synthesis reactor.

The flow reactor consisted of a 20 kHz, 600-Watt Sonics & Materials Vibracell high intensity ultrasonic processor and a stainless steel shell. Based on the initial screening studies (Chapter 5 & [26]), the clearance between the steel shell and the titanium probe was modified to be only 1/16" (1.59 mm) to reduce the volume of material being processed. The titanium alloy ultrasonic probe is placed into the shell, which has an inlet port opening directly in front of the probe tip and an outlet port positioned above the level of the probe tip. The shell was designed such that the internal volume through which the precipitated gel must pass encounters the full intensity produced by the ultrasonic probe.

At the end of a synthesis, the product slurry was collected and then centrifuged three times, at 10 000 rpm, in a Beckman model J2-21 centrifuge equipped with a JA-10 rotor. After the first centrifugation, the supernatant solution was decanted from the concentrated slurry. For additional centrifugations, the supernatant was decanted and replaced with fresh, deionized water to wash the product. The washed solid was then dried overnight at 105 °C prior to x-ray diffraction (XRD) analysis. For some of the lower concentration gold syntheses, centrifugation was not satisfactory in settling the slurries, so they were evaporated for a longer period of time in order to isolate the solid product.

The dried materials were calcined to 400 °C in air to verify the identity of the

product and to make a particle size estimate. All XRD patterns were collected on a Rigaku Geigerflex x-ray diffractometer using a Cu K_α ($\lambda = 1.5418$ Å) radiation source with a graphite secondary monochromator. Particle size measurements obtained from the XRD patterns were calculated using the Scherrer equation on the anatase(101) $K_{\alpha 1}$ and gold(200) $K_{\alpha 1}$ peaks, after correction for instrumental line-broadening.

Catalyst synthesis via hydrodynamic cavitation (HC–1)

Three catalyst samples were synthesized via hydrodynamic cavitation using a machine which will be designated HC–1 (see Figure 4.3). For these experiments, two orifices in series were used to produce cavitation; a 0.005 inch diameter orifice followed by a 0.007 inch diameter orifice. The process pressure before the first orifice was maintained at approximately 12,000 psig for all runs. The concentrations and amounts of solutions were identical to those used in the acoustic cavitation syntheses. The precipitating agent was recirculated through the HC–1 during the entire gold/titania solution addition (14.33 minutes) and then the product slurry was pumped out of the device for centrifugation and subsequent processing.

Catalyst synthesis via classical precipitation

For comparison with the ultrasound experiments, three catalyst samples were synthesized using conventional high-powered mechanical agitation. The concentrations and amounts of solutions were identical to those used in the acoustic cavitation syntheses. The flasks used for the precipitations contained all of the precipitating

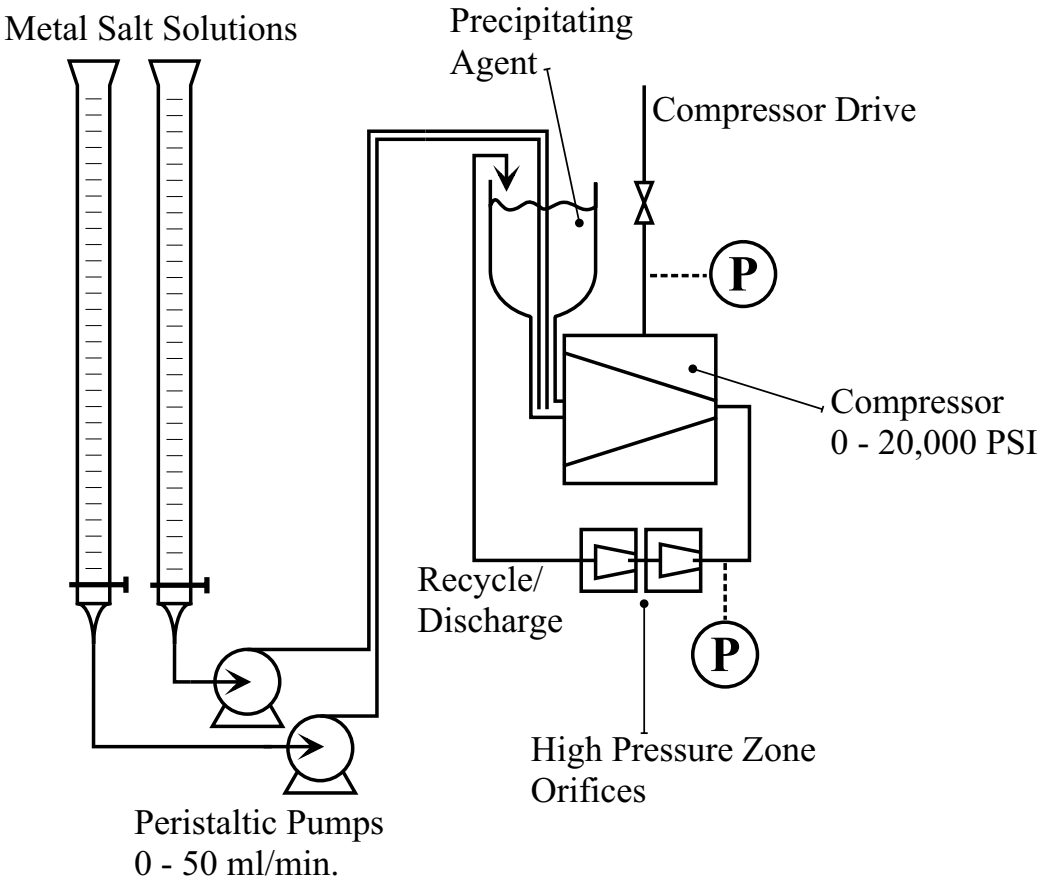

Figure 4.3: Schematic of HC–1 Hydrodynamic Cavitation setup.

agent solution for each experiment and the gold/titania solution was pumped in over 25 minutes followed by 5 minutes of additional mixing. Experiments performed in this manner are referred to as “classical” syntheses.

4.2.3 Synthesis procedure for HC–2 factorial studies (Chapter 7)

The experimental setup used for the synthesis of the catalysts was a hydrodynamic cavitation device consisting of a single orifice operating in a pressure range of 100–700 psig with an internal recirculation flow rate of several liters per minute. This device, which schematically is similar to the HC–1, shown previously in Figure 4.3, shall be designated HC–2. For this study, process streams containing solutions of chloroauric acid ($HAuCl_4 \cdot 3H_2O$), titanium (IV) butoxide ($Ti[O(CH_2)_3CH_3]_4$), isopropyl alcohol, and hydrazine were metered into the inlet of the device using a peristaltic pump.

At the start of a typical experiment, the HC–2 was turned on to begin recirculation of a precipitating agent. The precipitating agent consisted of either an aqueous ammonium hydroxide solution and enough 25% cetyltrimethylammonium chloride (CTMA-Cl) to provide three moles of CTMA-Cl per mole of gold; an aqueous solution of ammonium hydroxide, sodium hydroxide, potassium hydroxide, or ammonium carbonate; or deionized water. Once the precipitating agent was flowing through the system, one or more process streams were introduced into the HC–2, resulting in the immediate formation of a precipitated gel of the metal oxide com-

ponents. The gel solution flowed through the orifice section and was continuously recirculated throughout the addition of the process streams, followed by 5 additional minutes of recirculation. The temperature of the recirculating material was regulated by cooling the gel solution with an ice bath.

At the end of a synthesis, the product slurry was collected and then pressure filtered under 100 psig of nitrogen using 142 mm diameter, 0.2 μm nylon filter paper. After the initial pressure filtration, the filter cake was then washed twice by adding 150 mL of deionized water and pressure filtering the water through the cake at 100 psig. The washed solid was then dried overnight (at least 12 hours) at 105 $^{\circ}$C.

The dried materials were calcined to 400 $^{\circ}$C in air to verify the identity of the product and to make a particle size estimate. All XRD patterns were collected on a Rigaku Geigerflex x-ray diffractometer using a Cu K_{α} ($\lambda = 1.5418$ Å) radiation source with a graphite secondary monochromator. Particle size measurements obtained from the XRD patterns were calculated using the Scherrer equation on the anatase(101) $K_{\alpha 1}$ and gold(200) $K_{\alpha 1}$ peaks, after correction for instrumental line-broadening.

4.2.4 Synthesis procedure for the HC–3 (Chapters 7 & 8)

The experimental setup used for the synthesis of the catalysts was a hydrodynamic cavitation device consisting of two orifices operating in a pressure range of 10000–20000 psig with an internal recirculation flow rate varying from approximately 244 to 706 mL/min, depending on the pressure and orifices used. This device, which

schematically is similar to the HC–1, shown previously in Figure 4.3, shall be designated HC–3. For this study, process streams containing solutions of chloroauric acid ($HAuCl_4 \cdot 3H_2O$), titanium (IV) butoxide ($Ti[O(CH_2)_3CH_3]_4$), isopropyl alcohol, and hydrazine were metered into the device using a peristaltic pump.

The HC–3 could be modified to use only a single orifice. In this work, when two orifices are used in combination, the notation used will be x/y, where x is the first orifice diameter (expressed in thousandths of an inch) and y is the second orifice diameter. When the HC–3 was modified to use a single orifice, either only that orifice diameter is quoted, or 0 is used to designate the absence of the second orifice. For example, the notation 6/0 indicates a single 0.006 inch diameter orifice, whereas 6/14 denotes the use of a 0.006 inch orifice followed by a 0.014 inch orifice.

At the start of a typical experiment, the HC–3 was turned on to begin recirculation of the precipitating agent (water). Once the water (125 mL) was flowing through the system, 100 mL of titanium butoxide solution (0.88 mol/L Ti) was added to immediately form a precipitated titanium hydroxide gel. The gel solution flowed through the orifice section and was continuously recirculated throughout the experiment. After the titanium butoxide was precipitated, 30 mL of a 1 mol/L sodium hydroxide solution was added over 5 minutes to adjust the pH from 5 to approximately 10. Then a 100 mL solution of hydrazine in water (typical pH$\approx$8–9) was added such that the molar ratio of hydrazine to total gold was approximately 1.55/1. After the hydrazine and caustic additions, 500 mL of gold solution (1.4509×10^{-3} mol/L Au), consisting of chloroauric acid dissolved in water, was added at 4 mL/min to precipitate the gold and form the final catalyst. The total

gold processing time was thus 125 minutes. The temperature of the recirculating material was regulated at approximately 32 ± 2 °C by cooling the gel solution with an in-line, water cooled heat exchanger.

At the end of a synthesis, the product slurry was collected and then pressure filtered under 100 psig of nitrogen using 142 mm diameter, 0.2 μm nylon filter paper. After the initial pressure filtration, the filter cake was then washed twice by adding 100 mL of deionized water and pressure filtering the water through the cake at 100 psig. The washed solid was then *immediately* placed in an oven and dried overnight (at least 12 hours) at 105 °C.

The dried materials were calcined to 400 °C in air to verify the identity of the product and to make a particle size estimate. All XRD patterns were collected on a Rigaku Geigerflex x-ray diffractometer using a Cu K_α ($\lambda = 1.5418$ Å) radiation source with a graphite secondary monochromator. Particle size measurements obtained from the XRD patterns were calculated using the Scherrer equation on either the gold(200) $K_{\alpha 1}$ or gold(311) $K_{\alpha 1}$ peaks, after correction for instrumental line-broadening.

4.3 Characterization

4.3.1 X-ray Line Broadening Analysis

X-ray diffraction (XRD) patterns were collected on a Rigaku Geigerflex x-ray diffractometer using a Cu K_α ($\lambda = 1.5418$ Å) radiation source with a graphite secondary monochromator. Gold crystallite size measurements obtained from the

XRD patterns were calculated using the Scherrer equation after correction for instrumental line-broadening [53, 97–99].

Line broadening assumptions

The major assumption in this approach to x-ray line broadening is that there is no line broadening due to lattice strain in the material. That is, all of the broadening in the x-ray pattern is due to crystallite size effects and machine broadening. In addition, it is assumed that the two major wavelengths, $K_{\alpha 1}$ and $K_{\alpha 2}$, give rise to identical peak profiles, so that the same peak function can be fitted for each wavelength. It is also assumed that the height of the $K_{\alpha 2}$ peak is exactly half the height of the $K_{\alpha 1}$, which is true theoretically.

Furthermore, to constrain the number of variables present in the curve fitting, the relationship between the full widths at half of maximum (FWHM) for both the $K_{\alpha 1}$ and $K_{\alpha 2}$ is approximated by the ratio of the Scherrer equation for both wavelengths. To simplify the relationship, and thus avoid having to do multiple refinement fitting, it is assumed that machine broadening is negligible compared to crystallite size broadening. This has been verified experimentally and therefore does not influence the analysis presented here. The final assumption in this analysis is that the background can be approximated as being linear, which should be true over short ranges of the Bragg angle.

Peak fitting algorithm

The peak of interest is fitted with a function which consists of a linear function plus two Pearson VII peaks for each of the two wavelengths produced by the radiation source ($K_{\alpha 1}$ & $K_{\alpha 2}$). Empirically, it was determined that this approach was better able to fit XRD patterns where the $K_{\alpha 1}$ and $K_{\alpha 2}$ peaks were partially resolved, than using a combination of Gaussian and Lorentzian (a Pseudo-Voigt) peaks for each wavelength. The mathematical representation of this function is given by Equation 4.1,

$$\begin{aligned} f(x) = u_0 \quad + \quad u_1 x + \frac{u_2}{\left[1 + \left(\frac{2(x-u_3)\sqrt{2^{1/u_4}-1}}{u_5}\right)^2\right]^{u_4}} \\ + \quad \frac{\frac{1}{2}u_2}{\left[1 + \left(\frac{2\left(x - 2\arcsin\left(\frac{\lambda_{K\alpha 2}}{\lambda_{K\alpha 1}}\sin\frac{u_3}{2}\right)\right)\sqrt{2^{1/u_4}-1}}{\left(\frac{\lambda_{K\alpha 2}}{\lambda_{K\alpha 1}} u_5 \frac{\cos\left(\arcsin\left(\frac{\lambda_{K\alpha 2}}{\lambda_{K\alpha 1}}\sin\frac{u_3}{2}\right)\right)}{\cos\frac{u_3}{2}}\right)}\right)^2\right]^{u_4}} \end{aligned} \tag{4.1}$$

where u_0 is the intercept of the linear background function; u_1 is the slope of the background; u_2 is the intensity or peak height of the $K_{\alpha 1}$ peak; u_3 is the diffraction angle, 2θ; u_4 is the Pearson VII width, assumed to be the same for both peaks; and u_5 is the FWHM of the $K_{\alpha 1}$ peak. The curve-fitting is performed using a nonlinear Marquardt-Levenberg algorithm implemented in the Sigmaplot technical graphing program [100].

Grain size determination

Given the assumptions mentioned above, the crystallite size can be approximated by the Scherrer equation, shown in Equation 4.2,

$$D(\text{Å}) = \frac{0.9\lambda}{\beta \cos\theta} \frac{360}{2\pi} \tag{4.2}$$

where D is the grain size, λ is the radiation wavelength, β is the true FWHM of the x-ray peak due to crystallite size effects, and θ is the Bragg angle. To use the Scherrer equation correctly, the broadening caused by the diffractometer equipment ("machine broadening") must be removed in order to obtain the true FWHM, β. A simplified approach uses the Warren approximation, shown in Equation 4.3,

$$\beta^2 = b^2 - b_0^2 \tag{4.3}$$

where b is the observed peak breadth and b_0 is the contribution to the observed width due to machine broadening. The Warren approach inherently assumes that the peak shapes are Gaussian, but this introduces a slight error in the analysis, since for nanostructured materials the grain size broadening is much larger than the machine broadening [53].

In order to use the Warren approximation, the machine broadening must be known as a function of the diffraction angle so that it can be calculated for the exact position of the XRD peak being analyzed. An α-Al_2O_3 sample included in the National Institute of Standards & Technology (NIST) Standard Reference

Material set 674a (X-ray Powder Diffraction Intensity Set), was used to determine this function. The NIST alumina has a particle size distribution such that 90% of the particles are less than 1.5 μm and 50% are less than 0.6 μm in size. Since the sample is in the micron size range, the peak width is assumed to be due only to machine broadening. The NIST alumina pattern was recorded and each peak analyzed using Equation 4.1. A second order polynomial was fitted to the $K_{\alpha 1}$ FWHM of each peak, given in Equation 4.4, which is used for computing the machine broadening contribution for all samples.

$$b_0 = 0.20185 - 2.03385 \times 10^{-3}(2\theta) + 1.98731 \times 10^{-5}(2\theta)^2 \tag{4.4}$$

The procedure for x-ray analysis of a sample involves fitting Equation 4.1 to the sample peak of interest to obtain the FWHM of the $K_{\alpha 1}$ peak and its position. Then the machine broadening is calculated from Equation 4.4. Substitution of the Warren approximation into the Scherrer equation, plus entering the value for copper $K_{\alpha 1}$ (1.540562 Å) and converting from Ångstroms to nanometers, results in Equation 4.5.

$$D(\text{nm}) = \frac{7.9441}{\sqrt{b^2 - b_0^2}\cos\theta} \tag{4.5}$$

Entering the FWHM, peak position, and machine broadening FWHM into this equation results in the direct calculation of the mean crystallite size.

An x-ray diffraction pattern was obtained from a commercial sample of Degussa P-25 fumed titania, lot number 1523, at a diffraction angle range of 5–90° at 0.1° per step with a 4 second per step count time. The analysis sheet for this sample

indicated that the typical average primary particle size determined by TEM for this grade of titania was 21 nm. The anatase (101) peak was analyzed using the line-broadening procedure described above, yielding a mean anatase crystallite size of 22.6 nm, confirming the relative accuracy of this technique for particle size determination.

4.3.2 Gold concentration analysis by neutron activation

Most samples used in this study were analyzed for gold content via neutron activation in WPI's nuclear reactor facility. For each analysis, approximately 300 mg of solid material was exposed for 3 minutes to the reactor core operating at 5 kW. A waiting time of 15 minutes existed between irradiation and gamma-ray detection to allow peaks from the support material to decay away so that there would be no interference with the metal spectra.

The irradiated samples were placed in a gamma-ray detector for a count time of 12 minutes. The peak areas obtained were normalized for sample weight and detector "live time." The peak areas were then compared to a calibration curve generated from aqueous standards of the metal salts to determine the final metal concentration of each sample. A more thorough description of the mathematical details of the analysis is given below.

NAA mathematical details

Equation 4.6 describes the gamma-ray counts emitted from a neutron activated sample [101].

$$C = \eta \frac{m\%N_A\sigma_a\phi f}{1.128A\lambda}\left[1-e^{-\lambda t_i}\right]e^{-\lambda t_w}\left[1-e^{-\lambda t_c}\right] \tag{4.6}$$

The various constants in front of the three exponential terms characterize details of the sample and the experimental setup, such as the type of element being analyzed and the efficiency of the gamma-ray detector. However, if a sample being analyzed by NAA is being compared directly to a standard using the same experimental setup, then the ratio of the counts of the sample to the counts of the standard obviates the need to determine these parameters. Thus, the ratio of the sample counts to the standard counts can be calculated via Equation 4.7,

$$\frac{C_1}{C_2} = \frac{\left[1-e^{-\lambda t_i}\right]e^{-\lambda t_w}\left[1-e^{-\lambda t_c}\right]}{\left[1-e^{-\lambda t_i}\right]e^{-\lambda t_w}\left[1-e^{-\lambda t_c}\right]} \tag{4.7}$$

where λ is the decay constant for the radioisotope produced, t_i is the irradiation time in the nuclear reactor, t_w is the wait time between irradiation in the reactor and detection in the gamma-ray detector, and t_c is the counting time in the gamma-ray detector. If these three experimental times are the same for both the sample and the reference standard, then the counts of the two samples are directly related to one another.

The counts for a sample can be replaced by the peak area obtained from a

gaussian fit to the peak of interest. The peak area, A_t, corrected for the portion of the signal not measured by the gamma-ray detector, or "live time," t_L, is given by multiplying the peak area, A_p, by the ratio of the live time to the total count time, as shown in Equation 4.8.

$$A_t = A_p \frac{t_L}{t_c} \tag{4.8}$$

This area must then be adjusted to the reference sample weight for a calibration curve to yield the weight adjusted area, A_w. This is obtained by ratioing the reference sample weight, w_r, to the actual sample weight, w_s, as shown in Equation 4.9.

$$\begin{aligned} A_w &= A_t \frac{w_r}{w_s} \\ &= A_p \frac{t_L}{t_c} \frac{w_r}{w_s} \end{aligned} \tag{4.9}$$

Thus, assuming that the irradiation, wait, and count times are the same for the sample as for the reference standard, Equation 4.9 is all that is required to determine the composition of the sample. A calibration curve is generated to give peak area as a function of concentration of the element of interest. The sample is then analyzed to give a peak area which is corrected for the differences in sample weight and live time between the sample and the calibration curve. Using this corrected peak area, the concentration of the element is then determined from the calibration curve.

NAA example calculation

For example, a 0.2328 g sample of titania supported gold was analyzed using the conditions mentioned above. The live time during the 720-second gamma-ray counting was 685.30 seconds. The area of the Au–198 peak at 411.8 keV [102], A_p, was found to be 130081. The calibration curve generated for gold, assuming a sample weight of 0.757 g, is given by Equation 4.10.

$$\text{Au(wt\%)} = -3.985 \times 10^{-3} + 4.450 \times 10^{-6}(A_w) + 4.693 \times 10^{-12}(A_w)^2 \quad (4.10)$$

Using Equation 4.9, the area is normalized to a live time of 720 seconds and a sample weight of 0.757 g, yielding a value of 402601.15 (see Equation 4.11).

$$\begin{aligned} A_w &= A_p \frac{t_L}{t_c} \frac{w_r}{w_s} \\ &= (130081) \frac{685.30}{720} \frac{0.757}{0.2328} \\ &= 402601.15 \end{aligned} \quad (4.11)$$

Using the gold calibration curve, this means that the sample contains 2.548% gold.

4.3.3 Gold concentration analysis by inductively coupled plasma emission spectroscopy (ICP)

Due to the high gold concentrations of the samples shown in Chapter 8, which can affect the accuracy, as well as the radioactivity, of the gold analysis by neutron

activation; and the unavailability of the WPI nuclear reactor facility during the time of interest, all samples analyzed in Chapter 8 were examined for gold content via inductively coupled plasma emission spectroscopy (ICP). The ICP analysis was performed by an outside laboratory (Galbraith Laboratories, Inc. of Knoxville, TN), and the general procedure described here is from their method summary.

Each sample was decomposed/digested in preparation for analysis. The decomposition procedure was as follows [103].

> The sample is charred using H_2SO_4. If analyzing for metals that form insoluble sulfates, $HClO_4$ and HNO_3 are used to char the organic material. After charring the sample, HNO_3 is added and the sample is refluxed to solubilize the metals present. If the solution becomes cloudy, HCl is added to affect complete digestion. HF can be used if silicon is present in the sample but is not an analyte of interest. All HF use is restricted to Teflon vessels. The clear digestate is quantitatively transferred to a Class A volumetric flask and brought to final volume. The sample is now ready for analysis.

After each sample was digested and decomposed, either a Perkin-Elmer P 2000 or Optima 3000 ICP instrument was used to determine the gold content by examining the 242.8 nm primary wavelength of gold.

4.3.4 Transmission electron microscopy (TEM) & X-ray photoelectron spectroscopy (XPS) analysis

Transmission electron microscopy (TEM) analysis was performed at the Massachusetts Institute of Technology's (MIT) Center for Materials Science Shared Experimental Facilities by Mike Frongillo. A JEOL JEM–2010 electron microscope was used for the measurements at an acceleration potential of 200 kV. Samples were thoroughly ground and then dispersed in isopropyl alcohol prior to deposition on a copper/graphite sample grid.

X-ray photoelectron spectroscopy (XPS) (also known as elemental spectroscopy for chemical analysis (ESCA)) was performed by Ute Wild of the Department of Inorganic Chemistry at the Fritz-Haber-Institut der Max-Planck-Gesellschaft in Berlin. The XPS analysis was done with a custom apparatus using a Mg K_α source.

4.4 Catalytic activity measurements

Catalytic activity measurements were made in a fixed bed recycle reactor with a Senior Flexonics MB–21 metal bellows recirculation pump (see Appendices A & B for mathematical details). In a typical experiment, 200 mg of catalyst sieved to 80–120 mesh was mixed with 4 g of 28–48 mesh, low surface area α-Al_2O_3 from Strem Chemicals (0.04 m^2/g) and loaded into the stainless steel reactor. For each experiment, the reactor was heated to 400 °C in air for one hour to "activate" the catalyst. After this pretreatment, a 3.51% carbon monoxide in air

gas mixture was passed through the reactor at 0.020 g/s (78.6 cm^3(STP)/min), and the temperature was reduced to measure the CO activity and determine the activation energy. The conversion of carbon monoxide was measured by sampling the reactor effluent with a gas chromatograph (GC). The GC was equipped with a 6 foot (1.83 m) stainless steel column packed with a 13X molecular sieve and a thermal conductivity detector.

The reaction rate per gram of catalyst was determined for each catalyst from the CO conversion by the following equation,

$$-r_A = \frac{F_{A_0}}{W} X \tag{4.12}$$

where $-r_A$ is the reaction rate, F_{A_0} is the molar flow rate of CO, W is the catalyst weight, and X is the fractional conversion of CO. In the absence of gold surface areas or dispersions, the turnover rate for each catalyst was approximated by an atomic rate, obtained by normalizing the specific reaction rate by the total moles of gold present in each catalyst. As a result, these atomic rates are equivalent to assuming 100% dispersion and are thus minimum CO turnover rates.

A recycle reactor was chosen for activity measurements because CO oxidation is known to be a severely transport controlled reaction [104], and a recycle reactor minimizes external transport limitations. A series of experiments were performed where the recirculation flow rate was varied from the typical flow rate of 1.8 L/min to 0.06 L/min for a 80–120 mesh catalyst. A typical result for a 1.028% gold on titania catalyst at 150 °C is plotted in Figure 4.4 as the atomic rate versus the bed

linear velocity. These data demonstrate that even at low recycle ratios, external transport limitations have been eliminated. For all activity results reported here, the recirculation rate was maintained at the maximum setting for the pump, which was approximately 1.8 L/min, yielding a recycle ratio of 23/1.

To ensure that the rates reported here represent the true kinetic data, an empirical approach was taken to eliminate the possibility of internal transport limitations affecting the data. In the absence of transport limitations and temperature effects, the rate of reaction should not show a dependence on catalyst particle size. Thus, a series of experiments were performed where catalysts were sieved to four different mean particle diameters: 0.420 mm (30–60 mesh), 0.214 mm (60–80 mesh), 0.151 mm (80–120 mesh), and 0.115 mm (120–140 mesh). Figure 4.5 shows a plot of the atomic rate versus the inverse mean particle diameter for a 1.028% gold on titania catalyst at 150 °C and 200 °C. It is clear from this figure that the 30–60 mesh catalyst has a large enough diameter that there are internal transport limitations, but that much smaller particle diameters show no transport dependencies (*i.e.* 80–120 mesh & 120–140 mesh). Thus, for all data reported here, the catalysts were sieved to 80–120 mesh.

Although reducing the particle size of the catalysts reduces the chances of encountering internal transport limitations by reducing the mean diffusion path, there might still be a temperature effect which will mask the kinetic rate. As the temperature increases, the rate of reaction will increase and may become faster than the diffusion rate, so that mass transfer becomes the rate limiting step. All rates in this study are reported at an arbitrary temperature of 150 °C to minimize the

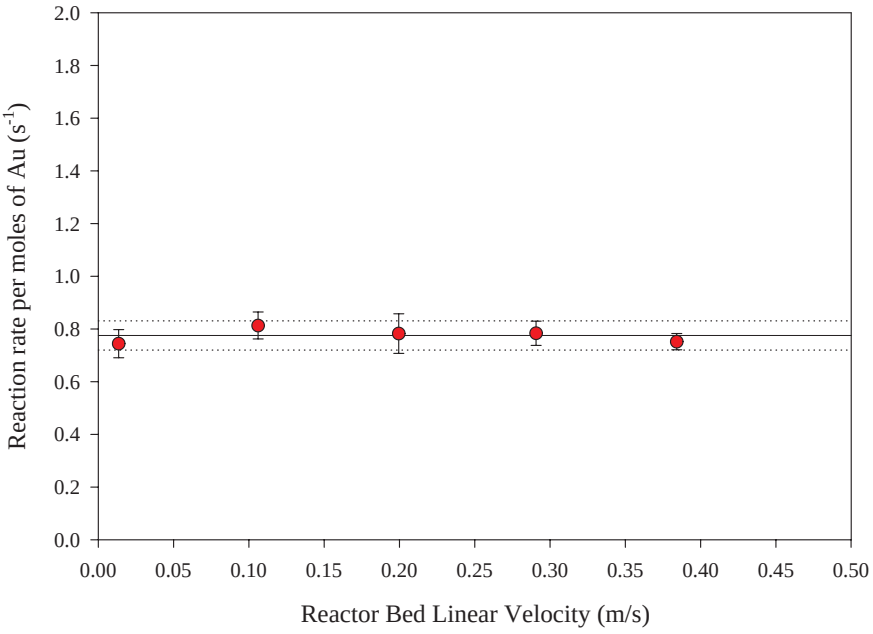

Figure 4.4: Recirculation flow rate test at 150 °C for external transport limitations with a 1.028% gold on titania catalyst. The lack of variation in the atomic oxidation rate with recirculation flow rate indicates an absence of external transport limitations.

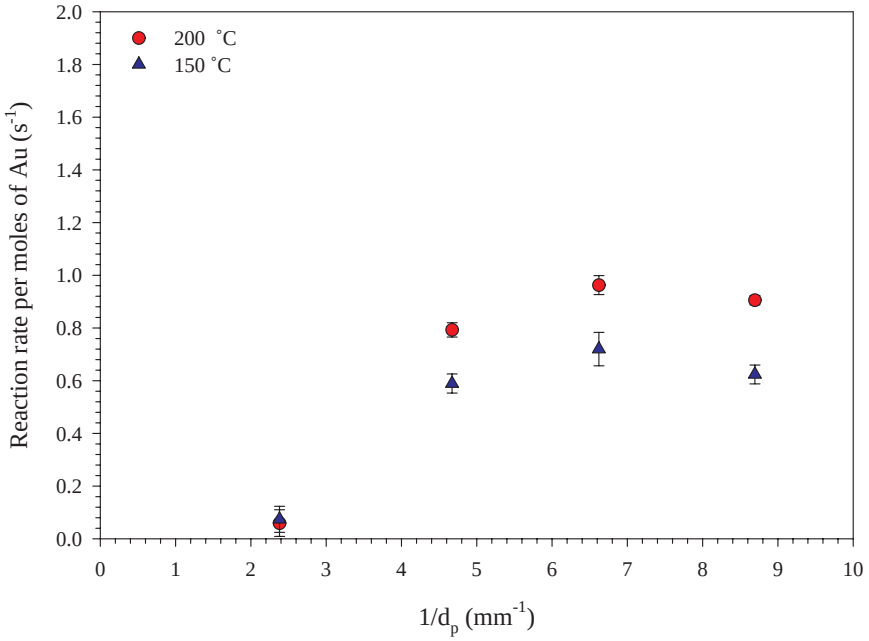

Figure 4.5: Particle size test for internal transport limitation. A 1.028% gold catalyst was sieved to mean particle sizes of 0.115, 0.151, 0.214, and 0.420 mm and each sieved sample was tested for CO oxidation. At the largest mean particle size, there is significantly less activity compared to the other sizes, indicated an internal transport limitation. Thus, the average sieved size used for subsequent catalytic runs was 0.151 mm to minimize the transport problems.

error in the GC measurements due to small conversions, but for some experiments the true rate could not be obtained at this temperature. Figure 4.6 shows a typical Arrhenius plot for a 2.150% gold on titania catalyst used to obtain both the rate and activation energy.

As the figure shows, above 120 °C, the activation energy was approximately 5 kJ/mol, which compared to the activation energy of 24 kJ/mol for lower temperatures, clearly indicated that there was a diffusion limitation. The activation energies reported here were obtained over a temperature range of approximately (90–200) °C but in cases like the one just shown, which were typically the higher metal loaded catalysts, the values reported were from the lower temperature data (*e.g.* from 120 °C and lower). Also, for catalysts where a diffusion limitation existed at 150 °C, the rate was extrapolated from the lower temperature data.

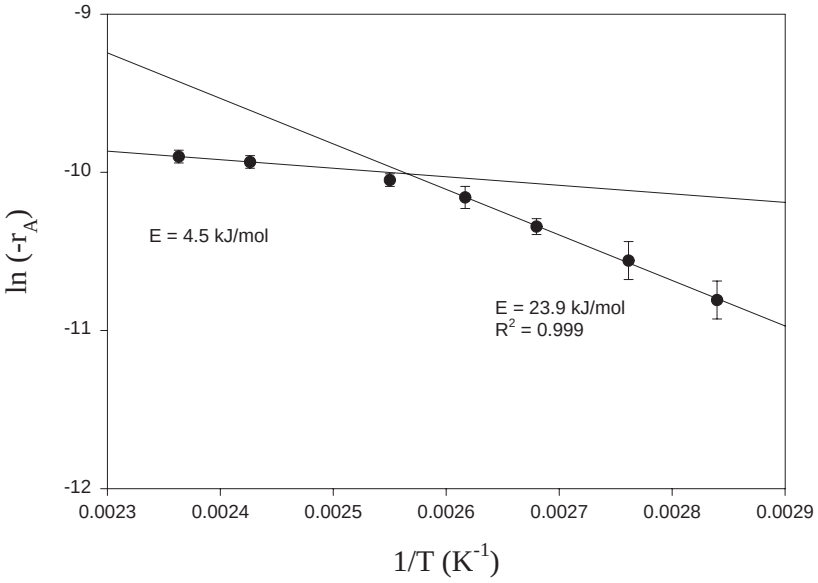

Figure 4.6: Typical titania supported gold Arrhenius plot.

Chapter 5

The Ultrasonic Synthesis of Nanostructured Metal Oxide Catalysts

5.1 Introduction

Several research groups over the last few years have reported both beneficial effects in catalyst performance and novel effects in materials synthesis by the application of high powered ultrasound [20, 105–107]. Other recent studies demonstrated that the rates of certain catalytic reactions were accelerated by factors of 10–100 when the grain sizes of the catalysts were systematically reduced into the 2–10 nm range [8, 10, 28, 108]. The focus of this part of the research was to examine a wide range of metal oxide and supported metal catalysts to determine whether ultrasonic

treatment affords any advantages for the preparation of nanostructured materials as compared to their identical synthesis by classical precipitation technology.

The investigation concentrated on a determination of ultrasound effects during synthesis on reducing and controlling grain sizes, improving phase purities of complex metal oxides, improving the degree of alloy formation for supported bimetallic catalysts, and the capability to systematically vary and control grain sizes of the metallic particles. The strategy used during synthesis was to precipitate all components of the catalyst's composition, including support materials, within the zone of highest intensity of the ultrasound horn. The expectation based on the well known dynamics of acoustic cavitation generated by ultrasound energy was that both high shear and high local temperatures would result [1–4]. The effect of high shear on the incipient formed gel would be to efficiently mix all metal components so that the final catalyst would demonstrate a high phase purity, and the shear forces would also result in the formation of nanostructured materials. The effect of the high local temperatures would result in an *in situ* calcination of the metal oxide grains preventing their further grain growth.

A variety of material property modifications have been attributed to the use of ultrasound during synthesis. Suslick and co-workers examined a wide range of alloy and nanostructured metal particle syntheses by irradiating solutions of the corresponding metal carbonyls with ultrasound [21]. Nanostructured iron-cobalt alloys prepared in this way resulted in greatly improved activity and selectivity in cyclohexane dehydrogenation to benzene [21]. Materials produced in the presence of ultrasound have exhibited higher surface areas compared to materi-

als synthesized in a conventional manner [105, 109]. Crystallization and gelation rates for zeolites and gels have been dramatically increased by ultrasound treatment [109, 110]. In addition, exposure to ultrasound can modify catalyst surfaces, removing undesirable impurities and increasing the dispersion of precious metals on a support [107, 111]. Recent findings by Dhas *et al.* showed that ultrasound treatment of aqueous ammonium dichromate solutions resulted in an *in situ* reduction forming Cr_2O_3 as amorphous fine grains [112].

These modifications to conventional catalyst preparations normally result in increased catalytic activity. Bosch *et al.* noted that silica supported platinum catalysts which were treated with ultrasound during synthesis and reduced at 673 K exhibited three times the activity for the hydrogenation of phenylacetylene than classically prepared materials [106]. Bernal *et al.* prepared a series of TiO_2-SiO_2 gels as supports for rhodium catalyzed n-butane hydrogenolysis [109]. The activities of the catalysts where the support was synthesized with ultrasound, were higher than those of the conventional supported materials, most likely due to increased dispersion of the rhodium. Bianchi noted similar results for the reduction of acetophenone with palladium supported catalysts [107].

The use of ultrasound during metal oxide precipitation to produce advanced catalysts and materials has been investigated before in several laboratories [105, 107, 109, 113]. The ability of acoustic cavitation to synthesize materials of varying small grain sizes with high phase purity was of particular interest for this part of the research; however, it was important to demonstrate that catalysts prepared by ultrasound possessed properties that could not be achieved by classical methods

of synthesis. For this reason, the sonication syntheses reported here were directly compared to classical syntheses under identical synthesis conditions within the same equipment but with the ultrasound power turned off.

Based on the effects of acoustic cavitation, it was expected that the precipitation of catalysts within an ultrasound interaction zone should result in high phase purity, nanometer-size particles which can be adjusted over a wide range of grain sizes from 1–50 nm. From frontier electron theory concepts [5], it is expected that every catalytic reaction would have a unique grain size within the 1–50 nm region where maximum rates are observed. Several catalytic systems synthesized in the 2–8 nm range have demonstrated sharply enhanced rates within this range as compared to conventionally prepared materials [10,28]. Enhanced rates within this range could also be due to a much higher edge to stable basal plane ratio of any crystallite as the grain size is reduced, leading to more reactive sites of low coordination [6].

5.2 Results

5.2.1 Synthesis of ceria

The synthesis of ceria was studied for both its usefulness as a catalytic support (*e.g.* three-way automotive catalysts) [114, 115] and the fact that it forms grain sizes which are easily discernible by XRD upon drying. The majority of the materials synthesized in this investigation exhibited very broad x-ray diffraction patterns after drying at 105 °C. This makes the determination of any grain size reduction via ultrasound unreliable. As a result, the materials were calcined to

progressively higher temperatures which resulted in coarsening and grain growth to a size which permitted grain size determination by XRD.

Typical XRD patterns for ceria synthesized in the presence of ultrasound and subsequently calcined to higher temperatures are shown in Figure 5.1. The initial grain size after drying was approximately 7 nm and increased to 13 nm upon calcination to 600 °C. This result demonstrates that control over grain size can also be maintained in materials produced via acoustic cavitation by choosing the appropriate calcination temperature.

In addition to temperature control, the concentration of the metal salt in solution was also used to study the variability of grains. Figure 5.2 shows the crystallite sizes of ceria as a function of the cerium concentration after the materials were calcined to 200 °C. Three different experimental setups were used to produce these data: the ultrasonic flow reactor, a classical synthesis technique, and hydrodynamic cavitation using a Microfluidizer. The classical synthesis was performed under the same conditions and reactor geometry as the ultrasound experiments, except that the probe was turned off. The single Microfluidizer experiment was conducted using hydrodynamic cavitation at pressures alternating between atmospheric and 21,000 psig. The use of hydrodynamic cavitation to produce nanostructured materials has been discussed previously [19].

From Figure 5.2 it can be seen that as the concentration of cerium was decreased, a greater difference was observed in the crystallite size between the classical and ultrasonic syntheses (approximately 3 nm at 0.15 mol/L). It would also appear that the ultrasonic flow reactor setup produces materials with grain sizes comparable

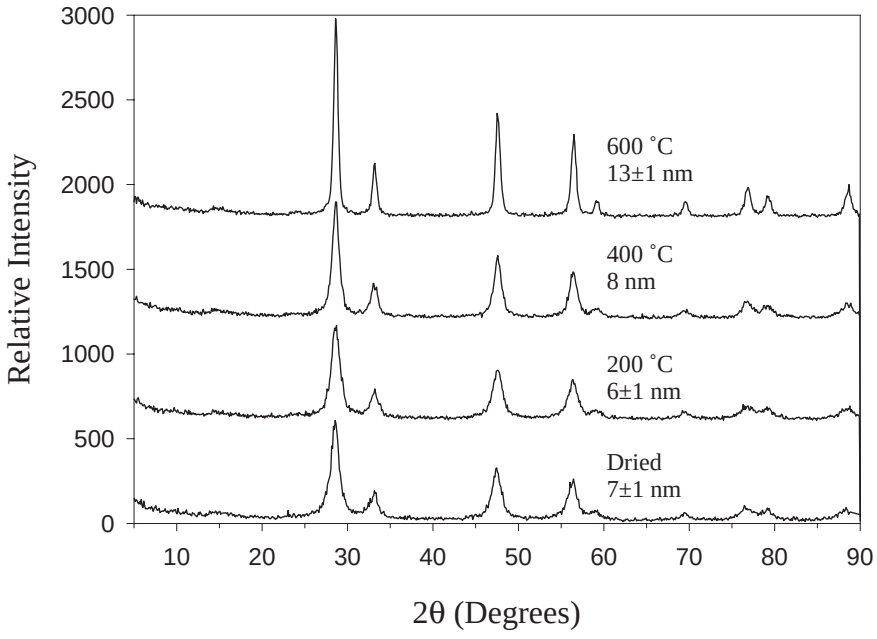

Figure 5.1: X-ray diffraction patterns for ceria synthesized with 20 kHz ultrasound and calcined to different temperatures.

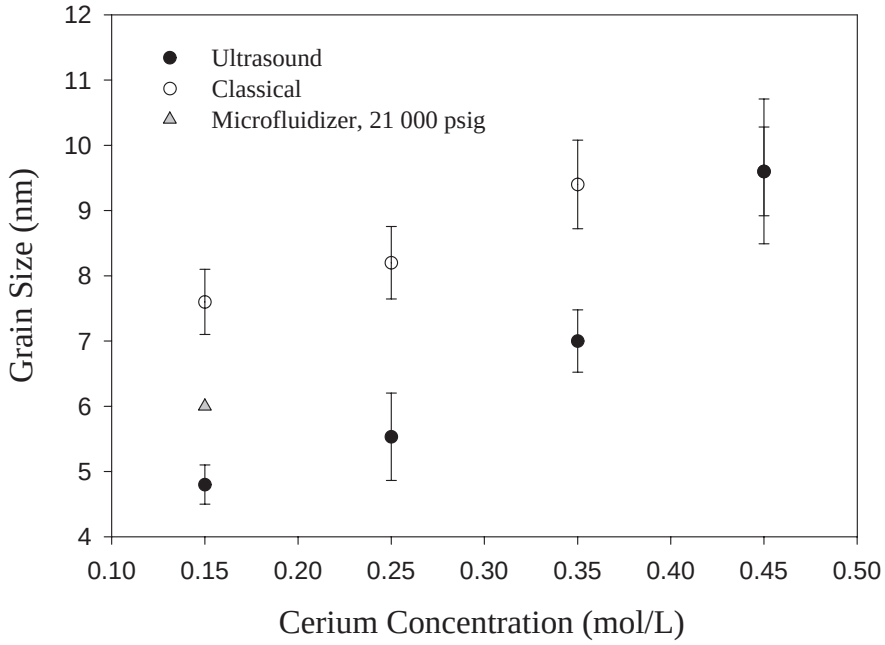

Figure 5.2: Grain size differences at 200 °C between 20 kHz ultrasound, Microfluidizer, and classical flow syntheses.

to hydrodynamic cavitation.

To increase the exposure time of the precipitated ceria to the ultrasound, and to simplify the system geometry, several ceria experiments were performed in the semi-batch reactor. Since the effects of metal concentration and calcination temperature were known, a response surface study was initiated to determine the effects of the salt solution feed rate coupled with the ultrasound amplitude on the ceria grain size. The salt feed rate was varied between 2 and 48 mL/min while the amplitude was adjusted from 0% (classical synthesis) to 100%. The results of this study are plotted in Figure 5.3.

At low salt solution flow rates, the effect of amplitude was rather moderate, but consistent with the flow reactor results (approximately 5 nm material at 100% amplitude and 8 nm at 0% amplitude). At intermediate flow rates, it appeared that the effect of ultrasound was nil. However, at the highest flow rate (48 mL/min), the largest difference between ultrasound and classical experiments was observed (6 nm at 100% versus 12 nm at 0%).

The reasons for this behavior are unknown, although the change in the effect as a function of flow rate suggested that nucleation and growth rates, as well as mass transfer issues were a factor in this phenomenon. To examine the effect of higher frequency ultrasound, parallel experiments were conducted using 20 kHz and 40 kHz probes. The results of two experiments conducted at a flow rate of 4 mL/min with and without 40 kHz ultrasound are shown in Figure 5.4. The grain sizes were 12 nm for the classical material and 7 nm for the sonicated sample. These results are more consistent with the 20 kHz results for the 48 mL/min flow

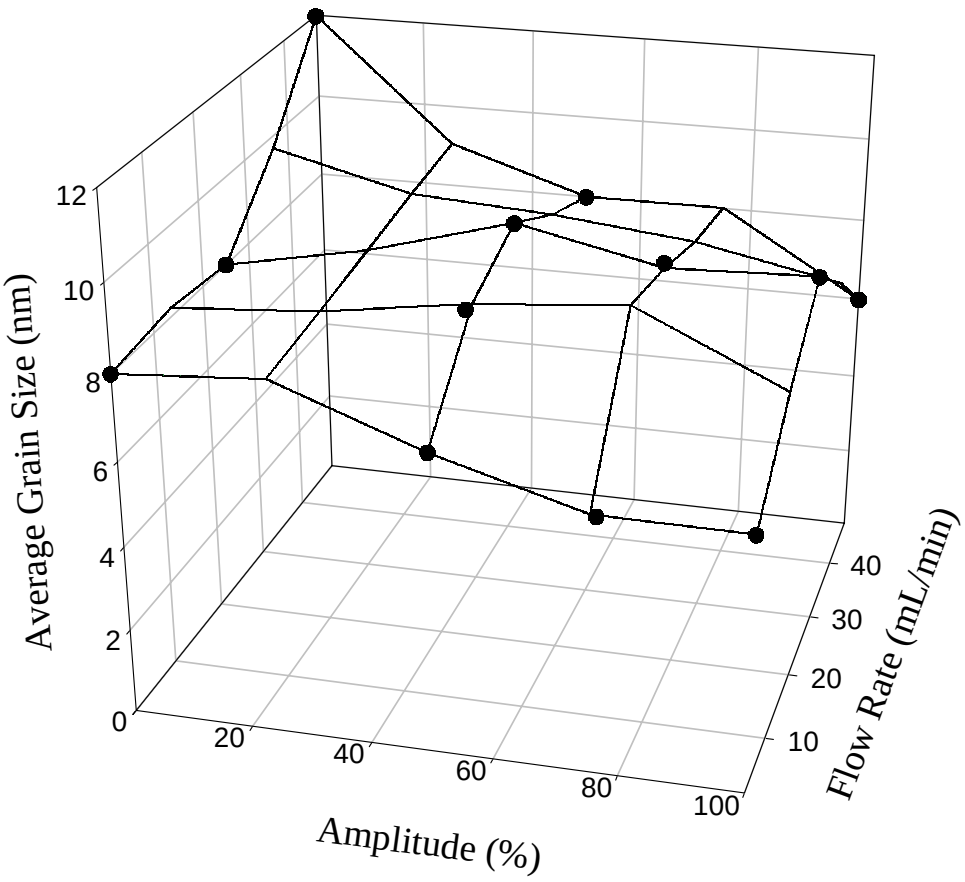

Figure 5.3: Ceria grain size (at 105 °C) response surface study as a function of amplitude (20 kHz ultrasound) and flow rate (mL/min).

rate, suggesting that the change from 20 kHz to 40 kHz also alters the nucleation and growth of ceria.

The conclusions for the ceria studies are: (1) that ultrasound processing coupled with other synthesis parameter variations permits the synthesis of metal oxides having variable grain sizes in the 2 nm to 20 nm range; (2) the degree of shear induced by cavitation in this type of experiment is not large enough to cause a radical difference in grain size compared to classical syntheses; and (3) the major changes occurring are on the surface rather than in the bulk, since nearly all of the metal oxide systems studied resulted in slight color changes between sonicated and classically prepared compounds. For example, the ceria synthesized classically were yellow powders while those prepared with ultrasound were green-colored.

5.2.2 Synthesis of titania

Titania was synthesized from solutions of $Ti_2(SO_4)_3$ by precipitating with ammonium hydroxide. The differences in grain size between sonicated and classical materials were small, on the order of 1–2 nm. To determine whether there were any synthesis parameter areas of consequential effects due to acoustic cavitation, a response surface study was conducted with feed flow rate and amplitude as the dependent variables. The grain size results for this study are shown in Figure 5.5.

At all extreme conditions (*e.g.* high flow rate and no ultrasound or low flow rate and 100% amplitude), the grain sizes of materials calcined to 300 °C were approximately 10 nm. However, as the conditions were adjusted toward the "middle" of the response surface (50% amplitude, 25 mL/min), the grain size was reduced

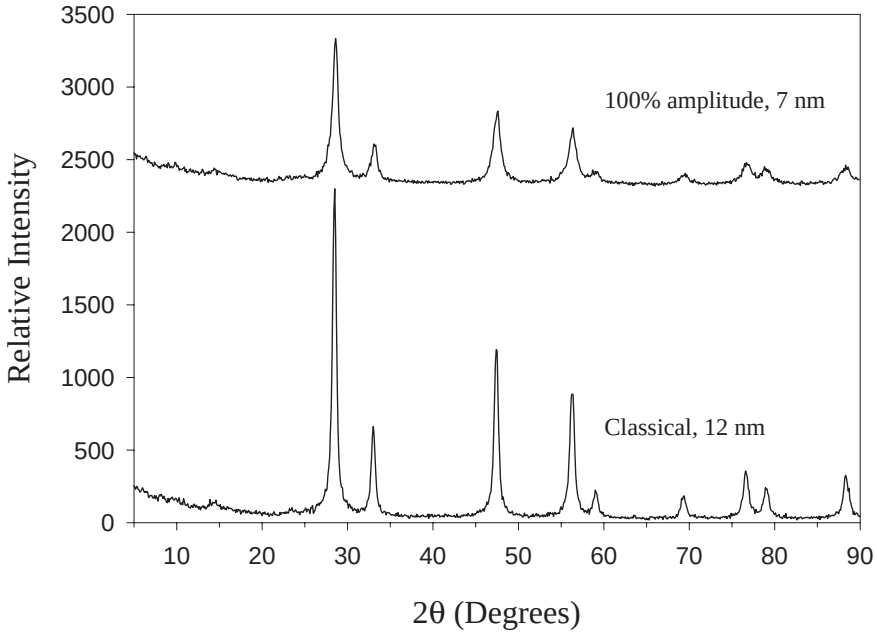

Figure 5.4: X-ray diffraction patterns for ceria synthesized with and without 40 kHz ultrasound, dried at 105 °C.

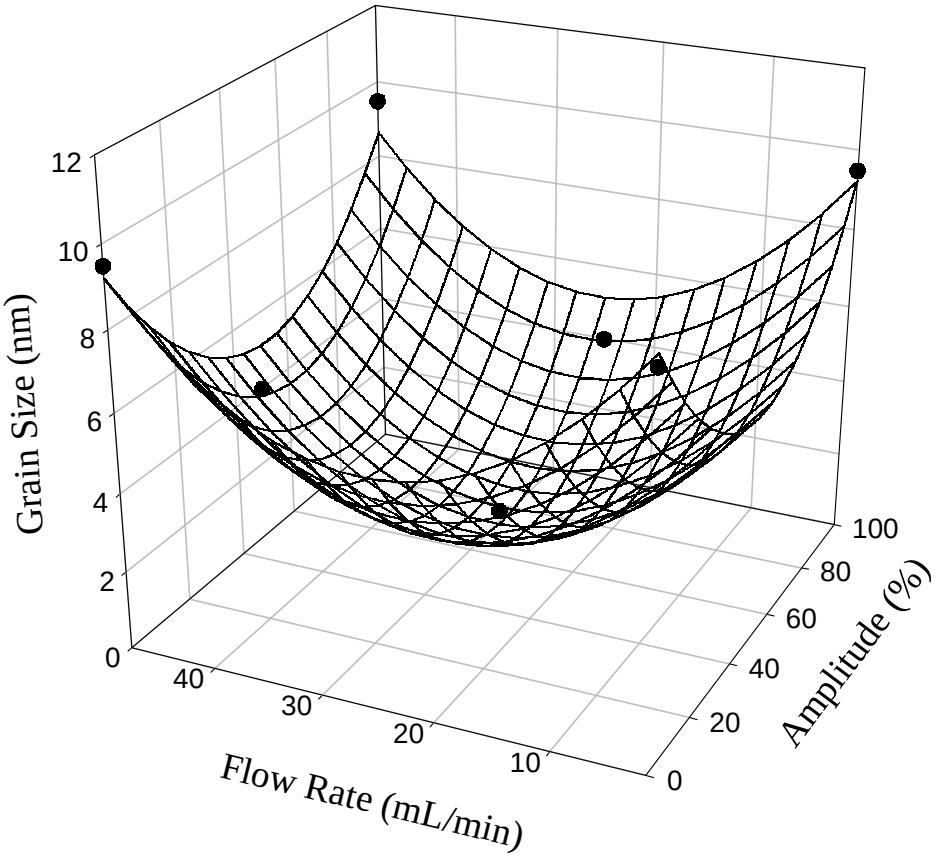

Figure 5.5: Titania grain size (at 300 °C) response surface study as a function of amplitude (20 kHz ultrasound) and flow rate (mL/min).

below the level at which the peaks could reliably be measured (approximately 2 nm). Selected area diffraction analysis (SAD) showed that the 50% amplitude, 25 mL/min samples were amorphous with a negligible amount of crystalline titania. Examples of two XRD patterns from this response surface are shown in Figure 5.6. The middle portion of the response surface was reproduced by several experiments and represents one of the most striking effects of ultrasound on metal oxide grain size.

The use of a 40 kHz probe at a flow rate of 4 mL/min showed a very slight difference (approximately 1–2 nm) between acoustic cavitation and classical synthesis. However, this slight difference is negligible compared to the dramatic interaction between flow rate and amplitude demonstrated in the 20 kHz study.

5.2.3 Synthesis of titania supported Au-Pt alloys

Although this chapter concentrates on determining whether the application of acoustic cavitation in metal oxide synthesis has the capabilities to synthesize nanostructured materials having systematically controllable grain sizes, the efficacy of mixing of the synthesis components was also an important question. To evaluate the capabilities of ultrasound to mix the components of a synthesis mixture by acoustic cavitation, a variety of gold-platinum alloys supported on titania were synthesized. The objective of the synthesis study was to determine whether the precipitation of Au and Pt salts in an ultrasonic field while titania was also being precipitated would result in a higher degree of alloy formation as contrasted to a classical synthesis. It was expected that shear induced during the acoustic cavita-

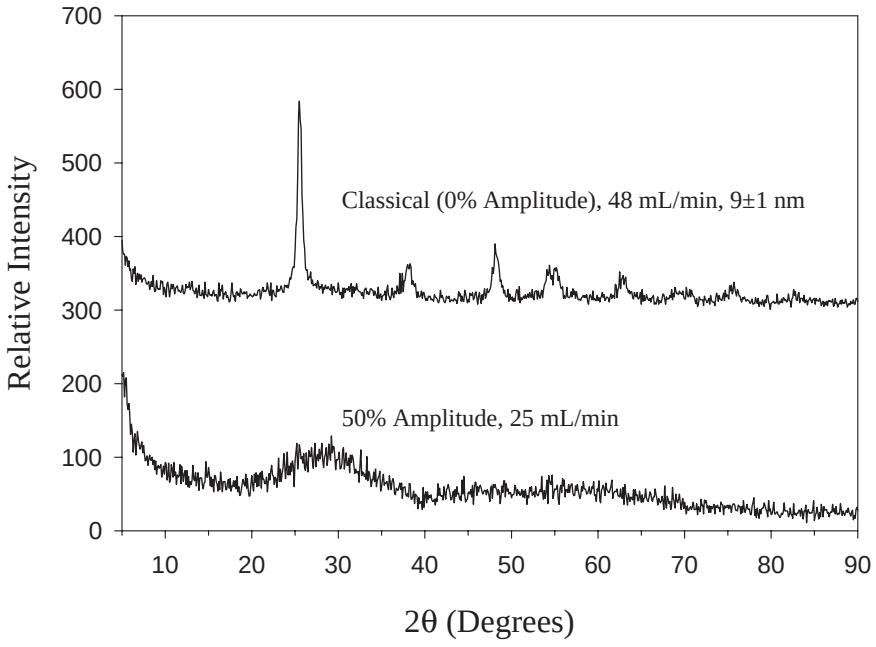

Figure 5.6: X-ray diffraction patterns (at 300 °C) for titania response surface study.

tion experiment would be significantly greater than that obtained during a classical preparation and that this higher degree of mixing of the precipitating components would lead to a higher degree of alloy formation. Furthermore, it was expected that both the alloy and the support would be formed as nanostructured materials even when calcined to high temperatures.

To test these concepts, catalysts were prepared having different compositions of Au and Pt supported on titania having 2 wt% Au with Pt/Au atom ratios of 0.25, 0.50, 0.75, and 1.0. In addition, a catalyst was synthesized having the same amount of Pt as the 1/1 Au/Pt material but with no Au. All of the syntheses were carried out in the semi-batch ultrasound reactor using a flowing stream of $Ti_2(SO_4)_3$ in water which mixed with a second stream of $H_2PtCl_6 \cdot 6H_2O$ and $HAuCl_4 \cdot 3H_2O$ just before the two streams were mixed with a sodium hydroxide solution which was contained in the reactor vessel. To precipitate the Au and Pt salts, two moles of hexamethonium bromide monohydrate per mole of Pt and Au was contained in the sodium hydroxide solution. The synthesis used the 20 kHz ultrasonic probe and a 30 minute precipitation time under ambient conditions.

All of the materials synthesized were dark blue in color after filtration and drying at 120 °C. XRD analysis indicated titania primary particle grain sizes of 3–8 nm. Transmission electron microscopy (TEM) analysis also indicated the titania grains were in this range. Selected area electron diffraction analysis (SAD) showed these materials to be anatase, and that the Au-Pt grains were in the range of 6–10 nm. Energy dispersive x-ray analysis on the particles in the 1/1 Au/Pt samples showed that all particles analyzed contained both Au and Pt. Detailed

XRD analysis of the entire species of alloys, where the extent of alloy formation was evaluated from their shift from the pure gold XRD reflection, demonstrated that the degree of alloy formation was consistent with the fraction of each metal in the applied synthesis solution. For example, modeling of the alloy reflection at 45.430 $^{\circ}2\theta$ measured on the 2% Au sample with a 1/1 Au/Pt ratio resulted in d-spacing shifts in the XRD analysis corresponding to a 45% Au- 55% Pt alloy. This analysis also indicated that the best fit showed the presence of little free gold or platinum. When the identical classical synthesis was carried out with the exception that the ultrasound power was turned off, the XRD analysis as indicated above showed only a 62% Au-38% Pt alloy formation which constituted about 50% of the total metal along with reflections for free gold and platinum. These data were taken to indicate that the ultrasound experiment resulted in a far greater degree of mixing of components than the classical experiment as a result of acoustic cavitation. The XRD analysis indicated that the grain size of the alloy was in the range of 3–5 nm.

All of the catalysts were examined in a micro-reactor for their activities for the total oxidation of methane in a 3.8% methane in air stream between 350 and 600 $^{\circ}$C. The catalytic results are shown in Figure 5.7. The figure shows that all of the gold containing catalysts were substantially less active compared to the pure platinum catalysts. Furthermore, the 2% Au 1/1 Au/Pt catalyst prepared by ultrasound and classical techniques demonstrated exactly the same reactivity profile, as did the pure Pt on titania prepared by ultrasound and classical techniques. The conclusion from the synthesis and catalytic reactivity data is that acoustic cavitation does not lead to

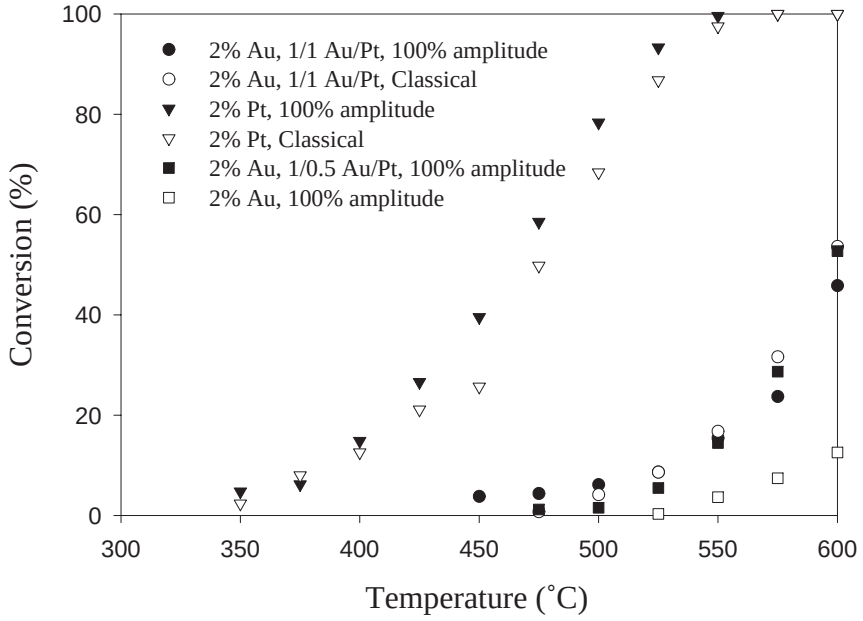

Figure 5.7: Microreactor results for titania Au/Pt catalysts synthesized with and without 20 kHz ultrasound.

catalytic surfaces having important differences for methane total oxidation despite the fact that the alloy composition of the two catalytic surfaces were significantly different.

5.2.4 Synthesis of cobalt oxide

An interesting side effect of exposure to ultrasound for all oxide systems is a change in the shade or color of the samples. For example, in the ceria system the typical classical synthesis produced a yellow solid. When the same synthesis was performed in the presence of ultrasound, the final solid was a shade of green. Although these color changes could be due to changes in grain size, they might also be due to differences in the surface defect concentrations, as ultrasound is known to provide surface roughening [107, 110].

One system not only exhibited a color change, but a phase transformation as a result of exposure to ultrasound. Figure 5.8 shows the XRD patterns for the synthesis of cobalt oxide with and without 20 kHz ultrasound using $Co(NO_3)_2 \cdot 6H_2O$ as the metal salt. When the material was synthesized in the presence of ultrasound and dried, the final product was dark brown and exhibited an XRD pattern which was indexed as cobalt oxide, Co_3O_4. However, the dried, classically synthesized sample was light brown and was identified by XRD to be β-cobalt hydroxide. Further calcination of the classical sample to higher temperatures transformed the sample to cobalt oxide, Co_3O_4.

This interesting formation of the oxide, rather than the hydroxide may be evidence of some *in situ* heating which has been attributed to acoustic cavitation. The

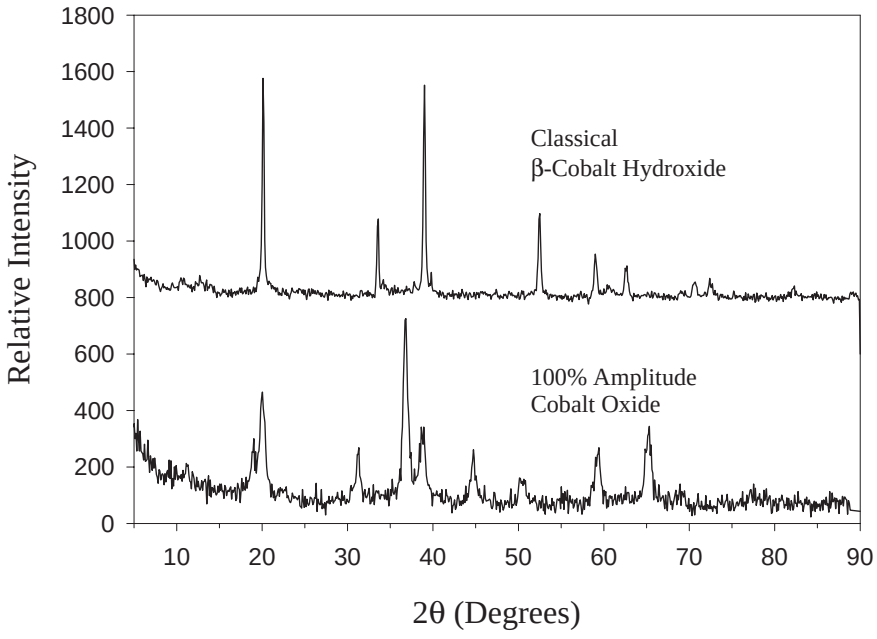

Figure 5.8: X-ray diffraction patterns for cobalt compounds (dried at 105 °C) synthesized with and without 20 kHz ultrasound in the semi-batch reactor.

bulk temperature during the ultrasonic synthesis was approximately 56 °C due to the energy input by the probe, while the classical synthesis bulk temperature was 20 °C. This difference in temperature was negligible compared to the heating at 105 °C which both samples endured prior to XRD analysis.

5.2.5 Synthesis of β-bismuth molybdate

The synthesis of β-$Bi_2Mo_2O_9$ using hydrodynamic cavitation (*i.e.* Microfluidizer) was previously shown to give higher phase pure materials as compared to conventional synthesis which yields mixed phases [19]. Thus, the synthesis of bismuth molybdate is an indicator as to the quality of mixing during syntheses which use two or more metal ions.

Figure 5.9 shows XRD patterns for classical, 40 kHz, and Microfluidized syntheses. These materials were synthesized by preparing two separate solutions of bismuth nitrate pentahydrate ($Bi(NO_3)_3 \cdot 5H_2O$) and ammonium molybdate tetrahydrate ($(NH_4)_6Mo_7O_{24} \cdot 4H_2O$) and co-precipitating them with isopropyl alcohol. The figure shows that the classically prepared material has the largest degree of phase impurities, and the ultrasound treated material showed a modest improvement. The hydrodynamic cavitation prepared sample resulted in a material of exceptionally high phase purity as compared to the calculated XRD pattern [19].

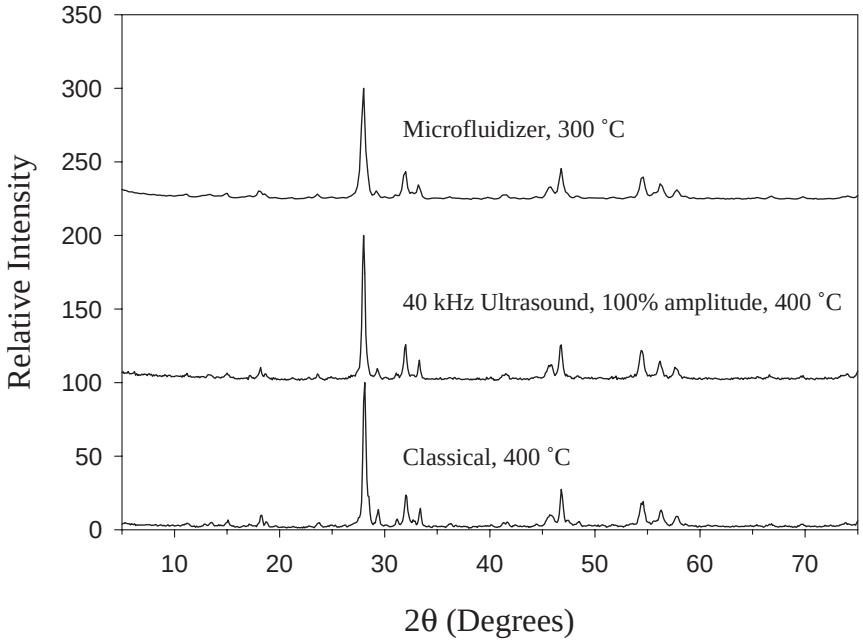

Figure 5.9: X-ray diffraction patterns for bismuth molybdate synthesized via hydrodynamic cavitation (Microfluidizer), acoustic cavitation (40 kHz ultrasound), and classical means.

5.2.6 Synthesis of zirconia-alumina

The zirconia-alumina phase diagram exhibits a miscibility gap below approximately 1850 °C [116]. Smyser *et al.* have shown that the coprecipitation of less than 30% alumina with zirconia can inhibit the phase transformation of small grain zirconia from the tetragonal to monoclinic phase [36]. Because zirconia and alumina are immiscible phases, they act as diffusion barriers to one another, which allows smaller grain material to be stabilized below the critical size necessary for phase transformation. The ability to retain the cubic or tetragonal phase of zirconia at high temperatures is beneficial for thermal barrier coatings, to prevent cracking, and for high temperature catalytic applications.

Zirconia-alumina was synthesized by preparing a combined solution of zirconium dinitrate oxide and aluminum nitrate nonohydrate and precipitating with a 2 mol/L ammonium hydroxide solution. Three different zirconia-alumina ratios were used, resulting in 20%, 15%, and 7.5% alumina in the final materials. Except for the 7.5% alumina material, repeats of the syntheses were done with and without 40 kHz ultrasound. All samples were calcined to 600, 800, and 1000 °C for 4 hours to observe the effects of heat treatment on phase stability.

Figure 5.10 shows XRD patterns for the 40 kHz synthesized 85% zirconia–15% alumina sample calcined to the various temperatures. Below 600 °C, the diffraction peaks are too broad to determine the phase composition, but at 800 °C, the material appears to be cubic zirconia, with the possible presence of a small amount of tetragonal zirconia. At 1000 °C, the material has transformed to contain a mixture of both cubic and tetragonal zirconia, but does not contain any monoclinic

zirconia. Figure 5.11 shows a comparison between the acoustically and classically synthesized 15% alumina materials calcined to 800 °C. In this figure, as with all other zirconia-alumina materials, there is no significant difference between the XRD patterns. Thus, although alumina inhibits the phase transformation of zirconia to the monoclinic phase, the effect of ultrasound on the synthesis appears to be negligible.

5.2.7 Synthesis of zirconia and zirconia supported platinum

Zirconia would be an ideal support for high temperature catalytic applications, such as methane oxidation. As a result, zirconia was synthesized classically, as well as with 20 kHz and 40 kHz ultrasound using zirconium dinitrate oxide as the precursor, and ammonium hydroxide as a precipitating agent. Figure 5.12 shows the x-ray patterns for all three syntheses calcined to 600 °C. As shown in the figure, there is no noticeable difference between using the 40 kHz ultrasound and the classical synthesis, with both samples being composed of cubic zirconia. However, the 20 kHz sample shows some differences, containing some monoclinic and tetragonal zirconia, with cubic zirconia being the bulk phase.

A response surface study was performed on zirconia supported platinum to see the effect of 40 kHz acoustic cavitation on grain size. For this study, three factors were examined: platinum weight loading from 0–2%, ultrasound amplitude from 0–100% (0% indicating that the probe was turned off), and zirconium solution concentration from 0.4–0.8 mol/L. For all syntheses, there appeared to be no effect due to zirconium concentration or amplitude on the grain size of the zirconia or

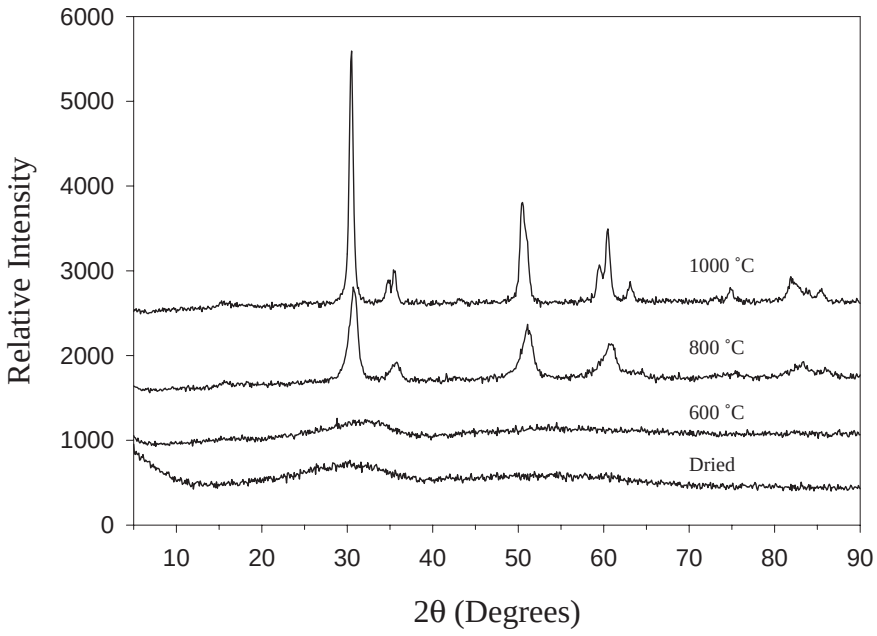

Figure 5.10: X-ray diffraction patterns for 85%–15% zirconia-alumina synthesized via acoustic cavitation (40 kHz ultrasound) calcined to various temperatures.

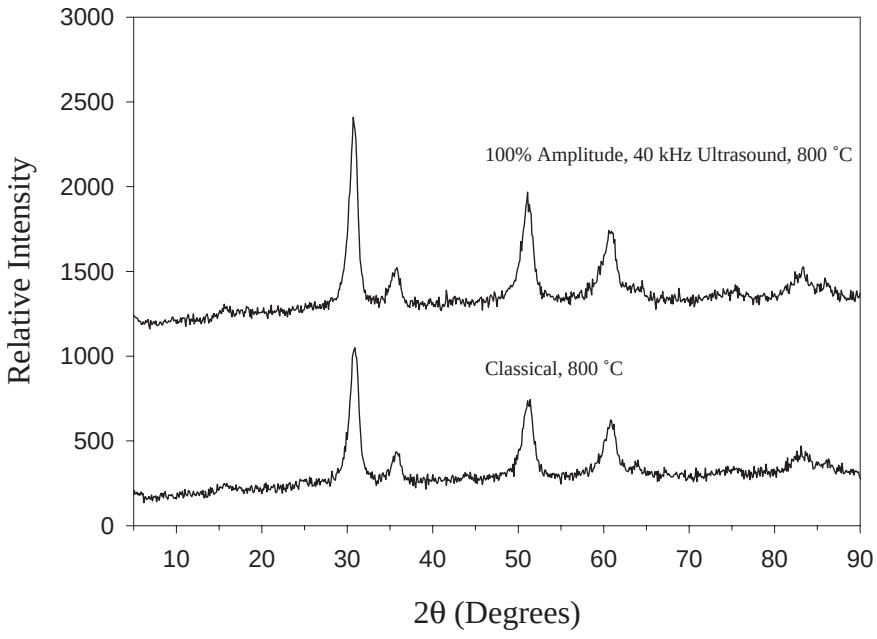

Figure 5.11: X-ray diffraction patterns for 85%–15% zirconia-alumina synthesized via acoustic cavitation (40 kHz ultrasound) and classical means calcined to 800 °C.

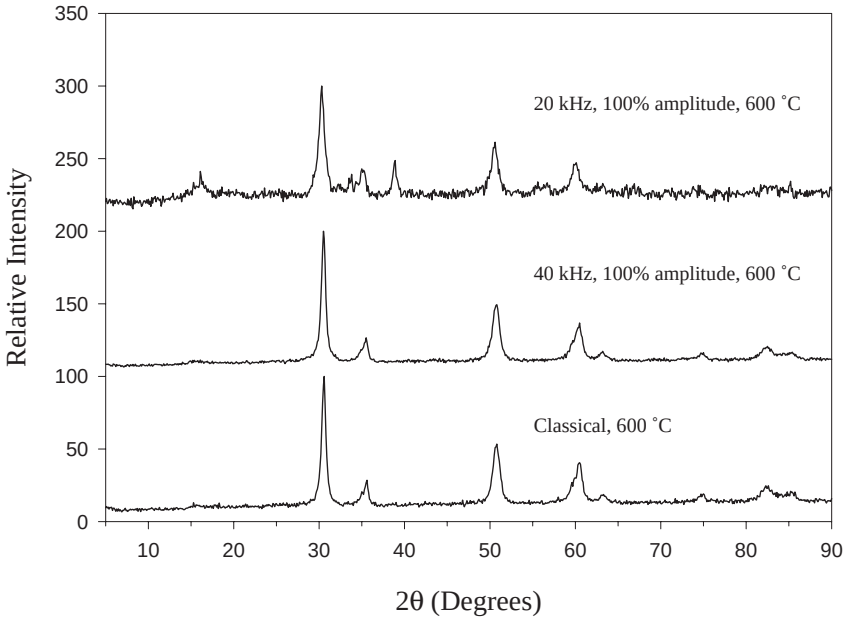

Figure 5.12: X-ray diffraction patterns for zirconia synthesized via acoustic cavitation with 20 kHz ultrasound, acoustic cavitation with 40 kHz ultrasound, and classical means calcined to 600 °C.

the platinum. Figure 5.13 shows typical x-ray diffraction patterns for zirconia supported 2% platinum synthesized with and without ultrasonic treatment. As in the case of the zirconia synthesis, the effects of acoustic cavitation appear negligible compared to the system chemistry.

5.3 Conclusions

Based on these experimental results, it seems that the general effect of ultrasound on these syntheses is relatively minor, and in a few cases consequential. In some cases, such as ceria and titania, the effect was more dramatic; however, the degree of variability of grain sizes and phase purity were less than expectations. This conclusion is in contradiction with much of the literature which reports reduced crystallization times and reduced particle size distributions for syntheses involving ultrasound [105,109,110]. Additional metal oxide systems were studied along with parallel classical syntheses, and in all cases this comparison led to modest changes as reported for the above described systems.

However, it would appear that for a majority of the systems in which ultrasound has been reported to have a beneficial effect, the materials affected either would not have been produced without the intervention of ultrasound, or the material formation kinetics are slow (*e.g.* zeolite synthesis and the formation of sol gels). In such systems, it is expected that acoustic cavitation would increase the rate of precipitation/crystallization and even reduce particle size distributions due to an increase in mass transfer and high energy collisions. The increase in mass transfer

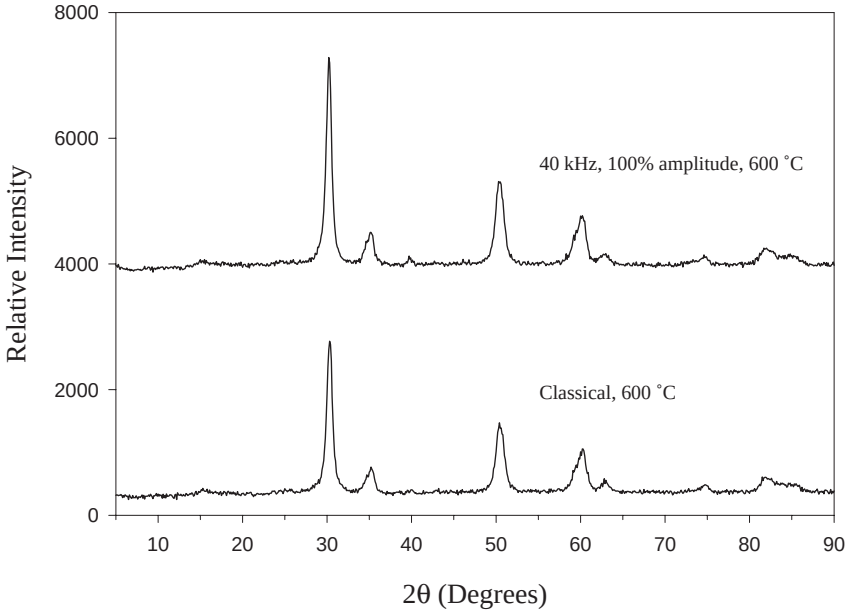

Figure 5.13: X-ray diffraction patterns for zirconia supported 2% platinum synthesized via acoustic cavitation (40 kHz ultrasound) and classical means calcined to 600 °C.

rates could be seen as due to the increase in the interfacial area as well as the micromixing and acoustic streaming produced by ultrasound [1].

For the systems studied in this chapter, the rate of precipitation was extremely fast. Based on previous work with hydrodynamic cavitation done in this laboratory, it was desired to produce a soft metal oxide gel immediately and then subject it to the high shear cavitation created by a Microfluidizer. This methodology was naturally extended to the work with acoustic cavitation, which may be exactly why the acoustic cavitation results were so poor.

In a Microfluidizer, the newly formed soft gel is forced through a very small volume, high shear environment. Thus, the particles are forced to collide with one another. In both of the ultrasonic reactor designs presented in this dissertation, it may have been possible for the bulk of the newly precipitated metal oxide precursors to avoid the effects of the ultrasound for two reasons. First, the reactor volumes are fairly large. It may be possible in the flow reactor, with a volume on the order of 1–2 mL, for particles to take a flow path such that they do not "feel" the maximum amplitude of the probe. Certainly, in the semi-batch reactor, the wall of the reactor is a few centimeters from the probe, and thus it is possible the acoustic field is not strong very far from the probe. Second, the ultrasonic probe produces an acoustic force which may propel particles away from it. If one pours a small amount of water onto an ultrasonic probe and then activates it, the water is propelled rapidly from the surface of the probe. Similarly, it is possible to make light objects move by bringing the tip of an ultrasonic probe close to them. Thus, it is not inconceivable to imagine newly formed precipitates in solution being pushed away

from an ultrasonic probe and therefore avoiding the effects of acoustic cavitation.

Chapter 6

Gold Concentration Effect on CO Oxidation over Titania Supported Catalysts

6.1 Introduction

The hypothesis that synthesizing a catalytic material with a grain size less than 50 nm will lead to structure sensitivity and enhanced activity requires a simple test reaction. For this study, the oxidation of carbon monoxide (CO) was chosen primarily because there is no possibility of a secondary reaction taking place, and thus there are no selectivity issues which could confuse the results. In addition, CO oxidation is not equilibrium limited under the conditions used in this investigation.

CO oxidation is not only a good test reaction for particle size effects, but is

also an important environmental and industrial reaction. The oxidation of CO is primarily of importance for the treatment of hydrocarbon combustion emissions. In addition, the removal of CO from air in submarines and space craft, the oxidation of CO in CO_2 lasers, respirator masks, CO gas sensors, and the removal of CO from the reformate feed for fuel cells are other useful applications of this reaction [28, 30–32, 117].

One of the most active catalysts for CO oxidation is supported gold, which has been investigated by many researchers [27–32, 108, 117–134]. A unique feature of supported gold is that although unsupported and large grain supported gold has little or no catalytic activity, when the gold grain size is reduced to less than 20 nm, the supported gold catalysts become unusually active for a variety of reactions. This catalytic behavior, which was shown in Figure 2.20, follows the trend of a Case II reaction described under the structural hypothesis in Chapter 2, where the rate may be dependent on the number of low-coordination metal edge sites. The number of low-coordination sites necessarily increases with decreasing metal crystallite size.

Nanometer-size gold catalysts have also been found to be active for other reactions. Titania supported gold is highly selective for the vapor phase epoxidation of propylene to propylene oxide, a major chemical feed for producing resins [120]. Nanostructured gold is also active for the catalytic combustion of hydrocarbons and trimethylamine, as well as the reduction of NO_x with CO [30]. Decreasing the size of gold clusters from 6 nm to 2 nm resulted in enhanced glucose oxidase enzyme activity which has applications for glucose sensors [135]. High selectivities

at conversions comparable to platinum and palladium catalysts were found for the liquid phase oxidation of diols to produce glycolic acid and lactic acid [131]. In addition, gold has been found to be active for the hydrogenation of CO_2 to make methanol [30].

There are several methods for producing supported gold: classical impregnation onto a support via incipient wetness; impregnation using organic gold phosphine complex precursors [32, 122–128]; coprecipitation of the support and gold [117, 119]; precipitation-deposition, where the gold is deposited onto a preformed support [29, 119]; co-sputtering the gold and support material [27]; and chemical vapor deposition [27]. In addition, photochemical reduction of gold chloride in the presence of a titania colloid [130] and the thermal relaxation technique, where gold is vapor deposited onto a nylon-11 oligomer and then deposited onto a titania support in solution [134], are two other novel techniques. Most of the more active materials have been produced via the precipitation-deposition method and impregnation via organic gold complex precursors, because classical impregnation techniques yield catalysts with larger gold grain sizes, and hence lower activity [28, 117].

The choice of support also has influence on the activity of nanometer-size gold. The reactivity toward different reactions can be fine tuned by changing the support. For CO oxidation, titania, iron oxide, cobalt oxide, and manganese oxide are more active than other supports. Zinc oxide and zirconia improve the activity for methanol synthesis, while cobalt oxide supported catalysts have been shown to be as active as palladium catalysts for methane oxidation [27]. This support effect

may be partially due to the concentration of hydroxyl groups found on the various materials and their interaction with the metal.

Iwasawa's group, in the course of their gold organic complex impregnation work, discovered that the use of metal hydroxide precursors during preparation leads to smaller gold particles and hence more active catalysts than simply using the metal oxides [32]. Their analysis has been that gold precursors are stabilized on the surface of the support by hydroxyl groups and/or adsorbed water, and that during calcination the decomposition of the gold precursors coinciding with the phase transformation of the hydroxide to the oxide leads to higher metal dispersions [125–128]. Thus, it is more desirable to precipitate the support material as a hydroxylated species and precipitate or impregnate gold onto the newly formed support prior to calcination at higher temperatures.

Based on literature results of coprecipitation and precipitation-deposition studies on titania supported gold, it is expected that by decreasing the concentration of gold on the catalyst, the crystallite size will also be decreased. Thus, the primary goal here was to determine whether acoustic cavitation synthesis will lead to enhanced CO oxidation activity compared to conventional coprecipitation by increasing the dispersion of gold on the titania. In addition, the dispersion of the titania supported gold onto silica was attempted similar to the work of Salama *et al.* [49] to see if activity is increased. An initial comparison of acoustic and hydrodynamic cavitation was also explored. Finally, the effect of changing gold concentration on CO oxidation was quantified for the coprecipitation of titania and gold.

6.2 Results

Seven samples were synthesized with different weight loadings of gold using the acoustic cavitation setup. For comparison, three samples each were synthesized via classical and hydrodynamic cavitation synthesis. In addition, one sample was produced with an approximately 1% gold/19% titania on silica (Cabosil) to investigate the effect of dispersing the gold on titania on another support. For all calcined samples, the titania XRD pattern was indexed as the pure anatase phase, and the gold was determined to be metallic gold when visible by XRD. The data obtained from these fourteen samples are shown in Table 6.1.

6.2.1 Crystallite size and synthesis efficiency

In general, the gold concentrations obtained from neutron activation agree quite well with the predicted theoretical content for most of the catalysts. For some of the samples, the gold content was less than the theoretical value, and the 95% confidence interval for the percentage of theoretical gold deposited for all samples was $84 \pm 9\%$. Thus, it would appear that this method of directly precipitating the gold with the titania allows a greater control over the metal concentration compared to other techniques, such as deposition-precipitation, where only about 18% [28] to 40–60% [29, 120] of the gold is deposited on the catalyst.

Three samples were analyzed via ESCA/XPS: the 0.053% gold classical sample; the 0.220% gold, acoustically synthesized sample; and the acoustically synthesized 2.020% gold catalyst. Due to the low concentration, it was not possible to

Table 6.1: Catalyst data for gold concentration study. The catalysts are arranged by synthesis method: (A) acoustic cavitation, (S) acoustic cavitation with silica support, (C) classical, and (H) hydrodynamic cavitation.

Synthesis method	Gold content (wt %)	Titania grain size (nm)	Gold grain size (nm)	Activation energy (kJ/mol)	Reaction rate per moles of Au (s^{-1})
A	0.068	13.4	-	26	5.52 ± 0.48
A	0.130	13.5	-	32	4.67 ± 0.67
A	0.220	12.9	-	33	2.97 ± 0.17
A	0.454	13.1	-	32	0.99 ± 0.14
A	0.664	12.7	16.7	18	1.17 ± 0.09
A	1.195	11.1	15.6	28	1.62 ± 0.11
A	2.020	10.7	15.7	31	0.85 ± 0.11
S	0.919	-	22.8	37	0.57 ± 0.06
C	0.053	13.7	-	28	16.9 ± 1.2
C	0.393	13.1	-	31	1.04 ± 0.10
C	2.150	12.0	11.8	24	0.74 ± 0.05
H	0.492	12.0	-	21	0.54 ± 0.10
H	1.028	14.2	15.9	21	0.74 ± 0.03
H	1.368	12.1	12.1	21	0.66 ± 0.05

analyze the gold in the 0.053% sample. However, the Au 4f spectra for the other two samples indicated that all of the gold present on the surface of each sample was Au(0). Thus, it appears that there was no Au(I) or Au(III) species present after calcination to 400 °C. In addition, ESCA analysis indicated that chlorine, which could act as a catalytic poison, was absent from all three catalysts.

The mean gold crystallite sizes could only be determined for the higher weight loaded materials. TEM analysis of the three ESCA samples was unable to give an accurate picture of the gold particle size distributions due to the lack of enough gold particles in the samples. In the 0.053% and 0.220% samples, after several hours of searching in the TEM, no gold particles were observed. For the 2.020% gold sample, two gold particles were found with mean diameters of approximately 13 nm. Thus, TEM was found to be impractical as a technique to measure the gold grain sizes, as these catalysts contain very low gold concentrations.

The mean gold grain size determined by XRD does not appear to change much for the higher weight loaded samples, with the 95% confidence interval for the three acoustically synthesized materials being 16.0 ± 1.5 nm. However, it appears that there may be a small difference between the three techniques, with the classical synthesis giving slightly smaller grain sizes. This might partially explain the higher oxidation activity for the 0.053% classical catalyst compared to the 0.068% acoustically synthesized catalyst (see below).

The anatase grain size appears to be unaffected by the synthesis technique. The mean crystallite sizes were 12.5 ± 1.0 nm, 12.9 ± 2.1 nm, and 12.8 ± 3.1 nm for the acoustic, classical, and hydrodynamic techniques, respectively. The overall 95%

anatase mean grain size confidence interval was 12.7 ± 0.6 nm. This suggests that the different synthesis methods have no effect on the titania, but as the alkoxide solutions in this study had a fixed titanium content, this grain size result does not rule out the possibility of controlling titania crystallite size by other means, such as varying the titania concentration.

6.2.2 Catalytic activity

The specific CO oxidation rates per gram of catalyst at 150 °C for all the samples are shown in Figure 6.1 as a function of their gold contents. With the exception of the 1.195% gold sample, it appears that the oxidation rate is proportional to the amount of gold present in the samples until a concentration of approximately 0.5% gold is reached, where for many of the samples the rate either remains constant as the gold concentration is decreased, or begins to increase.

This behavior becomes more clear when the rates are normalized to the amount of gold in each sample, as shown in Figure 6.2. For gold concentrations between approximately 0.5 and 2.2%, the atomic rate appears to be relatively constant. However, when the concentration is reduced below 0.5%, the atomic rate increases quite dramatically.

Figure 6.2 agrees qualitatively with Haruta's CO turnover rate versus grain size data for titania supported gold (see Figure 2.20). Taken with the lack of an XRD peak for gold at lower concentrations, this suggests that by decreasing the gold concentration, the mean gold crystallite size was decreased, and thus the catalytic activity was increased. The continuous nature of Figure 6.2 also suggests that

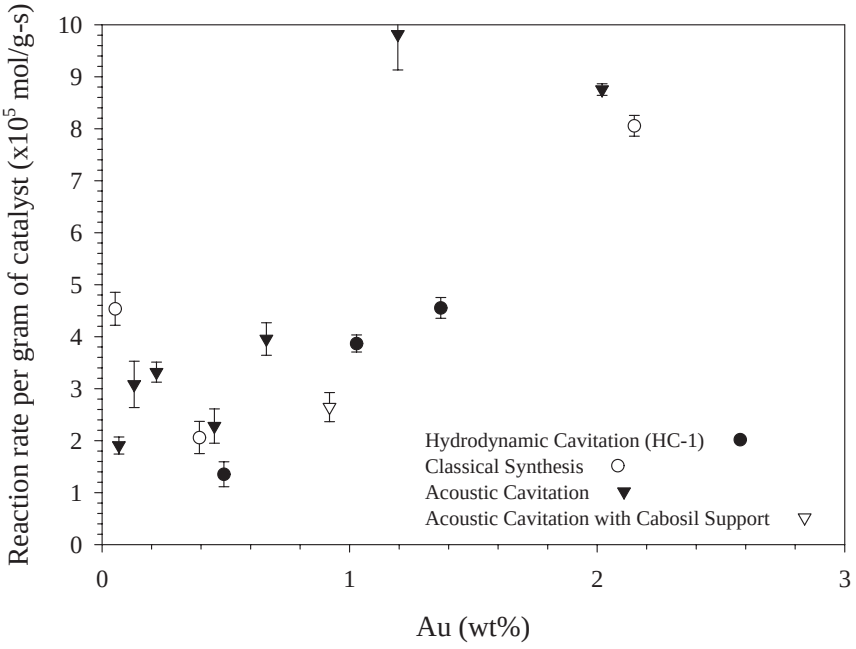

Figure 6.1: CO oxidation rate per gram of catalyst at 150 °C as a function of gold loading on the catalysts.

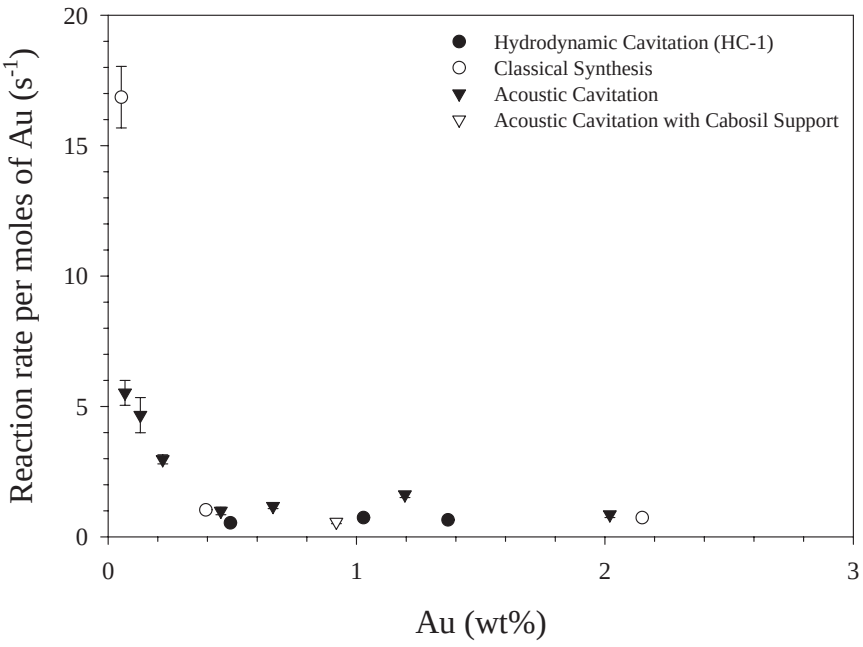

Figure 6.2: CO oxidation rate per moles of gold at 150 °C as a function of gold loading on the catalysts.

there is little difference, under the current synthesis conditions, between the three synthesis methods, and also that depositing the gold on titania onto silica appears ineffective.

In addition to qualitative agreement in the trend of concentration/grain size with the precipitation-deposition results of Haruta, the activation energies shown in Table 6.1 are in agreement with the values reported in the literature, which vary from 3.9 to 8.4 kcal/mol (16.3–35.1 kJ/mol) [28]. The agreement in the reactivity trend occurs over a much lower and narrower range of gold concentration, approximately 0.1–2.0% gold versus 0.5–8.0% gold for the precipitation-deposition work of Haruta, suggesting differences between the two techniques in the number of active sites produced for a given gold concentration.

6.3 Conclusions

Gold concentration was determined to be a dominant factor controlling the catalytic activity of titania supported gold catalysts, presumably by changing the dispersion and crystallite size of the gold. By varying the gold concentration from about 2.0% down to approximately 0.1%, the oxidation rate of 3.51% CO in air was increased by a factor of nearly 19 at 150 °C. The gold yield by this method of coprecipitation from a homogeneous solution was $84 \pm 9\%$, which offers a very efficient method of producing crystalline gold on titania compared to most other methods.

Unfortunately, the processing techniques employed to influence the grain size of the gold: acoustic cavitation, acoustic cavitation with silica dispersion, and hy-

drodynamic cavitation; were unable to definitively show any differences compared to “classical” syntheses. The hydrodynamic cavitation experiments performed with the HC–1 were limited in scope compared to acoustic cavitation, as there were other factors such as pressure and orifice diameters which could be studied. Therefore, further study at a fixed gold concentration was pursued with hydrodynamic cavitation to determine whether cavitation can affect gold crystallite size independent of concentration. The details of this work will be discussed in the following chapter.

Chapter 7

Factorial Study of Hydrodynamic Cavitation with the HC–2 for Titania Supported Gold Synthesis at Constant Gold Content

7.1 Introduction

The results from Chapter 6 showed that acoustic cavitation was not effective for producing nanometer-size gold on titania under the synthesis conditions chosen. Although varying gold concentration on the titania catalysts is a means of controlling the grain size, it would be more desirable to independently control crystallite size. Therefore, the objective of this portion of the dissertation was to determine

synthesis conditions (precipitating agent, orifice size, etc.) where this independent grain size control might exist using hydrodynamic cavitation. Statistical design of experiments was used to identify the most effective synthesis parameters to allow cavitation to affect crystallite size at a fixed gold concentration. Using this approach, it is possible to efficiently arrive at a set of experimental conditions which enable an understanding of the relationship between cavitation conditions and material properties.

7.1.1 Hydrodynamic cavitation to control gold dispersion

As was shown in Chapter 3 on page 108, the energy dissipation per mass of liquid surrounding a cavitation bubble is given by Equation 7.1.

$$\epsilon = \frac{\dot{W}}{m} = 0.366 \frac{1}{\delta} \left(\frac{P}{\rho} \right)^{\frac{3}{2}} \tag{7.1}$$

Assuming that the liquid layer thickness around the bubble, δ, does not depend on the size of the bubble, only the hydrostatic pressure and the type of liquid will determine the energy transmitted during a bubble collapse.

In the current hydrodynamic cavitation setup (HC–2), it is possible to change the orifice diameter through which the process fluid flows. By changing the orifice diameter through which a precipitated slurry passes, it should be possible to alter the pressure drop enough to alter the frequency and intensity of cavitation bubble collapses after the orifice (see Chapter 3, especially with regard to simulation results). In addition, according to Equation 7.1, by changing the hydrostatic pres-

sure, we may also change the degree of energy transmitted via a shockwave to the precipitated particles during bubble collapse. Thus, it was expected that the use of hydrodynamic cavitation would produce a high shear environment produced by the kinetic energy exchange of particles caught in and around the bubbles which might result in modification of the grain sizes of the materials.

7.1.2 Statistical design of experiments

Statistical design of experiments (DOE) is an organized, scientific strategy for collecting, analyzing, and drawing conclusions about experimental data with the minimum amount of experimentation, which has been previously described (*e.g.* [136,137]). DOE is an alternative to methods, such as one-factor-at-a-time (OFAT), where all factors (variables) but one are fixed, while the remaining factor is changed. OFAT works in many cases, but fails to account for possible interactions between different factors in an experiment, and may thus miss optimum settings of the variables.

For example, assume three variables are being studied, such as temperature, pressure, and time. One way of implementing an OFAT strategy would be to fix two of these three factors at some fixed level, either extremes (maximum or minimum possible values) or some intermediate value, while varying the third factor (*e.g.* the temperature) to observe its effect on a desired response, such as a material property or conversion of a reactant. Once the optimum results are achieved with the temperature experiments, then temperature would be fixed, and one of the remaining variables examined to determine the best conditions to give the desired

results. This approach will work, and has worked for scientists in the past, but it is not necessarily the most efficient approach.

With DOE, the three variable problem could be approached as follows. First, an experimental design is chosen which will reveal the effects of each of the variables plus any possible interactions between the variables which might not be revealed with an OFAT approach. One such design is a 2^k factorial where k is the number of variables in the study. In a factorial design, all possible combinations of the high and low settings of each variable are investigated. For this example, eight (2^3) runs would be the minimum necessary to explore all the combinations of high and low settings of three variables. Visually, a three variable factorial design can be represented by the vertices of a cube, where each dimension of the cube represents a high or low setting of each variable in the study.

Once a suitable design is chosen, each experiment is performed in random order to minimize response variation from other factors not controlled in the experiment. For example, an analog clock used to time an experiment could continually slow down or the humidity in a room could rise during the day of a given set of experiments. If so, then a trend or pattern might appear in the data that was a result of these changing conditions and not the factors being studied unless care was taken to run the experiments in a random order.

Data analysis with DOE can be reduced to a series of steps: response transformation, selection of a suitable model, statistical analysis of the model, and examination and interpretation of the model. These steps are iterative, in that the results of the first attempt to analyze the model may suggest a response transfor-

mation, and hence another analysis of the data. In response transformation, the experimenter decides whether to examine directly the effects of the factors on the response (experimental result), or to apply a numerical transformation on the response. For example, if the rate of a reaction is being investigated, it would not be expected that the rate would vary linearly with respect to temperature and pressure, but the logarithm of the rate (a transformation of the data results) might.

The next step is to choose a model to represent the data. In the case of factorial designs, the simplest model is the result of linear combinations of each factor, plus terms to include the interaction of the factors. For three factors, designated x_1, x_2, and x_3, this example model would be:

$$f(x) = b_0+b_1x_1+b_2x_2+b_3x_3+b_{12}x_1x_2+b_{13}x_1x_3+b_{23}x_2x_3+b_{123}x_1x_2x_3 \quad (7.2)$$

where the bs are coefficients for each of the terms. One easy way to select the important terms for a model is to calculate the effect of each term and plot the result on a normal probability plot (a linearized probability distribution plot). Factors which are insignificant, and thus do not contribute to the response, should lie on a straight line, while factors which may be significant will deviate from this line.

Once a model is selected, an analysis of variance (ANOVA) is performed to determine whether any of the terms contributes statistically to the model. The important things to look for in an ANOVA table are the results of statistical significance tests for each factor and interaction and the P-value for each test. A P-value less than 0.05 suggests that 95% or more of the time, a factor that is believed to be

statistically significant from the ANOVA, will be significant.

After a model has been screened with a normal probability plot for significant factors and analyzed by an ANOVA, the model needs to be examined for its ability to explain the data and whether the results make sense. For example, if a given model agrees well with the data, then a normal probability plot of the studentized residuals (the residuals divided by the estimated standard deviations of the residuals) should give an approximately straight line. Also, there should be no noticeable trends in plots of the residuals versus the run order or the predicted responses from the model. If there are trends in these types of plots, then a suitable transformation of the response or a new model, or perhaps a new set of experiments may be required.

In any experimental design, once a model has been analyzed and found to be suitable, it should not be assumed that it is true. The model must be tested for its predictive capability and its reproducibility, especially if there was no replication of the experimental data. For example, if a model suggests that a certain combination of variables will give the optimum result for a response, then experiments should be performed at those settings to verify the result.

7.2 Results

7.2.1 Factorial study on orifice size, gold-titanium solution feed rate, and ammonium hydroxide concentration.

An initial factorial study was performed on the HC–2 to explore the effect of orifice size, solution feed rate, and ammonium hydroxide concentration on the gold and titania grain sizes. This was a two-level factorial design, so each factor was studied at two different settings. The orifice diameter was set to be either 0.073 inches or 0.095 inches, the feed solution was fed at either 2 mL/min or 10 mL/min, and the ammonium hydroxide concentration was varied from 0.40 mol/L to 0.77 mol/L. The gold concentration for all samples in this study were set to be 2% gold by weight.

Since this study was designed to explore the main effects of the three factors, the focus was on analyzing the gold content of the samples and the grain sizes of the titania and gold as the three major responses to be studied. All samples were calcined to 400 $^{\circ}$C to crystallize the anatase phase of titania. Table 7.1 contains the run order, experimental conditions, and NAA and XRD results for the samples in this factorial design.

There were no statistically significant changes in gold or titania grain size when the three factors were varied. The 95% confidence interval for the mean gold crystallite size by XRD was 14.7 $\pm$ 1.4 nm and the titania crystallite size was 13.1 $\pm$ 0.5 nm. The mean gold concentration for the eight samples was 2.42 $\pm$ 0.18%, which combined with the approximately 80% yields suggested

Table 7.1: Material data for first HC–2 factorial study.

Run order	Orifice diameter ($\times 10^{-3}$ in.)	Feed rate (mL/min)	NH_4OH conc. (mol/L)	Gold content (wt %)	Titania grain size (nm)	Gold grain size (nm)	Steady state pressure (psig)
1	73	2	0.77	2.548	11.8	16.5	620
2	73	2	0.40	2.222	12.9	15.3	670
3	95	10	0.77	2.626	13.4	14.3	200
4	95	2	0.40	2.473	12.8	12.0	260
5	73	10	0.40	2.230	14.1	17.0	660
6	73	10	0.77	2.382	13.3	13.2	530
7	95	10	0.40	2.728	13.2	14.2	240
8	95	2	0.77	2.124	13.3	15.2	220

that approximately 20% of the titania was either lost in the processing or not precipitated.

Given these crystallite size results it appeared that under these conditions, the HC–2 was not capable of controlling grain size by hydrodynamic cavitation. However, it may have been that the feed solutions were too concentrated, and that the nucleation and growth rates were too rapid for the HC–2 to affect the crystallite sizes. Dilution of the feed might also be a general requirement for cavitation to have any sort of grain size control. Thus, another factorial design, where feed concentration and orifice size were varied was performed to explore this concept.

7.2.2 Factorial study on orifice size and gold-titanium feed concentration.

In this second study, the concentration of the titania was reduced from the 0.88 mol/L in the first study and varied at the 0.1 mol/L and 0.5 mol/L levels. The gold

concentration for all solutions in this study was calculated to be 2% gold by weight. The orifice diameter was varied from 0.075 inches to 0.115 inches. The feed rate was kept constant at 10 mL/min and the ammonium hydroxide concentration was fixed at 0.77 mol/L.

The data for this second factorial study are given in Table 7.2. As with the first study, there were no statistically significant changes in the gold or titania grain size as observed by x-ray diffraction. The titania mean crystallite size was 14.2 ± 0.5 nm (95% confidence level, 3 degrees of freedom), and the gold mean crystallite size was 16.5 ± 4.9 nm, which are effectively the same results obtained in the first study. This suggested that the process conditions are still not in a region where the grain size can be controlled by hydrodynamic cavitation. However, the large variation in gold crystallite size numbers suggested that although there was no *statistical* significance to the two factors, given that this was an unreplicated set of samples, there was an observed difference in the grain size that may be more than simple experimental error.

Table 7.2: Material data for second HC–2 factorial study.

Run order	Orifice diameter ($\times 10^{-3}$ in.)	Titanium conc. (mol/L)	Gold content (wt %)	Titania grain size (nm)	Gold grain size (nm)	Steady state pressure (psig)
1	115	0.10	-	12.8	13.5	100
2	75	0.50	-	14.7	20.6	450
3	115	0.10	-	14.8	16.7	100
4	75	0.50	-	14.3	15.0	530

7.2.3 Test of methanol to increase solution vapor pressure.

The throat cavitation number, shown in Equation 7.3, is an indicator of when cavitation will occur. In this equation, p is the upstream feed pressure, p_V is the vapor pressure of the process fluid, and u is the fluid velocity in the orifice (throat). Thus, the cavitation number represents the ratio of the pressure difference between the fluid pressure and its vapor pressure to the dynamic pressure across an orifice.

$$\sigma_T = \frac{p - p_V}{\frac{1}{2}\rho u^2} \tag{7.3}$$

An analysis of the cavitation number suggested that as the vapor pressure of the fluid being processed increases, the cavitation number decreases, and thus the likelihood of cavitation occurring increases [1,23,77]. (See also Chapter 3.) This might result in an intensification of the cavitational events by generating more bubble nuclei.

Therefore, an attempt was made to increase the vapor pressure of the system by replacing most of the water in the precipitating solution with methanol, which has approximately five times the vapor pressure of water at 25 °C. The synthesis was performed with a solution feed rate of 10 mL/min, an ammonium hydroxide concentration of 0.77 mol/L, and an orifice diameter of 0.073 inches. Unfortunately, x-ray analysis indicated that the gold crystallite size at 400 °C was 16.0 nm and that the titania grain size was 15.8 nm, which are within the ranges of the previous experiments. Thus, the addition of methanol had no effect on the synthesis.

7.2.4 Factorial study on orifice size, order of addition of titania and gold, and gold dilution volume.

Based on the results of the first two factorial designs, a third factorial study was performed using the HC–2. One of the factors was the orifice diameter, which was varied from 0.075 inches to 0.115 inches. The second factor was order of addition of gold and titania. In the previous studies, the gold and titania precursors were combined in the same solution which might somehow be inhibiting the size control of the gold. By precipitating either the gold followed by the titania and vice versa, it was hypothesized that the HC–2 might be able to influence the crystallite size without the interference of the other material. The third factor was the dilution of the gold solution from 50 mL to 100 mL to see if that has an effect on the grain size.

In addition, the co-precipitating agent, cetyltrimethylammonium chloride, was changed to hydrazine; thus, no ammonium hydroxide was required for the gold precipitation. Furthermore, hydrazine was shown independently to give an immediate reduction of the chloroauric acid to gold. The hydrazine was placed in a 100 mL aqueous solution at a concentration to maintain a hydrazine to gold ratio of 16.7 and co-fed with the gold solution. Since the gold solution volume changed, a constant gold solution feed rate of 4 mL/min was maintained, while the hydrazine solution feed rate was adjusted so that both solutions were added over equal time periods. The feed rate of the 0.88 mol/L solution (100 mL) was kept constant at 4 ml/min.

Table 7.3: Material data for third HC–2 factorial study.

Run order	Orifice diameter ($\times 10^{-3}$ in.)	Volume of Au soln. (mL)	First material precipitated	Titania grain size (nm)	Gold grain size (nm)
1	75	50	Au	10.7	63.6
2	75	50	TiO_2	12.5	78.6
3	115	100	TiO_2	11.7	54.7
4	75	100	TiO_2	11.6	33.6
5	115	50	TiO_2	14.3	43.7
6	115	50	Au	15.0	44.6
7	115	100	Au	12.8	41.7
8	75	100	Au	12.5	35.4

The experimental design, including the gold and titania crystallite size results, is shown in Table 7.3. After careful analysis of these data, it was determined that there was no significant effect on the anatase crystallite size, as in previous studies, with the mean crystallite size being 12.6 ± 1.2 nm. However, there was a statistically significant effect on the gold crystallite size, with a correlation with inverse gold grain size giving the best result.

If we assume that the metal particles are roughly hemispherical in shape, then the metal surface area is simply $\frac{1}{2}\pi D^2$. The mass of a metal cluster would then be $\frac{1}{2}\rho(\frac{\pi}{6}D^3)$, where ρ is the density of the metal. The surface area per mass of metal, S, is the ratio of these two terms, as shown in Equation 7.4.

$$S = \frac{\pi D^2}{\frac{\pi}{6}\rho D^3} = \frac{6}{\rho D} \tag{7.4}$$

However, the metal surface area per gram of metal can also be expressed as the dispersion (fraction of atoms exposed), times the number of atoms in the sample,

times the average surface area per atom of metal, S_m, as shown in Equation 7.5.

$$S = \left(\frac{\%\text{dispersion}}{100}\right)\left(\frac{6.023 \times 10^{23}\,\frac{\text{atoms}}{\text{mol}}}{\text{MW}\,\frac{\text{mass}}{\text{mol}}}\right)\left(S_m\,\frac{\text{area}}{\text{atoms}}\right) \tag{7.5}$$

Setting both of these definitions of metal surface equal to one another results in Equation 7.6, where K is a collection of constants.

$$\%\text{dispersion} = \frac{6K}{\rho D} \tag{7.6}$$

Thus, the inverse of the grain size makes physical sense, as this is directly related to the dispersion, or amount of metal exposed, on the surface of a catalyst.

Figure 7.1 shows the normal probability plot of the factors and interaction terms for inverse gold crystallite size. It is very obvious that the volume of gold solution and the interaction of orifice size and gold solution volume deviate significantly from the line produced by the other effects. Based on this result, a hierarchical model consisting of the linear combination of gold solution volume V (mL), the orifice diameter D_o ($\times 10^3$ inches), and their interaction term was chosen.

This model (see Equation 7.7) was analyzed, and shown to be statistically significant with a P-value of 0.0149, which means that approximately 98.51% of the time, the overall model would be significant.

$$\frac{1}{D} = -0.047 + (9.070\times10^{-4})V + (6.138\times10^{-4})D_o - (8.152\times10^{-6})D_oV \tag{7.7}$$

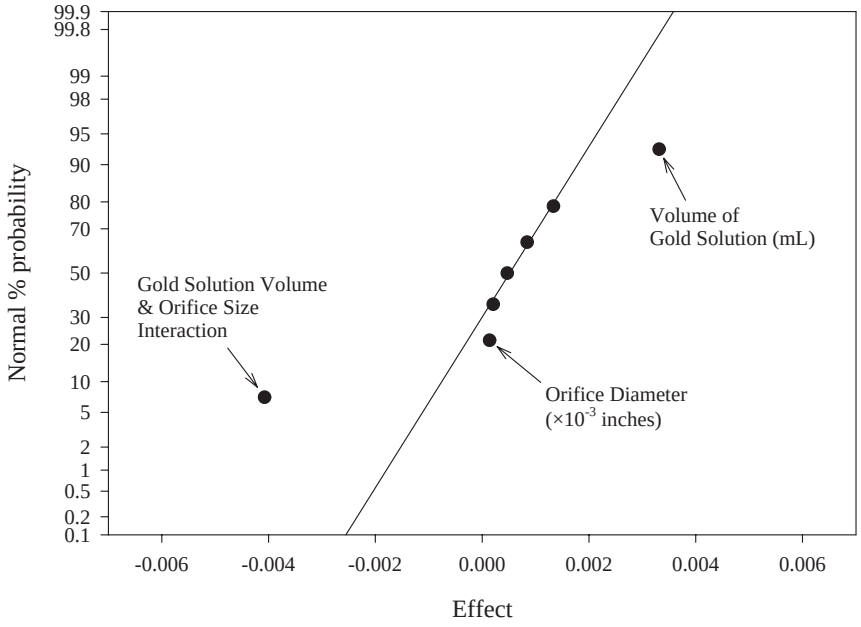

Figure 7.1: Normal probability plot of third HC–2 factorial design effects for inverse gold crystallite size.

Table 7.4: ANOVA for inverse gold crystallite size model.

Source	Sum of Squares	DF	Mean Square	F Value	Prob > F
Model	0.000220984	3	7.36615E-05	13.3964	**0.0149**
Residual	2.19944E-05	4	5.49861E-06		
Cor Total	0.000242979	7			
Root MSE	0.00234491		R-Squared	0.90948	
Dep Mean	0.0217529		Adj R-Squared	0.84159	
C.V.	10.7797		Pred R-Squared	0.63792	
PRESS	8.79778E-05		Adeq Precision	8.91518	Desire > 4
Factor	Coefficient Estimate	DF	Standard Error	t for H0 Coeff=0	Prob > |t|
Intercept	0.0217529	1	0.000829052		
V - Gold soln. volume	0.00331526	1	0.000829052	3.99886	**0.0161**
D_o - Orifice Diameter	0.000138845	1	0.000829052	0.167475	**0.8751**
Interaction ($D_o \times V$)	-0.00407588	1	0.000829052	-4.91632	**0.0080**

The ANOVA table for this model is shown in Table 7.4. From this table, it is clear that both the gold solution volume and the interaction of gold solution volume with orifice diameter are significant, having P-values less than 0.05. However, the orifice diameter term itself is not very significant, having a P-value of 0.8751. The adjusted R^2 of this model is 0.8416, which suggests that the model produced from the eight data points can be expected to predict gold crystallite size correctly about 84% of the time. A normal plot of the studentized residuals, shown in Figure 7.2, also demonstrates that this model adequately predicts the experimental data.

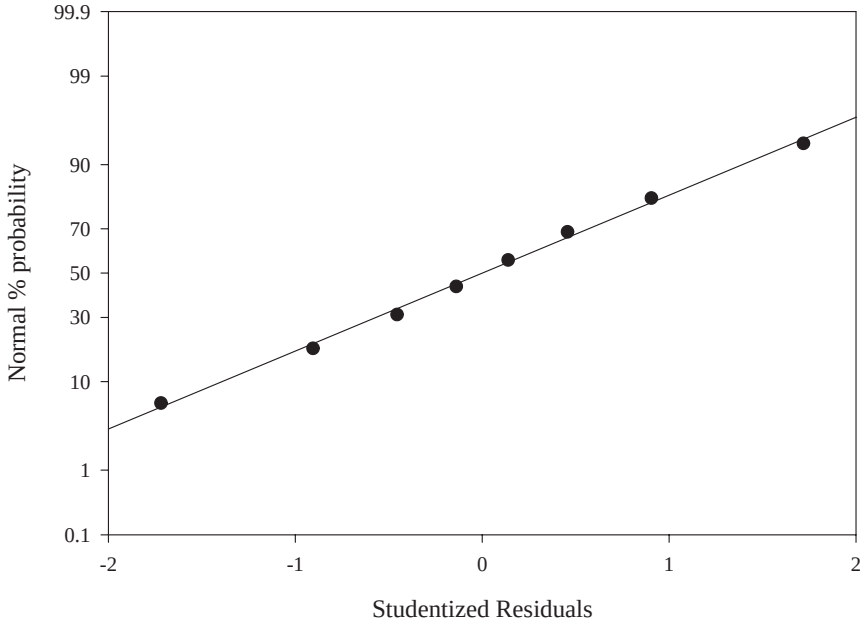

Figure 7.2: Normal probability plot of third HC–2 factorial design studentized residuals for inverse gold crystallite size.

7.2.5 Investigation of gold solution volume effect.

In all DOE studies, it is necessary to verify the models produced. Since the order of addition did not appear to be very significant, the order was fixed at precipitating the titania first, followed by the gold. To test this model, the orifice diameter was also fixed at 0.075 inches. Two of the third factorial study experiments were run under these settings, so the model was extrapolated at this orifice setting. Three additional experiments were performed with gold solution volumes of 200, 400, and 1000 mL to determine if the trend predicted by the DOE model would hold true. For each experiment, the gold solution feed rate was maintained at 4 mL/min and the hydrazine feed rate was adjusted to ensure that the hydrazine solution ended at the same time as the gold solution (*e.g.* for the 1000 mL experiment, the hydrazine flow rate was 0.4 mL/min).

Table 7.5 shows the data for the five experiments performed with the 0.075 inch orifice at different gold solution volumes. It appears that the gold crystallite size definitely decreases as the solution volume increases. A plot of inverse crystallite size versus gold solution volume, shown in Figure 7.3, demonstrates that qualitatively the model from the third factorial study was correct, although some experimental variation was present in the low volume data. The gold mean crystallite size of 7.5 nm, obtained from the 1000 mL experiment, is the smallest obtained so far for all samples synthesized with approximately 2% gold. Although the elemental analysis is not available to confirm this, the fact that the gold peaks are visible in the XRD patterns suggests that a significant amount of gold is present.

The total run time for these experiments with a gold feed rate of 4 mL/min is

Table 7.5: Data for extended gold solution volume study with the HC–2 using a 0.075” orifice.

Gold conc. (mol/L)	Volume of Au soln. (mL)	Au soln. feed rate (mL/min)	Au molar feed rate (mol/min)	H_2NNH_2 feed rate (mL/min)	Titania grain size (nm)	Gold grain size (nm)
0.0145	50	4.0	5.80×10^{-5}	8.0	12.5	78.6
0.0073	100	4.0	2.90×10^{-5}	4.0	11.6	33.6
0.0036	200	4.0	1.45×10^{-5}	2.0	11.4	27.9
0.0018	400	4.0	7.25×10^{-6}	1.0	12.0	16.0
0.0007	1000	4.0	2.90×10^{-6}	0.4	12.9	7.5

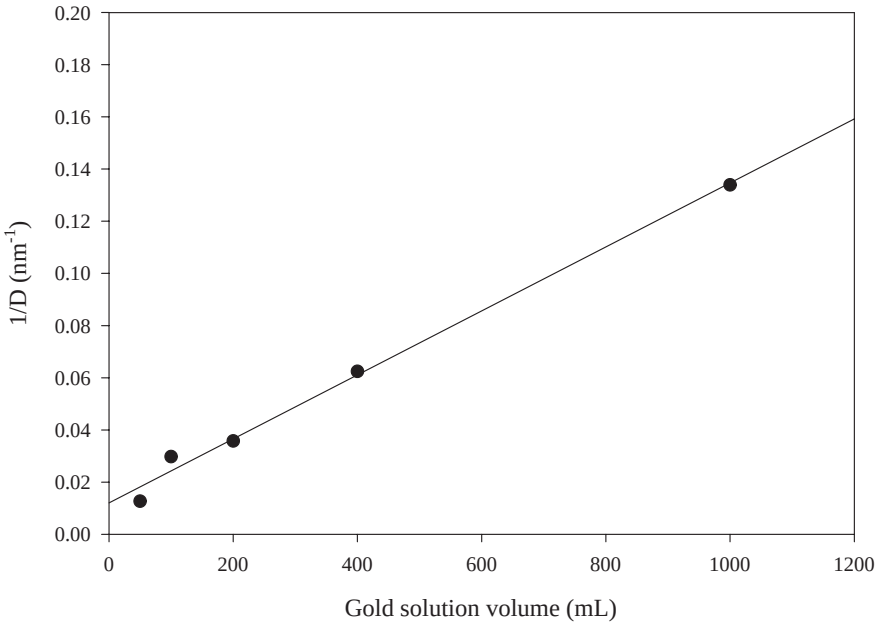

Figure 7.3: Inverse gold crystallite size model test experiments at different gold solution volumes.

not convenient for the even larger volumes required to obtain 2 nm gold particles, which would also exceed the processing volume of the HC–2; and the lower hydrazine flow rates would be difficult to control. For example, to synthesize a 2 nm gold catalyst would require a gold solution volume of approximately 4 L, with a hydrazine feed rate of approximately 0.1 mL/min, for a total experimental time of approximately 17 hours. Depending on the diameter of the tubing used for the feed pumps, the lower flow rate limit varies between 0.4 and 1.3 mL/min. Another major concern for an experimental run of this length would be the difficulty in adequately controlling the temperature during the experiment with an ice bath.

Thus, six additional experiments were performed to see if the same results could be obtained with only 30 minutes of titania synthesis time and 30 minutes of gold processing time. The first three experiments were performed with gold solution volumes of 100, 400, and 1000 mL with the 0.075 inch diameter orifice, but with the feed rates adjusted so that the total gold processing time was approximately 30 minutes. The second three experiments were repeats of the first three, except that they were performed in a stirred beaker, without the HC–2 (*i.e.* "classical" experiments).

The results for these six experiments are shown in Table 7.6. From these data, it appears that changing the gold solution volume had no effect on the gold grain size. A comparison between these data and the previous five experiments is shown in Figure 7.4. One feature of these data which is somewhat disturbing is the poor reproducibility of the 100 mL experiments. In the initial series, the gold crystallite size was 33.6 nm, yet in the constant time series, the 100 mL experiment performed

Table 7.6: Data for constant processing time experiments with the HC–2 using a 0.075” orifice (H) and a classical setup (C).

Method	Gold conc. (mol/L)	Au soln. volume (mL)	Au soln. feed rate (mL/min)	Au molar feed rate (mol/min)	H_2NNH_2 feed rate (mL/min)	Titania grain size (nm)	Gold grain size (nm)
H	0.0007	1000	40	2.90×10^{-5}	4.0	11.0	15.1
H	0.0018	400	16	2.90×10^{-5}	4.0	11.4	15.7
H	0.0073	100	4.0	2.90×10^{-5}	4.0	12.9	17.3
C	0.0007	1000	40	2.90×10^{-5}	4.0	15.4	23.2
C	0.0018	400	16	2.90×10^{-5}	4.0	12.3	25.4
C	0.0073	100	4.0	2.90×10^{-5}	4.0	12.1	29.8

in exactly the same manner produced a grain size of 17.3 nm. This suggests that either there is a large grain size variation at the lower solution volumes, which can be partially seen in the 50 mL and 100 mL volume experiments, or that there are other factors which are responsible for this result.

One possibility is that processing time and not the solution volume or concentration is the dominant factor in the results shown in Figure 7.3. It is known that for hydrodynamic cavitation, the number of processing passes through a device can achieve different results, and as the processing time increases, so does the number of passes through the machine [138]. As a result, the data in Figure 7.4 are replotted in Figure 7.5, as a function of gold processing time.

Although Figure 7.5 does not help to determine why the two sets of constant time experiments are different from the original variable time experiments, it is clear that there is a significant difference between using the HC–2 and performing the identical experiment in a classical setup. This suggests that the hydrodynamic

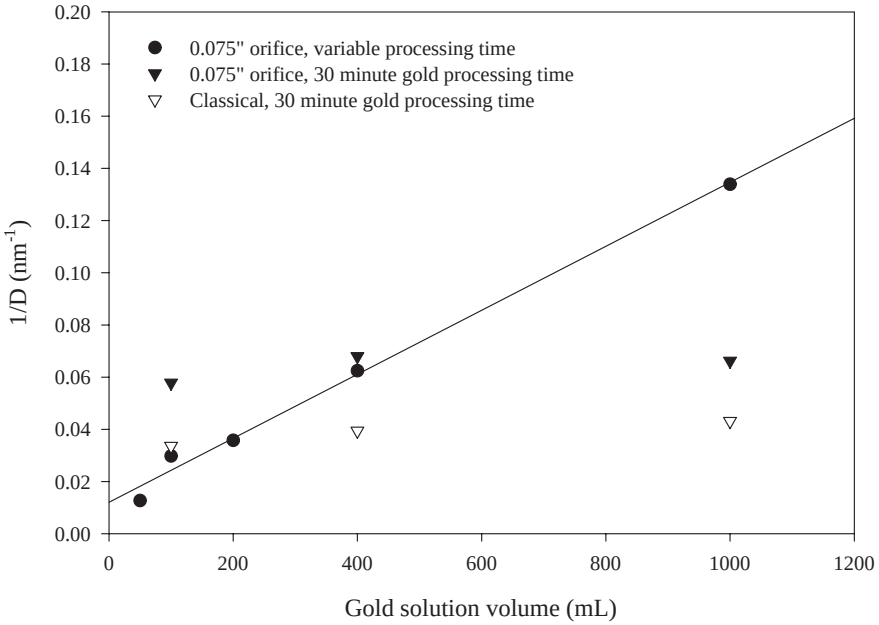

Figure 7.4: Inverse gold crystallite size test experiments comparing variable time HC–2 samples with constant processing time HC–2 runs and constant time classical experiments.

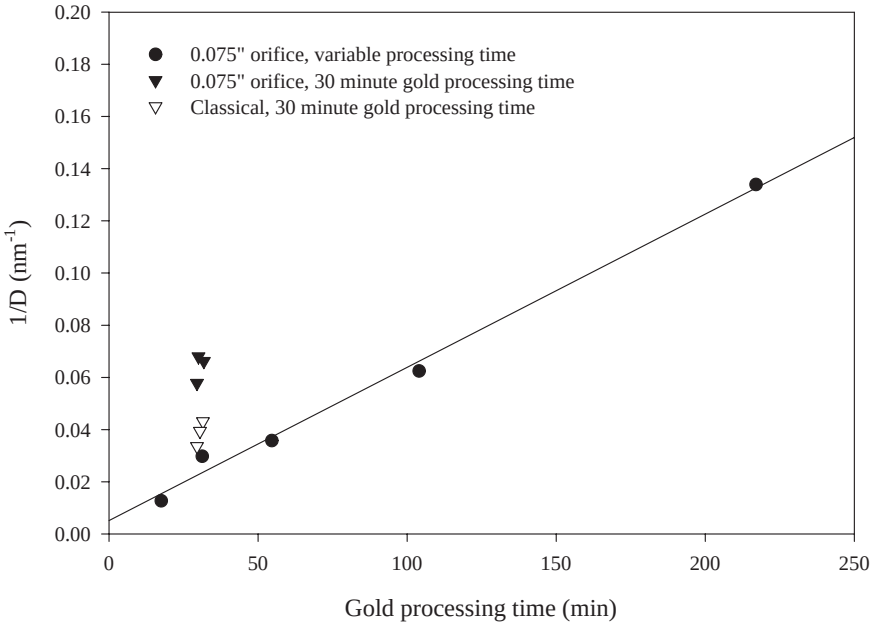

Figure 7.5: Inverse gold crystallite size as a function of gold processing time in the HC–2 or in a classical setup.

cavitation produced by the HC–2 is having some influence on the gold crystallite size. Since the data for the two sets of constant time experiments are very similar, one or more of the factors which were kept constant during those runs may be interacting with the processing time to produce the unexpected results. For example, the total molar feed rate of gold and the volumetric feed rate of the hydrazine were constant during these experiments, although they varied in the original volumetric experiments.

7.2.6 Investigation of processing time

To investigate the effect of processing time within the HC–2, two additional syntheses were performed using a 100 mL gold solution with gold and hydrazine solution flow rates of 4 mL/min in the HC–2. The orifice diameter was fixed at 0.075 inches to compare with previous results. The two syntheses were performed at gold processing times of 116 and 210 minutes. The 116-minute synthesis resulted in a gold mean crystallite size of 18.8 nm, and the 210-minute synthesis yielded a 39.7 nm grain size.

Figure 7.6 shows these experiments, as well as two additional syntheses under the same conditions, plotted as a function of gold processing time. There appears to be a large variation in the experimental data which suggests that gold processing time is not the major factor in the control of gold crystallite size. It is possible that hydrazine concentration or gold and hydrazine rates of addition may be responsible for the previous experimental results with this system.

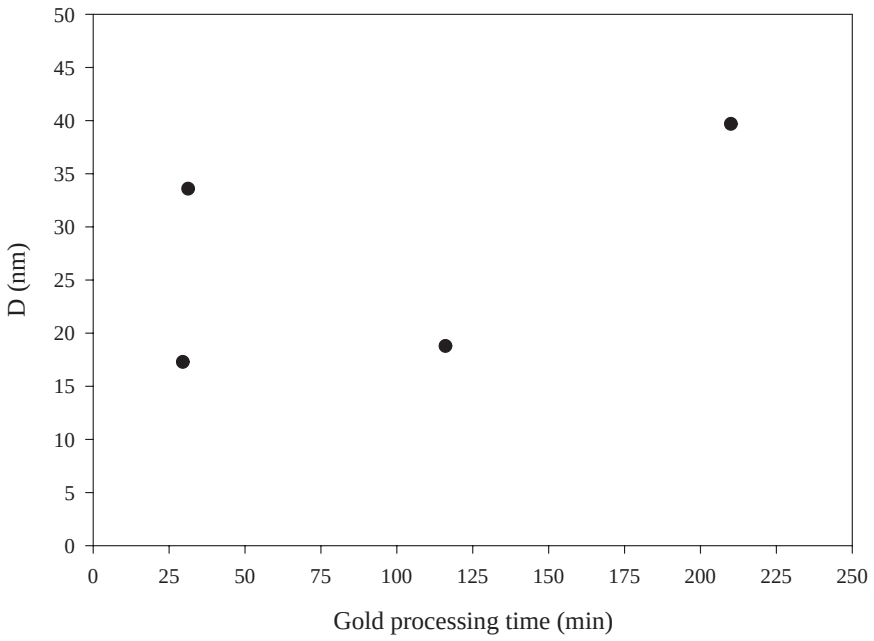

Figure 7.6: Mean gold crystallite size versus gold processing time in the HC–2 (100 mL gold solution; 4 mL/min feed rate; 0.075” orifice).

7.2.7 Hydrazine molar feed rate

Given that processing time is not the controlling factor, the possibility that the hydrazine feed rate might be a controlling variable for gold crystallite size was investigated. Figure 7.7 shows all experiments described so far in the HC–2 using the 0.075 inch orifice with hydrazine, including the results from Section 7.2.8 discussed below. It appeared from this figure that there was a weak trend of decreasing gold crystallite size with decreasing hydrazine molar feed rate, although there also appeared to be a large variation in grain sizes for similar feed rates.

Thus, two experiments were performed at low hydrazine feed rates: 4.5×10^{-5} mol/min and 1.1×10^{-5} mol/min. Unfortunately, the gold crystallite sizes for these two runs were 27.9 nm and 31.4 nm, respectively. These results are plotted with the data from Figure 7.7 in Figure 7.8, and show that the molar feed rate of hydrazine does not really control the gold crystallite size. Furthermore, analysis of the molar feed rate of gold and various combinations of the two feed rates (such as their product), yield the same conclusion as for the hydrazine feed rate.

7.2.8 Factorial study on cavitation number and hydrazine/gold ratio

To further elucidate the variables which might control gold crystallite size, given the results to this point with hydrazine reduction, a forth factorial study was performed on the HC–2. In this study there were only two factors: the throat cavitation number and the hydrazine to gold ratio. The initial volume of water used for the experiments

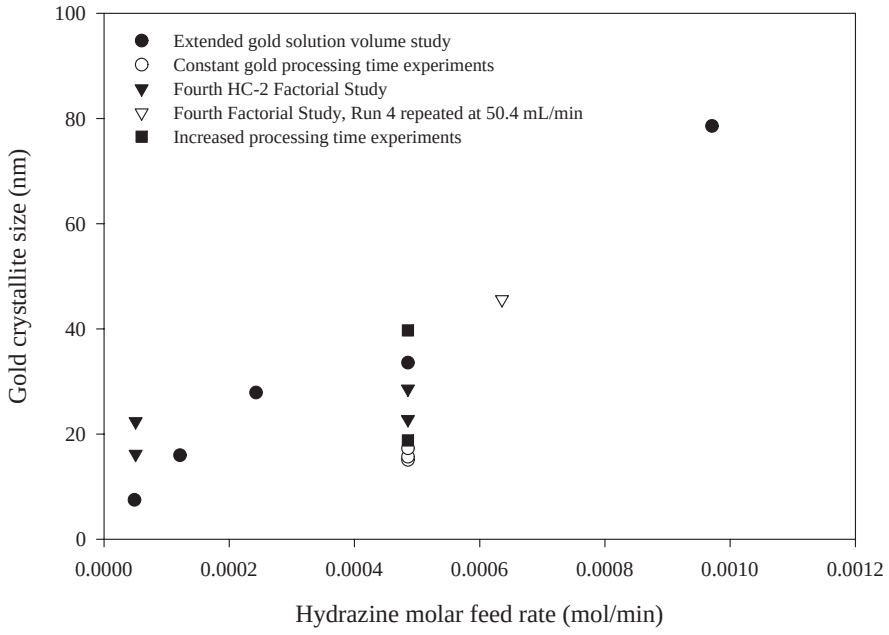

Figure 7.7: Gold crystallite size versus hydrazine molar feed rate for all gold experiments performed with the 0.075” orifice.

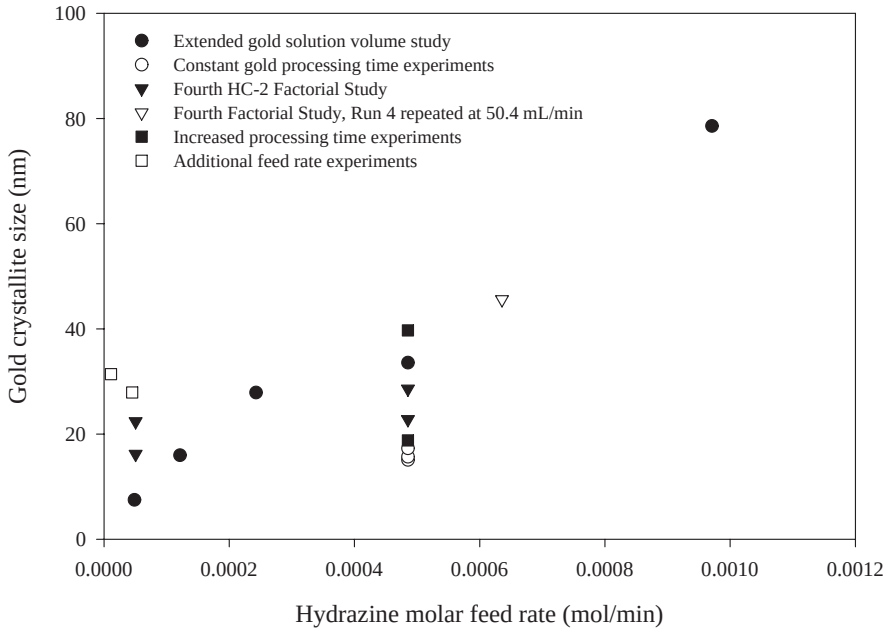

Figure 7.8: Gold crystallite size versus hydrazine molar feed rate for the 0.075” orifice, including additional hydrazine feed rate experiments.

was increased to 1000 mL, in contrast to previous experiments where only 650 mL of water was used. It was hoped that this might help reduce experimental variability due to turbulence on the surface of the HC–2 feed vessel. In addition, the feed rates of the gold and hydrazine solutions were fixed at 4 mL/min.

The cavitation number was varied from 1.04 to 1.39 (0.115" & 0.075" orifices) and the hydrazine/gold ratio was set at either 1.74 or 16.7. Both hydrazine/gold values are still above the stoichiometric ratio required for total reduction (0.75), and therefore a change in this ratio would examine the possibility that the amount of excess hydrazine might affect the rate of gold reduction. Due to the nature of the fixed flow rate pump on the HC–2, a change in the orifice diameter results in both a change in the Reynolds number *and* the throat cavitation number. Thus, a change in the cavitation number in this study essentially reflects a change in the only machine parameter on the HC–2, the orifice.

The experimental design consisted of eight experiments at four different run conditions. The replication at each condition allows a better interpretation of the data to compensate for the experimental response variation exhibited in previous experiments. The data for this study are given in Table 7.7.

The analysis of the titania grain sizes again showed no significant trends as in previous experiments. However, a statistical analysis of the gold crystallite size data showed that the cavitation number was a significant factor, and that the hydrazine/gold ratio, and thus the concentration of the hydrazine, made no difference. This is also in agreement with the hydrazine feed rate experiments. Furthermore, the gold crystallite sizes observed in this study reinforces the observation that hy-

Table 7.7: Material data for fourth HC–2 factorial study.

Run order	Throat cavitation number	Hydrazine to gold ratio	Titania mean crystallite size (nm)	Gold mean crystallite size (nm)
1	1.39	1.74	10.6	16.2
2	1.04	16.7	13.2	29.5
3	1.39	16.7	11.4	22.8
4	1.04	1.74	12.3	34.5
5	1.04	16.7	13.0	32.5
6	1.39	1.74	12.4	22.4
7	1.04	1.74	12.2	38.3
8	1.39	16.7	11.8	28.6

drazine reduction results in large grain sizes compared to ammonium hydroxide coprecipitation with CTMA-Cl (Sections 7.2.1–7.2.3).

The statistical analysis indicated that by increasing the cavitation number, the gold grain size was decreased. This might suggest that there is increased mixing when the orifice size is decreased to 0.075 inches, as the Reynolds number increases with decreasing orifice size from 94664 (0.115” orifice) to 145151 (0.075” orifice). The correlation was not very strong, however (R^2 = 0.68), indicating that there may be other extraneous factors at work for this system.

7.2.9 Reinvestigation of alternative precipitation agents

Based on the wide range of results produced by the use of hydrazine reduction, the use of other precipitating agents to produce titania supported gold catalysts was re-investigated. The average grain size of hydrazine reduced gold is approximately 32 nm, whereas the use of coprecipitation with ammonium hydroxide yielded

a mean gold grain size of approximately 16 nm for the same theoretical gold loading. Therefore, four different titania supported gold samples were classically synthesized by first precipitating the gold under dilute conditions (1000 mL) using ammonium hydroxide, sodium hydroxide, potassium hydroxide, and ammonium carbonate. This would lead to the formation of a gold colloid prior to the formation of the titanium hydroxide, which might interfere in determining the best aqueous base to investigate further.

For each synthesis, 2 mL of a 2 mol/L base solution was added to the chloroauric acid solution and allowed to stir for two minutes. Titanium hydroxide was precipitated separately in a stirred beaker and then added to the gold solution at the end of the two minutes. The total gold/titania slurry was then stirred for one hour before filtration and water washing. The x-ray analysis results for each sample after calcination are shown in Table 7.8. Due to the low classical gold grain sizes, it would appear that any one of the hydroxide bases would serve as a better starting point for gold crystallite size reduction using hydrodynamic cavitation compared to the previous experimental approaches.

Table 7.8: Grain size results for the classical synthesis of 2% gold on titania using different aqueous 2 mol/L bases.

Base (2 mol/L)	Titania mean crystallite size (nm)	Gold mean crystallite size (nm)
NH_4OH	12.1	11.3
NaOH	9.6	10.2
KOH	10.0	10.0
$(NH_4)_2CO_3$	13.4	14.8

7.2.10 Orifice studies with ammonium hydroxide & sodium hydroxide produced colloids

Initial ammonium hydroxide orifice study with the HC–2

Based on the scoping studies just described, a series of experiments was undertaken to form a gold colloid in the HC–2 using ammonium hydroxide. In each experiment, a 1000 mL solution of gold was placed in the HC–2 and 2 mL of a 2 mol/L ammonium hydroxide solution was added to form a gold colloid, the presence of which was verified by laser light scattering from a laser pointer. After five minutes of recirculation, a classically precipitated titanium hydroxide slurry was added to the gold colloid and the combined slurry was recirculated for an additional 25 minutes. The final solution pH for each synthesis was between 4 and 5. The orifice diameter was changed to four different sizes to see if the grain size of the gold particles could be altered by changes in hydrodynamic conditions.

Figure 7.9 shows the crystallite size results for the gold and anatase after each sample had been calcined to 400 °C. As expected from previous experiments, the grain size of titania did not vary appreciably for the different orifices. However, there were some interesting variations in the grain size of the gold.

For the 0.075 inch orifice, there was no gold peak visible in the calcined sample, indicating that either there was an extremely low gold content in the sample, or that the crystallite size was small enough to have become sufficiently broad as to not be visible. This would indicate that the gold crystallite size might be less than 4.5 nm. For the 0.095 inch orifice synthesis, the grain size was between the measured value

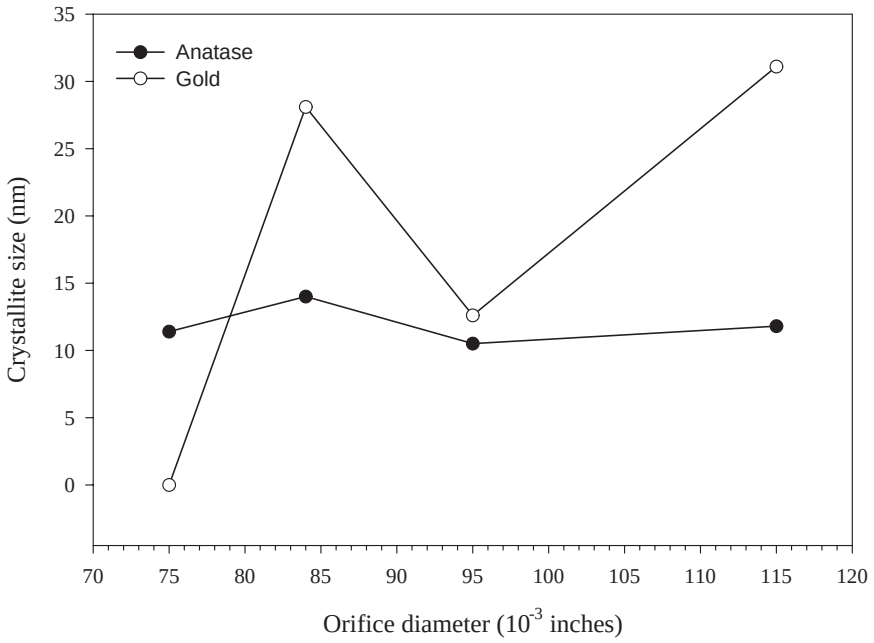

Figure 7.9: Initial gold colloid with ammonium hydroxide experiments where the orifice diameter in the HC–2 was changed and the final system pH was between 4 and 5.

for the 0.075 inch and the 0.084 inch orifices, suggesting that there might be a large experimental variation from experiment to experiment. However, the 0.095 inch synthesis was the second synthesis performed in the HC–2, and further examination revealed that the crystallite size increased in the order of synthesis.

This increase in crystallite size with the order of experimentation suggested two possibilities: (1) the ammonium hydroxide solution might not have been stable, as it was an older solution and this was causing the variation; or (2) the amount of time a sample was left to dry out in the air before being placed in the oven to dry at a higher temperature was affecting the grain size. This second possibility might be important, because as syntheses were performed, it was standard practice to leave the samples on a watch glass until all samples were synthesized before placing them into the oven to dry overnight. To eliminate the effects of slow ammonium hydroxide or gold complex evaporation, it was decided to perform a series of experiments using sodium hydroxide. In order to investigate the effect of drying, it was decided to split each sodium hydroxide synthesis into two batches, one where the sample was air dried only, and one where the sample was placed into an oven immediately after filtration.

Sodium hydroxide orifice study & investigation of drying effects

The synthesis of each sample for the sodium hydroxide study was identical to the procedure described for the ammonium hydroxide syntheses above. The only exceptions were that 2 mL of a 2 mol/L sodium hydroxide solution was used and that the final filtered samples were split in half for air drying and oven drying. The

pH of the gold colloids after addition of the sodium hydroxide was approximately 6.8. After the addition of the titanium hydroxide slurry, the pH of the system dropped to 5.

Figures 7.10 & 7.11 show the crystallite sizes for the gold and titania syntheses calcined to 400 °C, respectively. From Figure 7.10, it appears that for the oven dried samples, there is no large change in gold crystallite size with a change in orifice diameter. However, it would appear that air drying results in a greater variability in grain size after calcination, as evidenced by the 17.1 nm result for the 0.115 inch orifice. This larger variability may be the reason for factorial studies performed on the 0.075 inch and 0.115 inch orifices which showed that the orifice size had a statistically significant effect but could not explain much of the response variation (see Section 7.2.8).

As shown in Figure 7.11, direct oven drying also appears to reduce the crystallite size of the anatase compared to air drying by approximately 4 nm. As in the case of the gold, there does not appear to be an appreciable effect due to changing the orifice diameter. Based on the anatase and gold results, it was concluded that immediate oven drying is preferred to any amount of air drying, as it leads to smaller titania crystallite sizes and less variability in the gold crystallite sizes. It was also concluded that there was no effect due to changing the orifice size in the HC–2 for the sodium hydroxide system, and thus additional ammonium hydroxide experiments were needed with direct oven drying to verify the results of the previous experiments for that system.

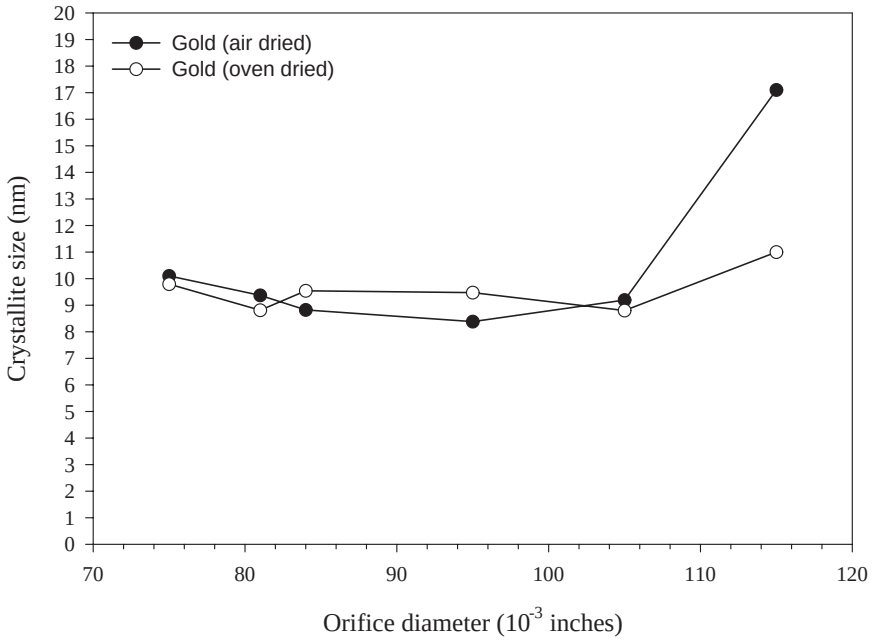

Figure 7.10: Gold crystallite size measurements for NaOH drying effect study with varying orifice size. The final pH for both air and oven dried samples was 5.

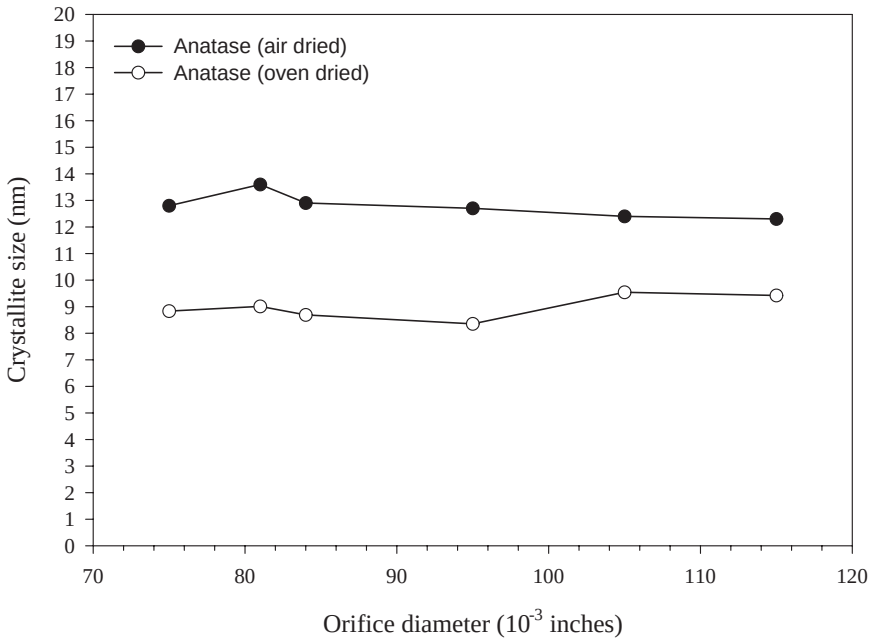

Figure 7.11: Anatase crystallite size measurements for NaOH drying effect study with varying orifice size. The final pH for both air and oven dried samples was 5. The differences in $Ti(OH)_4$ drying techniques resulted in an approximately 4 nm difference in grain size of the anatase.

Second ammonium hydroxide orifice study at a pH of 11

In this second ammonium hydroxide study, it was decided to use an excess of base in order to maintain a constant system pH for each synthesis. Thus, 250 mL of 2 M ammonium hydroxide was added to the 1000 mL gold solution, which made the gold colloid at a pH of 11. After five minutes of processing in the HC–2, 100 mL of titanium butoxide solution was added directly to the gold colloid and the combined solution was recirculated in the HC–2 for an additional 25 minutes. The pH was constant during all experiments at 11. At the end of each synthesis, the final filtered solid was immediately placed in an oven to dry overnight.

Initially, a classical synthesis was performed outside of the HC–2, and four syntheses were performed with the HC–2, using the new stainless steel 0.075 inch orifice, and the 0.084, 0.095, and 0.115 inch orifices. Based on these results, which are shown in Figure 7.12 along with all other results which were determined for this system, it appeared that the 0.075 inch orifice still might have had some ability to decrease the grain size of the gold, but that the other orifices had little effect. As a result, three additional syntheses were performed using the new 0.075 inch orifice: (1) a repeat synthesis where the gold colloid was formed first, followed by the titania precipitation, but with the back pressure on the HC–2 set at 300 psig using a downstream valve attachment for the HC–2; (2) a synthesis where no back pressure was applied, but where the titanium hydroxide was precipitated first, followed by a 25 minute addition of the 1000 mL solution; and (3) a synthesis where a 100 mL solution of gold and a 100 mL titanium butoxide solution were co-fed into the HC–2 with no back pressure applied.

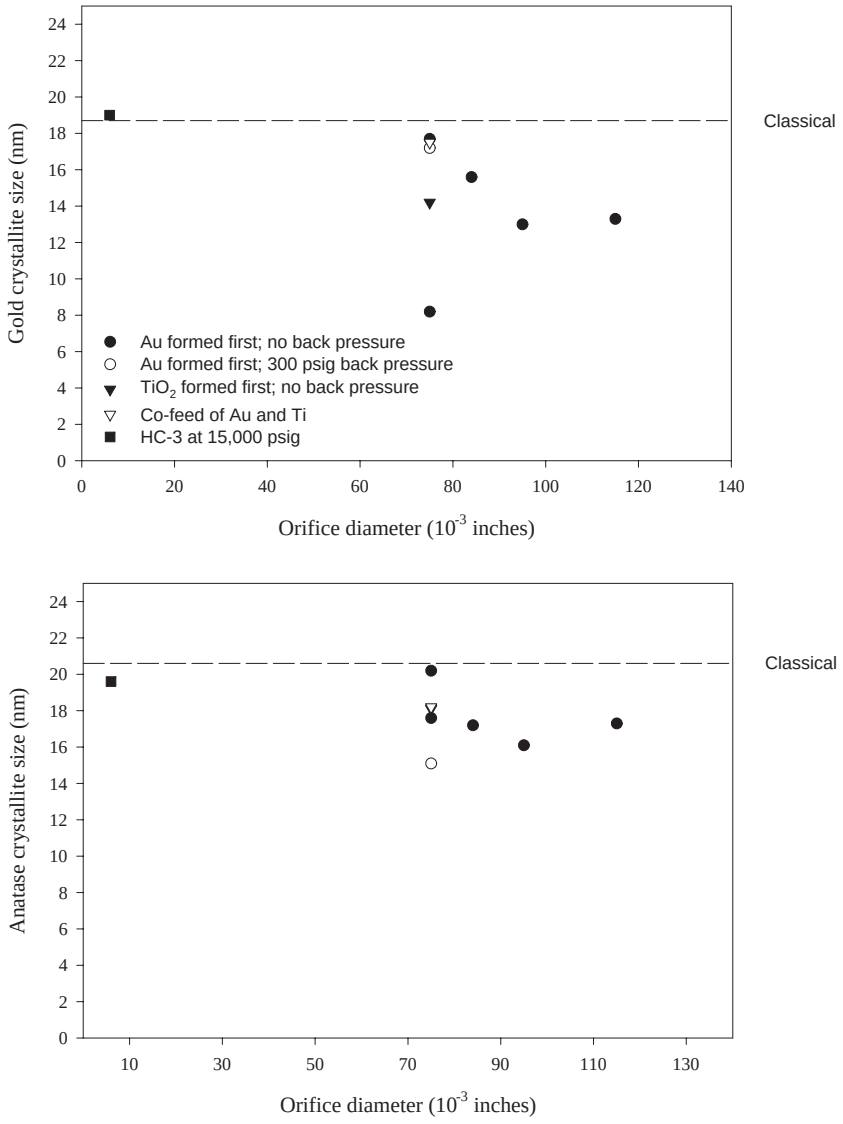

Figure 7.12: Crystallite size measurements for gold and anatase synthesized with excess ammonium hydroxide. The final pH of each system was 11 and all samples were oven dried immediately after filtration.

The results of all of these ammonium hydroxide syntheses are shown in Figure 7.12. When taken with the initial four syntheses in the HC–2, it would appear that there is a large experimental variation in the precipitation of gold using ammonium hydroxide, and that changing the conditions in the HC–2 has little effect on the crystallite size. The mean gold crystallite size for the initial ammonium hydroxide study described above plus all of the subsequent experiments performed for this study (a total of 11 samples performed in the HC–2) is 15.9 ± 5.2 nm, assuming the non-detectable peak from the first 0.075 inch sample was approximately 4.5 nm.

Two additional experiments were performed with the ammonium hydroxide system at a pH of 11. One was performed in the HC–2 with no back pressure using a new 0.075 inch orifice in an attempt to reproduce the 8.2 nm result. The other experiment was done in the HC–3 using the 6–14 orifice set at 15,000 psig, to determine if there would be differences between the HC–3 and the HC–2. The HC–3 is similar in concept to the HC–1 used for the gold concentration studies, using two orifices placed in series. Thus, the designation 6–14 implies the use of a 0.006 inch diameter orifice followed by a 0.014 inch orifice.

As shown in Figure 7.12, the HC–2 experiment did not reproduce the lower grain size result, and the HC–3 experiment yielded approximately the same crystallite size as the classical experiment. Thus, it would appear that neither device is capable of exerting influence over the gold crystallite size for this type of synthesis approach. Furthermore, it would appear that the reproducibility of the ammonium hydroxide synthesis is less than desirable, varying from approximately 9 to 19 nm.

7.3 Discussion

Using a design of experiments strategy, it was determined that hydrodynamic cavitation has no statistical effect on the crystallite sizes of either anatase or gold using the chemical system of ammonium hydroxide and CTMA-Cl *at a fixed gold content*. Thus, the only apparent control of the gold grain size for the coprecipitation from a combined solution of gold and titanium is the concentration of gold on the catalyst, as determined in Chapter 6. Altering the orifice size (and thus the system pressure, Reynolds number, and cavitation number); as well as solution feed rates, ammonium hydroxide concentration, gold and titanium feed dilution, and the vapor pressure of the system; has no effect on the gold grain size.

However, using the same statistical design of experiments approach, a different chemical system was investigated where the gold and titanium precursors were precipitated from separate solutions using hydrazine reduction. It was proved that by changing orifice diameter and gold solution concentration in the HC–2, different gold crystallite sizes could be obtained at a fixed gold concentration. The dispersion of the gold was statistically affected by changing the dilution volume of the gold for fixed flow rates, as well as the interaction of the HC–2 orifice diameter with the gold solution volume. The individual contribution of changing the orifice diameter was not statistically significant. Although typical hydrazine reduction results in a mean grain size of approximately 32 nm, using the approach of increasing the gold solution volume at a fixed orifice size (0.075 inch) and fixed gold feed flow rate (4 mL/min) allowed the systematic adjustment of the gold crystallite size from

approximately 80 nm to 8 nm. The grain size of anatase was not controllable by any factors examined in this system, which was consistent with the ammonium hydroxide/CTMA-Cl results.

Unfortunately, both the difficulty of regulating the extremely low hydrazine flow rates and the total solution volumes in the HC–2 required to extend this approach made continuing this gold grain size trend into the 1–10 nm range impractical. Thus, the various extraneous factors which could be leading to the observed grain size control were investigated to see if shorter processing times or lower solution volumes could reproduce these results. The effect of order of addition of the gold and titanium precursor solutions was found to be negligible. Furthermore, it was shown that changing the gold solution volume over a fixed time period had no effect on the gold crystallite size. But the results of the latter investigation did reveal that there was a definite difference between performing the synthesis in the HC–2 and in a stirred beaker ("classical" experiment). This suggests that the hydrodynamic cavitation and the resultant enhanced mixing present in the HC–2 is a contributing factor to the original gold dispersion trend.

The results of the constant time hydrazine reduction experiments did not agree well with the results of the inverse crystallite size model as a function of gold solution volume. Some possible factors which could have been interacting to produce these discrepancies were the processing time in the HC–2, the hydrazine flow rate, and the gold molar flow rate. However, it was found through additional experimentation that the alteration of the processing time in the HC–2 seemed to have no discernible effect on the gold grain size. Likewise, although there appeared

to be a weak trend with the reduction in the hydrazine molar feed rate, additional experimentation confirmed that both the hydrazine and gold feed rates had no direct control over the gold crystallite size.

The infeasibility to extend the inverse crystallite size experiments to larger gold solution volumes (and consequently very low hydrazine addition rates) combined with the inability to find a controllable process variable such as a time, volume, or flow rate; necessitated the further investigation of additional chemical systems. Thus, the concept of producing a gold colloid in a hydrodynamic cavitation environment prior to the influence of titania precipitation was investigated. Initial "classical" scoping studies with four different bases showed that it was possible to start off with a grain size of 10–15 nm using this approach.

A series of orifice studies were performed using the gold colloid formation technique to see if the HC–2 could alter the gold crystallite size prior to the introduction of titania into the system. In an initial ammonium hydroxide study at a pH of 5, it was suspected that there was a trend with decreasing orifice size leading to smaller gold grain sizes. However, the variability in this trend from orifice to orifice was too large. Further examination of the data suggested that the grain size variation was correlated with the amount of time samples were allowed to "air dry" prior to drying in an oven. Subsequent experimentation with sodium hydroxide confirmed that air drying lead to variability in gold grain size results. However, two additional empirical facts were observed: changing the orifice size was ineffective in controlling the gold grain size, and varying the drying method resulted in a difference in the final grain size of the titania. Even further experimentation

showed that there appeared to be no real effect on varying the orifice size in the ammonium hydroxide system, although the variability in the ammonium hydroxide system was still vary large. Nevertheless, a difference between "classical" synthesis and hydrodynamic cavitational processing was observed, as in the case of the hydrazine experiments.

For a fixed theoretical gold loading of 2% on titania (anatase), the use of ammonium hydroxide leads to mean gold grain sizes of 15.9 ± 5.2 nm, whereas the use of hydrazine reduction results in mean crystallite sizes of 32.2 ± 14.6 nm. It is possible to control the grain size in the hydrazine system, within equipment limitations, between approximately 8 and 80 nm by varying the gold solution volume for a fixed feed rate in the HC–2. However, individual physical processing variables cannot be adjusted to move outside of this range and into the desired region of 1–10 nm. The use of ammonium hydroxide leads to a wider variability in grain size results at identical conditions compared to hydrazine reduction, presumably through a sensitivity to drying conditions. In addition, the use of hydrodynamic processing appears to give smaller grain size results than the equivalent "classical" experiments whether hydrazine or an aqueous base is being used.

7.4 Conclusions

Low pressure hydrodynamic cavitation (less than 700 psig) had little or no effect on gold crystallite size for most chemical systems. However, by changing the system chemistry to hydrazine reduction of the gold, a synergy existed between the dilution

of the gold precursor solution, the orifice diameter, and the reducing agent addition rate. Individually, these factors had little effect and only their interaction allowed gold grain size control in the range of 8–80 nm.

The experiments performed with low pressure hydrodynamic cavitation lead to the conclusion that the chemistry of the system (*i.e.* pH, concentration, chemical environment) appears to be the dominant factor for the synthesis of titania supported gold, although hydrodynamic cavitation appears to have a small, secondary role. Due to the variability exhibited in the ammonium hydroxide system, it seems that a chemical modification of the hydrazine system offers the best opportunity to allow the synthesis of gold in a grain size range of 1–10 nm. This grain size region is where the greatest CO oxidation activity is expected to occur. Therefore, the next chapter will explore this approach of modifying the hydrazine reduction of gold.

Chapter 8

Synthesis of Titania Supported Gold with the HC–3 using Hydrazine Reduction under Basic Conditions

8.1 Introduction

The factorial studies described in Chapter 7 clearly show that the chemical environment is the controlling force for the synthesis of titania supported gold at a fixed gold concentration. Based on a review of the chemical approaches used so far, the system of hydrazine reduction under basic conditions was chosen to further explore the effects of hydrodynamic cavitation. Until this point, it appeared that hydrodynamic cavitation played a secondary role to the chemistry of the system, showing some differences in grain sizes when the same synthesis was carried out

under cavitational conditions versus standard "classical" experiments. In addition, the only adjustable parameters on the HC–2, orifice diameter and back pressure, failed to exhibit any controllable influence on crystallite size. Therefore, the new chemical system of reduction under basic conditions was explored using another cavitational device introduced at the end of Chapter 7, the HC–3. It was assumed that the more adjustable parameters of the HC–3: orifice size, number of orifices, and pressure; would lead to a higher degree of control over the gold grain size.

When titanium (IV) butoxide ($Ti[O(CH_2)_3CH_3]_4$ or $Ti(OBu)_4$) dissolved in isopropyl alcohol for stability, is added to water, a titanium hydroxide is formed, as well as butyl alcohol (BuOH).

$$Ti(OBu)_4 + 4H_2O \rightarrow Ti(OH)_4 + 4BuOH \tag{8.1}$$

As a result, the pH of the system has been observed to drop to between 4 and 5 due to the presence of the titanium hydroxide gel reacting with water and the butyl alcohol. The reduction of chloroauric acid ($HAuCl_4 \cdot 3H_2O$), with hydrazine (N_2H_4) in an aqueous environment results in the production of hydrochloric acid and nitrogen gas.

$$4HAuCl_4(aq) + 3N_2H_4(aq) \rightarrow 4Au(s) + 16HCl(aq) + 3N_2 \uparrow \tag{8.2}$$

Thus, the generation of hydrochloric acid also contributes to dropping the system pH during reduction. Therefore, the inherently acidic nature of the precipitation approach used so far may partly explain the inability to synthesize catalysts with

a mean gold grain size less than 7.5 nm.

Haruta's group looked at the effect of pH on precipitation-deposition of gold onto titania using sodium hydroxide [27, 29]. What they observed was that acidic conditions lead to larger gold particles than basic conditions. Above a pH of 6, the gold in solution is converted from $AuCl_4^-$ to a gold chloride/hydroxide complex ($Au(OH)_nCl_{4-n}$, $n = 1$–3). This gold complex eventually forms $Au(OH)_3$ on the surface of the titania. The solubility of this gold hydroxide also changes when the pH increases above 6. The combination of changes in the gold complex and the solubility of the gold hydroxide lead to the formation of smaller gold particles on the final catalysts.

Haruta's pH behavior is consistent with the observed large gold crystallite sizes when gold is reduced with hydrazine (32.2 ± 14.6 nm) in this thesis. Therefore, it was proposed that the direct reduction of the chloroauric acid with hydrazine results in larger grain gold sizes due to the fluctuation of pH into the more acidic regions during synthesis. When aqueous bases, such as ammonium hydroxide, are used, the gold crystallite sizes are on average smaller for a fixed gold concentration (*e.g.* 15.9 ± 5.2 nm), presumably due to the basic nature of the synthesis.

This hypothesis may also help to explain the excellent trend observed in the HC–2 when gold solution volume was increased, and thus the gold concentration was decreased. The pH fluctuations during synthesis were probably minimized as the gold solution volume was increased. This would imply that the variability present at low dilutions would disappear at higher dilutions.

Under acidic conditions, small reduced gold particles would have a tendency

to be redissolved back into solution due to both their size and the increased solubility of gold in acids. These redissolved, smaller gold particles might then be reprecipitated onto larger gold particles, exhibiting a form of Ostwald ripening that would tend toward larger gold clusters being formed. This mechanism might be minimized as the system became more dilute and would partly explain the good control exhibited in the gold solution volume study in the HC–2, which showed a trend of decreasing mean crystallite size with the simultaneous increase in gold dilution and decrease in the hydrazine molar feed rate. Both factors working together ensured that very little hydrazine was present in the system at any given moment and that the local pH fluctuations were minimized. Neither factor alone was observed to produce small gold grain sizes (less than 10 nm).

8.2 Results

8.2.1 Examination of support effect on the precipitation-deposition of 2% gold on titania

In the precipitation-deposition technique, two factors which are different from the approach used in this thesis are the use of a preformed support and the use of high temperature aging [28, 29]. Since the precipitation-deposition method serves as a useful benchmark for the production of small gold particles on titania, syntheses were performed using this technique to learn more about gold precipitation. For the syntheses reported here, a theoretical gold loading of 2% was used for comparison

with previous results.

Using sodium hydroxide as a precipitating agent, the effect of support preparation was explored via classical synthesis. Three experiments were performed, one with a titania which was precipitated *in situ*; a titania which was precipitated separately, then dried; and a titania which was precipitated separately, dried, and then calcined. All three syntheses were done as close as possible to Haruta's precipitation-deposition technique, including an aging of the solution at high temperature.

The *in situ* titania experiment was performed as follows. A standard stock gold solution was diluted to a volume of 500 mL and then placed in a 1000 mL flask. Then 100 mL of titanium butoxide in isopropyl alcohol was added to the mixture. A 100 mL aliquot of 1 mol/L NaOH was then added to the solution to make the total solution basic at a pH of 13. The solution was then heated to 75 °C for one hour, which caused the solution to turn from white to purple. X-ray analysis of the dried material indicated that the gold crystallite size was 13.8 nm. Upon calcination to 400 °C, the gold grain size increased to 18.0 nm, but the titania remained amorphous, indicating that either the anatase failed to crystallize, or that it was too small to be detected by x-ray diffraction.

The two other experiments were performed with pre-synthesized titania supports. For both support materials, 100 mL of titanium butoxide in isopropyl alcohol was added to 500 mL of water to precipitate a titanium hydroxide. Both precipitated solids were washed, filtered, and dried. The first of these was used only in the dried state, while the second was calcined to 400 °C. For both syntheses, a 500 mL

gold solution was made as per the *in situ* experiment above, and the support was then placed into the solution and stirred with a magnetic stir bar. The pH in both experiments was adjusted to 8 with 1 mol/L NaOH, and then the solutions were heated to 70 °C for one hour while maintaining the pH with additional sodium hydroxide. Upon filtration and water washing, clear red filtrates were produced, which scattered laser light, indicating the presence of colloidal gold which was not deposited onto the supports. Both samples were calcined to 400 °C after drying overnight.

For both of these *ex situ* support experiments, no gold was detected on either the dried or calcined materials by x-ray diffraction. Both calcined samples were blue, however, indicating that gold was present. Based on Haruta's work on precipitation-deposition of gold on titania, only somewhere between 13 and 40% of the gold was expected to have deposited onto the supports, and thus the inability of x-ray diffraction to detect the gold was not unexpected. However, these three experiments (including the *in situ* support synthesis) show that the effect of the support preparation is significant to Haruta's precipitation-deposition approach.

Given the color changes which occurred upon aging these syntheses at high temperature for one hour, it may be that the precipitation-deposition method actually results in the reduction of gold which has been deposited onto the support. By keeping the conditions basic with sodium hydroxide, the chloroauric acid was converted to a gold hydroxide/chloride complex, which might then more easily interact with a preformed support. The color change to purple is indicative of the colors obtained during hydrazine reduction observed in previous syntheses, and

thus the aging at approximately 60–80 °C may serve the purpose of reducing the gold hydroxide/chloride complex to metallic gold on the surface.

8.2.2 Concentration effect

An initial classical experiment was performed to reduce the gold under basic conditions with sodium hydroxide. The titanium hydroxide support was formed first by adding 100 mL of titanium butoxide in isopropyl alcohol to 500 mL of deionized water. Portions of a 1 mol/L NaOH solution were then added to adjust the pH from 4.5 to approximately 9. Then a 100 mL solution containing enough hydrazine to have a hydrazine to gold ratio of 1.55/1 was added to this solution, the goal being to make the hydrazine concentration constant and dilute as much as possible during the experiment. Then a dilute 500 mL gold solution was added slowly at 4 mL/min to ensure that any pH changes would be gradual.

During the course of the approximately 2 hour gold addition, the pH was maintained at 8 with the addition of sodium hydroxide as needed. No heat aging was applied, and the final slurry color was a light gray, which was different from other hydrazine reductions performed previously. Upon filtration, a clear and colorless filtrate was produced, which may indicate that the majority of the gold was deposited onto the titanium hydroxide surface. However, approximately five minutes after two water washes had been performed, the wash solution turned from colorless to blue, which meant that some of the gold was washed off of the wet filter cake.

After drying overnight, the product was light purple in color, indicating the

presence of gold, but x-ray diffraction analysis was unable to detect gold peaks, suggesting that if gold was present, it was less than 4.5 nm in size or was in a concentration lower than 1%. Upon calcination to 400 °C, the solid changed to a different shade of light purple, but x-ray diffraction analysis did not detect gold peaks nor the presence of anatase (the support appeared amorphous). This result suggested that finely dispersed gold particles had been produced similar to the support effect experiments discussed above, but without the need for higher temperature aging and possibly with a higher loading of gold.

Five additional classical syntheses were performed to test this concept. The theoretical gold content of each sample was varied from 2.06% to 7.8%. As shown in Table 8.1, it appeared that the grain size was very small for the theoretically 2.06% sample, and that the grain size increased with increasing gold concentration, as expected. Three of the classical samples were analyzed via ICP to determine their actual gold content as shown in Table 8.1.

The three classical samples all showed low gold yields using this basic reduction

Table 8.1: Classical titania supported gold produced by hydrazine reduction under basic conditions.

Theoretical gold loading (wt%)	Actual gold content (wt%)	Gold yield (%)	Gold mean crystallite size (nm)
2.06	0.45	21.8	-
3.06	1.43	46.7	6.5 ± 0.6
4.04	2.62	64.9	8.8
5.94	-	-	9.1
7.76	-	-	10.2

technique. However, when the yields or the actual gold contents are plotted versus the theoretical gold concentrations, an excellent linear trend results, as shown in Figure 8.1. This suggests that a chemical equilibrium process is occurring in the system, as a distribution coefficient would be expected to vary with concentration in a similar fashion.

Another interesting feature of the classical syntheses was the lack of a crystalline support even after the 400 °C air calcination. For all five syntheses, there was no indication of crystalline anatase and the x-ray patterns suggested that the support was amorphous. This result is similar to that observed for the *in situ* precipitation-deposition experiment described above, where it appeared that an amorphous or extremely small crystalline support was formed instead of the typical anatase.

8.2.3 Synthesis of titania supported gold in the HC–3

Based on the classical results, it was decided that a series of experiments would be performed at 3.06% theoretical gold loading using the HC–3, because the grain size was visible by x-ray diffraction and was fairly small. At the time this decision was made, the gold analytical results shown in Table 8.1 were not available.

Two different synthesis series were performed in the HC–3. The first series used two orifices, with the second one fixed at 0.014 inch. The first orifice was varied from 0.006 to 0.012 inch with the process pressure maintained at 13,000 psig for a total of four runs. The second series used only the 0.006 inch orifice, with the pressure being varied in four runs from 10,000 to 20,000 psig. A repeat run at 20,000 psig was also performed to check the reproducibility of the synthesis. For

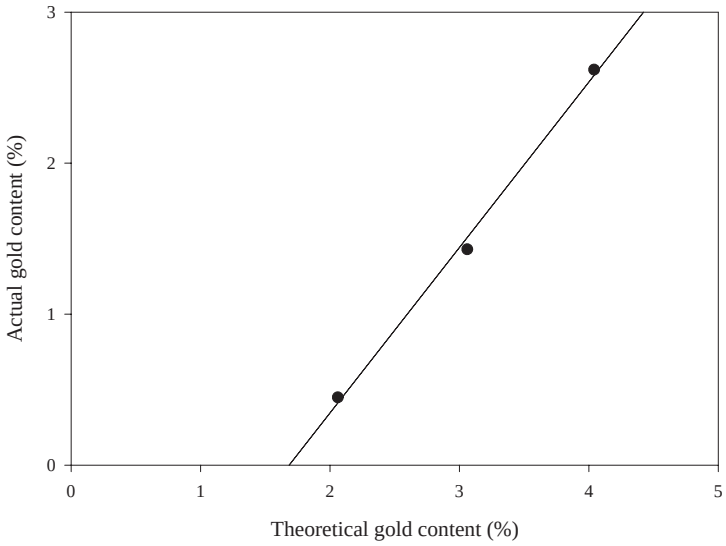

Figure 8.1: Comparison of actual and theoretical gold loadings for the classical reduction of gold with hydrazine under basic conditions. The slope of the fit is 1.0956, the intercept is -1.8451, and the R^2 is 0.996.

comparison, an experiment was performed in the HC–3 without the sodium hydroxide using a single 0.006 inch diameter orifice at a feed pressure of 20,000 psig. As expected, the gold grain size for this acidic synthesis (the pH began at 5 and ended at 4) was 19.8 nm, and the support crystallized to a 15.2 nm anatase. The data for these experiments, including the gold crystallite size measurements and the three "classical" experiments, are shown in Table 8.2.

Gold crystallite size and yield

There appears to be a mixing advantage to using the HC–3 with respect to gold incorporation into these catalysts. For a theoretical gold loading of 3.06%, the classically synthesized sample only contained 46.7% of the gold. All of the HC–3 samples were synthesized with this same theoretical gold concentration, yet the gold yields were much higher. The sample synthesized without base (only hydrazine) contained 100% of the theoretical gold content, which was expected due to the strong reducing effects of hydrazine. However, the samples synthesized in the HC–3 with sodium hydroxide had a gold concentration of $2.27 \pm 0.17\%$ (95% confidence interval), which is a mean gold yield of $74.1 \pm 5.6\%$. Assuming that the gold yield for the classical synthesis has approximately the same level of variation, there is a clear and strong effect due to the HC–3. Most likely, this is due to the strong molecular mixing from the cavitation.

The mean crystallite size for all basic hydrazine experiments performed at a theoretical gold loading of 3.06% in the HC–3 was 6.0 ± 1.9 nm (95% confidence). The range for these experiments was 6.2 nm, with the smallest crystallite size

Table 8.2: Catalyst data for gold basic hydrazine reduction samples. The catalysts are arranged by synthesis method: (C) classical, (H) hydrodynamic cavitation, and (HA) hydrodynamic cavitation under acidic conditions.

Synthesis method	Gold content (wt %)	Gold yield (%)	Orifice diameter (inches)	Feed pressure (psig)	Reynolds number	Throat cavitation number	Gold grain size (nm)	Activation energy (kJ/mol)	Atomic rate @ 150 °C (s^{-1})	Specific rate @ 150 °C (mol/g-s $\times 10^5$)	Atomic rate @ 200 °C (s^{-1})	Specific rate @ 200 °C (mol/g-s $\times 10^5$)
C	0.45	21.8	-	-	-	-	-	34	0.36 ± 0.07	0.83 ± 0.17	1.00 ± 0.08	2.29 ± 0.17
C	1.43	46.7	-	-	-	-	6.5 ± 0.6	40	0.08 ± 0.03	0.59 ± 0.19	0.28 ± 0.03	2.03 ± 0.24
C	2.62	64.9	-	-	-	-	8.8	29	0.08 ± 0.01	1.10 ± 0.09	0.19 ± 0.01	2.58 ± 0.10
H	2.03	66.3	0.006/0.014	13000	38979	2.72	7.5	31	0.07 ± 0.02	0.74 ± 0.21	0.19 ± 0.04	1.91 ± 0.45
H	2.46	80.4	0.008/0.014	13000	41406	4.28	7.1 ± 1.4	28	0.07 ± 0.03	0.90 ± 0.31	0.16 ± 0.03	2.04 ± 0.32
H	2.53	82.7	0.010/0.014	13000	44195	5.88	7.7	†	0.04 ± 0.02	0.50 ± 0.27	0.02 ± 0.01	0.28 ± 0.18
H	1.88	61.4	0.012/0.014	13000	48968	6.89	8.7	37	0.05 ± 0.02	0.47 ± 0.16	0.17 ± 0.01	1.66 ± 0.14
H	2.31	75.5	0.006/-	10000	33874	2.77	2.5 ± 1.2	38	0.06 ± 0.02	0.72 ± 0.26	0.20 ± 0.03	2.33 ± 0.39
H	2.09	68.3	0.006/-	13000	38702	2.76	8.2	27	0.06 ± 0.03	0.62 ± 0.32	0.13 ± 0.03	1.41 ± 0.28
H	2.29	74.8	0.006/-	17000	43279	2.88	5.8	†	0.12 ± 0.03	1.35 ± 0.39	0.15 ± 0.03	1.69 ± 0.33
H	2.41	78.8	0.006/-	20000	45326	3.07	3.8	37	0.07 ± 0.02	0.85 ± 0.26	0.20 ± 0.02	2.41 ± 0.19
H	2.42	79.1	0.006/-	20000	45326	3.07	2.7 ± 2.6	22	0.05 ± 0.01	0.62 ± 0.17	0.10 ± 0.02	1.20 ± 0.24
HA	3.08	100.7	0.006/-	20000	45326	3.07	19.8	27	0.14 ± 0.02	2.17 ± 0.36	0.30 ± 0.02*	4.69 ± 0.28*

*Estimated from lower temperature data due to transport limitation at high conversion.

†Unable to calculate activation energy due to catalyst deactivation.

produced being 2.5 nm and the largest 8.7 nm. Thus, this method gives the smallest grain sizes for high gold weight loadings compared to other synthesis techniques used so far at high gold weight loadings. For example, the conventional hydrazine reduction technique yields grain sizes on the order of 32.2 ± 14.6 nm for fixed processing conditions, and ammonium hydroxide synthesis gives gold crystallite sizes of 15.9 ± 5.2 nm. Furthermore, the range of grain sizes produced with basic hydrazine reduction in the HC–3 are in the targeted desirable region of 1–10 nm.

It also appears that the synthesis results from the HC–3 are reproducible, given that the two 20,000 psig runs under the same process conditions had nearly identical gold yields, and that the grain sizes from x-ray line broadening were reproducible within the precision of the technique. Three long count time scans of the Au(311) peak made on random portions of the 2.42% gold catalyst indicated that the grain size was 2.7 ± 2.6 nm. The relatively large experimental error was expected due to the limitations of the x-ray line broadening technique. However, the x-ray measurement of the gold peak on the 2.41% catalyst yielded a result of 3.8 nm, which was within the statistical variation of the 2.42% material.

The gold crystallite sizes obtained with the HC–3 do not appear to correlate significantly with either the Reynolds number or the throat cavitation number, as shown in Figures 8.2 & 8.3. And as Figure 8.4 reveals, there is also no satisfactory correlation with the orifice size and the gold grain sizes. However, when the gold results are plotted as a function of the feed pressure, as in Figure 8.5, the data appear to show a trend. The gold crystallite size appears to increase with increasing pressure, moves through a maximum, and then decreases with increasing pressure.

In addition, the data from the 13,000 psig experiments exhibit a range which is within the precision for the x-ray measurements, further reinforcing the observation that pressure is the dominant controlling factor in the HC–3.

The variation of gold grain size with respect to pressure can be explained in terms of the theoretical modeling from Chapter 3, where it was predicted that the use of a small orifice, while varying the upstream pressure, should result in alteration of the frequency and intensity of the cavitation bubble collapses. A low system pressure would naturally result in relatively fast recovery times (τ). This in turn would lead to rapid, intense bubble collapses. All things being equal, this would result in a trend of decreasing cavitational effects with increasing pressure, which by analogy would imply an increase in the mean gold crystallite size with increasing system pressure.

However, increasing pressure will naturally lead to a higher absolute value for the recovery pressure (p_2). Furthermore, a larger feed pressure might also lead to a larger pressure drop across an orifice, which would result in a lower initial pressure after the orifice (p_0). Both of these effects would imply a trend of more intense cavitational events with increasing pressure. In addition, increased pressure would result in more mechanical mixing as per Equation 3.36.

Competition between these driving forces and the change in the recovery time would result in the grain size behavior observed in Figure 8.5. As the pressure in the HC–3 is increased, one effect is to decrease the recovery time, which would lead to rapid, intense bubble collapses. This in turn would lead to high energy shock waves and microjets which presumably decrease the mean crystallite size

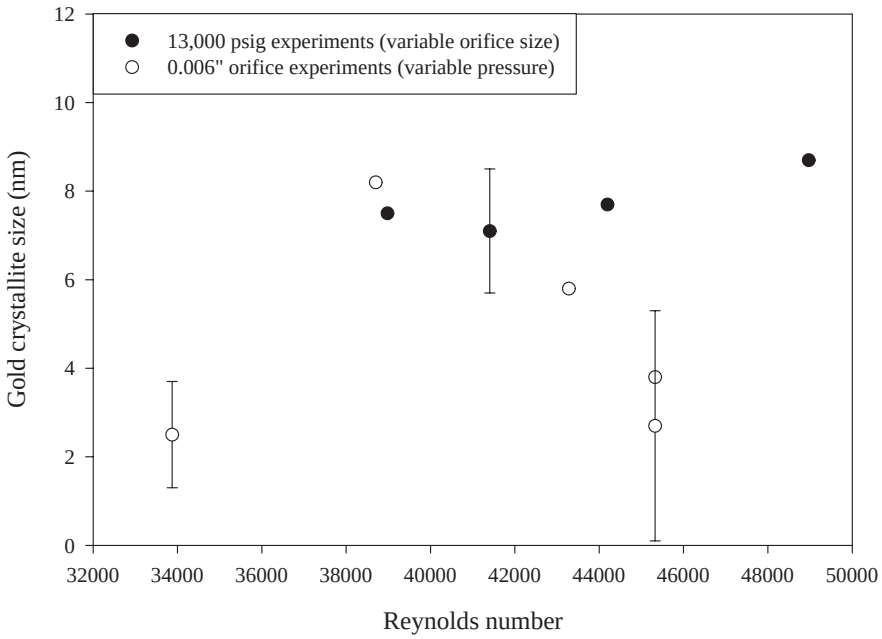

Figure 8.2: Gold crystallite sizes obtained from x-ray line broadening measurements as a function of the orifice Reynolds number. All materials were synthesized in the HC–3 with hydrazine reduction under basic conditions.

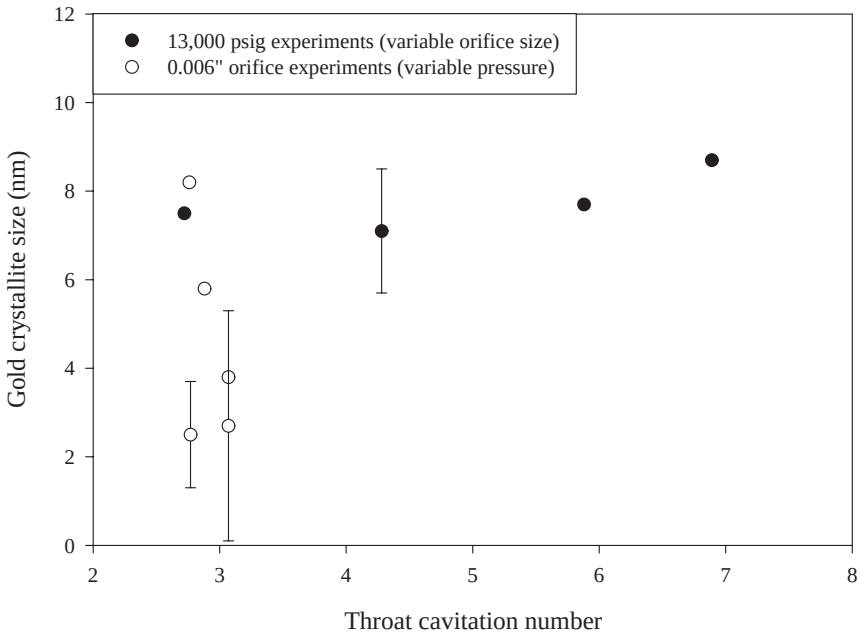

Figure 8.3: Gold crystallite sizes obtained from x-ray line broadening measurements as a function of the throat cavitation number. All materials were synthesized in the HC–3 with hydrazine reduction under basic conditions.

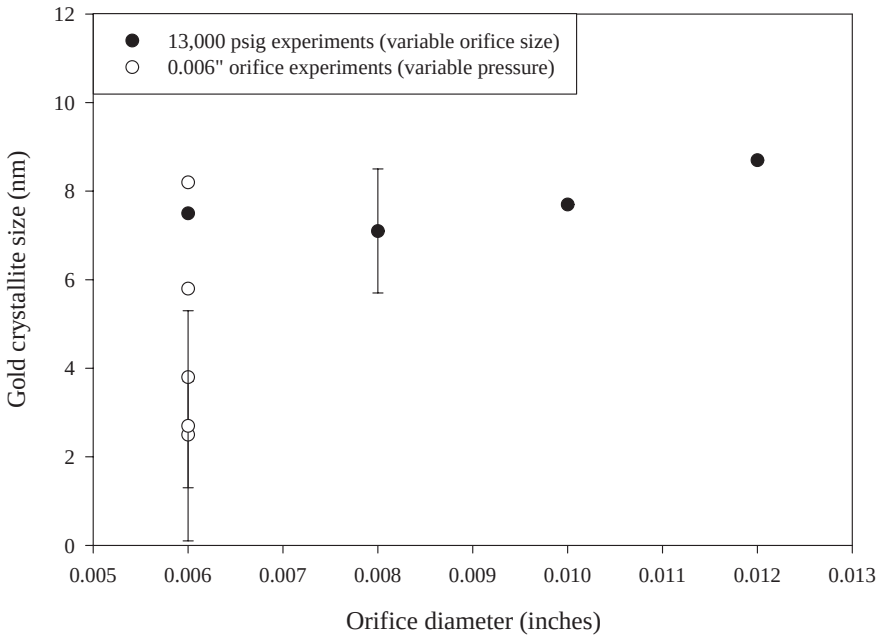

Figure 8.4: Gold crystallite sizes obtained from x-ray line broadening measurements as a function of orifice diameter. All materials were synthesized in the HC–3 with hydrazine reduction under basic conditions.

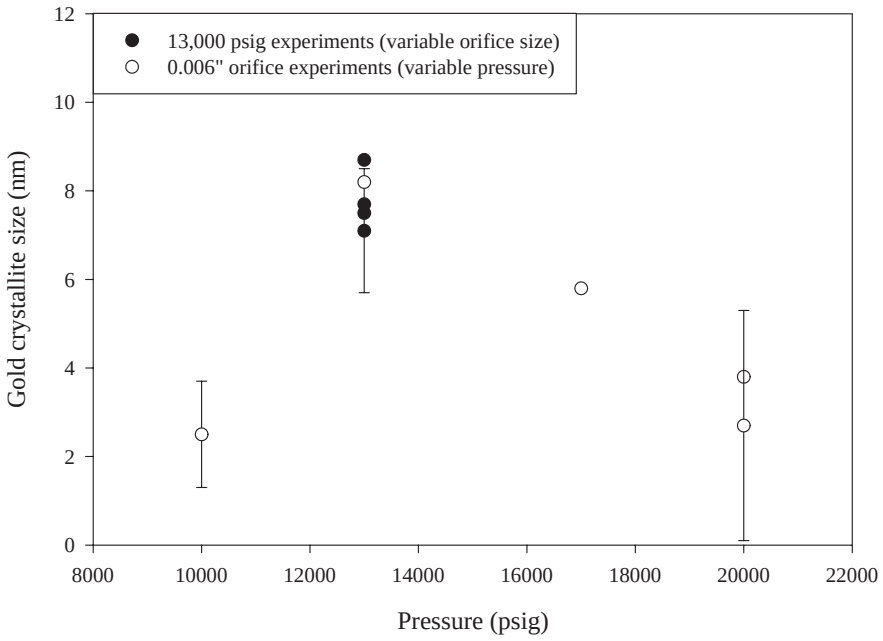

Figure 8.5: Gold crystallite sizes obtained from x-ray line broadening measurements as a function of process pressure. All materials were synthesized in the HC–3 with hydrazine reduction under basic conditions. A cubic fit to this data, yielding a P-value from an ANOVA of 0.0009 and an R^2 of 0.954, is $D = -119.32 + 0.024p - 1.441 \times 10^{-6}p^2 + 2.786 \times 10^{-11}p^3$.

of the forming gold particles. As the pressure is increased further, the recovery time would continue increase, and thus the intensity of the cavitation events would diminish, and the gold crystallite sizes would not be as small as at lower pressures. But when the system pressure continues to be increased, the recovery pressure will also increase, which would result in the intensification of the cavitational events. This, combined with the potential for higher pressure drops across an orifice and increased mechanical energy being applied to the fluid, would counteract the recovery time effect and reverse the pressure trend, leading to the apparent maximum in grain size observed in the HC–3.

An alternative way of expressing this trend is in terms of the comparison modeling work done by Moholkar *et al.* between acoustic cavitation and hydrodynamic cavitation [85]. In their paper, they make the analogy between the effects of recovery pressure and recovery time in hydrodynamic cavitation with intensity (I) and frequency (f) in acoustic cavitation. For example, the increase in frequency in acoustic cavitation produces effects similar to the reduction in the pressure recovery time. By doing a thorough simulation analysis for acoustic cavitation under various conditions, Gogate and Pandit produced a correlation for the pressure pulse generated by a bubble on collapse as Equation 3.24, which for convenience is reproduced here as Equation 8.3 [84].

$$P_{\text{collapse}} = 114(R_0)^{-1.88}(I)^{-0.17}(f)^{0.11} \tag{8.3}$$

Since the initial bubble size, R_0, is a function of the vapor pressure, gas com-

position, and the number of pre-existing gas cavities in the system, it is effectively a constant for a given chemical precipitation system. Thus, Equation 8.3, can be rewritten as

$$P_{\text{collapse}} = K(I)^{-0.17}(f)^{0.11} \tag{8.4}$$

where K is a constant of proportionality. By analogy, a similar correlation should exist for hydrodynamic cavitation, such as

$$P_{\text{collapse}} = K(p_2)^a(1/\tau)^b \tag{8.5}$$

where both a and b are positive coefficients. Thus, as the upstream pressure increases, τ increases, and the collapse pressure decreases, leading to less reduction in gold grain size and mixing effects. But as the pressure increases, p_2 also increases, tending to increase the collapse pressure. The competition between these two trends leads to the maximum shown in the gold size data.

Figure 8.5 represents the first evidence of hydrodynamic cavitation influencing the gold crystallite size on titania supported gold catalysts. This observation is especially important to catalysis, since nanometer-size metallic particles in the range of 1–10 nm exhibit higher activities for chemical reactions compared to larger grain particles. The implications are that by simply making a mechanical adjustment (*i.e.* adjusting the pressure), the mean metal crystallite size for a supported metal catalyst can be controlled.

Nature of the support

One interesting feature about all experiments, including the classical ones, performed with hydrazine reduction under basic conditions, was that the supports appeared to be mostly amorphous. This is in contrast to normal hydrazine reduction and other precipitation methods, which produce crystalline anatase after calcination to 400 °C. Either hydrazine or sodium hydroxide, when used individually, result in anatase, yet when the two are combined, as in these experiments, the supports are unusually different.

In many of the samples synthesized with the HC–3, there are two phases of titania which appear to be present in addition to the amorphous portion of the support: anatase and a monoclinic β-TiO2 (ICDD 35–88) which is classified as an "unnamed mineral". The presence of the monoclinic phase complicated the gold crystallite size measurements, resulting in the need to use the Au(311) peak for line broadening measurements. Examples of the XRD patterns produced by the HC–3 syntheses are shown in Figure 8.6 for the variable orifice experiments. Although for this series it appears that the amount of crystalline titania decreases with increasing orifice diameter, the appearance of crystalline titania is random with the other experiments.

Three samples were analyzed via ESCA/XPS: the 1.43% gold classical sample; the 2.46% gold, 13,000 psig, 8/14 experiment in the HC–3; and the 2.42% gold, 20,000 psig, 6/0 synthesis. All three samples were originally synthesized with the expectation of a 3.06% theoretical gold content. However, as noted earlier, the gold yield was lower in the classical sample compared to the two HC–3 samples.

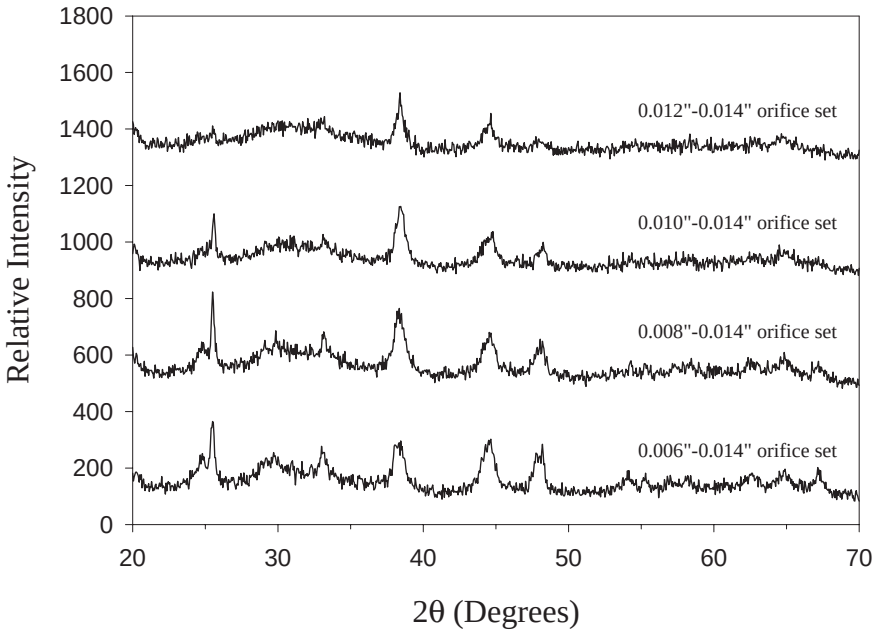

Figure 8.6: X-ray diffraction patterns for basic hydrazine reduction syntheses in the HC–3 under constant pressure with variable orifice diameters. The patterns suggest that the support is mostly amorphous material with varying amounts of crystalline anatase and monoclinic β-TiO_2.

Figure 8.7 shows the Au 4f spectra for the three samples, which indicates that all of the gold present on the surface of each sample was Au(0), and that the gold state was identical for both the classical and HC–3 preparations. Thus, it appears that there was no Au(I) or Au(III) species present after calcination to 400 °C.

An interesting feature of the ESCA analysis was the detection of a significant amount of sodium on the surface of these samples. The sodium to gold atomic ratio was 0.81 for the 2.42% sample, 0.70 for the 2.46% sample, and 0.65 for the 1.43% classical synthesis. This represented sodium which was irreversibly bound to the catalysts and was not removable by water washes. Assuming that the ESCA sodium measurements are representative of each sample, then using the bulk gold analyses, it is possible to calculate the percentage of sodium. Thus, the 2.42% gold sample appears to contain 0.23% sodium, the 2.46% catalyst contains 0.20% sodium, and the 1.43% classical synthesis contains 0.11% sodium. If all of the sodium added in the form of sodium hydroxide to the system during synthesis were incorporated into these catalysts, then the sodium content would be approximately 11.9%. Thus, the sodium levels calculated from the ESCA data are on the order of 1–2% of the total sodium which was available in the system.

The 1.43% classical and the 1.88% gold, 12/14 orifice set, HC–3 samples were calcined to 530 °C to see if the amorphous portion of the support material could be crystallized. The x-ray diffraction patterns for both materials after calcination were identical, and showed that the support was indeed crystallized at a higher temperature. This result supports the conclusion that the unusual nature of the support was due to the chemistry of the system (the combination of NaOH &

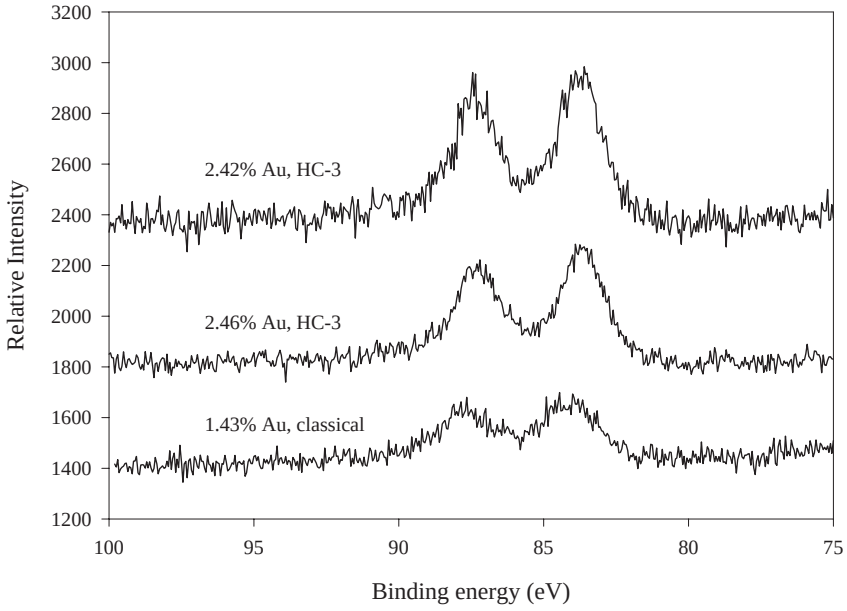

Figure 8.7: Gold 4f ESCA spectra for the 1.43%, 2.42%, and 2.46% gold samples.

N_2H_4), and not due to the influence of the HC–3.

Figure 8.8 shows the XRD patterns for the 1.88% gold, 12/14 orifice set, HC–3 sample calcined to 400 and 530 °C. The sample at 530 °C appears to be composed of a mixture of materials. Metallic gold is present, as well as what appears to be the monoclinic β-TiO_2 with some anatase as was first deduced from the 400 °C pattern. However, in light of the ESCA results, several peaks which could not immediately be identified as a form of titanium were attributed to a mixture of sodium titanium oxides.

The two most likely candidates are $Na_2Ti_3O_7$ (ICDD 31–1329) and $Na_{0.8}Ti_3O_{6.4}$ (ICDD 47–562). Assuming that the sodium concentrations, calculated from the ESCA data and the bulk gold analysis, are due to the presence of these two materials, then all of the catalysts contain approximately 1–3% sodium titanium oxide. The ICDD data card for 31–1329 indicates that it was formed by a high temperature (1250 °C) reaction between Na_2CO_3 and anatase, followed by mixing with NaOH and additional heat treatments at 950–1000 °C. The card for 47–562 says that it was obtained by heating a sample of $Na_{0.8}H_{1.2}Ti_3O_7$ to 800 °C in air. Both of these materials imply high temperature reactions involving sodium. Thus, it would not be unreasonable to assume that the local temperature fluctuations due to cavitation described in Chapter 3, which are on the order of a few thousand degrees, might be partially responsible for the formation of the sodium titanium oxide species present in the HC–3 samples. However, the fact that the classical sample also contains the mixture of these compounds points to the chemistry of the system as being the underlying cause.

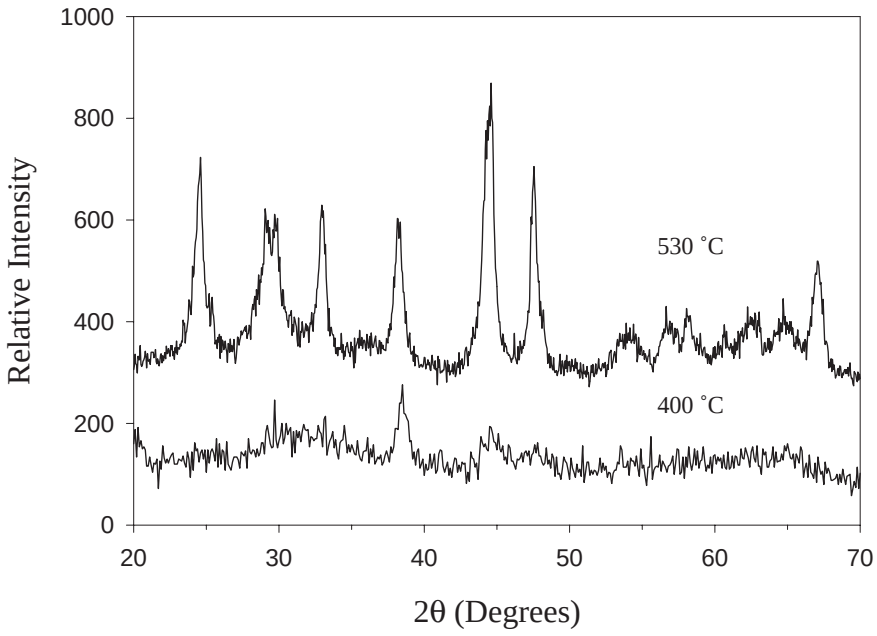

Figure 8.8: X-ray diffraction patterns for the basic hydrazine reduction synthesis in the HC–3 with the 12/14 orifice set at 13,000 psig, calcined to 400 and 530 °C.

Transmission electron spectroscopy

The same three samples used for the ESCA analysis were also examined by TEM. Examination of the classically synthesized sample revealed no evidence for crystalline support material. Figure 8.9 shows a typical gold particle sitting on the amorphous support. The presence of the gold in this, and the other samples, was confirmed by EDX analysis of the region being photographed. Although an insufficient number of gold particles were observed to allow the construction of a gold particle size distribution, gold particles in the range of 2–30 nm were observed throughout the sample. Comparison with the x-ray line broadening measurement of the mean crystallite size suggests that the distribution is considerably broader than the response variation of the x-ray measurements (6.5 ± 0.6 nm).

TEM analysis of the two hydrodynamically synthesized samples was also unable to give an accurate picture of the gold particle size distribution due to the lack of enough gold particles in the samples to be observed. As with the classical sample, both cavitation samples revealed a range of particle sizes from about 2–30 nm, although qualitatively, the number of smaller particles was greater in the 2.42% gold sample, in agreement with the x-ray line broadening results.

In contrast to the classical sample, both cavitation samples clearly exhibited the presence of some crystalline support material which contains both sodium and titanium as determined by qualitative EDX analysis. This qualitative information, combined with the XRD analysis described previously, confirms that there was sodium titanium oxide present in the 400 °C samples. Throughout both samples, the crystalline non-gold support material was associated mostly with the regions

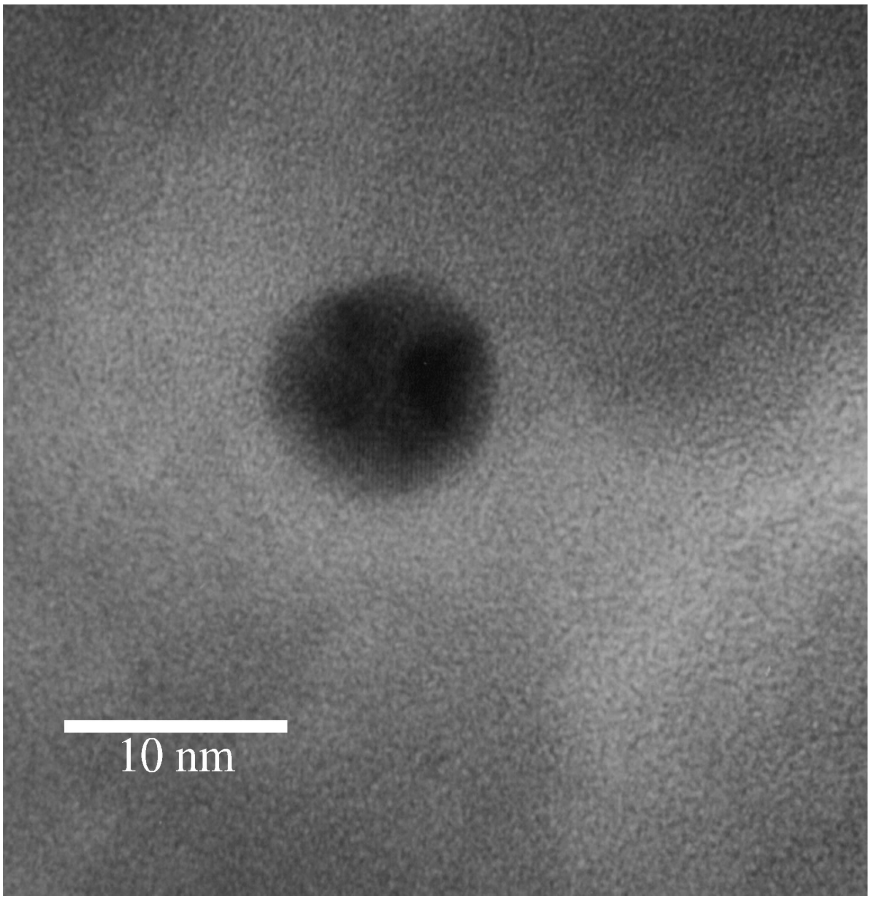

Figure 8.9: TEM image of 1.43% gold sample synthesized classically with hydrazine reduction under basic conditions. Image was taken by Mike Frongillo of MIT at a magnification of 1000000× with an acceleration potential of 200 kV. The darker spherical region was confirmed by EDX analysis to be gold.

containing gold particles, whereas the majority of the amorphous material was seen everywhere else. Also in contrast with the classical sample, there were many gold particles which appeared to be either partially or completely covered by the crystalline support material. Figure 8.10 shows a representative image of the 2.46% gold sample where the lattice fringes of the crystalline support material can be seen both associated with, and partially covering, gold particles.

8.2.4 Catalytic activity

All samples which were synthesized via hydrazine reduction under basic conditions and analyzed for gold content were tested for their CO oxidation activity. In addition, the sample which was produced using only a normal hydrazine reduction in the HC–3 was also measured for catalytic activity. The various reaction rates at 150 and 200 °C, as well as the activation energies, for these catalysts are reported in Table 8.2 as well as their relevant synthesis conditions and gold contents. The activation energies obtained during the Arrhenius experiments were consistent with those measured for other titania supported gold catalysts in this thesis.

With the exception of the 0.45% gold classical sample, the activities of all of these samples were very low. In two samples, noted in Table 8.2, the catalysts deactivated over the course of the Arrhenius experiments. As a result, the data at all but 150 °C for these two runs are suspect, and the activation energies could not be obtained. This deactivation is in stark contrast to the samples synthesized via ammonium hydroxide/CTMA-Cl coprecipitation in Chapter 6, where it was observed that those catalysts showed no deactivation even after 15–20 hours of

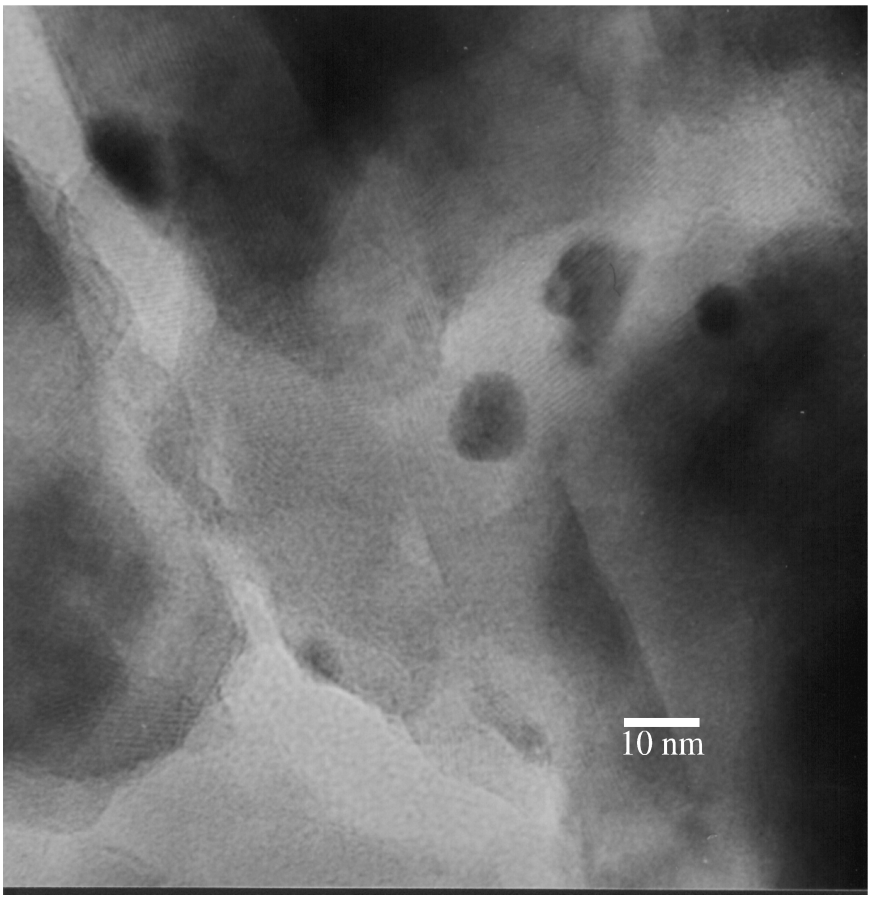

Figure 8.10: TEM image of 2.46% gold sample synthesized in the HC–3 with hydrazine reduction under basic conditions. Image was taken by Mike Frongillo of MIT at a magnification of 600000× with an acceleration potential of 200 kV. The darker spherical region in the center of the image was confirmed by EDX analysis to be gold. The lattice fringes of the crystalline support material associated with the gold particles can be seen throughout. The support lattice fringes can also be seen to partially cover the center gold particle.

reaction measurements.

This extremely low activity is illustrated in Figures 8.11 & 8.12, which show the basic hydrazine reduced samples' catalytic activities at 150 °C compared to other catalysts synthesized in this thesis, as a function of gold content. There was no distinguishable difference in activity per gram of catalyst (specific reaction rate) between the classical and HC–3 samples, regardless of the processing conditions or the mean gold crystallite size as determined by x-ray line broadening. However, the classical samples appeared to contain more active gold particles, as they contained less gold, yet had the same or better activity per mole of gold (atomic reaction rate).

Due to their extremely low activity, the rates for these catalysts is better expressed at a higher temperature, where the conversion was more appreciable. Figures 8.13 & 8.14 show the specific and atomic oxidation rates, respectively, for the basic hydrazine reduced samples. From these figures, it is clear that the classical and cavitationally processed samples both have the same activity per gram of catalyst as a function of gold loading. Furthermore, it appeared that even the 19.8 nm gold catalyst synthesized without sodium hydroxide exhibited more activity, although less than expected based on the trends established by the ammonium hydroxide/CTMA-Cl coprecipitation method. However, Figure 8.14 does indicate that, despite the low activity, there is still the beginning of an increase in the atomic rate at 0.45% gold as was observed with other catalysts. This reinforces the idea that this gold concentration may be a constant breakpoint for gold on titania, below which the gold is in a highly dispersed, and hence active, state.

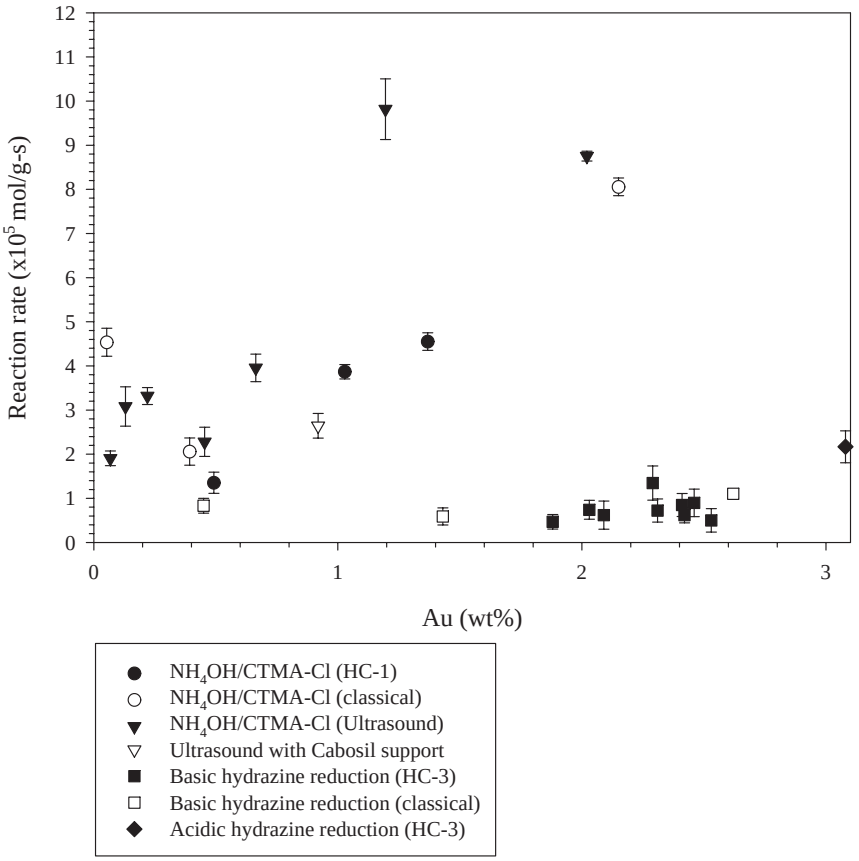

Figure 8.11: CO oxidation rate per gram of catalyst (specific rate) at 150 °C for diverse synthesis methods as a function of gold loading on the catalysts.

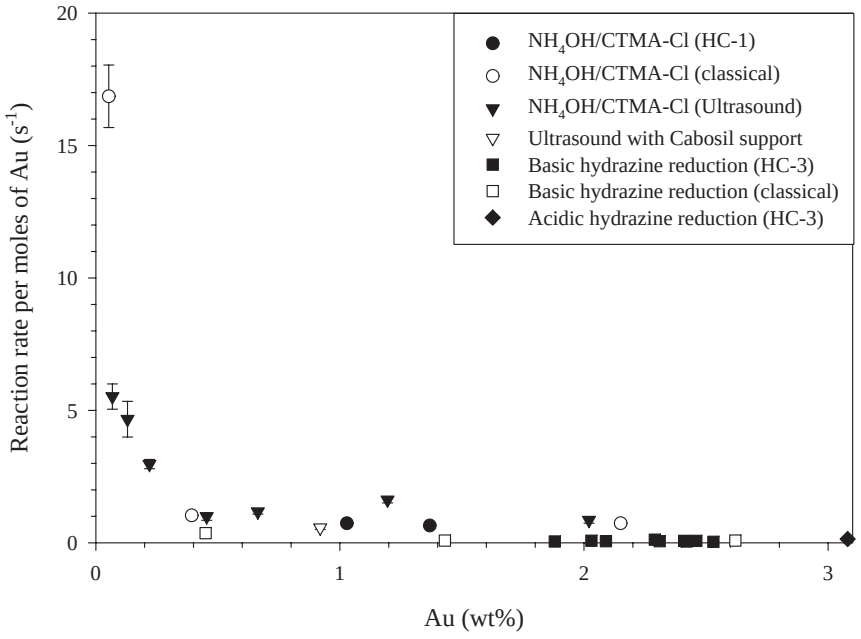

Figure 8.12: CO oxidation rate per moles of gold (atomic rate) at 150 °C for diverse synthesis methods as a function of gold loading on the catalysts.

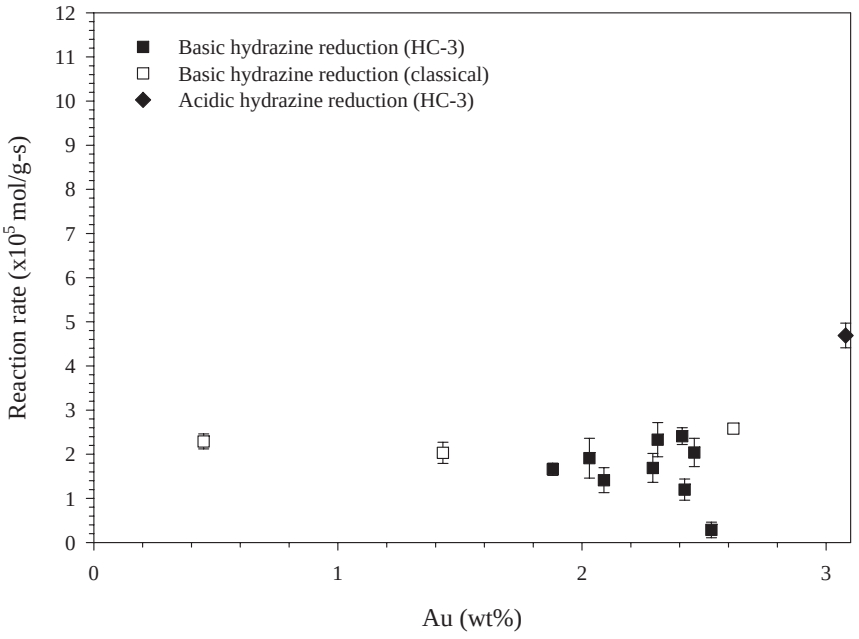

Figure 8.13: CO oxidation rate per gram of catalyst (specific rate) at 200 °C for samples synthesized via basic hydrazine reduction as a function of gold loading on the catalysts.

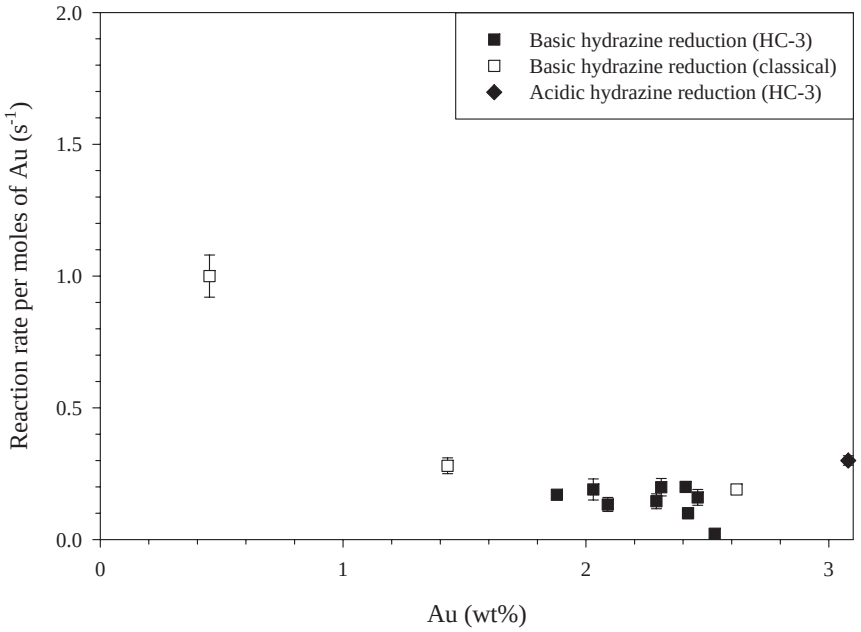

Figure 8.14: CO oxidation rate per moles of gold (atomic rate) at 200 °C for samples synthesized via basic hydrazine reduction as a function of gold loading on the catalysts.

One possibility for the low catalytic activities was that the samples lacked fully crystalline supports. It might be that the interaction between gold and crystalline titania is critical for higher CO conversions [28]. Thus, the 530 °C calcined 1.88% gold catalyst, whose XRD pattern was shown in Figure 8.8, was tested for CO activity. The atomic rate for this catalyst at 200 °C after calcination to 400 °C was 0.17 ± 0.01 s^{-1}. When the catalyst was calcined to 530 °C its measured CO activity at 200 °C was also 0.17 ± 0.01 s^{-1}. Thus, the lack of a fully crystalline support failed to explain the low CO rates compared to other synthesis methods.

In light of the TEM and ESCA data, the low activities is explainable in terms of the sodium present in these samples. For other synthesis methods, the support has been crystalline anatase. The samples discussed here were synthesized in the presence of both hydrazine and sodium hydroxide which led to the production of nonremovable sodium in the form of sodium titanium oxides. In the case of the HC–3 synthesized samples, it was observed in the TEM that this material was primarily associated with the gold particles, and in fact appeared to be partially or totally covering the gold in the samples. For the classical sample, the TEM revealed almost no crystalline support material, which was consistent with the x-ray diffraction patterns for that material.

Figure 8.15 shows the CO oxidation atomic rate at 200 °C for the three samples analyzed by TEM and ESCA as a function of sodium content. The sodium concentrations were based on the values detected by ESCA combined with bulk gold analysis as described above. This plot clearly shows that the CO oxidation activity decreases with increasing sodium content. Thus, the sodium titanium oxides

present in these samples act as catalytic inhibitors.

Another more subtle trend exhibited in Figure 8.15, is the effect of cavitation on the presence of sodium in the system, and thus the activity of the catalysts. The sample with the lowest sodium content and highest activity was the classically prepared sample, which also had the lowest gold due to the absence of cavitational mixing. The trend which continued for the next two samples was that the increase in the HC–3 feed pressure resulted in increased sodium incorporation into the catalysts. The increase in hydrodynamic pressure which led to the increased sodium incorporation also led to smaller grain size gold. This further supports the observation made previously that increased cavitation intensity (*i.e.* increased process pressure) leads to greater cavitational mixing.

Based on the available catalytic data, it would appear that crystalline anatase without sodium containing species is a necessary requirement for increased catalytic activity like that observed for the coprecipitation catalysts shown in Figure 8.11. Furthermore, the observation of buried gold in the HC–3 samples, combined with the higher gold yields compared to the corresponding classical sample, suggests that the enhanced mixing due to the HC–3 exacerbated the low activity. By burying too much of the gold, and intimately mixing it with the sodium titanium oxides, a low concentration of active metal was left exposed to the reaction gas. In addition, the strong interaction between the gold and the support material appears to have reduced the activity further, leading to deactivation in some cases.

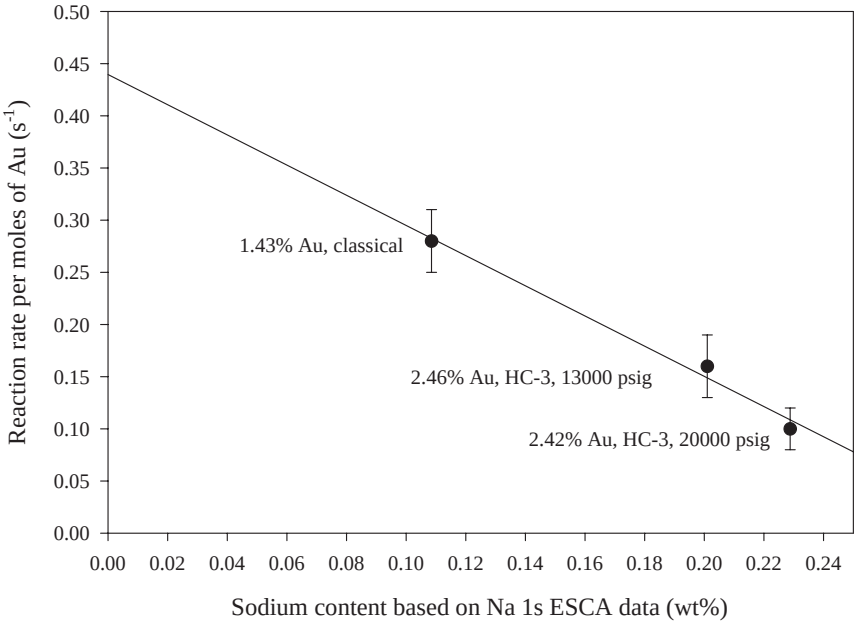

Figure 8.15: CO oxidation rate per moles of gold (atomic rate) at 200 °C for samples synthesized via basic hydrazine reduction as a function of sodium loading on the catalysts. The sodium concentration was calculated from the sodium to gold molar ratio obtained from the Na 1s and the Au 4f ESCA spectra combined with the known bulk gold analysis from ICP.

8.3 Conclusions

Changing the chemistry of the titania/gold system to hydrazine reduction under basic conditions using sodium hydroxide, combined with the use of hydrodynamic cavitation via the HC–3, resulted in the formation of gold crystallites with mean sizes in the 2–8 nm range. The gold crystallite size was found to be dependent only on the upstream pressure of the orifice in the HC–3, and was not an apparent function of Reynolds number, throat cavitation number, or the orifice diameter. The mean gold grain size was observed to pass through a maximum of 7–8 nm as the pressure was increased. In addition, the use of hydrodynamic cavitation led to a greater degree of mixing compared to classical syntheses as evidenced by the larger incorporation of gold and unremovable sodium into the catalysts and the partial burying of gold particles within the support.

The observed effects due to hydrodynamic cavitational processing would not be possible without two important changes which were made: a higher pressure device and system chemistry. Clearly, the high pressures produced in the HC–3, which are an order of magnitude greater than in the HC–2, allowed the controlled adjustment of the gold crystallite size. However, this may not have occurred unless the chemistry of the system was altered to the current reduction scheme.

Unfortunately, the change in the system chemistry from acidic reduction to basic reduction introduced an unforeseen side effect: the formation of a sodium titanium oxide species. The sodium incorporation resulted in the poisoning of the catalytic properties of these materials. Thus, the ability to control the gold grain

size to less than 10 nm was gained at the loss of CO oxidation activity.

The fact that chemistry alterations were necessary suggests that the rate of precipitation may be a factor. By forming a gold hydroxide complex with sodium hydroxide and subsequently reducing it to metallic gold, the rate of gold reduction may have been reduced compared to direct reduction with only hydrazine. Based on simulation results presented in Chapter 3, the time scale for bubble collapse is on the order of 100 μs. If a precipitation occurs faster than the bubble collapses, it may be that cavitation will have a minor role in the adjustment of particle size. However, if the precipitation time is increased (*i.e.* a slower reduction step), then the shock waves and microjets may have more of a chance to affect the crystallite size.

Chapter 9

Recommendations for Future Work

The research completed in this dissertation is hopefully the beginning of a relatively new research area: the application of hydrodynamic cavitation to the synthesis of nanometer-size materials. As such, everything that might be explored on this topic could not be completed in a single Ph.D. research project. However, there are several directions in which this research can be extended.

A project to develop a non-sodium synthesis route for titania supported gold should be pursued. Additional exploratory work should be done to determine an adjustment of the precipitation chemistry to replace the sodium hydroxide used in the basic hydrazine reduction experiments of Chapter 8. Perhaps the use of a combination of hydrazine, and a base such as ammonium hydroxide or ammonium carbonate would work. Another alternative would be to move back to the original coprecipitation technique used in Chapter 6 in the hope that higher pressure cavitation experiments could alter the gold crystallite size compared to the unsuccessful

HC–2 experiments. Assuming such a chemical system can be developed, a repetition of the work done in Chapter 8 could be pursued to see if the changes in gold crystallite size can be obtained and a correlation made with catalytic activity. In addition, the exploration of this methodology for other supported metal catalysts would be fruitful to determine whether hydrodynamic cavitation can be used as a general catalyst synthesis technique.

Using the chemical modification approach, the use of acoustic cavitation could also be further explored. Assuming a chemical change can be made to adjust the chemical kinetics relative to the dynamics of cavitation, acoustic cavitation may allow the control of metal crystallite size. Such an investigation will likely require using equipment capable of adjusting acoustic probe intensity and frequencies over a wider range than that employed in this dissertation. The larger goal of such a research project would be to relate the grain size control to a bubble collapse pressure correlation such as Gogate and Pandit's [84].

Another direction of research should approach the investigation of the dynamic pressure relation to recovery pressure and recovery time. This would entail experimental work on a well-defined chemical system, such as the Weissler reaction. This research project could also focus on the mathematical description of all of the geometric and physical parameters related to the bubble dynamics. Assuming a similar mathematical analysis can be performed on the chemical kinetics of precipitation, a comparison of the bubble dynamic kinetics and the chemical kinetics would help researchers identify chemical approaches to allow cavitation to affect the crystallite size distribution of the precipitates.

Appendix A

Recycle Reactor Formulae Derivations

A recycle reactor setup was used for measuring the CO oxidation rates for two reasons: to minimize transport limitations and to improve measurement precision. Transport limitations are minimized in this reactor type because the conversion per pass through the reactor is low compared to the overall conversion. With a high overall conversion, which will allow greater measurement precision, the conversion per pass approximates that of a differential reactor. The derivation which is presented here to demonstrate this numerically was modified for a heterogeneous catalytic reactor from an excellent description given in the book by Metcalfe [139].

The schematic for a typical recycle reactor is shown in Figure A.1. An overall material balance on species A, which in the case of this dissertation is carbon

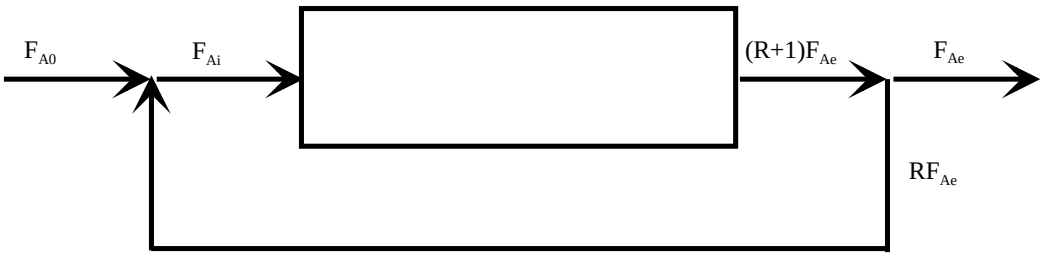

Figure A.1: Schematic of recycle reactor for material balance calculations.

monoxide (CO), yields

$$0 = F_{A_0} - F_{A_e} + r_A W \tag{A.1}$$

where F_{A_0} is the system molar inlet flow rate of CO, F_{A_e} is the system molar outlet flow rate of CO, W is the catalyst weight, and r_A is the reaction rate. The exiting flow rate can be defined in terms of the overall fractional conversion for the reactor,

$$\begin{aligned} X &= \frac{F_{A_0} - F_{A_e}}{F_{A_0}} \\ F_{A_e} &= F_{A_0}(1 - X) \end{aligned} \tag{A.2}$$

X, which can be combined with Equation A.1 to yield the equation used to measure the overall reaction rate per gram of catalyst.

$$-r_A = \frac{F_{A_0}}{W} X \tag{A.3}$$

If a recycle ratio, R, is defined as the moles of CO returning to the reactor divided by the moles of CO leaving the system, then a material balance can be

performed around just the reactor (in contrast to the overall balance) to yield the conversion per pass through the reactor, x

$$x = \frac{F_{A_i} - (R+1)F_{A_e}}{F_{A_i}} \tag{A.4}$$

where F_{A_i} is the molar feed rate at the inlet of the reactor, as opposed to the inlet of the reactor system, F_{A_0}. A material balance around the mixing point prior to the reactor inlet yields

$$\begin{aligned} F_{A_i} &= F_{A_0} + RF_{A_e} \\ F_{A_i} &= F_{A_0}(1 + R + RX) \end{aligned} \tag{A.5}$$

which, combined with the balance around the reactor (Equation A.4), enables the definition of the conversion per pass in terms of the overall conversion and the recycle ratio.

$$x = \frac{X}{1 + R - RX} \tag{A.6}$$

Given this definition of the conversion per pass, there are two extreme variations in the recycle reactor behavior. If R is 0, such that there is no recycle taking place, then the conversion per pass is equal to the overall conversion, and the reactor will behave like a plug flow reactor. If R approaches infinity, then for a finite overall conversion, the conversion per pass will approach zero, and the reactor will behave as if it were a continuous stirred tank reactor (CSTR). Thus, the recycle ratio should be relatively high in order to achieve a situation where the overall conversion is

fairly high for a differential reactor (greater than approximately 10%) with a low conversion per pass.

The recycle ratio can also be expressed in terms of the fraction recycled, α,

$$\begin{aligned} \alpha &= \frac{R}{R+1} \\ R &= \frac{\alpha}{1-\alpha} \end{aligned} \tag{A.7}$$

which varies from 0 to 1. Plugging this relation into Equation A.6

$$x = \frac{(1-\alpha)X}{1-\alpha X} \tag{A.8}$$

allows the determination of the conversion per pass in terms of the fraction recycled and the overall system conversion.

The standard conditions for the reactor runs performed in this dissertation involved setting the recirculation pump at its maximum flow rate. This resulted in a volumetric ratio of the internal flow rate to the exit flow rate of 23/1. For the sake of this argument, it will be assumed that this value approximates the value of R. For a recycle ratio of 23, the fraction recycled calculated from Equation A.7 is 0.9583. Assuming that the reaction rate is such that the overall fractional system conversion, X, is 0.20, then the conversion per pass, x, would be 0.0103. This simple example demonstrates numerically that even at high overall conversions, the conversion per pass in the reactor is sufficiently low to approximate a differential reactor, and thus eliminate transport effects.

Appendix B

Error Analysis

Where possible in this study, the 95% confidence interval is estimated for all values reported. The method for calculating the confidence interval is described below. In addition, two examples of calculating the propagation of error in an equation using the confidence intervals of several variables is given.

B.1 Confidence intervals

When the variance of a population used to calculate a mean is unknown, which is typically true of experimental data, then the normal distribution cannot be used to accurately describe the confidence interval [140]. Instead, the confidence interval, δq, for a mean, q, should be calculated using Equation B.1, especially when the

sample size used to calculate the mean is less than 20 [140,141].

$$\delta q = \frac{ts}{\sqrt{n}} \tag{B.1}$$

Using this equation, the mean can thus be reported as $q \pm \delta q$.

In Equation B.1, s is the standard deviation calculated from the population sample, n is the number of measurements in the sample, and t represents the value of the t distribution for $n-1$ degrees of freedom (one degree of freedom is used to calculate the mean). Values for the t distribution for selected degrees of freedom for 95% confidence intervals are given in Table B.1 [142]. Note that as the sample size increases beyond 20 items, the value of t changes less and is approximately 2. At an infinite sample size, the value of t is 1.9600, the value for 95% confidence intervals calculated by the normal distribution, showing that as the sample size increases, the t distribution approaches the normal distribution.

B.2 Recycle reactor propagation of error

Given a function Q, which is made up of n variables q_n (see Equation B.2), the variation can be represented as the function plus an error term ($Q \pm \Delta Q$).

$$Q = f(q_1, q_2, \cdots, q_n) \tag{B.2}$$

This error term can be expanded with a Taylor series to produce Equation B.3, where the dqs represent the experimental variations in each of the variables [143].

Table B.1: t distribution values for 95% confidence interval calculations.

Degrees of freedom (df)	t for 95% confidence limits
1	12.706
2	4.3027
3	3.1824
4	2.7764
5	2.5706
6	2.4469
7	2.3646
8	2.3060
9	2.2622
10	2.2281
11	2.2010
12	2.1788
13	2.1604
14	2.1448
15	2.1314
20	2.0860
25	2.0595
30	2.0423
40	2.0211
60	2.0003
120	1.9799
∞	1.9600

To obtain Equation B.3 it was assumed that these experimental variations are fairly small and that the second order and higher order terms could be ignored in the Taylor expansion.

$$dQ = \frac{\partial f}{\partial q_1} dq_1 + \frac{\partial f}{\partial q_2} dq_2 + \cdots + \frac{\partial f}{\partial q_n} dq_n \tag{B.3}$$

If the differential variations are assumed to be equal to small, finite values, Δqs, then Equation B.4 can be used to represent the total experimental error for a given function with known confidence limits on the individual variables.

$$\Delta Q = \frac{\partial f}{\partial q_1} \Delta q_1 + \frac{\partial f}{\partial q_2} \Delta q_2 + \cdots + \frac{\partial f}{\partial q_n} \Delta q_n \tag{B.4}$$

When Equation B.4 is applied, any negative terms will be assumed positive so that there is no cancellation of error terms. Thus, this expression is a conservative estimate of the total experimental error resulting from propagation of variable errors. The following sections detail the use of Equation B.4 for the calculation of fractional conversions and rates of reaction from gas chromatography (GC) data.

B.2.1 Conversion calculation from GC peak areas

Given a reference GC peak area obtained by bypassing the reactor feed, A_b, and a product stream GC peak area, A_p, then the fractional conversion is simply the difference between the inlet feed concentration, represented by A_b, and the outlet

concentration, A_p, divided by the inlet concentration.

$$X = \frac{A_b - A_p}{A_b} = 1 - \frac{A_p}{A_b} \tag{B.5}$$

Applying Equation B.4 to this definition (Equation B.5), we arrive at Equation B.6,

$$\begin{aligned} \Delta X &= \frac{\partial X}{\partial A_b}\Delta A_b + \frac{\partial X}{\partial A_p}\Delta A_p \\ &= -\frac{\Delta A_b}{A_b} + \frac{\Delta A_p}{{\Delta A_b}^2}\Delta A_p \end{aligned} \tag{B.6}$$

where ΔA_b and ΔA_p are the experimental errors in the bypass and product GC peak areas, respectively.

Since the confidence interval for the mean fractional conversion is represented by $X \pm \Delta X$, the final equation for the error in conversion is given by Equation B.7.

$$X \pm \Delta X = \left(1 - \frac{A_p}{A_b}\right) \pm \left(\frac{\Delta A_b}{A_b} + \frac{\Delta A_p}{{\Delta A_b}^2}\Delta A_p\right) \tag{B.7}$$

The errors for the two mean peak areas can be determined by the method described at the beginning of this Appendix.

B.2.2 Rate of reaction calculation

The CO oxidation rate per gram of catalyst can be determined for a recycle reactor from the CO conversion by the following equation,

$$-r_A = \frac{F_{A_0}}{W} X \tag{B.8}$$

where $-r_A$ is the reaction rate, F_{A_0} is the molar flow rate of CO, W is the catalyst weight, and X is the fractional conversion of CO. The molar flow rate can be related to the mass flow rate, $\dot{m}$, by the molecular weight and mass fraction of the CO, so this equation can be rewritten as Equation B.9,

$$-r_A = \frac{y}{\mathrm{MW}} \frac{\dot{m}}{W} X \tag{B.9}$$

where y is the mass fraction of CO and MW is the molecular weight of the CO.

Application of Equation B.4 to this function results in an expression for the error in the rate of reaction.

$$\Delta r_A = \frac{y}{\mathrm{MW}} \left(\frac{X}{W} \Delta\dot{m} + \frac{X\dot{m}}{W^2} \Delta W + \frac{\dot{m}}{W} \Delta X \right) \tag{B.10}$$

Combining this expression with Equation B.9 then gives the formula for the confidence interval on the rate of reaction, given the confidence intervals for the fractional conversion, mass flow rate, and weight of catalyst.

$$-r_A \pm \Delta r_A = \frac{y}{\mathrm{MW}} \frac{\dot{m}}{W} X \pm \frac{y}{\mathrm{MW}} \left(\frac{X}{W} \Delta\dot{m} + \frac{X\dot{m}}{W^2} \Delta W + \frac{\dot{m}}{W} \Delta X \right) \tag{B.11}$$

Appendix C

Information on the HC–1, HC–2, & HC–3

The equipment used for hydrodynamic cavitation in this thesis is commercially available from Five Star Technologies of Cleveland, Ohio. The HC–1 used in the initial experimental work was a dual orifice device denoted as the Submicronizer™ model P–150. The HC–2 used for the work in Chapter 7 was a high volume, high flow rate (approximately 13.1 $\pm$ 0.2 L/min), low pressure (100-700 psig) cavitational device with an electrically driven motor which is a model CaviMax™. The final cavitation device used in this study was the HC–3 (see Chapters 7 & 8), which was a larger, more developed version of the HC–1, called the CaviPro™ model 300. Both the P–150 Submicronizer™ and the CaviPro™ use air driven pumps to achieve processing pressures in excess of 10,000 psig.

The design of equipment for cavitational processing is very complex, as the

information given in Chapter 3 suggests. Thus, it was decided in this experimental program to focus on the effects of cavitation rather than on the design of equipment to produce cavitation. Although the design information for the equipment used in this study is proprietary to Five Star Technologies, there are several patents pertaining to some of the work [144–146].

The three pieces of equipment used for this research, as well as some financial contribution, were supplied by Five Star Technologies, and their support is gratefully acknowledged.

References

[1] F. R. Young. *Cavitation*. McGraw-Hill: London, 1989.

[2] A. A. Atchley and L. A. Crum. *Ultrasound: Its Chemical, Physical and Biological Effects*, page 1. VCH: New York, 1988.

[3] J. A. Rooney. *Ultrasound: Its Chemical, Physical and Biological Effects*, page 65. VCH: New York, 1988.

[4] K. S. Suslick. *Ultrasound: Its Chemical, Physical and Biological Effects*, page 123. VCH: New York, 1988.

[5] R. A. van Santen and J. W. Niemantsverdriet. *Chemical Kinetics and Catalysis*. Plenum: New York, 1995. 224.

[6] R. van Hardeveld and F. Hartog. *Adv. Catal.*, 22:75, 1972.

[7] E. L. Venturini, J. P. Wilcoxon, and P. P. Newcomer. *Mater. Res. Soc., Symp. Proc.* volume 351, pages 311–316, 1994.

[8] J. P. Wilcoxon, A. J. Martino, R. L. Baughman, E. Klavetter, and A. P. Sylwester. *Mater. Res. Soc., Symp. Proc.* volume 286, page 131, 1993.

[9] J. P. Wilcoxon, R. L. Williamson, and R. Baughman. *J. Chem. Phys.*, 98:9933, 1993.

[10] W. G. Busser, J. G. van Ommen, and J. A. Lercher. *Advanced Catalysts and Nanostructured Materials*, page 213. Academic: San Diego, 1996.

[11] D. W. Matson, J. C. Linehan, and M. E. Geusic. *Particulate Science and Technology*, 10:143–154, 1992.

[12] D. W. Matson, J. C. Linehan, and R. M. Bean. *Materials Letters*, 14:222–226, 1992.

[13] W. R. Moser, J. D. Lennhoff, J. E. Cnossen, K. Fraska, J. W. Schoonover, and J. R. Rozak. *Advanced Catalysts and Nanostructured Materials*, page 535. Academic: San Diego, 1996.

[14] K. E. Shriver, J. L. Persson, E. E. Honea, and R. L. Whetten. *Phys. Rev. Letter*, 64:2539, 1990.

[15] D. M. Cox, A. Kaldor, P. Fayet, W. Eberhardt, R. Brickman, R. Sherwood, Z. Fu, and D. Sondericher. *Novel Materials in Heterogeneous Catalysis*, page 172. American Chemical Society, 1990.

[16] R. W. Siegel. *Annu. Rev. Mater. Sci.*, 21:559–578, 1991.

[17] R. W. Siegel. *Encyclopedia of Applied Physics*, volume 11, page 173. VCH, 1994.

[18] W. R. Moser, editor. *Advanced Catalysts and Nanostructured Materials*. Academic: San Diego, 1996.

[19] W. R. Moser, B. J. Marshik, J. Kingsley, M. Lemberger, R. Willette, A. Chan, J. E. Sunstrom IV, and A. Boye. *J. Catal.*, 10:2332, 1995.

[20] K. S. Suslick, S. Choe, A. A. Clchowlas, and M. W. Grinstaff. *Nature*, 353:414, 1991.

[21] K. S Suslick, T. Hyeon, M. Fang, and A. A. Cichowlas. *Advanced Catalysts and Nanostructured Materials*, page 197. Academic: San Diego, 1996.

[22] K. S Suslick, T. Hyeon, M. Fang, and A. A. Cichowlas. *Mater. Res. Soc. Symp. Proc.* volume 351, pages 201–206, 1994.

[23] C. E. Brennan. *Cavitation and Bubble Dynamics*. Oxford University: New York, 1995.

[24] R. T. Knapp, J. W. Daily, and F. G. Hammitt. *Cavitation*. McGraw-Hill: New York, 1970.

[25] F. G. Hammitt. *Cavitation and Multiphase Flow Phenomena*. McGraw-Hill: New York, 1980.

[26] S. C. Emerson, C. F. Coote, H. Booth, J. C. Tufts, R. LaRocque, and W. R. Moser. *Stud. Surf. Sci. Catal.* volume 118, page 773. Elsevier: Amsterdam, 1998.

[27] M. Haruta. *Catalysis Today*, 36:153–166, 1997.

[28] M. Haruta, S. Tsubota, T. Kobayashi, H. Kageyama, M. Genet, and B. Delmon. *J. Catal.*, 144:175, 1993.

[29] S. Tsubota, D. A. H. Cunningham, Y. Bando, and M. Haruta. *Stud. Surf. Sci. Catal.* volume 91, pages 227–235. Elsevier: Amsterdam, 1995.

[30] S. Tsubota, A. Ueda, H. Sakurai, T. Kobayashi, and M. Haruta. *Environmental Catalysis*, pages 420–428. American Chemical Society, 1994.

[31] R. M. T. Sanchez, A. Ueda, K. Tanaka, and M. Haruta. *J. Catal.*, 168:125–127, 1997.

[32] Y. Yuan, A. P. Kozlova, K. Asakura, H. Wan, K. Tsai, and Y. Iwasawa. *J. Catal.*, 170:191–199, 1997.

[33] J. J. Burton. *Cat. Rev. Sci. Eng.*, 9:209, 1974.

[34] M. R. Hoare and P. Pal. *J. Crystal Growth*, 17:77, 1972.

[35] B. K. Laurich, D. C. Smith, and M. D. Healy. *Mater. Res. Soc., Symp. Proc.* volume 351, pages 49–54, 1994.

[36] B. M. Smyser, J. F. Connelly, R. D. Sisson, and V. Provenzano. *Mater. Res. Soc. Symp. Proc.* volume 457, pages 335–340, 1997.

[37] R. C. Garvie. *J. Phys. Chem.*, 82:219, 1978.

[38] K. Parks, L. Zhu, J. Ho, and S. J. Riley. *Z. Phys. D: At. Mol. Clusters*, 26:41–45, 1993.

[39] W. A. de Heer. *Rev. Mod. Phys.*, 65:611, 1993.

[40] R. C. Baetzold. *J. Chem. Phys.*, 55:4355, 1971.

[41] R. C. Baetzold. *J. Chem. Phys.*, 55:4363, 1971.

[42] R. C. Baetzold. *Surf. Sci.*, 36:123, 1973.

[43] R. C. Baetzold. *J. Catal.*, 29:129, 1973.

[44] C. R. Henry, C. Chapon, S. Giorgio, and C. Goyhenex. *Chemisorption and Reactivity on Supported Clusters and Thin Films*, pages 117–152. Kluwer Academic: Dordrecht, 1997.

[45] I. Stará and V. Matolín. *Surf. Sci.*, 313:99–106, 1994.

[46] M. Andersson, L. Holmgren, J. L. Persson, T. Åklint, and A. Rosén. *Mater. Res. Soc., Symp. Proc.* volume 351, pages 299–304, 1994.

[47] A. Kaldor and D. M. Cox. *J. Chem. Soc. Faraday Trans.*, 86:2459–2463, 1990.

[48] S. Bernal, J. J. Calvino, G. A. Cifredo, J. M. Rodríguez-Izquierdo, V. Perrichon, and A. Laachir. *J. Catal.*, 137:1–11, 1992.

[49] T. M. Salama, H. Hattori, H. Kita, K. Ebitani, and T. Tanaka. *J. Chem. Soc. Faraday Trans.*, 89:2067, 1993.

[50] M. S. Spencer. *J. Catal.*, 93:216–223, 1985.

[51] J. M. Montejano-Carrizales and J. L. Morán-López. *Nanostructured Materials*, 1:397–409, 1992.

[52] J. G. Allpress and J. V. Sanders. *Aust. J. Phys.*, 23:23, 1970.

[53] F. Kaeble. *Handbook of X-Rays*. McGraw-Hill: New York, 1967.

[54] H. W. King. *Handbook of Chemistry and Physics*, pages **12–**10. CRC Press: Boca Raton, 73 edition, 1992.

[55] G. A. Somorjai. *Introduction to Surface Chemistry and Catalysis*. John Wiley & Sons: New York, 1994. 529.

[56] E. B. M. Doesburg, R. H. Höppener, B. de Koning, X. Xiaoding, and J. J. F. Scholten. *Stud. Surf. Sci. Catal.* volume 31, page 767. Elsevier: Amsterdam, 1987.

[57] A. Masson, B. Bellamy, Y. H. Romdhane, M. Che, H. Roulet, and G. Dufour. *Surf. Sci.*, 173:479, 1986.

[58] J. A. Cusumano, G. W. Dembinski, and J. H. Sinfelt. *J. Catal.*, 5:471–475, 1966.

[59] S. Fuentes and F. Figueras. *J. Catal.*, 61:443–453, 1980.

[60] W. F. Taylor and H. K. Staffin. *Trans. Faraday Soc.*, 63:2309, 1967.

[61] V. Nikolajenko, V. Bosáček, and Vl. Daneš. *J. Catal.*, 2:127–130, 1963.

[62] J. C. Volta and J. L. Portefaix. *Appl. Catal.*, 18:1–32, 1985.

[63] J. C. Volta and J. M. Tatibouet. *J. Catal.*, 93:467–470, 1985.

[64] A. N. Desikan and S. T. Oyama. *Surface Science of Catalysis: In situ Probes & Reaction Kinetics*, volume 482 of *American Chem. Soc. Symposium Series*, page 260. American Chemical Society: Washington, D. C., 1992.

[65] J. Haber. *Stud. Surf. Sci. Catal.* volume 48, page 447. Elsevier: Amsterdam, 1989.

[66] S. N. Goncharova, E. A. Paukshtis, and B. S. Bal'zhinimaev. *Appl. Catal. A*, 126:67–84, 1995.

[67] H. W. Sarkas, S. T. Arnold, J. H. Hendricks, L. H. Kidder, C. A. Jones, and K. H. Bowen. *Z. Phys. D: At. Mol. Clusters*, 26:46–50, 1993.

[68] I. Stará, V. Nehasil, and V. Matolín. *Surf. Sci.*, 331–333:173–177, 1995.

[69] A. S. McLeod and L. F. Gladden. *J. Catal.*, 173:43–52, 1998.

[70] S. F. Jones, G. M. Evans, and K. P. Galvin. *Advances in Colloid and Interface Science*, 80:27–50, 1999.

[71] B. C. Kim, B. C. Pak, N. H. Cho, D. S. Chi, H. M. Choi, Y. M. Choi, and K. A. Park. *Flow Meas. Instrum.*, 8:85–92, 1997.

[72] K. Ramamurthi and K. Nandakumar. *Flow Meas. Instrum.*, 10:133–143, 1999.

[73] L. C. Hagenson and L. K. Doraiswamy. *Chemical Engineering Science*, 53:131–148, 1998.

[74] R. Rajan, R. Kumar, and K. S. Gandhi. *Chemical Engineering Science*, 53:255–271, 1998.

[75] D. V. P. Naidu, R. Rajan, R. Kumar, K. S. Gandhi, V. H. Arakeri, and S. Chandrasekaran. *Chemical Engineering Science*, 49:877–888, 1994.

[76] S. Fujikawa and T. Akamatsu. *J. Fluid Mech.*, 97:481–512, 1980.

[77] K. S. Suslick, M. M. Mdleleni, and J. T. Ries. *J. Am. Chem. Soc.*, 119:9303–9304, 1997.

[78] I. Z. Shirgaonkar and A. B. Pandit. *Ultrasonics Sonochemistry*, 4:245–253, 1997.

[79] P. S. Kumar, M. S. Kumar, and A. B. Pandit. *Chemical Engineering Science*, 55:1633–1639, 2000.

[80] T. Uchiyama. *Appl. Math Modelling*, 22:235–250, 1998.

[81] Lord Rayleigh. *Phil. Mag.*, 34:94–98, 1917.

[82] S. Sochard, A. M. Wilhelm, and H. Delmas. *Chemical Engineering Science*, 53:239–254, 1998.

[83] V. S. Moholkar and A. B. Pandit. *AIChE Journal*, 43:1641–1648, 1997.

[84] P. R. Gogate and A. B. Pandit. *AIChE Journal*, 46:372–379, 2000.

[85] V. S. Moholkar, P. S. Kumar, and A. B. Pandit. *Ultrasonics Sonochemistry*, 6:53–65, 1999.

[86] V. S. Moholkar, P. S. Kumar, and A. B. Pandit. *Ultrasonics Sonochemistry*, 2:S19–S25, 1995.

[87] S. Majumdar, P. S. Kumar, and A. B. Pandit. *Ultrasonics Sonochemistry*, 5:113–118, 1998.

[88] J.-L. Li and T Inui. *Appl. Catal. A*, 139:87–96, 1996.

[89] M. Schacham and M. B. Cutlip. *POLYMATH*. CACHE Corporation, 1996.

[90] MicroMath Scientific Software. *Scientist*, 1994.

[91] M. Kishida, T. Fujita, K. Umakoshi, J. Ishiyama, H. Nagata, and K. Wakabayashi. *J. Chem. Soc., Chem. Commun.*, 91:763–764, 1995.

[92] W-Y. Kim, T. Hanaoka, M. Kishida, and K. Wakabayashi. *Applied Catalysis A: General*, 155:283–289, 1997.

[93] M. Kishida, K. Ichiki, T. Hanaoka, H. Nagata, and K. Wakabayashi. *Catalysis Today*, 45:203–208, 1998.

[94] W-Y. Kim, H. Hayashi, M. Kishida, H. Nagata, and K. Wakabayashi. *Applied Catalysis A: General*, 169:157–164, 1998.

[95] B. R. Munson, D. F. Young, and T. H. Okiishi. *Fundamentals of Fluid Mechanics*. John Wiley & Sons: New York, 1990.

[96] J. Find, S. C. Emerson, I. M. Krausz, and W. R. Moser. In preparation. 2000.

[97] H. P. Klug and L. E. Alexander. *X-ray Diffraction Procedures*. John Wiley & Sons: New York, 1954.

[98] B. E. Warren. *X-ray Diffraction*. Addison-Wesley: Reading, 1969.

[99] B. D. Cullity. *Elements of X-ray Diffraction*. Addison-Wesley: Reading, 1978.

[100] SPSS, Inc. *SigmaPlot 4.0 for Windows*, 1997.

[101] WPI Nuclear Engineering Laboratory Handout. Neutron activation analysis.

[102] GE Nuclear Energy. Nuclides and isotopes, 1989.

[103] Galbraith Laboratories Incorporated. Gold by inductively coupled plasma emission spectroscopy, procedure E 79–3. FAX Transmittal, February 2000.

[104] R. H. Venderbosch, W. Prins, and W. P. M. van Swaajj. *Chem. Eng. Sci.*, 53(19):3355–3366, 1998.

[105] U. Kunz, C. Binder, and U. Hoffman. *Stud. Surf. Sci. Catal.* volume 91, page 869. Elsevier: Amsterdam, 1995.

[106] P. Bosch, T. López, M. Asomoza, R. Gómez, M. A. Cauqui, and J. M. Rodríguez-Izquierdo. *Langmuir*, 11:4328, 1995.

[107] C. L. Bianchi, R. Carli, C. Fontaneto, and V. Ragaini. *Stud. Surf. Sci. Catal.* volume 91, page 1095. Elsevier: Amsterdam, 1995.

[108] C. Sze, E. Gulari, and B. G. Demczyk. *Mater. Res. Soc., Symp. Proc.* volume 286, page 143, 1993.

[109] S. Bernal, J. J. Calvino, M. A. Cauqui, J. M. Rodríguez-Izquierdo, and H. Vidal. *Stud. Surf. Sci. Catal.* volume 91, page 461. Elsevier: Amsterdam, 1995.

[110] J. Lindley. *Ultrasonics*, 30:163, 1992.

[111] A. Tai, T. Kikukawa, T. Sugimura, Y. Inoue, S. Abe, T. Osawa, and T. Harada. In Guczi et al., editor, *New Frontiers in Catalysis: Proceedings of the 10th International Congress on Catalysis*, page 2443. Elsevier, 1993.

[112] N. A. Dhas, Y. Koltypin, and A. Gedanken. *Chem. Mater.*, 9:3159, 1997.

[113] L. D. David. *U.S. Patent 4 588 575*. 1986.

[114] H. C. Yao and Y. F. Yu Yao. *J. Catal.*, 86:254, 1984.

[115] F. Fajardie, J. Tempére, G. Djèga-Mariadassou, and G. Blanchard. *J. Catal.*, 163:77, 1996.

[116] R. S. Roth, J. R. Dennis, and H. F. McMurdie, editors. *Phase Diagrams for Ceramists*, volume VI. American Ceramic Society: Westerville, Ohio, 1987.

[117] M. Haruta, T. Kobayashi, H. Sano, and N. Yamada. *Chemistry Letters*, pages 405–408, 1987.

[118] S. Tsubota, M. Haruta, T. Kobayashi, A. Ueda, and Y. Nakahara. *Stud. Surf. Sci. Catal.* In G. et al. Poncelet, editor, *Preparation of Catalysts V*, page 695. Elsevier: Amsterdam, 1991.

[119] M. Haruta, H. Kageyama, N. Kamijo, T. Kobayashi, and F. Delannay. *Successful Design of Catalysts*, pages 33–42. Elsevier: Amsterdam, 1988.

[120] T. Hayashi, K. Tanaka, and M. Haruta. *J. Catal.*, 178:566–575, 1998.

[121] D. A. H. Cunningham, W. Vogel, H. Kageyama, S. Tsubota, and M. Haruta. *J. Catal.*, 177:1–10, 1998.

[122] Y. Yuan, K. Asakura, H. Wan, K. Tsai, and Y. Iwasawa. *Catalysis Letters*, 42:15–20, 1996.

[123] Y. Yuan, K. Asakura, H. Wan, K. Tsai, and Y. Iwasawa. *Chemistry Letters*, 9:755–756, 1996.

[124] Y. Yuan, K. Asakura, H. Wan, K. Tsai, and Y. Iwasawa. *Chemistry Letters*, 2:129–130, 1996.

[125] Y. Yuan, K. Asakura, A. Kozlova, H. Wan, K. Tsai, and Y. Iwasawa. *Catalysis Today*, 44:333–342, 1998.

[126] A. Kozlova, S. Sugiyama, A. Kozlov, K. Asakura, and Y. Iwasawa. *J. Catal.*, 176:426–438, 1998.

[127] A. Kozlova, A. Kozlov, S. Sugiyama, Y. Matsui, K. Asakura, and Y. Iwasawa. *J. Catal.*, 181:37–48, 1999.

[128] H. Liu, A. I. Kozlov, A. P. Kozlova, T. Shido, K. Asakura, and Y. Iwasawa. *J. Catal.*, 185:252–264, 1999.

[129] M. Valden, X. Lai, and D. W. Goodman. *Science*, 281:1647–1650, 1998.

[130] C. Wang, C. Liu, J. Chen, and T. Shen. *Journal of Colloid and Interface Science*, 191:464–470, 1997.

[131] L. Prati and R. Rossi. *J. Catal.*, 176:552–560, 1998.

[132] J. Grunwaldt, C. Kiener, C. Wögerbauer, and A. Baiker. *J. Catal.*, 181:223–232, 1999.

[133] D. Kondarides and X. Verykios. *J. Catal.*, 158:363–377, 1996.

[134] K. Sayo, S. Deki, and S. Hayashi. *Journal of Colloid and Interface Science*, 212:597–599, 1999.

[135] X. Chen, J. L. Li, X. Li, and L. Jiang. *Biochemical and Biophysical Research Communications*, 245:352–355, 1998.

[136] D. C. Montgomery. *Design and Analysis of Experiments*. John Wiley & Sons: New York, 1997.

[137] G. E. P. Box, W. G. Hunter, and J. S. Hunter. *Statistics for Experimenters*. John Wiley & Sons: New York, 1978.

[138] A. B. Pandit, P. S. Kumar, and M. S. Kumar. *Chemical Engineering Progress*, 95(5):43–50, May 1999.

[139] I. S. Metcalfe. *Chemical Reaction Engineering: A First Course*. Oxford University: Oxford, 1997.

[140] H. S. Mickley, T. K. Sherwood, and C. E. Reed. *Applied Mathematics in Chemical Engineering*, pages 66–68. McGraw-Hill: New York, 1957.

[141] R. J. Freund and W. J. Wilson. *Statistical Methods*, page 102. Academic Press: San Diego, 1997.

[142] R. J. Freund and W. J. Wilson. *Statistical Methods*, page 638. Academic Press: San Diego, 1997.

[143] H. S. Mickley, T. K. Sherwood, and C. E. Reed. *Applied Mathematics in Chemical Engineering*, page 54. McGraw-Hill: New York, 1957.

[144] Oleg V. Kozyuk. *U.S. Patent 5 931 771*. 1999.

[145] Oleg V. Kozjuk, A. A. Litvinenko, B. K. Kravets, and V. V. Berezin. *U.S. Patent 5 492 654*. 1996.

[146] Oleg V. Kozyuk. *U.S. Patent 5 937 906*. 1999.